Johannes Wüthrich

Low Temperature Wafer-Wafer Bonding For Particle Detection

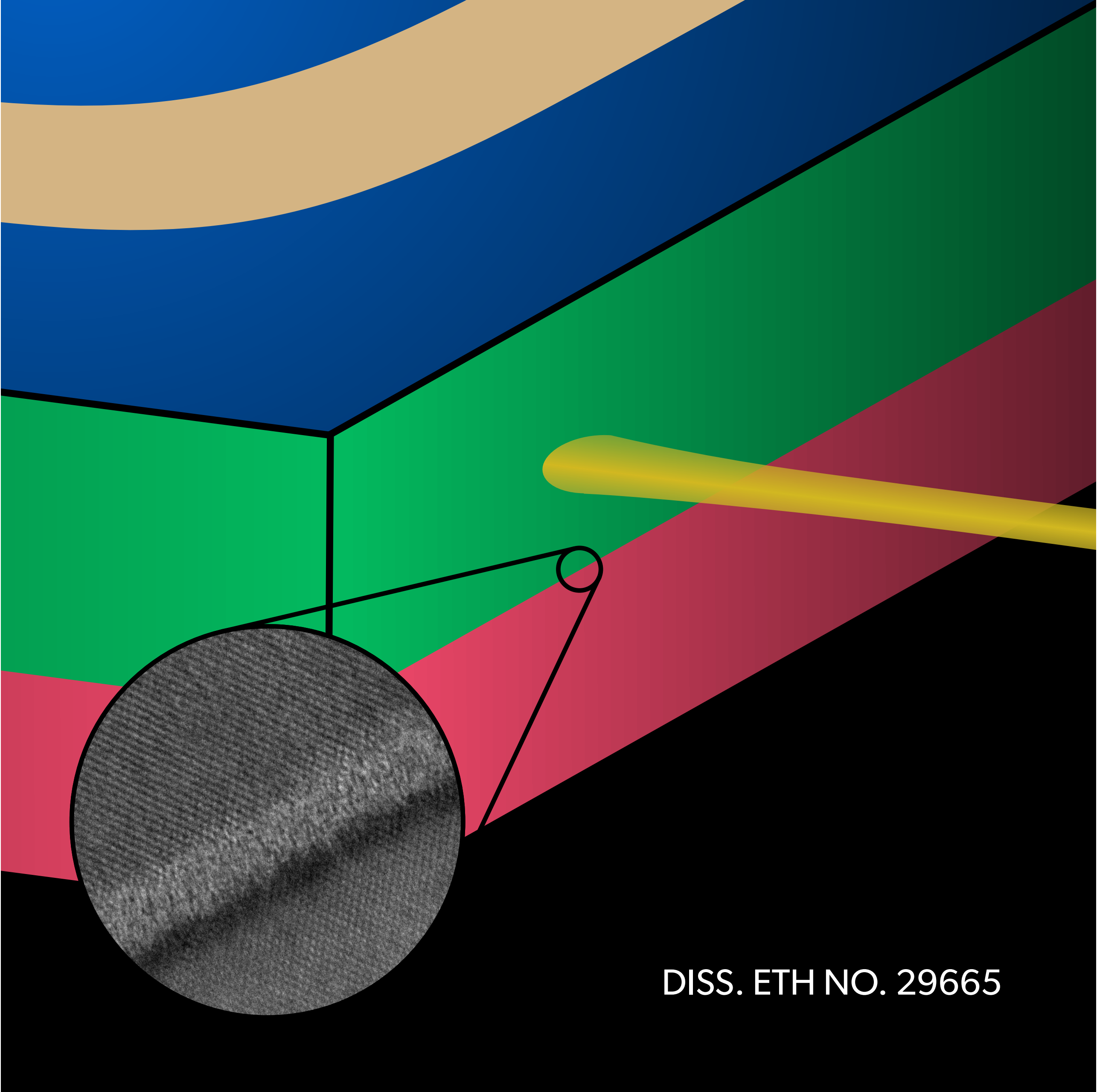

DISS. ETH NO. 29665

DISS. ETH NO. 29665

LOW-TEMPERATURE WAFER-WAFER BONDING FOR PARTICLE DETECTION

A thesis submitted to attain the degree of

DOCTOR OF SCIENCES
(Dr. sc. ETH Zurich)

presented by

JOHANNES MARTIN WÜTHRICH
MSc. EPFL

born on 07.03.1993

accepted on the recommendation of

Prof. Dr. André Rubbia
Prof. Dr. Rainer Wallny
Dr. Luciano Musa

2023

Johannes Wüthrich:
Low-temperature wafer-wafer bonding for particle detection © 2023

DOI: 10.3929/ethz-b-000658117

To my tiny family.

ABSTRACT

Given the omnipresence and economical availability of silicon semiconductor processes, it is no surprise that direct detection particle pixel detectors are commonly fabricated using these processes. However, silicon is not the ideal sensor material for certain applications, such as X-ray imaging, due to its low stopping power of higher energy particles. For these applications, high-Z semiconductor materials, e.g., GaAs, SiGe and CdZTe, enable a more efficient conversion of incident particles into electrical signals. For economic reasons, it is not feasible to implement the highly integrated detector electronics in such high-Z materials. Therefore, in order to build detectors using these materials, one has to combine a high-Z sensor layer with the readout electronics implemented in silicon. Traditionally, such hetero-detectors are built using bump bonding, which connects the sensor and the readout electronics using a grid of small solder joints. This thesis investigates the use of surface activated wafer bonding as an alternative technique to build hetero-structure detectors.

This low-temperature covalent bonding technique allows to directly fuse different semiconductor layers without any additional materials at the bonding interface. This enables the creation of hetero structures by directly bonding a high-Z sensing layer to a silicon-based readout layer. Imposed by the bonding technique, the transition between the two bonded layers is not abrupt, but includes a thin (nm) layer of amorphous material. This amorphous region has a high concentration of crystalline defects and thus influences the electrical behaviour of the assembled detectors.

Previous studies proposed that the effect of these defects could be minimized by placing the P/N junction of the detector at the bonding interface. In order to investigate this claim, covalently bonded pad diodes are fabricated by bonding high resistivity P- to N-type silicon wafers as commonly used in pixelized particle detectors. Transmission electron microscope (TEM) measurements of these samples show the formation of a ca. 3 nm wide amorphous layer at the bonding interface. Energy-dispersive X-ray spectroscopy (EDXS) measurements of the samples highlight the presence of additional metal contaminants, which can be traced back to the bonding process.

The feasibility of using such structures for particle detection is investigated based on transient current technique (TCT) measurements. The TCT measurements show a one-sided depletion behaviour of the samples, whereas only the P-type wafer can be depleted. This one-sided depletion indicates that the bonding interface of the fabricated samples behaves like a highly doped N++ layer, strongly influencing the electrical behaviour of the sensor structure. Based on this observation, a model, which includes an extension to the Shockley-Ramo theorem, is developed to predict the time domain signal shape produced by particles interacting in the fabricated samples. This model is shown to accurately predict the signals measured with an americium-241 (Am-241) α-source from first principles.

ZUSAMMENFASSUNG

Angesichts der weiten Verbreitung und wirtschaftlichen Verfügbarkeit von Silizium-Halbleiterprozessen ist es nicht überraschend, dass direkt detektierende Teilchen-Pixeldetektoren üblicherweise aus Silizium hergestellt werden. Aber für bestimmte Anwendungen, wie beispielsweise Röntgenbildgebung, ist Silizium aufgrund seines geringen Bremsvermögens für hochenergetische Teilchen nicht das ideale Sensormaterial. Für solche Anwendungen ermöglichen Halbleitermaterialien mit hoher Ordnungszahl (*High-Z*), wie z. B. GaAs, SiGe und CdZTe, eine effizientere Umwandlung der wechselwirkenden Teilchen in elektrische Signale. Aus wirtschaftlichen Gründen ist es jedoch nicht praktikabel die integrierte Detektorelektronik in solchen Materialien zu realisieren. Um also Detektoren mit solchen Materialien zu bauen muss eine *High-Z*-Sensorschicht mit einer in Silizium implementierten Ausleseelektronik kombiniert werden. Üblicherweise werden solche Hetero-Detektoren via Bump-Bonding hergestellt, bei welchem der Sensor und die Ausleseelektronik durch miniaturisierte Lötpunkte miteinander verbunden werden. In der vorliegenden Doktorarbeit wird die Verwendung von *surface activated wafer bonding* als alternative Technik zur Herstellung von Hetero-Detektoren untersucht.

Diese kovalente Wafer-Bonding Technik ermöglicht das direkte Verbinden verschiedener Halbleiterschichten bei niedrigen Temperaturen ohne das Zuführen von zusätzlichen Materialien an der Bindungsgrenzfläche. Dadurch wird die Herstellung von Heterostrukturen ermöglicht, indem eine *High-Z*-Sensorschicht direkt mit einer auf Silizium basierenden Ausleseelektronik verbunden wird. Bedingt durch den Bonding-Prozess ist der Übergang zwischen den verbundenen Schichten nicht abrupt, sondern schliesst eine dünne (nm) amorphe Schicht ein. Diese amorphe Schicht weist eine hohe Konzentration an kristallinen Defekten auf welche das elektrische Verhalten des hergestellten Detektors beeinflussen.

In früheren Forschungsarbeiten wurde vorgeschlagen, dass die Auswirkungen dieser Defekte minimiert werden könnten, indem man den P/N-Übergang des Detektors an der Bindungsgrenzfläche platziert. In

dieser Doktorarbeit wird dieser Vorschlag untersucht indem kovalent gebundene Pad-Dioden hergestellt werden durch das Bonden von P- und N-dotierten Siliziumwafern. Die Wafer haben einen hohen spezifischen Widerstand, wie es bei Pixel-Teilchendetektoren üblich ist. TEM-Messungen dieser Proben zeigen die Bildung einer ca. 3 nm breiten amorphen Schicht an der Bindungsgrenzfläche. EDXS-Messungen der Proben weisen auf das Vorhandensein von metallischen Verunreinigungen hin, welche auf den Bonding-Prozess zurückzuführen sind.

Das Verhalten der hergestellten Strukturen als Teilchendetektoren wird anhand von TCT-Messungen untersucht. Die TCT-Messungen zeigen die Bildung einer einseitigen Raumladungszone in den Proben, wobei nur der P-dotierte Wafer verarmt werden kann. Dies deutet darauf hin, dass die Bindungsgrenzfläche in den hergestellten Proben sich wie eine hoch dotierte N++ Schicht verhält und somit einen starken Einfluss auf das elektrische Verhalten der Sensorstruktur hat. Basierend auf dieser Beobachtung, und unter Verwendung einer Erweiterung des Shockley-Ramo-Theorems, wird ein Modell entwickelt um das zeitliche Signal vorherzusagen, welches durch Wechselwirkungen von Teilchen in den hergestellten Proben erzeugt wird. Dieses Modell ermöglicht die korrekte quantitative Vorhersage von Signalen welche mit einer Am-241 α-Quelle gemessen wurden.

ACKNOWLEDGEMENTS

I would like to thank Professor André Rubbia for giving me the opportunity to write this thesis. André very enthusiastically answered to my cold email five years ago which eventually led to my employment at ETHZ and to the results presented in this document. I am very grateful for the liberties and the continued support André has given me during this time. I would also like to thank Professor Paolo Crivelli for his support, as well as Professor Davide Sgalaberna especially for all the interesting and inspiring discussions. The beginning of this project was in very close collaboration with G-Ray Medical Sàrl and I very much enjoyed the collaboration and discussions with Hans, Jorge, Ivan and Nasser during this phase of the project, and I would like to thank all of you very much for all your inputs.

I had the privilege of working at the Institute of Particle and Astrophysics of ETHZ giving access to outstanding infrastructure. I would like to thank Adamo, Diogo, Jan, Bruno and Patrick from the institute Techpool for all the electronics and mechanical work they have carried out for me and this project. A big thank you also goes out to Bettina, Jennifer and Gabriela for all the administrative help. The other advantage of working in this institute comes in the form of great colleagues, who helped making this very demanding phase of my life much more enjoyable. Thank you to Alex, Irene, Botao, Till, Matt, Emilio, Gianluca, Lucas, Philipp, Benjamin, Laura, Saúl, Tim and Umut to name a few. I would like to especially thank Sebastien Murphy and Christoph Alt for their collaboration on my project in the beginning and towards the end of my thesis respectively. Thank you very much for your help, your contributions, and for all the discussions.

During these five years I had the pleasure to interact with many different groups and people. Most of the time it was me contacting somebody out of the blue with a request to use some of their equipment or infrastructure. And, to my continuing surprise, I very often got positive responses to my requests. I would like to thank Vasilije Perovic, Maren Meinhard and Malte Backhaus for enabling me to do measurements using the X-Ray cabinet at ETHZ. A warm thank you to Ute Drechsler and Ronald Grundbacher

from the BRNC cleanroom operations team for all the help with the processing of the wafer-wafer bonded diodes samples. I am thankful for all the work Eszter, Peng and Fabian of ScopeM have carried out to characterize the bonding interface of the fabricated samples using STEM and EDXS measurements. A big thank you also goes out to Matías Senger and Anna Macchiolo from the CMS group at UZH, for giving me access to their probe station. Thank you very much to Michael Moll for giving me access to the TPA TCT measurement setup at CERN and to Sebastian Pape for helping me with these measurements, as well as the many very interesting discussions. And also a very big thank you to Burkhard Beckhoff and Philipp Hönicke from the PTB, for hosting me at BESSY II for a week to carry out the TXRF measurements on the unbonded wafers.

I am forever grateful to my family and my parents for giving me the foundation to build my path on, which lead me to where I am today. Spending a weekend back home, enjoying the garden, relaxing and playing Frantic was always something too look forward to. A big thank you also to Sam for all the (social) running, swimming and beers, which helped a lot to change my state of mind after especially stressful days. Finally I would like to thank my partner Ana for accompanying me throughout all this journey. Coming home to you and the two cats was always the nicest part of my day, even if it often happened very late in the evening. I am very happy that we took on this adventure to move to Zürich five years ago, and I am curious to see what the future has in store for us now that my thesis is coming to an end.

ABOUT THE QUOTES

The attentive reader notices that the quotes at the beginning of each chapter deviate from the usual approach of quoting famous physicists and scientists, as the quotes seem to be of a certain feline nature. The two names, Emmy and Hilbert, refer to the two cats who share their life with the author, and the content of the (made up) quotes illustrate the joys and struggles of living together with two very demanding and affectionate feline creatures. But the names also feel familiar to a reader having knowledge in the history of mathematics and physics. This is no coincidence as Emmy (the cat) is named after Emmy Noether and Hilbert (the cat) after David Hilbert.

It was only after making the decision to give these names to the cats that the author learned about the long lasting friendship of their real life name-sakes. Not only was Emmy Noether inspired by the work of David Hilbert, it was also Hilbert who invited Noether to join him in Göttingen. When she was initially refused a teaching position by the university on the account of her being a woman, Hilbert responded with indignation about this unfair and sexist treatment of Emmy Noether. Hilbert continued to support her over the next years, enabling her to hold lectures herself, although often not officially under her own name but under the name of Hilbert. All this adversity did not hinder Emmy Noether to have a lasting impact on her students and on physics, with Noether's theorem being one of the most fundamental principles of modern physics [1–3].

Therefore, the quotes in this thesis are not only an acknowledgement of the joy and happiness the two cats brought the author over the years, but also a celebration of the work and contributions of Emmy Noether and David Hilbert to mathematics and physics, as well as their friendship and support for each other.

NOTATIONS

SURFACE ACTIVATED BONDING The bonding technique used in this thesis is generally referred to as either *surface activated bonding* or *low/room temperature covalent wafer bonding*. The second term better highlights the fact that bonding at room temperature is possible. But the technique was originally presented as *surface activated bonding* which is the term also most commonly used in literature.

DETECTOR The terms *detector* and *sensor* in general do not have a clear distinction, but instead, depending on the field of research, a device might be called a *detector* or a *sensors*. In the field of radiation pixel detectors, especially hybrid detectors, *sensor* might refer to the part of the device which is sensitive to particle interactions. In this thesis, the two terms are used interchangeably without any distinction.

PARTICLE DETECTOR In the context of this thesis the two terms *particle detector / sensor* and *radiation detector / sensor* are used interchangeably. The terms *particles* and *radiation* refer to to ionizing particles and radiation.

WEIGHTING FIELDS AND VECTORS In this thesis the weighting field of the Shockley-Ramo theorem will be denoted as $\vec{W}_F$, in contrast to the notation $\vec{E}_v$ or $\vec{E}_w$ usually chosen in literature. This is done to better differentiate the weighting field from the electric field. For consistency, the weighting vector of the extended Shockley-Ramo theorem is denoted $\vec{W}_V$, instead of just W as used in the source material from W. Riegler [4]. Weighting fields and weighting vectors with respect to a specific electrode n or i will be denoted with superscripts as $\vec{W}_F^{(n)}$ or $\vec{W}_V^{(i)}$.

CONTENTS

List of Figures xv

List of Tables xix

List of Listings xix

1 INTRODUCTION 1
  1.1 Thesis overview 6

2 FUNDAMENTALS OF SEMICONDUCTOR PARTICLE DETECTORS 9
  2.1 Semiconductor materials 10
  2.2 Interaction of ionizing radiation with matter 14
  2.3 Signal generation via charge drift 20
  2.4 Extended Shockley-Ramo theorem 25
  2.5 Detector structures 30

3 WAFER-WAFER BONDED PARTICLE DETECTORS 33
  3.1 Wafer-wafer bonding 33
  3.2 Prior work by G-Ray 44
  3.3 The BigNovipix prototype 47

4 FABRICATION OF WAFER-WAFER BONDED DIODE SAMPLES 53
  4.1 Process development 55
  4.2 Production run 67

5 METAL CONTAMINATION OF THE BONDING INTERFACE 75
  5.1 STEM and EDXS measurements 76
  5.2 TXRF measurements of unbonded wafers 80
  5.3 Discussion 82

6 TRANSIENT CURRENT TECHNIQUE (TCT) 85
  6.1 Principle of TCT 85
  6.2 ETHZ TCT Measurement Setup 93
  6.3 Sandwich-type sample holder 106
  6.4 Edge polishing 109

7 DEPLETION BEHAVIOUR OF BONDED P/N JUNCTIONS 113
  7.1 Top / bottom TCT measurements 114
  7.2 Edge TCT measurements 118
  7.3 Empirical P/N++/N model 119

8 SIMULATION OF TIME-DOMAIN SIGNALS 127
  8.1 TCAD based simulations 127

8.2 Simulation via charge propagation 130
8.3 Simulation model for bonded diodes 136
9 TIME-DOMAIN SIGNALS OF BONDED SENSORS 155
9.1 TCT measurements with an Am-241 α source 156
9.2 Comparison with simulation 164
9.3 Influence of the bias voltage on the exponential tail 166
10 CONCLUSION AND OUTLOOK 169
A DETAILED FABRICATION PROCESS 173
A.1 Mask fabrication 173
A.2 Alignment mark etching 173
A.3 Contact doping 174
A.4 Wafer bonding 175
A.5 Contact metallization: N-side 176
A.6 Contact metallization: P-side 177
A.7 Dicing 178
B DERIVATION OF THE WEIGHTING VECTORS FOR THE BONDED SAMPLES 179
B.1 Case A: Partially depleted P-side 179
B.2 Case B: Fully depleted P-side 183

LIST OF ACRONYMS 185
BIBLIOGRAPHY 189

LIST OF FIGURES

Figure 1.1 First radiograph of a human hand, taken by Röntgen in 1895. 1
Figure 1.2 Schematic cross section of a single pixel of a detector fabricated by wafer-wafer bonding. 5
Figure 2.1 Illustration of the band structures under different doping regimes. 11
Figure 2.2 Schematic view of an abrupt P/N junction. 13
Figure 2.3 Energy loss function (stopping power) of positive muons in copper. 15
Figure 2.4 Attenuation of X-ray / gamma ray photons of different energies in Si. 17
Figure 2.5 Interaction probability of a 30 keV X-ray photon in various semiconductor materials. 18
Figure 2.6 Cross section of a single pixel of a particle pixel detector showcasing the different possible detector structures. 30
Figure 3.1 Schematic view of the surface activated bonding process. 38
Figure 3.2 Schematic view of different mechanical surface energy characterization methods for wafer-wafer bonds. 40
Figure 3.3 High resolution transmission electron microscope image of a silicon/silicon bonding interface produced by G-Ray. 47
Figure 3.4 High-level circuit diagram of a single pixel of the BNP. 48
Figure 3.5 Overview of the BNP sensor fabricated by G-Ray. . . 49
Figure 3.6 Example X-ray images acquired with the BNP samples as part of the characterization at ETHZ. 50
Figure 4.1 Schematic cross section view of a bonded diode sample as fabricated for this thesis. 54
Figure 4.2 Different elements of the mask set. 57
Figure 4.3 Behaviour of an ideal metal-semiconductor contact in the case of an N-type semiconductor in contact with a high-work-function metal. 58

Figure 4.4 Contact doping profiles as simulated with Sentaurus. 60
Figure 4.5 Simplified illustration of the different approaches for metal patterning via lift-off. 62
Figure 4.6 Different electrical test structures implemented on the wafers and used for process control. 64
Figure 4.7 Full mask set used in the fabrication of the bonded diode samples. 66
Figure 4.8 Detail view of the bonded diode structures. 67
Figure 4.9 Example results from the SAM measurements carried out by EVG right after bonding. 69
Figure 4.10 Analysis of the misalignment of the P- and N-wafer after bonding. 70
Figure 4.11 Example I/V curve of the sample **P301401-C7** showing a clear rectifying diode-like behaviour. 71
Figure 4.12 Average I/V curve for each diode type as measured with samples from **P301401**. 72
Figure 4.13 Current as a function of the diode surface are at various bias voltages for all measured samples of **P301401**. 73
Figure 4.14 Detailed view of the reverse bias current behaviour of all measured samples of **P301401**. 73
Figure 5.1 STEM-based interface characterization of a sample from **P301401**. 76
Figure 5.2 2D map of the contaminating metal elements observed via EDXS on a sample of **P301401**. 78
Figure 5.3 Quantification of the metal contamination observed at the interface via EDXS measurements. 79
Figure 5.4 Schematic view of the principle behind TXRF measurements. 81
Figure 5.5 Results from the TXRF measurements of unbonded wafers. 82
Figure 6.1 Schematic view of surface and edge TCT charge injection via laser. 86
Figure 6.2 Illustration of the principle of TPA TCT. 88
Figure 6.3 Simulated TCT signal illustrating the timing for a prompt current analysis. 91
Figure 6.4 View of the TCT system commissioned at ETHZ. . . 94

Figure 6.5 Schematic view of the biasing and signal path used in the ETHZ TCT system. 95
Figure 6.6 Software stack of the ETHZ TCT setup control framework. 98
Figure 6.7 Views of the TCT online data interface. 103
Figure 6.8 TCT pulses recorded with the Particulars *AM-02* amplifier operating at different gain levels. 104
Figure 6.9 Amplifier gain and input reflection of the Particulars *AM-02* amplifier at different supply voltages. 105
Figure 6.10 The sandwich-type sample holder. 106
Figure 6.11 Annotated top layer view of the two printed circuit boards (PCBs) used in the sandwich-type sample holder. 107
Figure 6.12 Different effects leading to bad edge TCT measurement results due to non-polished sample edges. . . . 110
Figure 6.13 Microscopic view of a sample edge at various stages of polishing. 111
Figure 6.14 Comparison of the edge TCT curves recorded before and after polishing of the sample edge. 112
Figure 7.1 Integrated signal vs. bias voltage for the six samples in the case of top and bottom TCT using the red and IR lasers. 115
Figure 7.2 Fraction of the integrated TCT signal under IR laser illumination of P-side vs. N-Side. 117
Figure 7.3 Integrated signal measured via edge TCT as a function of the position across the diode. 120
Figure 7.4 Integrated signal measured via TPA TCT for the sample **P301401-E2**. 121
Figure 7.5 Weighted prompt current curves extracted from the edge TCT measurements of all six samples. 123
Figure 8.1 Example of the mesh created in Sentaurus TCAD at a corner of the P-side contact of a bonded diode. . . . 130
Figure 8.2 View of the online simulation interface. 137
Figure 8.3 Schematic view of the two cases taken into account for the charge propagation simulation model of the fabricated bonded diodes. 138
Figure 8.4 Shapes of the different deposited charge distributions.141

Figure 8.5 Example electric field configurations at various bias voltages. 142
Figure 8.6 Electron (v_e) and hole (v_h) drift velocities. 144
Figure 8.7 Shape of the reduced weighting vector $\hat{W}_V(t)$ for various cases. 148
Figure 8.8 Equivalent circuit model of the sensor and the front-end electronics of the TCT system. 149
Figure 8.9 Bode plot of the $Z_{tot}(i\omega)$ transfer function for different cases. 150
Figure 8.10 Example curves simulated with the presented simulation model. 151
Figure 8.11 Evaluation of the performance and accuracy of the simulation model. 152
Figure 9.1 Example TCT time domain curves highlighting the presence of a long exponential tail. 156
Figure 9.2 Illustrations of the source placement for the α measurements. 157
Figure 9.3 Averaged time domain TCT signals measured with the Am-241 α source. 158
Figure 9.4 Distribution of the energy deposited by the α particles for the different air gap distances. 161
Figure 9.5 Comparison between simulated and measured α TCT curves. 162
Figure 9.5 (continued) 163
Figure 9.6 Comparison of the measured and simulated integrated signal. 165
Figure 9.7 Qualitative observation of the plasma effect. 165
Figure 9.8 Bias dependency of the exponential tail, based on edge TCT measurements of **P301401-E12**. 167
Figure B.1 Schematic view of the two cases taken into account for applying the extended Shockley-Ramo theorem to the fabricated bonded diodes. 180

LIST OF TABLES

Table 2.1 Average electron-hole pair creation energy $E_{e/h}$ and band gap E_g for various semiconductor materials. . . 19
Table 4.1 Ion beam implantation and doping activation parameters of the developed process. 60
Table 4.2 Overview of the different diode sizes implemented on a single wafer. 66
Table 4.3 Specifications of the wafers used for this production run. 68
Table 5.1 Surface density of the interface contamination observed on multiple samples. 79
Table 6.1 Measured overall electronics front-end gain with different SMA cables. 96
Table 8.1 Parameters of the implemented field dependent mobility model. 143
Table 9.1 Most probable α energies emitted by the decay of Am-241. 157
Table 9.2 Energy deposited in the P-side of the bonded samples by an α particle emitted from an Am-241 source. 161

LIST OF LISTINGS

Listing 6.1 Example YAML based TCT scan config for the ETHZ TCT setup. 99
Listing 6.2 Folder and file structure of the data generated and saved by a single TCT scan. 100
Listing 6.3 Example commands of the command-line utility used for manually controlling the ETHZ TCT setup. . 101
Listing 8.1 Pseudo code version of a simple charge propagation algorithm for time domain signal simulations. 133

1

INTRODUCTION

Miau!

— Emmy

The discovery of X-rays by Wilhelm Röntgen in 1895, for which he received the very first Nobel Prize in Physics in 1901, led to a revolution in medicine. Being able to penetrate human tissue, X-ray photons for the first time enabled to non-invasively investigate the inside of the human body. It was indeed Röntgen himself who applied this new discovery to the human body, by taking an X-ray image of the hand of his wife Anna Berta Ludwig who became the first *patient* to receive a radiograph (image on the right) [5]. Röntgen's discovery was immediately adopted around the world and only a few months after his initial publication X-rays were for the first time applied in a truly clinical setting for diagnostic purposes [5]. This established the domain of radiography and, more generally, medical imaging which is one of the main pillars of modern medicine.

FIGURE 1.1: First radiograph of a human hand, taken by Röntgen in 1895. It shows the hand of his wife Anna Berta Ludwig. Image in the public domain.

The general principle of creating an X-ray image has not changed since the discovery in 1895. A subject is placed in between an apparatus generating X-rays (source) and an apparatus able to detect two dimensional resolved X-rays (image detector). The subject is then illuminated with X-ray photons from the source and a fraction of these photons is absorbed by the tissue of the subject. The remaining photons are transmitted through the subject and a fraction of these are detected by the image detector. As the absorption and transmission of X-ray photons is dependent on the type and density of tissue, the different types or materials appear as light or dark areas on the recorded image. For example, human bones strongly absorb X-rays and accordingly appear as dark areas on the recorded image, while soft tissues (skin, muscles, etc.) only lightly absorb X-rays and therefore appear as bright areas.[1] The detection process is one aspect of X-ray imaging which has changed substantially. The earliest film-based X-ray images used a process very similar to black and white photography. As in photography, the film is usually composed of silver halide crystal grains which are ionized under X-ray exposure forming a latent image. Subsequent development and fixing steps form the X-ray image. In the 1950s the next development in X-ray image acquisition came with the introduction of the X-ray image intensifier (XRII). In an XRII the X-rays are converted into light photons using an input phosphor screen. A photo-cathode converts the light photons into electrons, which are accelerated using a potential difference. At the output screen of the XRII the electrons are converted back to visible light using another phosphor screen. With an overall amplification of a factor of several thousand, an XRII is highly sensitive to low doses [6]. In the 1980s a reusable alternative to X-ray films was introduced based on photostimulated luminescence (PSL). PSL is based on exposing a photostimulable phosphor plate with X-rays, leading to the excitation and trapping of electrons in the material. Scanning the exposed plate with a laser leads to the detrapping of these electrons and the emission of light, which can be captured and digitized using a photomultiplier tube (PMT) and processed into a digital image. The plates can be reused following an erasure procedure using white light [7]. The next iteration in X-ray image acquisition came with the development of semiconductor detectors and the introduction of flat panel detectors in the late 1990s. Two types of flat panel detectors exist, differentiated by their method of converting X-ray photons into electrical signals. Indirect detection flat panels make use of a scintillator layer to convert the X-ray photons into visible light. The visible photons are then detected via an image sensor, usually fabricated using a thin-film transistor technology based on amorphous silicon. In direct detector flat panels, the X-ray photons directly create free electron-hole pairs in a semiconductor, which leads to the formation of a current under an

---

[1] The absorption of X-rays depends on their energies. Low energy X-ray photons are also strongly absorbed by soft tissues. Further, thicker samples absorb more X-ray radiation than thinner samples. The exact energy used for taking an X-ray image is therefore chosen by the physician, depending on which part of the human body is being imaged and the type of tissue of interest.

external electric field. Commercial direct detector flat panels are commonly fabricated using amorphous selenium. Generally, in both direct detection and indirect detection flat panels, the charge generated by X-ray photons is accumulated in the sensor pixels, representing the local X-ray intensity [6]. The latest iteration in X-ray imaging comes with the development of sensors capable of detecting and discriminating single X-ray photons. This not only allows to reduce the detector noise, but also to measure the energy of the detected X-ray photons, thus enabling the acquisition of colour X-rays [8, 9]. The work presented in this thesis is situated within this active field of research.

The danger of X-ray radiation was discovered only months after Röntgen's initial publication [5]. Nowadays it is well known that the irradiation of the human body can lead to damage on the cellular level and that high radiation doses strongly increase the likelihood of developing cancer. Accordingly, modern radiography tries to decrease the dose to which a patient is exposed to as much as possible. But for a given X-ray detection system decreasing the X-ray dose automatically leads to less signal detected. The signal recorded by a detector from X-rays transmitted through a medium with an absorption factor of a is given by

$$\mathcal{S} = \alpha\eta(1-a)N_S \tag{1.1}$$

with N_S the X-ray dose emitted by the source and α a constant proportionality factor of the detector. η is the efficiency of the imaging detector, representing the probability that an X-ray photon arriving at the detector is registered as a signal. From (1.1) it is obvious that if one can increase the efficiency η of an X-ray detector, one can decrease the X-ray dose N_S without reducing the signal level and thus the quality of the image. This motivates the research into novel and more efficient X-ray imaging detectors.

In direct detection pixel sensors, the detector efficiency is directly proportional to the probability of an X-ray photon interacting with the sensitive layer of the detector. This sensitive layer is also commonly called the absorber layer, as its purpose is to absorb the incoming X-ray photons and to transform the absorbed X-ray energy into free electrical charges. For commonly used X-ray energies the dominant interaction mechanism with matter is the photoelectric effect. The probability that an X-ray photon of energy E_γ interacts via the photoelectric effect can be roughly approximated as

$$\tau \propto \frac{Z^n}{E_\gamma^{3.5}} \tag{1.2}$$

with n between 4 and 5 [10]. This shows a very strong dependence of the interaction probability (and by extension the detector efficiency η) on the atomic number Z of the material used as an absorber layer. Thus, X-ray detectors benefit from using high-Z materials such as gallium arsenide (GaAs), silicon-germanium (SiGe) or cadmium telluride (CdTe) as absorber layers. But directly implementing the integrated electronics necessary for building pixel detectors in these semiconductor materials is not feasible for economical reasons. The only material for which highly integrated electronics processes are available today is silicon (Si). Building a pixel detector which makes use of a high-Z absorber thus requires the combination of the high-Z absorber layer with a silicon, generally CMOS based, readout chip. To date this integration is achieved by making use of bump-bonding in so called hybrid pixel detectors, where both the absorber chip and the readout chip are pixelized, and the connection between the two parts is made using small solder balls. Bump-bonding is usually carried out on a per chip basis and leads to increased costs due to the complexity and the limited yield of the process [11–13].

The integration of high-Z absorber layers with CMOS-based readout chips via wafer-wafer bonding is a proposed alternative to hybrid detector fabrication [14, 15]. In this approach the absorber layer and the readout circuit are fused together on a per wafer basis, making use of the low-temperature wafer bonding offered by surface activated bonding (SAB). No bump bonding is necessary and the resulting hetero structure resembles a monolithically integrated detector. Figure 1.2 shows a schematic cross section of such a bonded detector. The bonding of wafers via SAB creates an abrupt transition from one material to the other one without any additional material at the interface. Thus the resulting bonding interface can be conductive when bonding different semiconductor materials. However, the bonding process does not lead to a perfect transition from one crystal structure to the other one, but results in a thin amorphous layer at the bonding interface with a thickness of a few nm. This amorphous layer is not passivated and thus has a high density of crystal defects, affecting the electrical behaviour of the resulting structure. The main topic of this thesis is to investigate the influence of this amorphous layer on the formation of signals in wafer-wafer bonded sensors.

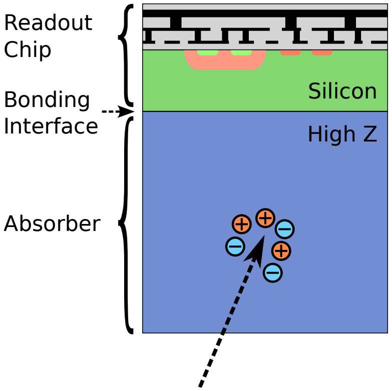

FIGURE 1.2: Schematic cross section of a single pixel of a detector fabricated by wafer-wafer bonding.

The idea of building X-ray detectors using SAB originated in the Novel Integrated Pixel X-ray Detectors (NOVIPIX) research project founded by the Swiss National Science Foundation (SNF) [14, 16]. This project led to the creation of a startup company called G-Ray Medical Sàrl (G-Ray), which tried to develop a commercial X-Ray pixel detector for medical application based on this principle.[2] In collaboration with the Swiss Center for Electronics and Microtechnology (CSEM) G-Ray developed a prototype of a pixel detector readout chip called the BigNovipix (BNP). Multiple prototype samples fabricated by G-Ray were tested and investigated as part of this thesis. These devices were created by bonding the BNP CMOS chip to high resistivity silicon absorber layers.[3] The detector P/N junction is formed at the bonding interface, as the substrate of the CMOS chip is N-type and the absorber layer is P-type. Measurements carried out as part of this thesis quickly showed that the behaviour of these samples was not as expected. This included unexpectedly high leakage currents and very low detector efficiencies. While it seemed obvious to attribute these effects to the presence of the amorphous layer at the bonding interface, proving this claim is not trivial. The BNP prototype from G-Ray is a very complex system which implements a full image acquisition and readout chain. It was thus not possible to fully explain the observed effects solely based on measurements made with the available prototypes, as issues linked to the BNP readout electronics could also not be excluded.

---

[2] G-Ray eventually ceased operations in September 2021 due to lack of funds.

[3] Silicon was used as an absorber layer for the first prototypes, as the process of integrating high-Z absorber layers (e.g. GaAs) was being optimized.

1.1 THESIS OVERVIEW

This thesis sets out to investigate the influence of the bonding interface on signal formation in bonded detectors. For simplicity reasons the focus is set on the influence of the bonding interface when bonding silicon to silicon wafers, as was the case for the initial BNP prototypes. Simple pad diodes were fabricated as part of this thesis for this investigation. The depletion behaviour of the bonded diodes as well as the behaviour of time domain signals is investigated, primarily based on transient current technique (TCT) measurements. The following chapters document this process:

CHAPTER 2 The second chapter gives an overview of fundamental principles of semiconductor particle pixel detectors. It includes a discussion of the physical interaction of particles with sensors and the formation of electron-hole pairs. The drift of these charges in the electric field of the sensor creates the detected signal. In this context the application of the Shockley-Ramo theorem for semiconductor detectors is presented. This is followed by a discussion of the extended Shockley-Ramo theorem which allows to apply the principle of charge propagation in cases of partially undepleted detectors. Finally an overview of different types of detector structures is given.

CHAPTER 3 The next chapter focuses on the principle of wafer-wafer bonding. It gives an overview of different wafer-wafer bonding techniques and introduces the concept of SAB. Mechanical, chemical and electrical properties of SAB are discussed. The second part of the chapter presents the BNP prototype from G-Ray in more detail. It also documents the unexpected results from measurements with these initial prototypes which did not allow to take any conclusions about the influence of the bonding interface.

CHAPTER 4 This chapter presents the fabrication process of the simple bonded pad diodes. The main focus lies on the creation of good ohmic contacts and the successful bonding of the wafers. In the second part of the chapter the fabricated samples are documented including multiple quality control measurements carried out during the production. These include scanning acoustic microscopy (SAM) and transmission line model (TLM) measurements.

CHAPTER 5 This chapter documents the mechanical and chemical characterization of the bonding interface of the fabricated diode samples. The crystal structure was investigated using scanning transmission electron microscope (STEM) measurements and the chemical composition using energy-dispersive X-ray spectroscopy (EDXS) measurements. An unexpected metal contamination is found at the bonding interface which is further investigated using total reflection X-ray fluorescence spectroscopy (TXRF) measurements of unbonded wafers. The contamination is found to be originating from the bonding machine.

CHAPTER 6 This chapter starts with an introduction of the principle of TCT measurements. It discusses different types of TCT systems, charge injection via laser and radioactive sources and the prompt current analysis method. The TCT setup installed at ETHZ is presented, together with its control software framework, as well as the dedicated sandwich-type sample holder designed for the bonded diode samples. Finally the edge polishing sample preparation for edge TCT measurements is discussed.

CHAPTER 7 The next chapter presents the investigation of the depletion behaviour of the fabricated samples, based on different TCT measurements. It is found that only one side of the fabricated samples can be depleted. This finding is confirmed via an independent measurements using a two photon absorption (TPA) TCT setup at CERN. These observations can be modelled using an empirical P/N++/N model where the interface acts as a highly doped N-type layer. Finally the link between the observed metal contamination and the observed depletion behaviour is discussed.

CHAPTER 8 In this chapter the principle of simulating time domain signals via charge propagation is presented. Based on the empirical P/N++/N model a charge propagation simulation model is created for the fabricated bonded samples. This model includes the application of the extended Shockley-Ramo theorem to handle the undepleted layers in the samples. The different physical and electrical aspects of the model are discussed in detail.

CHAPTER 9 The next chapter compares the time domain TCT signals, acquired using an americium-241 (Am-241) source, with the simulated signals based on the model derived in the previous chapter. The Am-241 source is used in order to have a clearly defined energy deposit, which allows for an absolute calibration. A very good agreement between the simulated and measured time domain curves is observed for different amounts of deposited energy.

CHAPTER 10 The concluding chapter summarizes the work carried out in this thesis and the observed results. Finally, a brief overview of potential future work is given.

2

FUNDAMENTALS OF SEMICONDUCTOR PARTICLE DETECTORS

Purrrrr!

— Hilbert

This chapter presents an overview of the fundamental concepts of direct detection semiconductor particle detectors. The focus of the chapter lies on concepts and techniques used in particle pixel detectors. The first section gives a brief introduction to semiconductor materials, with a focus on silicon (Si). In order for a sensor to detect a particle, said particle needs to interact with the sensitive volume of the sensor. Thus, the second section of this chapter discusses such interactions of particles with semiconductor detectors leading to the creation of free charges (electron-hole pairs). The third section presents how signals are formed via the drift of charges inside the electric field of the detector and also introduces the Shockley-Ramo theorem and its limitations. The following section discusses an extension to the Shockley-Ramo theorem, allowing for its application in the case of non-fully depleted detectors. Finally, the last section presents different types of detector structures, including hybrid and monolithic detectors, and introduces the concept of a wafer-wafer bonded detector.

CONTRIBUTION The information presented in this chapter has been compiled by the author based on existing literature. The first section is based on [17] and the professional training of the author. The second and third section is heavily inspired by [10]. Various publications by W. Riegler [4, 18, 19] are the basis for the section presenting the extended Shockley-Ramo theorem.

2.1 SEMICONDUCTOR MATERIALS

A semiconductor material is characterized by the presence of a forbidden gap within its energy-band structure, called the band gap E_g.[1] The band gap splits the energy-band structure into two distinct regions, the valence band and the conduction band, as shown in figure 2.1a. Electrons are forbidden to populate energy levels lying within the band gap and are thus confined to either the valence or the conduction band. At a temperature of absolute zero $T = 0\,\mathrm{K}$, all states in the valence band are occupied by electrons and no electrons occupy states in the conduction band. As indicated by its name, electrons in the valence band are tightly bound to their respective atoms and are not free to move. Thus, at absolute zero semiconductors are non-conducting. But the band gap of semiconductors is low enough that thermal excitation of electrons into the conduction band is possible for temperatures $T > 0\,\mathrm{K}$. The electrons excited to the conduction band are free to move within the semiconductor material. In addition, the empty state left behind by the excited electron, called a hole, can easily be occupied by a neighbouring electron within the valence band. The hole is thus also assumed to be free to move across the material, representing a mobile positive charge. Holes and free electrons are thus the charge carriers responsible for the non-zero conductivity of semiconductor materials. Free electrons are represented in figure 2.1 as blue circles with a $-$ sign and holes as white circles with a $+$ sign. As a hole is created by the excitation of an electron into the conduction band, the density of free electrons n and holes p is equal in a pure (intrinsic) semiconductor with $n = p = n_i$ with $n_i = 1.45 \times 10^{10}\,\mathrm{cm}^{-3}$ for silicon at room temperature [17]. Compared to the atomic density of silicon of ca. $5 \times 10^{22}\,\mathrm{atom\,cm}^{-3}$, one observes that in intrinsic silicon only a miniscule fraction of valence band electrons are excited to the conduction band. This leads to a relatively high resistivity, for example compared to any metal conductor where all valence electrons are mobile.

DOPING OF SEMICONDUCTORS The introduction of impurities into a semiconductor material for modifying its electrical behaviour is called doping. Two types of doping are possible, P- and N-doping. For Si, boron

---

[1] Isolating materials also exhibit a forbidden gap in their energy-band structure, but with a much larger band gap than semiconductors. This inhibits thermal excitation of electrons into the conduction band, leading to the very low conductivity of insulating materials.

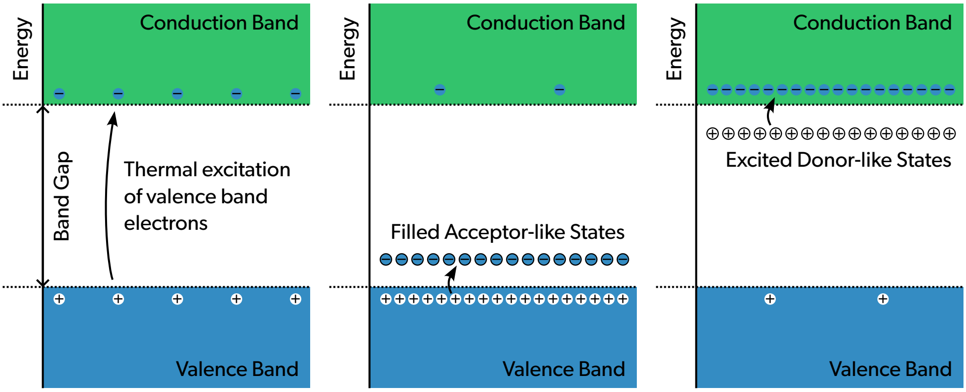

(a) Intrinsic (b) P-type doping (c) N-type doping

FIGURE 2.1: Illustration of the band structures under different doping regimes. Free electrons in the conduction band are represented with a blue circle and free holes in the valence band with a white circle. The filled acceptor-like states (P-doping) and the excited donor-like states (N-doping) act as fixed (non-mobile) charges.

is usually used for P-doping, having one valence electron less than Si (3 vs. 4). This introduces one additional hole per boron atom into the semiconductor material. From the point of view of the energy-band diagram, introducing boron into Si creates acceptor-like states within the band gap. As these states are very close to the valence band, electrons from the valence band are easily excited and captured by these acceptor states at low temperatures. This creates free holes in the valence band. This principle is illustrated in figure 2.1b. For N-type doping of Si, phosphorus is commonly employed as a dopant element, having one valence electron more than Si (5 vs. 4). This introduces one additional electron per phosphorus atom into the semiconductor material. In the energy-band diagram, introducing phosphorus into Si creates donor-like states within the band gap. As these states are very close to the conduction band, electrons from these states are easily excited to the conduction band at low temperatures, adding free electrons into the conduction band. This principle is illustrated in figure 2.1c. Doping with other elements than boron and phosphorus is also possible, and for non-silicon semiconductors different dopant elements are applicable, but the underlying principle of P- and N-type doping stays the same. In summary, P-doped semiconductors have an excess of free holes, which in this case are denoted the majority charge carries, with electrons denoted the minority charge carriers. N-doped semiconductors have an excess of free electrons, in this case denoted the majority charge carries, with holes denoted the minority charge carriers. The mass-action law imposes

$$pn = n_i^2, \tag{2.1}$$

for undoped and for doped semiconductors, with p the concentration of free holes and n the concentration of free electrons in the semiconductor, and n_i^2 the previously mentioned intrinsic carrier density [17]. In a doped semiconductor

$$p_P \approx N_A \text{ for } N_A \gg n_i \text{ (P-doping)} \tag{2.2}$$

$$n_N \approx N_D \text{ for } N_D \gg n_i \text{ (N-doping)} \tag{2.3}$$

with N_A and N_D the P- and N-type doping concentrations respectively. This implies that the minority carrier concentration in a doped semiconductor is very low

$$n_P \ll n_i \text{ (P-doping)} \tag{2.4}$$

$$p_N \ll n_i \text{ (N-doping)}, \tag{2.5}$$

and that the conductivity of a doped material is dominated by the majority carriers. Doping is thus very effective at modifying the electrical behaviour of semiconductors.

The discussion so far is limited to the behaviour of semiconductors in thermal equilibrium. The interaction of ionizing radiation with a semiconductor material also leads to the excitation of electrons from the valence to the conduction band leaving behind a hole. This way of creating electron-hole pairs is the underlying process of using semiconductors as particle detectors. The interaction of different types of radiation with semiconductor materials is discussed further in section 2.2.

P/N JUNCTIONS A P/N junction is created by bringing a P-type semiconductor region into contact with an N-type region.[2] The large difference in charge carrier concentrations ($p_P \gg p_N$ and $n_N \gg n_P$) leads to the diffusion of majority charge carriers across the P/N junction. The excess

---

[2] In reality P/N junctions are generally not formed by bringing into contact different semiconductor pieces, but, for example, by strongly N-doping a P-type semiconductor, thus creating a transition from a P-type to an N-type region.

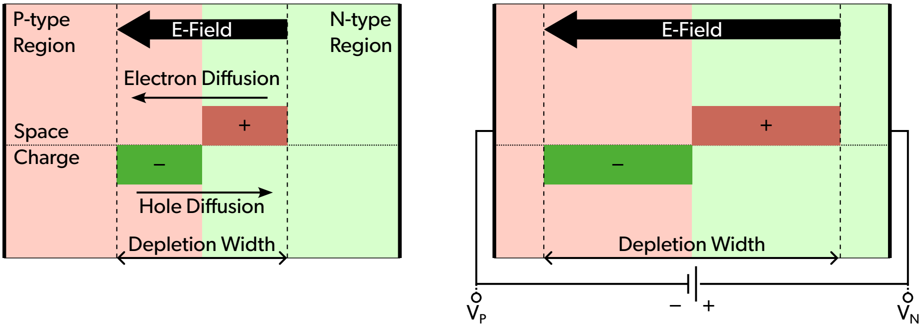

(a) Showing the built-in depletion region.

(b) Under reverse bias.

FIGURE 2.2: Schematic view of an abrupt P/N junction. The diffusion of majority carriers across the junctions leads to the formation of space-charge regions. These regions create an electric field, which counteracts the diffusion of charges. The results is the formation of a built-in depletion region. Under reverse bias the depletion region is increased by applying an external voltage across the P/N junction.

electrons diffusing from the N-side into the P-side will recombine with holes in P-side, and vice-versa for the excess holes diffusing from the P-side into the N-side. This effectively removes free charge carriers from the N- and P-regions close to the junction. The result is a region with a positive space-charge in the N-side and a region with a negative space-charge in the P-side, as illustrated in figure 2.2a. The presence of space-charge regions leads to the formation of an electric field, and thus to an electric force counteracting the diffusion of majority charge carriers. An equilibrium is reached once the electric force fully compensates the diffusion pressure. The equilibrium space charge regions create a potential difference between the N- and P-side, denoted the built-in potential V_{bi}. As these regions are devoid of majority charge carriers, the overall space-charge region around the P/N junction is called the depletion region. As mentioned, an electric field is present within the depletion region, oriented from the N-side towards the P-side. Applying an external voltage across the P/N junction with $V_N > V_P$, denoted as reverse biasing, forces additional majority charge carries to cross the P/N junction leading to an increase of the depletion region. Figure 2.2b illustrates this behaviour. This is the fundamental principle used in semiconductor detectors for creating an electric field within the sensitive detector volume. Often the reverse bias voltage of a detector is chosen so that the depletion region extends over the full volume of the detector, creating an electric field within its entire volume. This is called full depletion. Section 2.3 discusses how the electric field within the depletion region leads to the formation of a signal via the drift of charges injected by interacting particles.

As noted, the depletion region is devoid of majority charge carriers. Thus, in first order approximation, the current across a reverse biased P/N junction is zero. But the diffusion of minority charge carriers into the depletion region leads to a (low) reverse leakage current. As diffusion is a purely thermal effect, this reverse current does not depend on the applied bias voltage. Second order effects, as for example generation and recombination within the depletion region, can lead to higher reverse bias currents, and can also result in a bias voltage dependency of the leakage current. Applying a forward bias voltage across the P/N junction ($V_N < V_P$) decreases the width of the depletion region. Once $V_P - V_N > V_{Bi}$, the depletion region disappears and conduction via the majority charge carriers is possible. This leads to an exponential increase of the current across the P/N junction in forward bias, which is the characteristic behaviour of a diode (see also section 4.2.1).

2.2 INTERACTION OF IONIZING RADIATION WITH MATTER

Fundamental to the interaction of ionizing particles with a sensor is the transfer of energy from the particles to the detector material. This transferred energy can lead to three different macroscopic signatures to be detected in sensors: heat, light or charge. The macroscopic creation of heat for example is used for particle detection in bubble chambers and cloud chambers. The creation of light is the fundamental concept of scintillator detectors as well as Cherenkov detectors. Finally, the direct creation of free charges from the interaction energy transfer is the concept used in many different types of detectors, including gaseous ionization detectors and microchannel plate detectors. It is also the concept which applies in direct detection semiconductor detectors, discussed here in more detail. The two main fields of application of particle pixel detectors are as tracking detectors in physics experiments such as ATLAS and CMS at CERN, and as imaging detectors for applications such as medical X-ray imaging or in diffraction experiments as carried out at synchrotron light sources [20].

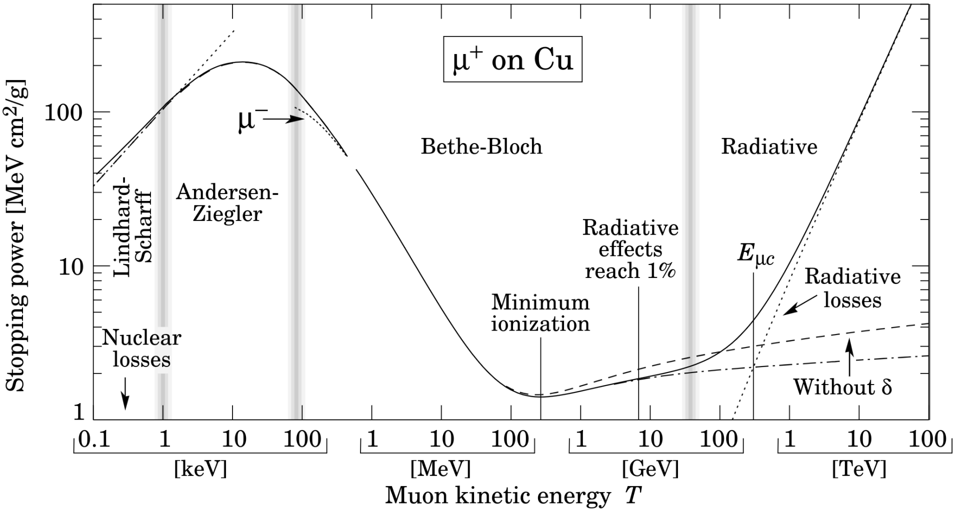

FIGURE 2.3: Energy loss function (stopping power) of positive muons in copper [21].[3] The muon reaches it minimum ionization for kinetic energies above 100 MeV.

Tracking detectors are used to detect and reconstruct the decay of short lived particles. This is primarily done by reconstructing the track and vertex of the charged decay products originating from these short lived particles, often in a magnetic field. The interaction of charged particles with a semiconductor detector (and any material in general) is primarily via ionizing Coulomb interaction with the electrons of the interaction material (inelastic scattering). This leads to a continuous transfer of energy from the particles to the detector medium and is generally characterized via an energy loss function

$$\frac{dE}{dx}(E,m) \tag{2.6}$$

which specifies the average energy E a particle of mass m loses while traversing a certain distance x of matter. The precise nature of the interaction mechanism and the energy loss function is specific to what charged particle is interacting with which material. An example of the energy loss function for positive muons in copper is shown in figure 2.3. At high energies radiative processes (such as Bremsstrahlung) are dominating. The energy

---

[2] Reprinted from *Atomic Data and Nuclear Data Tables*, 78, Donald E. Groom, Nikolai V. Mokhov, Sergei I. Striganov, MUON STOPPING POWER AND RANGE TABLES 10 MeV–100 TeV, 183-356., 2001, with permission from Elsevier.

loss function attains a minimum at medium energies and particles of such energies are designated minimum ionizing particles (MIPs). Heavier particles (such as α particles, ions or protons) experience only a small amount of momentum change when interacting via inelastic scattering with the (lightweight) electrons of the interaction material. Thus, these particles tend to have relative straight tracks across the material. But the higher mass of these heavy particles implies that they have a lower velocity at a given kinetic energy and thus a higher interaction cross section. This leads to a shorter range for heavier particles with a given energy compared to lighter ones with the same energy. Fast electrons, having the same mass as the electrons of the interaction material, can transfer a large amount of their momentum in a single interaction and thus experience much more bending in their tracks. Their lower mass also leads to a higher velocity at a given energy, and thus fast electrons have a much larger range compared to heavy charged particles of the same energy. Protons and $alpha$ particles which are fully absorbed in a material give rise to a so called Bragg peak, where a large fraction of the particles energy is transferred to the medium just before the particle is completely stopped [22].[4] The Bragg peak occurs because of an increase in interaction cross section with lower particle energies. Eventually the charge of the particle is reduced via electron pick up which finally leads to the drop in deposited energy [10].

Photons are not charged and thus do not interact via Coulomb forces. Therefore the interaction of a photon with matter in general does not lead to a continuous loss of energy, but is rather characterized by one or a few individual interactions, where all or a large fraction of the photons energy is transferred. There are four main interaction mechanisms of photons with matter, three of which lead to the transfer of energy from the photon to the material:

PHOTOELECTRIC EFFECT A photon ionizes a bound electron of the material leading to the full absorption of the photon. The result of the interaction is an energetic electron which further interacts with the material. But as the entire photon energy is transferred to the energetic electron, the amount of ionizing energy deposited in the material is equal to the original photon energy. The photoelectric effect is the dominant process at lower photon energies.

---

[4] The simulation of the interactions of α particles with silicon in section 9.1.1 shows the effect of the Bragg peak.

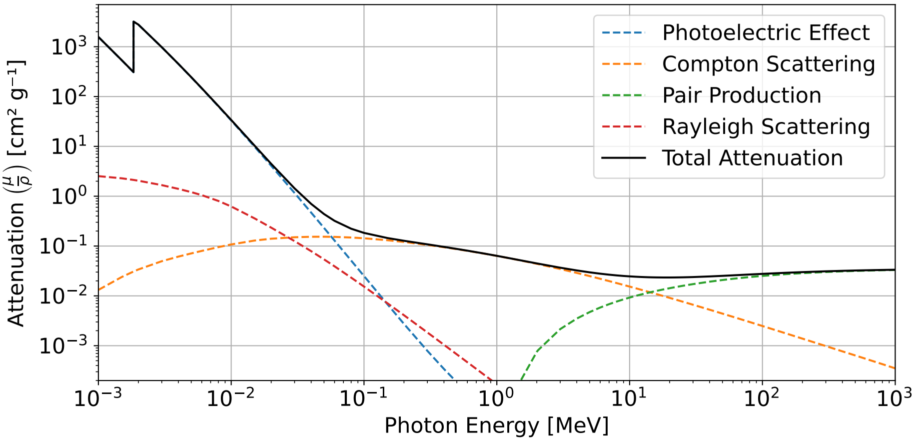

Figure 2.4: Attenuation of X-ray / gamma ray photons of different energies in Si. The contribution of the different interaction processes described in the text is shown. Based on data from the NIST XCOM database [23].

COMPTON SCATTERING Under Compton scattering an electron of the material interacts with a photon, deflecting it by an angle θ. A fraction of the photon energy is transferred to the interacting electron. The amount of energy exchanged depends on the scattering angle θ, which results in a wide range of possible energy deposits. Compton scattering is usually dominant for photons in the low MeV range.

PAIR PRODUCTION When the photon has an energy higher than twice the rest mass of an electron, pair production can occur when the photon interacts with the nucleus of the interaction material. Pair production is the dominant process at high photon energies. The high photon energy necessary (order of multiple MeV) makes this interaction process irrelevant for X-ray imaging detectors.

RAYLEIGH SCATTERING The photon can also scatter coherently with the interaction material. This usually does not result in the transfer of any energy to the interaction material, but only in a change of direction of the photon. In pixel detectors Rayleigh scattering can lead to a form of cross-talk as incoming photons are scattered into neighbouring pixels.

Figure 2.4 shows the interaction probability of photons with Si. The contribution of the different interaction processes at a given energy is shown.

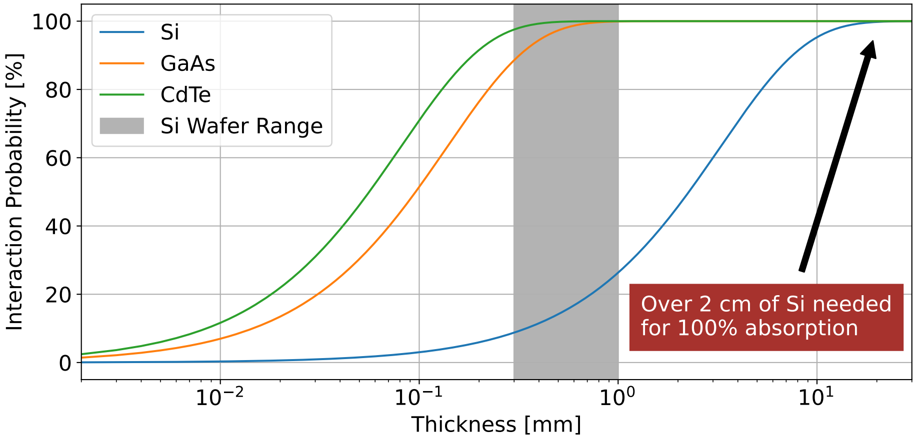

FIGURE 2.5: Interaction probability of a 30 keV X-ray photon in various semiconductor materials as a function of the absorber thickness. Based on data from the NIST XCOM database [23].

The interaction probability is characterized by a linear attenuation coefficient per density of material $\frac{\mu}{\rho}$. The absorption length μ highlights that the absorption of photons in a material follows an exponential decay law. The fraction of photons (of a given energy) being absorbed in a layer of material with thickness d is given by

$$A_\gamma = 1 - e^{-\mu d} \tag{2.7}$$

For an X-ray pixel detector this implies that the absorber material should have a high mass attenuation in order to be efficient in absorbing and detecting the X-ray photons of interest. This motivates the use of high-Z materials as absorbers for X-Ray pixel detectors, as the interaction probability (via photoelectric effect) scales with a power of the atomic number (Z) as previously shown in (1.2). To demonstrate this, figure 2.5 shows the fraction of X-ray photons with an energy of $E_\gamma = 30\,\text{keV}$ which are absorbed as a function of the thickness of absorber layers made from Si, gallium arsenide (GaAs) and cadmium telluride (CdTe). This X-ray energy lies in the range of energies commonly employed in mammography X-ray imaging [24]. It shows that over 2 cm of Si is necessary to fully absorb these X-ray photons. Such thick detectors can not be manufactured with modern Si processes. On the other hand the necessary thickness when using high-Z materials (GaAs and CdTe) is feasible. For energy resolving and photon-

	Si [25, 26]	Ge [25]	GaAs [27]	CdTe [13]	Diamond [28]
$E_{e/h}$ [eV]	3.6	2.8	4.2	4.43	13
E_g [eV]	1.12	0.66	1.42	1.44	5.5

TABLE 2.1: Average electron-hole pair creation energy $E_{e/h}$ and band gap E_g for various semiconductor materials. Values are valid at room-temperature.

counting X-ray image detectors the desired interaction mechanism is the photoelectric effect, as only this mechanism consistently leads to the entire photon energy being deposited as ionizing energy. Thus, interaction via Compton scattering is not desired. The threshold energy at which Compton scattering becomes dominant over the photoelectric effect also scales with the Z-number of the interaction material. And thus high-Z materials also have a higher probability of absorption via the photoelectric effect at a given photon energy [10].

The final results of the previously described particle interactions are a certain number $N_{e/h}$ of thermal electron-hole pairs which are free to move within the semiconductor crystal. The exact process in-between the interaction of the radiative particle with the material and the final state of thermal electron-hole pairs is complex and specific to each type of particle. For practical purposes a given material is characterized by the amount of deposited ionizing energy $E_{e/h}$ necessary to, on average, create one electron-hole pair. This value is given in table 2.1 for various materials, together with the band gap of the material. It can be seen that on average the energy necessary to create one electron-hole pair is higher than the band gap. For example for Si the band gap (at room temperature) is $E_g^{(Si)} = 1.12\,\text{eV}$ but on average 3.6 eV are necessary to create a single electron-hole pair. The energy difference is dissipated as acoustic and thermal phonons [25]. The $E_{e/h}$ values are temperature dependent, as also the band gap energies are. It should also be noted that the precise value seems to depend on the type of radiation which is interacting with the material. For Si and GaAs it has been observed that $E_{e/h}$ is slightly higher for interactions of electrons than for interactions of α particles [26, 27]. But in general these values allow to approximate the average number of electron-hole pairs created from a particle interaction in a detector

$$N_{e/h} = \frac{E_{Ionize}}{E_{e/h}} \tag{2.8}$$

with E_{Ionize} the ionizing energy lost by the particle in the material. This concept is used in chapter 9 to predict the time-domain signals from the interaction of α particles with the fabricated bonded diode samples.

2.3 SIGNAL GENERATION VIA CHARGE DRIFT

As discussed in the last section, the interaction of various particles with a semiconductor material leads to the creation of a number of electron-hole pairs, the number of which is proportional to the amount of ionizing energy deposited by the particle in the sensor. The creation of these electron-hole pairs by itself does not constitute a detectable signal. Rather, if left undisturbed, these charges will spread out due to diffusion effects and will eventually recombine with each other leaving behind no trace of their former presence.[5] Thus, in order to effectively detect these charges, an electric field is applied across the sensitive layer of the detector. This electric field will lead to drift movement of the free electrons and holes which were generated by the particle interaction.[6] Due to their opposite charge, the electrons and holes are drifted in opposite directions and thus will eventually reach the opposite ends of the detector where the electrons and holes are said to be collected at the metal contacts used for creating the electric field. The movement of the free charge carriers leads to a detectable current induced on the metal contacts, as predicted by the Shockley-Ramo theorem which will be discussed in detail in the next section. In semiconductor detectors, the reverse biasing of a P/N junction is used for generating the electric field within the sensitive volume of the detector, as discussed in section 2.1. Ignoring any signal contribution from charges diffusing into the depletion region, the active zone of the detector is defined by the extent of the depletion region, as only charges created

---

[5] The creation of permanent defects due to the interaction of radiation with the sensor material is left out of the discussion here. Nevertheless, radiation damage is an important subject, which is especially important in the context of detectors exposed to a high overall dose.

[6] This principle does not only apply to semiconductor detectors but is also the basic principle of most gaseous particle detectors.

within this region are subject to drift. Therefore, especially in calorimeter type detectors, one often tries to achieve a full depletion of the available detector volume in order to increase the detection efficiency. The size of the depleted region at a given reverse bias voltage is proportional to $\frac{1}{\sqrt{N}}$ with N the doping concentration of the volume to be depleted. Therefore the use of low doped / high resistivity substrates is favoured for building fully depleted particle detectors [17].

In first order approximation, the overall detected charge (integral of all signal currents) is equal to $Q_{signal} = N_{e/h}e$, with $N_{e/h}$ the number of electron-hole pairs created by the initial particle interaction. In pixel and strip detectors this collected charge can be spread over multiple pixels / channels due to charge-sharing. There are more sophisticated detector structures, such as avalanche photodiodes (APDs), low gain avalanche detectors (LGADs) and single-photon avalanche diodes (SPADs), which have specially crafted electric field configurations that lead to charge multiplication within the detector volume. Both APDs and LGADs are linear devices where the final detected charge is a multiple of the created charge $Q'_{signal} = GN_{e/h}e$. Their internal structure has a high electric field region where the field is high enough to lead to charge multiplication via impact ionization. APD generally have a gain in the range of $G_{APD} = 10 - 100$. However, such a gain leads to an increase in noise and in leakage current. This led to the development of LGADs with a gain in the range of $G_{LGAD} = 5 - 10$ [29]. APDs are generally used for detecting low energy particles and X-rays, while LGADs are extensively studied for applications as high precision timing detectors [30]. On the other hand, in SPADs the electric field is shaped so that a full avalanche breakdown occurs, leading to a gain G of up to 1×10^6. But due to the nature of the avalanche breakdown these devices are no longer linear. Any particle interaction leads to a fixed detected signal charge, independent of $N_{e/h}$. This allows these device to detect individual light photons which usually lead to the creation of only a single initial electron-hole pair ($N_{e/h} = 1$) [31].

2.3.1 *Shockley-Ramo theorem*

The Shockley-Ramo theorem[7] states that the (current) signal seen on a readout electrode is not given by charges physically arriving at a given electrode (*collection of holes* or *collection of electrons*)[8], but rather that the movement of the free charges within the detector volume induces a signal on the readout electrode [32, 33]. The current signal on a readout electrode i, induced by a charge q moving at a velocity $\vec{v}_q$ at a position $\vec{x}$ within the detector is defined as

$$I^{(i)} = q\vec{v}_q(\vec{x}) \cdot \vec{W}_F^{(i)}(\vec{x}) \tag{2.9}$$

where $\vec{W}_F^{(i)}(\vec{x})$ is the weighting field associated with the electrode i. The weighting field is static and fully defined by the geometrical arrangement of the electrodes of the detector. Formally the weighting field associated with an electrode i is given by

$$\vec{W}_F^{(i)}(\vec{x}) = \left.\frac{d\vec{E}(\vec{x})}{dV_i}\right|_{V_i=V_{Bias,i}} \tag{2.10}$$

where $\vec{E}(\vec{x})$ is the electric field in the detector at position $\vec{x}$ and $V_{Bias,i}$ is the static bias voltage applied to electrode i for normal detector operation.[9] The weighing field is thus closely related to the electric field inside the detector, but it should be stressed that the weighting field is not an electric field and has the unit $[W_F] = \mathrm{m}^{-1}$.

SHOCKLEY-RAMO IN SEMICONDUCTORS It needs to be stated that the Shockley-Ramo theorem is valid for currents induced on grounded

---

[7] The theorem is also simply known as Ramo's theorem. But in order to acknowledge its independent and concurrent discovery by William Shockley [32] and Simon Ramo [33] the name Shockley-Ramo theorem is used in modern texts.

[8] The usage of the term *charge collection* to describe the formation of signals in particle detectors is very prevalent, but can lead to the wrong impression that signal is only observed once charges physically arrive at the readout electrodes, and by extension that charges which do not physically arrive at a readout electrode do not create any signal. In the context of wafer bonded detectors this can lead to the wrong assumption that no signal is being observed if charges might be blocked by the bonding interface and thus can not physically reach the readout electrode. This is not the case.

[9] The definition of the weighting field given here differs from the one given by Shockley and Ramo. Both Shockley and Ramo define the weighting field associated with electrode i as the electric field present inside the detector when keeping all electrodes at ground and applying a unit potential to electrode i ($V_i = 1\,\mathrm{V}$) [32, 33]. For the signal induced on grounded electrodes by charges moving in vacuum the formulation presented above is equivalent to the definition by Shockley and Ramo. But in the case of complex fully depleted semiconductor detectors the approach for calculating the weighting field presented by Shockley and Ramo is not valid due to the presence of a necessary bias voltage.

electrodes by charges moving in vacuum.[10] These conditions are not met in semiconductor detectors, as the charges are moving within a medium (e.g. silicon) and the electrodes are held at constant bias voltages, with at least one electrode at a bias $V_{Bias} \neq 0\,\mathrm{V}$ to deplete the detector. It can be shown that the Shockley-Ramo theorem is still valid in the case of fully depleted semiconductor detectors [34, 35]. Using the superposition principle, the electric field at any point in the detector can be decomposed into three terms

$$\vec{E} = \vec{E}_1 + \vec{E}_2 + \vec{E}_3 \tag{2.11}$$

with $\vec{E}_1$ the field due to the bias applied to the electrodes but in absence of any volume charge, $\vec{E}_2$ the field due to the presence of fixed space charges (from the depletion), and $\vec{E}_3$ the field due to the movement of free charges (the charges created by particle interaction). Both $\vec{E}_2$ and $\vec{E}_3$ are calculated with the electrodes at ground. In the calculation of the current induced on the electrodes from the movement of the free charges the contributions from $\vec{E}_1$ and $\vec{E}_2$ cancel. Only the contribution from the moving free charges calculated with the electrodes at ground ($\vec{E}_3$) remains, which is equivalent to the Shockley-Ramo theorem.

For complex detector layouts (such as pixelized detectors) it is often not possible to analytically calculate the weighting field. In these situations, technology computer-aided design (TCAD) is usually employed to numerically calculate the weighting field. The detector is first simulated at the normal operation point and the corresponding electric field within the detector is extracted ($\vec{E}_{V_{Bias}}(\vec{x})$). A small additional voltage ΔV_i is then applied to the readout electrode i of interest and the corresponding electric field is again extracted ($\vec{E}_{V_{Bias}+\Delta V}(\vec{x})$). The weighting field can then be calculated as

$$\vec{W}_F^{(i)}(\vec{x}) = \frac{\vec{E}_{V_{Bias}+\Delta V_i}(\vec{x}) - \vec{E}_{V_{Bias}}(\vec{x})}{\Delta V} \tag{2.12}$$

which corresponds to solving the differential equation in (2.10) by Newton's method [4].

SHOCKLEY-RAMO WITH NON-GROUNDED ELECTRODES In general, the electrodes of a semiconductor detector are not only held at a constant bias voltage, but, especially the electrodes where the signal is recorded,

---

[10] This is by design, as the work of both Shockley and Ramo was done in the context of signals observed in vacuum tubes.

are usually connected to ground via an arbitrary impedance network. For example this can be the (virtual) input resistance of an amplifier or the additional parasitic capacities of the readout circuit. As shown in chapter 5 of [36], the Shockley-Ramo theorem can still be applied in these cases. The approach for calculating the induced voltages presented in said chapter is summarized here. First, the current induced onto the assumed to be grounded electrodes $\vec{I}_{ind}$ is calculated using the Shockley-Ramo theorem. An equivalent circuit is then created, taking into account the mutual capacitances of the electrodes $[c_{nm}]$ as well as the arbitrary admittances connected to the electrodes $[y_{nm}]$ in the form of a capacitance and admittance matrix respectively. By design c_{nm} and y_{nm} are in parallel and thus the total admittance matrix can be written as $[y^{tot}_{nm}] = s[c_{nm}] + [y_{nm}]$ in the Laplace domain [37]. The current induced onto grounded electrodes calculated via the Shockley-Ramo theorem is now imposed onto the electrodes as ideal current sources. It follows for the corresponding induced voltage

$$\vec{I}_{ind} = [y^{tot}_{nm}]\vec{V}_{ind} \Leftrightarrow \vec{V}_{ind} = [y^{tot}_{nm}]^{-1}\vec{I}_{ind}, \tag{2.13}$$

where $\vec{I}_{ind}$ and $\vec{V}_{ind}$ represent the current and voltage induced on the n electrodes in the Laplace domain. In simple cases, especially pad diodes with only two contacts, an inverse Laplace transform can yield the impulse response of a transfer function $H(s) = \frac{V_{ind}}{I_{ind}}$ as

$$h(t) = \mathcal{L}\{H(s)\} = \mathcal{L}\left\{\frac{V_{ind}}{I_{ind}}\right\} \tag{2.14}$$

which can be applied to the time domain induced current via convolution

$$i(t) = (h * i)(t) \tag{2.15}$$

In complex situations, the application of the electronics response is calculated separately via a circuit level simulation model (using for example any SPICE-like simulator). In such a simulation the electronics front-end is represented as a normal circuit model and the detector is represented via a lumped sum representation of the capacitance matrix $[c_{nm}]$. The induced current is included using arbitrary current sources.

This shows the versatility of the Shockley-Ramo theorem. Even though it was originally developed for a very specific application, the currents induced on grounded electrodes by charges moving in a vacuum, the previous paragraphs show that it can also be applied to signals induced on non-grounded electrodes by charges drifting in fully depleted semiconductor detectors. It needs to be stressed that the derivations so far are only valid for fully depleted semiconductor detectors. The case of partially depleted detectors, exhibiting layers with a non-zero conductivity, is treated in the next section.

2.4 EXTENDED SHOCKLEY-RAMO THEOREM

As discussed in the previous section, the Shockley-Ramo theorem can be applied to situations where the electrodes are not grounded and for charges moving in fully depleted semiconductor detectors. The use in depleted semiconductors is possible because the depleted medium acts similar to a vacuum, in the sense that the medium does not have any free charge carriers. Thus, the depleted medium has an apparent conductivity of $\sigma_{dep} = 0\,\mathrm{S\,m^{-1}}$. On the other hand, the Shockley-Ramo theorem is not valid for charges moving within a medium with non-zero conductivity. Both Ramo (explicitly) [33] and Shockley (implicitly) [32] assume that $\vec{\nabla}^2 V = 0$ within the medium. This is equivalent to assuming that a charge q placed at a fixed position $\vec{r}$ within the medium leads to a potential which is constant in time $\frac{\partial}{\partial t} V_q(\vec{x}) = 0$. This is the basis for the derivation of the Shockley-Ramo theorem. In the case of a medium with non-zero conductivity this is no longer the case, as the free charges of the medium react to the presence of the charge q. Accordingly, the presence of the charge q at a fixed position $\vec{r}$ can lead to a potential changing in time $\frac{\partial}{\partial t} V_q(\vec{x}) \neq 0$. This has two consequences which are not compatible with the derivations shown by Shockley and Ramo. First, in the general case $\vec{\nabla}^2 V \neq 0$, especially when there is an accumulation of charges at locations where $\vec{\nabla}\epsilon \neq 0$ or $\vec{\nabla}\sigma \neq 0$.[11] Second, the following relation does not hold any more

$$Q_A = -eV_e' \tag{2.16}$$

$$i_A = \frac{dQ_a}{dt} = -e\frac{dV_e'}{dt} \neq -e\left[\frac{\partial V_e'}{\partial x}\frac{dx}{dt}\right] \tag{2.17}$$

as $\frac{\partial}{\partial t} V_e' \neq 0$ (using the notation from Ramo's paper [33]).

---

[11] This is for example the case when a conductive layer ($\sigma \neq 0$) is in contact with a non-conductive layer ($\sigma = 0$), in which case charges can accumulate at the interface separating these layers. As shown later, this is precisely the case in the bonded samples.

W. Riegler developed an extension to the Shockley-Ramo theorem which can be applied to systems made up of elements with a non-zero conductivity, referred to as the extended Shockley-Ramo theorem from here on. This extension was originally developed for use with resistive plate chambers [18, 19], but can also be applied to semiconductor sensors as shown by W. Riegler in [4, 19]. The derivation of the extended Shockley-Ramo theorem is not reproduced here, but the most important results relating to its application in semiconductor detectors are shown. The interested reader is referred to [4] for the derivation of the extended Ramo-Theorem in the context of silicon sensors, and [18] for the derivation of calculating a time-dependent potential based on the substitution $\epsilon = \varepsilon + \frac{\sigma}{s}$ in the Laplace-domain, which is heavily used in [4]. The most important result for the simulation of transient signals in semiconductor detectors with conductive elements is *Theorem 3* in [4] which states[12]

> A pair of charges q, $-q$ is created in the detector at $t = 0$ and these charges are moving in the electric field $\vec{E}_D(\vec{x})$ along trajectories $\vec{x}_1(t)$ and $\vec{x}_2(t)$. The current $I_n^{ind}(t)$ induced on a grounded electrode [..] can be calculated by
>
> $$\begin{aligned} I_n^{ind}(t) = &- \frac{q}{V_0} \int_0^t \vec{W}_n[\vec{x}_1(t'), t - t']\dot{\vec{x}}_1(t') dt' \\ &+ \frac{q}{V_0} \int_0^t \vec{W}_n[\vec{x}_2(t'), t - t']\dot{\vec{x}}_2(t') dt' \end{aligned} \tag{2.18}$$
>
> where the weighting vector $\vec{W}_n(\vec{x}, t)$ is defined the following way [..]: the charges q, $-q$ are removed, an ´infinitesimal´ voltage pulse $V(t) = V_0[\Theta(t) - \Theta(t - \Delta t)]$ is added to electrode n, which results in a field $\vec{E}_{Dn}(\vec{x}, t, \Delta t)$, from which the weighting vector $\vec{W}_n(\vec{x}, t)$ is derived as
>
> $$\vec{W}_n(\vec{x}, t) = \lim_{\Delta t \to 0} \frac{1}{\Delta t} \left[\vec{E}_{Dn}(\vec{x}, t, \Delta t) - \vec{E}_D(\vec{x}) \right] \tag{2.19}$$
>
> [..] For the case where $\vec{E}_D(\vec{x}) = 0$, the weighting vector $W_n(\vec{x}, t)$ then becomes the response to a delta pulse $V_0\delta(t)$ on the electrode n.

---

[12] Reprinted from *Nuclear Instruments and Methods in Physics Research Section A: Accelerators, Spectrometers, Detectors and Associated Equipment*, 940, Riegler, W., An application of extensions of the Ramo–Shockley theorem to signals in silicon sensors, 453–461., 2019, with permission from Elsevier.

As previously stated, in this thesis the weighting vector with respect to electrode n will be denoted with $\vec{W}_V^{(n)}$, instead of $\vec{W}_n$ as used by W. Riegler. The simple multiplication of the weighting field with the velocity of the charge in the case of the Shockley-Ramo theorem has been replaced by a convolution-like operation between the now time-dependent weighting vector and the charge velocity. In section 8.3.3 it will be shown that in specific simple cases the extended Ramo-Theorem can be applied via convolution. The time-dependent weighting vector usually has a prompt component, corresponding to the direct induction of current due to the moving charge, and a delayed component, corresponding to the response of the conductive medium to the moving charge. In [4] a separate theorem is presented which allows to directly calculate the voltage induced onto a readout electrode (*Theorem 1*), taking into account the impedance elements connected to the readout electrodes. For this thesis the alternative approach is used, where first the current induced onto grounded electrodes is calculated. The voltage induced onto the electrodes is calculated in a second step, where the calculated currents are imposed as current sources onto an equivalent circuit. This is similar to the approach presented in section 2.3.1 in the case of non-grounded electrodes for the original Shockley-Ramo theorem. The difference is that the sensor itself is no longer represented by just a capacitance matrix, but needs to be represented by a full admittance matrix due to the conductive elements. This approach is proposed in *Section 5* of [19].

For complex cases TCAD or another finite element analysis (FEA) solver needs to be used for calculating both the time-dependent weighting vector as well as the admittance matrix of the sensor. The steps necessary for obtaining the weighting vector from TCAD (or similar) simulations is also outlined in [4]. This approach is used in [38] and [39] to simulate the signals in micromesh gaseous detectors (MICROMEGAS) with resistive elements. In the referenced work the induced charge is directly calculated using time-dependent weighting potentials (using *Theorem 2* in [4]) and the COMSOL software package is used for the calculation of the weighting potential. The time dependency of the weighting potential is evaluated as discrete slices in time. The charge propagation simulation is carried out using Garfield++, which is the only one of the existing software frameworks presented in section 8.2.2 which supports the extended Shockley-Ramo theorem.[13]

In simple cases, especially 1D problems, the weighting vector can be calculated analytically. It is assumed here that the static electric field inside the sensor is $E_D = 0$ for the purpose of calculating the weighting field and weighting vector. For semiconductor detectors this is a valid approach as previously shown in section 2.3.1. Revisiting the original Shockley-Ramo theorem, the weighting field with respect to an electrode n is defined as the electric field created by applying a voltage V_0 onto electrode n and grounding all other electrodes. Formally this corresponds to solving

$$\vec{\nabla}^2 V = 0 \tag{2.20}$$

with the boundary conditions $V_n = V_0$ and $V_{i \neq n} = 0\,\mathrm{V}$. The weighting field is then given by

$$\vec{W}_F = -\frac{\vec{\nabla} V}{V_0} \tag{2.21}$$

for electrode n.[14] In the case of a conductive medium the time-dependent weighting vector associated with electrode n is the electric field response to a Dirac delta pulse $V_0 \delta(t)$ applied to electrode n, while keeping all other electrodes grounded [4]. In [18], W. Riegler developed a formalism for analytically deriving this electric field response in the presence of conductive media. This derivation is summarized here.

Ampère's circuital law with Maxwell's addition reads

$$\vec{\nabla} \times \vec{H} = \vec{J}_f + \frac{\partial \vec{D}}{\partial t} = \vec{J}_f + \varepsilon \frac{\partial \vec{E}}{\partial t} \tag{2.22}$$

---

[13] A simple 1D example of a resistive plate chamber with a time-dependent weighting potential is shown at `https://garfieldpp.web.cern.ch/garfieldpp/examples/rpc/`.

[14] Both Ramo [33] and Shockley [32] in their publications assumed $V_0 = 1\,\mathrm{V}$ and thus completely ignored the voltage V_0 as a division by 1 does not alter the numerical value. But this leads to some inaccuracy regarding the units in their papers. To quote from Ramo [33] '[the weighting field] E_v is the component in the direction v of that electric field which would exist at the electron's instantaneous position [..]'. This gives the impression that the weighting field is an electric field and that it has the unit $\mathrm{V\,m^{-1}}$, when in reality (in accordance with (2.21)) it has the unit $\mathrm{m^{-1}}$. The exact value of V_0 does not change the derivation of the Shockley-Ramo theorem and explicitly including the normalization by V_0 removes the ambiguity with respect to the units of the weighting field W_F (E_v in the paper of Ramo).

assuming a linear and frequency independent material ($\vec{D} = \varepsilon\vec{E}$ with $\frac{\partial\varepsilon}{\partial t} = 0$).[15] In a conductive material the free current is given by $\vec{J}_f = \sigma\vec{E}$. Inserting this into (2.22) and taking the divergence one obtains

$$\vec{\nabla} \cdot (\vec{\nabla} \times \vec{H}) = 0 = \vec{\nabla} \cdot \left(\sigma\vec{E}\right) + \vec{\nabla} \cdot \left(\varepsilon\frac{\partial\vec{E}}{\partial t}\right) \tag{2.23}$$

Under the approximation of negligible magnetic coupling (i.e. $\frac{\partial\vec{B}}{\partial t} \approx 0$) this can be expressed in term of the electric potential Φ

$$\vec{\nabla} \cdot \left(\sigma\vec{\nabla}\Phi\right) + \vec{\nabla} \cdot \left(\varepsilon\frac{\partial\vec{\nabla}\Phi}{\partial t}\right) = 0 \tag{2.24}$$

Under the assumption that initially no potential is present $\Phi(\vec{x}, t = 0^-) = 0$ this can be expressed in the Laplace domain as

$$\begin{aligned} \vec{\nabla} \cdot \left(\sigma\vec{\nabla}\bar{\Phi}\right) + \vec{\nabla} \cdot (\varepsilon s\bar{\Phi}) &= 0 \\ \vec{\nabla} \cdot \left(\left(\frac{\sigma}{s} + \varepsilon\right)\vec{\nabla}\bar{\Phi}\right) &= 0 \end{aligned} \tag{2.25}$$

with $\bar{\Phi} := \mathcal{L}\{\Phi\}$. This expression is similar to the Poisson equation for electrostatic problems, with the substitution $\epsilon = \frac{\sigma}{s} + \varepsilon$. The time-dependent potential $\Phi(t)$ can thus be found by solving for the pseudo-electrostatic potential $\bar{\Phi}(s)$ in the Laplace domain, using the mentioned substitution for ϵ and applying the necessary boundary conditions. To find the weighting vector with for an electrode n, a Dirac voltage pulse $\Phi_n(t) = V_0\delta(t)$ is applied to said electrode while keeping all other electrodes grounded $\Phi_{i\neq n} = 0$. In the Laplace domain the voltage pulse on electrode n is a constant voltage $\bar{\Phi}_n(s) = \{V_0\delta(t)\} = V_0$. An inverse Laplace transform finally leads to $\Phi(t) = \mathcal{L}^{-1}\{\bar{\Phi}(s)\}$. According to [18] the weighting vector for electrode n is then given by

$$\vec{W}_V^{(n)} = -\vec{\nabla}\Phi \tag{2.26}$$

based on the relation between the electric potential and the electric field. This principle is heavily used in [4, 19] and in section 8.3 it is applied to the bonded P/N structures fabricated in the scope of this thesis, which can be treated as simple 1D structures.

---

[15] In [18], W. Riegler states that the developed formalism is also valid for any frequency dependent medium. In the opinion of the author this does not hold, as in the case of a frequency dependent medium $\frac{\partial\vec{D}}{\partial t} = \frac{\partial\varepsilon}{\partial t}\vec{E} + \varepsilon\frac{\partial\vec{E}}{\partial t} \neq \varepsilon\frac{\partial\vec{E}}{\partial t}$ due to the implied time dependency of ε ($\frac{\partial\varepsilon}{\partial t} \neq 0$). Thus, in this thesis only the case with $\frac{\partial\varepsilon}{\partial t} = 0$ is considered.

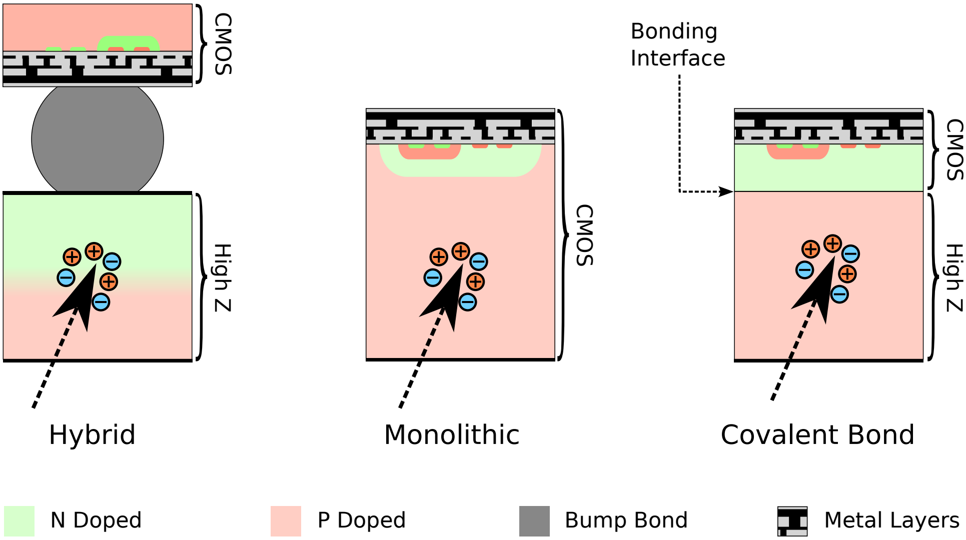

FIGURE 2.6: Cross section of a single pixel of a particle pixel detector showcasing the different possible detector structures. In hybrid detectors two separate chips (sensor and readout) are connected using bump bonds. In monolithic detectors the bulk of the CMOS readout chip acts as the interaction layer. A bonded detector acts similar to a monolithic detector, but based on the principle of wafer-wafer bonding the interaction layer can be made of a different (non-silicon) material. The arrow indicates a potential X-ray interaction leading to the creation of electron-hole pairs. The exact polarity and location of the N- and P-doping is for illustration only. Image not to scale.

2.5 DETECTOR STRUCTURES

One major difference between pixel detectors and simpler detector structures such as strip and pad detectors is that in pixel detectors the front-end electronics and signal acquisition for each pixel needs to be closely integrated with the sensitive pixel area itself. With pad and strip detectors it is possible to locate the front-end electronics in a dedicated part and connect the sensor and readout circuit via wire-bonding to a printed circuit board (PCB). The high number of individual channels (one per pixel) does not allow for such a solution with pixel detectors. Traditionally there are two different ways of integrating the readout circuit with the sensitive pixel layer: either via hybrid or monolithic integration. Both of these principles are represented in figure 2.6.

HYBRID DETECTORS In a hybrid detector the sensitive layer and the CMOS readout circuit are fabricated as two separate pixelated chips. The two parts are joined via bump-bonding, where the connection between each sensor pixel and the corresponding readout pixel is made by a small solder-like ball (bump) [20]. The advantage of hybrid detectors is that the two parts can be manufactured separately and thus also be made of different materials. As previously discussed, this for example allows to use high-Z materials for the fabrication of efficient X-ray image detectors. Bump bonding is a complex process which is often carried out on a per chip basis and which presents non-negligible costs. Its costs can also be driven up due to a limited process yield [12, 13, 40, 41]. In certain configurations the size of an individual bump bond can be the limiting factor for decreasing the pixel pitch [12]. Hybrid detectors are very common in physics applications for example as tracking detectors for the Large Hadron Collider (LHC) experiments such as ATLAS [11] and CMS [42]. The Medipix and Timepix family of detector readout chips are also designed for hybridization, and such a detector was used to acquire the first colour X-Ray tomographic image of human tissue [9, 12]. The principle of hybrid detectors is used by Dectris AG for building various types of X-ray detectors with either Si- or CdTe-based sensor layers [20, 43].

MONOLITHIC DETECTORS In a monolithic detector the sensitive part and the readout electronics form a single entity. The detector is designed so that the bulk of the readout chip acts as the sensitive layer for the particle interaction. In literature, monolithic pixel detectors are commonly referred to as monolithic active pixel sensors (MAPS) and depleted monolithic active pixel sensors (DMAPS), the difference being that DMAPS fully deplete the sensitive volume and thus collect signal purely via drift [40]. Compared to hybrid detectors, monolithic detectors can overall be built thinner and thus generally have a lower mass budget [40]. This is advantageous for tracking applications. The fabrication is also simpler as no bump bonding is necessary and only a single chip needs to be fabricated. For economic reasons it is only viable to implement monolithic detectors based on Si processes. Thus fabricating monolithic detectors with high-Z interaction layers is generally not possible. The readout circuitry also needs to be specifically designed for use in a monolithic detector. Given that the substrate of a monolithic detector needs to be (partially) depleted for signal formation, the readout electronics needs to be protected from the electric field in the bulk with special deep implants [40]. Further, high electric fields can occur in between pixels which, if not managed properly, can lead to premature breakdown of the sensor and inhibit proper biasing. Thus, the design of a monolithic detector can be more involved than the design of a hybrid detector. The current ALICE inner tracker (ITS2) is built using monolithic detectors. A future upgrade of the tracker (ITS3) will use ultra thin wafer scale monolithic detectors (ca. 30 µm thick) which will be bent to form a truly cylindrical tracker [44]. SPAD image detectors, as commonly employed for LIDAR applications can also be considered monolithic detectors [45].

BONDED DETECTOR Fabricating a detector via wafer bonding presents an alternative to the hybrid and monolithic fabrication methods. The underlying principle is to combine an absorber layer with a readout chip by the means of surface activated bonding (SAB). This low-temperature covalent bonding technique allows to fuse multiple semiconductor wafers via a conductive bonding interface. A bonded detector acts like a monolithic detector in the sense that the final product is one mechanical entity. Like in a monolithic detector the signal is collected through the bulk of the readout chip. But contrary to the monolithic approach, the detector can be made up of different materials which enables the use of a high-Z material as an absorber layer while economically implementing the readout circuitry in Si. As SAB can be carried out at room temperature, this method is compatible with bonding fully processed CMOS readout chips. Compared to a hybrid approach, a bonded detector does not need to undergo bump bonding. SAB is a process which is carried out on a wafer-level which might bring additional advantages of scale. The next chapter gives a more detailed description of the bonding process used.

3

WAFER-WAFER BONDED PARTICLE DETECTORS

Why would anybody eat something different than tuna?

— Emmy

In this chapter the concept of fabricating semiconductor particle detectors via surface activated bonding (SAB) is presented in more details. First an overview of different types of wafer-wafer bonding techniques is given. This allows to differentiate surface activated wafer-wafer bonding from other bonding techniques and allows to highlight why specifically this bonding technique is interesting for fabricating particle detectors. Next the surface activated wafer-wafer bonding technique is presented in more details. The second part of this chapter is dedicated to the attempt of building a functional pixel detector based on wafer-wafer bonding by G-Ray Medical Sàrl (G-Ray). The characterization of the initial prototypes built by G-Ray marked the start of the project presented in this thesis. Some results of these initial measurements with the BigNovipix (BNP) prototypes are presented in the third section of this chapter. Various problems and challenges were observed with these prototypes. This eventually led to the decision to fabricate the simple bonded diode samples, presented in chapter 4, which form the primary focus of this thesis.

CONTRIBUTION The first section of this chapter presents a review of the state of the art summarized by the author based on existing literature. The BNP detector prototype was designed and fabricated by G-Ray in close collaboration with the Swiss Center for Electronics and Microtechnology (CSEM). The first prototypes of the BNP were characterized at ETHZ by the author in the context of this thesis. Sebastien Murphy (ETHZ) collaborated on these initial characterizations.

3.1 WAFER-WAFER BONDING

In order to enable the integration of an absorber layer and a CMOS based readout chip via wafer-wafer bonding, the bonding technique needs to fulfil two requirements. First, the bonding process needs to be CMOS compatible, limiting the maximum processing temperature. At temperatures above 800 °C the increased solid solubility of certain dopants used in CMOS processes (especially phosphorus) becomes high enough to lead to additional diffusion of doping regions [46]. Aluminium (Al) metallizations, commonly used in CMOS, processes have a melting point of ca. 660 °C. An even stronger limit on the maximum post-processing temperature of CMOS circuits is given by the solubility of silicon (Si) in Al at temperatures in the range of 450-500 °C. In the worst case this can lead to spiking of Al, destroying the junctions of CMOS gates [46]. Giving an exact infimum of the upper limit at which CMOS wafers can be post-processed is in general not possible, as this is heavily dependent on the exact CMOS process used. But usually post-processing temperatures up to 250-300 °C are considered to be acceptable [47, 48], with lower temperatures presenting less risks of damaging the CMOS circuitry. A low process temperature is also important when bonding wafers of different materials to not introduce stress in the final assembly due to the mismatch of the thermal expansion coefficients. Second, a monolithic-like integration of the absorber and the readout is desired with the goal of having an electrically conductive connection between the two parts. Thus, no intermediary layers should be present at the bonding interface, allowing for a direct transition between the semiconductor crystal of the absorber wafer to the semiconductor crystal of the readout wafer. In the following, a (non-exhaustive) overview of existing wafer-wafer bonding techniques is presented. Only techniques which allow to bond two semiconductor wafers are described. If necessary, the bonding process is described using Si-Si wafer bonding as an example. But the bonding techniques described here are not limited to Si bonding, but are applicable to bonding of semiconductor wafers in general [46, 49, 50].

3.1.1 *Intermediate layer bonding*

The bonding processes listed in this section all use additional material at the bonding interface and thus do not fulfil the second requirement presented above.

ADHESIVE / POLYMER BONDING In adhesive bonding various polymers are used as intermediary (glue) layers between the wafers. The adhesive is applied to one or two of the mating surfaces and the two wafers are brought into contact, followed usually by curing / annealing step to achieve the final bond strength. This bonding is usually carried out at low, CMOS compatible, temperatures (typically below 250 °C) and the use of thick adhesive layers can reduce the need for planarized bonding surfaces [51]. The resulting bonding interface is not conductive [52].

GLASS FRIT BONDING In glass frit bonding a powder of glass with a low melting point is used as a bonding layer between two wafers. The glass frit is spread onto the contact surface and baked to remove binders. The two wafers are brought into contact, followed by another baking step under pressure at temperatures above 400 °C [46]. The resulting bonding interface is non-conductive.

SODIUM SILICATE BONDING In sodium silicate bonding two oxidized wafers are bonded via a spin coated layer of sodium silicate. The oxidized surfaces are first activated via a hot nitric acid treatment. Annealing of the bond is carried out at temperatures around 200 °C or lower, making this bonding technique CMOS compatible [46, 53]. The presence of SiO_2 results in a non-conductive bonding interface.

ANODIC BONDING Bonding of semiconductor wafers via anodic bonding works by first sputter depositing a thin layer of borosilicate glass on one wafer. The two wafers are then brought into contact while applying a high electrostatic voltage across the wafer stack. This leads to mobile alkali ions in the glass layer being drifted away from the bonding interface, leaving behind a charged region which attracts the wafers via electrostatic forces. Bonding temperatures can range from 200-400 °C and the resulting interface is not conductive [51].

THERMOCOMPRESSION BONDING In thermocompression bonding a thin metal layer is deposited on the wafer surfaces to be bonded. The bonding is then carried out under high temperature and pressure. Depending on the metal used, the temperatures can range from 250-500 °C. It is possible to obtain a conductive interface via the metal layer present at the bonding interface [46, 51].

EUTETIC BONDING Euthetic bonding is similar to thermocompression bonding, but instead of a pure metal a eutetic system of alloys is used. Such alloys have a lower melting point than their individual components. Similar to thermocompression bonding a conductive interface can be obtained [51].

3.1.2 *Direct / fusion bonding*

Direct (fusion) bonding allows to bond semiconductor wafers without any additional material at the interface. Covalent bonds are formed directly between the two wafers to be bonded, leading to high bond strengths. All the methodes described here share common requirements with respect to the quality of the surfaces to be bonded. The sensitivity to residual particles or organic contaminants on the bonding surface is high. Therefore a wet cleaning step (such as an RCA cleaning procedure[1]) usually precedes the bonding itself [54]. The local roughness of the bonding surfaces generally should be below 0.5 nm RMS and the wafers should have a very limited bow (few tens of µm) [54]. Thus, these types of bonding are usually only carried out with SEMI standard prime grade wafers and often chemical mechanical polishing (CMP) is employed pre-bonding to guarantee the roughness requirement. SAB, which is also a form of direct bonding, is discussed separately in the next section.

HIGH-TEMPERATURE HYDROPHILIC BONDING Two oxidized wafers are brought into contact at room temperature and without applied pressure. In the case of silicon wafers, the required flatness and cleanliness of the bonding surfaces leads to the exposed silanol groups ($\mathrm{Si{-}OH}$) of the two wafers to bond with each other, mainly via hydrogen bonds. The subsequent annealing step transforms these hydrogen bonds into covalent bonds via the following reaction

$$\mathrm{Si{-}OH + OH{-}Si \longrightarrow Si{-}O{-}Si + H_2O}.$$

The annealing is carried out at temperatures in the range of 800-1000 °C. Bonding can be carried out using the native oxide present on the wafer surfaces or using a thermally grown oxide, as for example employed in the fabrication of silicon on insulator (SOI) wafers [46, 49, 54]. The resulting

---

[1] RCA cleaning refers to a two step wet cleaning process. In the first step a mixture of ammonia and hydrogen peroxide removes organic residues and in the second step a mixture of hydrochloric acid and hydrogen peroxide removes metallic contaminants. Optionally, a hydrofluoric acid (HF) step in-between removes oxides [46].

bond has an oxide layer at the interface, separating the two semiconductor crystals.

LOW-TEMPERATURE PLASMA ACTIVATED BONDING This is a modification of the hydrophilic bonding process. Before bringing the two wafers into contact the surfaces to be bonded are activated using a plasma treatment (for example oxygen- or argon-plasma) [50]. The annealing step can then be carried out at much lower temperatures in the range of 200-400 °C while achieving similar bond strengths as classical hydrophilic bonding [49]. The bonds are formed via a thin oxygen layer at the interface, $Si - O - Si$ in the case of silicon, separating the two semiconductor layers.

HIGH-TEMPERATURE HYDROPHOBIC BONDING In hydrophobic bonding the native oxide on the wafers is first removed via a hydrofluoric acid (HF) based solution. In the case of silicon this leads to the formation of a hydrogen passivated $Si{-}H$ surface with some $Si{-}F$ groups present [50]. After bringing the two wafers into contact the initial bonding is mainly via van der Waals bonds between the hydrogen terminated surfaces. Thus, the pre-annealing bond strength of hydrophobic bonding is generally lower than for hydrophilic bonding [46]. Annealing at temperatures in the range of 700-800 °C leads to the formation of covalent bonds ($Si - Si$) [54]. Contrary to hydrophilic bonding, hydrophobic bonding does not result in an oxygen layer at the interface but leads to an abrupt transition between the two semiconductor crystals. This allows to form abrupt P/N junctions [46].

It is evident that none of these bonding techniques is compatible with the two requirements established in the beginning of this section. All the bonding processes which use an intermediate layer do not allow for a monolithic-like integration of an absorber with a CMOS-based readout chip. The is also true for the (either high-temperature or low-temperature) hydrophilic bonding processes due to the residual oxygen layer at the interface. The only process which allows to directly fuse two semiconductor wafers is hydrophobic bonding. But the necessary annealing temperatures of up 800 °C make this technique incompatible with CMOS circuits.

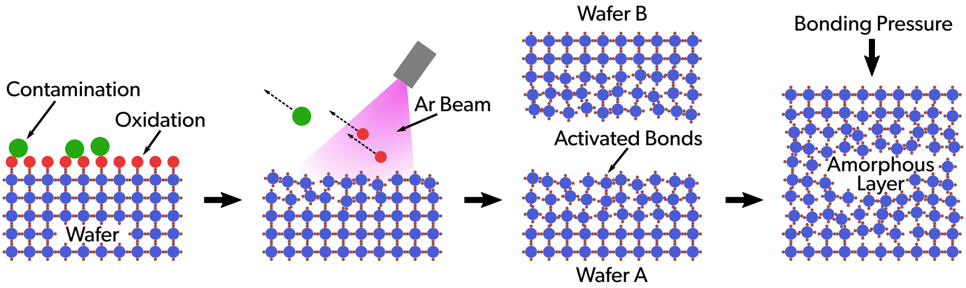

FIGURE 3.1: Schematic view of the surface activated bonding process: surface oxidation and contamination is removed from a substrate via Ar-beam sputtering, leading to activated bonds at the wafer surface. Bringing two activated wafers into contact leads to spontaneous bonding even at room temperature. A thin amorphous layer is present at the interface after bonding. Figure previously published in [62].

3.1.3 *Surface activated bonding (SAB)*

Low-temperature covalent wafer bonding via SAB fulfils both previously mentioned requirements. It allows to bond wafers at room temperature without any adhesive layer at the bonding interface. Post bonding annealing is possible but not necessary to achieve good bond strengths [51]. The use of SAB for bonding semiconductor wafers has first been shown by a group in Japan in 1996 for bonding Si to Si [55, 56].[2] Since then various combinations of materials have been demonstrated to be bondable using SAB. Examples include Si to gallium arsenide (GaAs) [57], Si to germanium (Ge) [58], Ge to Ge [59] and Si to diamond [60, 61]. SAB is based on two principles: the complete removal of the native oxide on the wafer surfaces via ion beam sputtering and the inhibition of re-oxidation of said surfaces by carrying out the process in ultra-high vacuum. The general process follows the principle illustrated in figure 3.1. The wafers to be bonded are introduced into the vacuum chamber of the bonding machine without any special pretreatment. On each wafer the surface to be bonded is cleaned using ion beam sputtering. Most commonly an argon (Ar) ion beam is used at an energy of a few hundred eV [14, 49, 63].[3] The sputtering removes the native oxide and adsorbed contaminants. In the case of silicon this leaves behind activated Si− bonds at the wafer surface [55]. As the process

---

[2] Even earlier work was done on SAB of metals [49].

[3] Sputter cleaning with other elements, such as neon (Ne), is also possible [14]. In the context of this project all bonding has been carried out with Ar.

is carried out in vacuum, these activated bonds do not re-oxidate.[4] The two wafers are finally brought into contact under moderate pressures in the order of 1 MPa and the bonding occurs spontaneously. Ideally, the resulting bond would be an abrupt transition from the semiconductor crystal of the first wafer to the crystal of the second wafer. In reality, the sputter cleaning disturbs the crystalline wafer surfaces, leaving behind a thin amorphous layer. Thus, bonds created via SAB will always have an amorphous layer with a thickness in the order of a few nm at the bonding interface. This amorphous layer presents a region with a high density of defects and dangling bonds [63, 65]. But even without an amorphous layer lattice defects would be expected at the bonding interface, either due to a difference in the lattice constants of the two crystals, or because of the axial and radial misalignment of the crystals of the two wafers. The amorphous layer indeed helps to gap any mismatch and misalignment of crystal structures and might be critical for achieving high bond strengths at room temperature [14]. SAB leads to a conductive bonding interface but the amorphous layer and its high defect density has a major influence on the transport of charge carriers. The exact nature on how this layer influences the electrical properties of the resulting bonded structure is the main question of this thesis.

MECHANICAL CHARACTERIZATION Mechanical characterization of any wafer-wafer bond is traditionally carried out using a double cantilever beam test, colloquially also known as the razor blade method or the Maszara method [49, 66]. A thin blade is inserted between the bonded wafers, leading to the opening of the bond along the bonding interface up to a distance L. The principle is illustrated in figure 3.2a. Based on the wafer thicknesses $t_{W1,W2}$, the blade thickness t_B and the measured length L the surface energy of the bond can be calculated. There exist multiple models for calculating the surface energy γ, a commonly used one being the original Maszara model [67]. Another commonly employed method is by using a standard tensile testing apparatus. The bonded sample is glued to studs which can be mounted in the testing apparatus and a force is applied to pull the bond apart until failure of the sample occurs. Figure 3.2b illustrates the principle. Both methods have certain inherent limitations which need to

---

[4] More precisely, the high vacuum levels ensure that redeposition of oxygen occurs on a time scale of minutes, leaving sufficient time for carrying out the bonding after sputter cleaning [64].

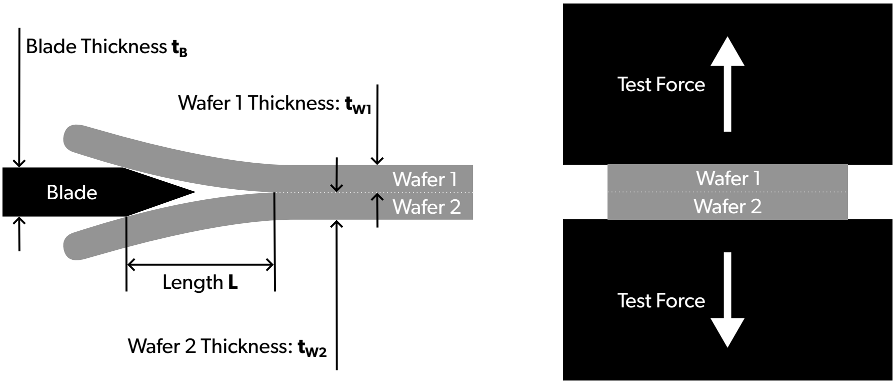

(a) Razor blad / Maszara method (b) Tensile test method

FIGURE 3.2: Schematic view of different mechanical surface energy characterization methods for wafer-wafer bonds.

be taken into account when doing measurements, especially in the case of high bond strengths. An extensive overview and discussion of the two methods is given in [66]. The theoretical maximum surface energy for $\langle 1\,0\,0 \rangle$ silicon is $\gamma = 2.5\,\mathrm{J\,m^{-1}}$ [49]. Si/Si bonds fabricated with SAB (without high-temperature annealing) generally achieve bond strengths close to this value [51].

The overall quality of the bonding interface on a macroscopic scale can also be assessed by scanning acoustic microscopy (SAM) measurements [46]. SAM images are especially useful for detecting voids introduced at the bonding interface for example due the presence of contaminating particles, as the phase transition between solid semiconductor and void leads to strong acoustic reflections. See section 4.2.1 for SAM measurements carried out as part of the fabrication of the bonded diode samples.

CHEMICAL CHARACTERIZATION To assess the structural and chemical composition of the bonding interface on a microscopic scale scanning transmission electron microscope (STEM) and energy-dispersive X-ray spectroscopy (EDXS) are employed. STEM allows to acquire high resolution cross section views of the bonding interface. Figure 3.3 presents an example STEM image of a Si/Si bond, showing the two crystalline bulk regions separated by the amorphous layer created by the SAB. Images acquired with STEM thus allow to measure the thickness of this amorphous layer.

Without any post-bonding annealing an amorphous layer thickness in the order of a few nm is very common [14, 54, 58, 63]. The thickness is strongly correlated with the ion beam energy used during the bonding [14, 68].[5] The modified bonding process used by G-Ray, which allowed to achieve the thin amorphous layer shown in figure 3.3, is discussed in 3.2.1. The atomic composition of the interface can be investigated by EDXS measurements. The electron beam of an electron microscope (such as a STEM) is used to locally excite the atoms of the sample under investigation. The subsequent atomic relaxation emits characteristic X-ray photons at clearly defined energies which can be used to identify the chemical components of the sample. See section 5.1 for high resolution STEM and EDXS measurements carried out on the fabricated bonded diode samples. If carried out correctly, SAB does not introduce any additional elements at the bonding interface, apart from a small deposition of the element used for sputtering (e.g. Ar). But, as discussed in more detail in section 5.3, accidental introduction of additional elements, such as metals, is not uncommon in non-optimized bonding processes.

ELECTRICAL CHARACTERIZATION In existing literature the electrical characterization of bonds created with SAB is usually limited to investigating the stationary conduction by means of I/V curves. Most of the available literature on surface activated Si/Si bonds uses substrates with much lower resistivities and thus much higher bulk doping concentrations than what is commonly used for the fabrication of fully depleting particle detectors. In general, there is no indication that results from low resistivity bonds are also directly applicable to bonds made from high resistivity substrates.

In [69], Morimoto et al. investigated the electrical behaviour of N-Si/N-Si and P-Si/P-Si bonds fabricated from low resistivity wafers ($\rho_N = 0.15\,\Omega\,\mathrm{cm}$ and $\rho_P \approx 0.12\,\Omega\,\mathrm{cm}$). The defects at the bonding interface are assumed to enable trapping of charge carriers which leads to a double Schottky like barrier at the bonding interface. From I/V curve measurements at different temperatures the height of this barrier is extracted, under the assumption that conduction across the barrier is dominated by thermionic emission. A barrier height of $\phi_B^{(P)} \approx 0.4\,\mathrm{eV}$ and $\phi_B^{(N)} \approx 0.15\,\mathrm{eV}$ was noted for samples annealed at 200 °C for the P/P and N/N bonded structures respectively.

---

[5] The thickness of the amorphous layer should be approximately twice the interaction depth of the ion beam used for surface activation [58].

They also investigated the I/V behaviour after annealing of the bonds at different temperatures. Interestingly, they found that the current density initially decreases when annealing up to 400 °C, before increasing again for annealing temperatures up to 1000 °C. A similar investigation was also carried out by Reznicek et al. in [70] for a different bonding technique which uses HF dipping instead of an argon beam for surface activation. They also extracted an interface barrier height assuming a double Schottky barrier. Further, they report that high doping of the interface leads to strongly increased current densities.

In [71], Shigekawa et al. characterized N-Si/N-Si and N-Si/P-Si bonds fabricated with low resistivity wafers ($\rho_N = \rho_P = 0.02\,\Omega\,\mathrm{cm}$). I/V measurements of the N-Si/N-Si bonds showed a near linear ohmic conduction across the bonding interface. The N-Si/P-Si structures showed a clear rectifying diode-like behaviour with a strong voltage dependency of the reverse bias current. A strong dependency of the diode turn-on voltage on the temperature was observed, and a diode ideality factor of > 2 was extracted for temperatures $\leq -50\,^{\circ}\mathrm{C}$. Based on the assumption that the conduction under reverse bias is dominated by trap-assisted tunnelling, the depth of the corresponding traps is estimated to be at $\approx 0.2\,\mathrm{eV}$.

In [57], Liang et al. investigated the electrical behaviour of N-Si/N-Si, P-Si/N-Si and $\mathrm{P^-}$-Si/$\mathrm{N^+}$-Si bond fabricated with very low resistivity wafers ($\rho_N, \rho_P = 0.02\,\Omega\,\mathrm{cm}$, $\rho_{P^-} = 0.1\,\Omega\,\mathrm{cm}$ and $\rho_{N^+} = 0.002\,\Omega\,\mathrm{cm}$).[6] The I/V curves measured on the N-Si/N-Si bonded structures showed a nearly ohmic behaviour very close to a pure N-type substrate, similar to what was observed in [71]. The I/V curves measured on the P-Si/N-Si and $\mathrm{P^-}$-Si/$\mathrm{N^+}$-Si structures show a rectifying behaviour, but deviate from the curves expected from the ideal diode model. The deviation is especially large in the case of the P-Si/N-Si structures. C/V measurements were also carried out on the P-Si/N-Si and $\mathrm{P^-}$-Si/$\mathrm{N^+}$-Si samples. The results show growing depletion widths under reverse bias for both cases, and in the case of the $\mathrm{P^-}$-Si/$\mathrm{N^+}$-Si bond a linear fit to the $\frac{1}{C^2}$ curve confirms that the $\mathrm{P^-}$-side is primarily being depleted. In both cases, P-Si/N-Si and $\mathrm{P^-}$-Si/$\mathrm{N^+}$-Si, the

---

[6] It should be noted that the bonds fabricated for the work presented in [57] also have a contamination with metal atoms at the bonding interface (see chapter 5 in this thesis). But due to the much higher bulk doping concentration in [57] the influence of this contamination might not be as drastic as it probably is in the case of the work presented in this thesis.

reverse bias current shows a strong dependency on the reverse bias voltage, which is attributed to conduction via trap-assisted tunnelling as well as the Frenkel-Poole model [72].

Research in the context of integrating multi junction III/V based solar cells with SAB shows that a high doping concentration at the bonding interface leads to improved conduction [73–75]. This is also reported in [69] in the context of bonding Si to Si. Under the assumption that the defects at the bonding interface lead to the formation of a double Schottky barrier, the presence of a high doping concentration at the bonding interface will reduce the width of the effective barrier. A reduced thickness of the barrier allows for conduction via tunnelling across the interface [73]. The effect at play is similar to the one when using high doping concentrations for forming ohmic metal-semiconductor contacts (see section 4.1.2).

As noted, none of these results can directly be applied to the case of bonded P/N junctions for particle detection due to the large difference in the resistivity of the used substrates. Further, none of these previous publications investigate the depletion behaviour of bonded P/N junctions under reverse bias in detail. The steady state current conduction across the bonding interface is not the primary interest when fabricating P/N junctions for particle detectors. Understanding the depletion behaviour under reverse bias, as well as the applicability of the signal induction as per the Shockley-Ramo theorem, is of higher importance.[7]

APPLICATIONS SAB has not yet been established as a widely used bonding technique in the industry [76]. The need for ultra-high vacuum processing, as well as the low surface roughness required, make this technique non-trivial to apply and can add additional complexity compared to other bonding techniques. SAB has been used for wafer-level packaging of microelectromechanical systems (MEMS) devices and research in the field of 3D integration of heterogeneous devices is under way [76]. Additional applications could also be specially engineered substrates for micro- and power-electronics [76]. One of the most promising application of SAB is in the field of solar cells where SAB allows to integrate different types of

---

[7] The fact that the depletion behaviour of a bonded P/N junctions might not be symmetric, as shown in chapter 7, was not obvious at the beginning of the efforts documented in this thesis.

junctions into one single two-terminal device. The low process temperature of SAB enables the integration of materials with different thermal expansion coefficients, and the possibility of creating electrically conductive bonds is a necessity for fabricating solar cells [77]. For this application, the resistivity of the bonding interface is usually minimized by dedicated high-dose implants on the surfaces to be bonded [78]. SAB is used to integrate the III/V part of the solar cell with a Si based solar cell. Tripple- and four-junction solar cells have been published with efficiencies exceeding 35 % [75, 77–80].

3.2 PRIOR WORK BY G-RAY

The idea of building novel high efficiency X-ray detectors based on high-Z materials originated from the NEXRAY project funded by Nano-Tera[8]. The original idea was to directly grow thick Ge layers on the backside of fully processed CMOS pixel detectors, thus forming a highly efficient absorber layer [81]. Growing a thick and continuous layer of Ge on Si leads to cracks and defects due to the difference in the thermal expansion coefficients of the two materials. As part of the NEXRAY project, a novel technique for growing thick epitaxial layers was developed, where the Ge is not grown as a continuous layer but as individual high aspect ratio and space-filling pillars. It was shown that strain- and defect-free layers with a thickness of multiple tens of µm could be grown by using pillars with a lateral size of ca. 5 µm [82]. This concept was further developed in the context of the NOVIPIX[9] and PIXISENS[10] projects. Instead of pure Ge, up to 200 µm tall silicon-germanium (SiGe) pillars were grown. The alloy between Si and Ge has a higher band gap than pure Ge and thus should have a lower leakage current, which would be beneficial to detector operations [14]. The direct growth of the SiGe material on the silicon substrate exposes the processed CMOS circuits to temperatures of up to 700 °C. This is incompatible with standard CMOS processes as previously discussed in section 3.1. The possibility of using a modified CMOS process with tungsten (W) metallization was considered, but abandoned due to the very limited availability of foundries offering W-based CMOS processes [14]. Instead, the approach of using wafer-wafer bonding was pursued. Under this approach, the SiGe pillars would be fabricated and grown on a non-

---

[8] The project website can be found at `http://www.nanotera.ch/projects/85.php`.

[9] SNF Sinergia grant number 147639: `https://data.snf.ch/grants/grant/147639`

[10] Innosuisse / CTI project number 17703.1 PFNM-NM

processed Si wafer and subsequently bonded to the already processed wafer containing the CMOS readout structures [14]. The bonding would be carried out by SAB which, due to its low processing temperature, is compatible with processed CMOS wafers. G-Ray was founded in 2014 with the goal of commercializing this type of detector, primarily focusing on medical X-ray applications. The use of a low-temperature bonding technology opens up the possibility of using any high-Z semiconductor material as an absorber layer, independent of the mismatch in thermal expansion coefficients. As previously stated, SAB allows to stress-free bond Si wafers to Ge, GaAs and other materials. In light of this, using patterned absorbers with individually grown SiGe pillars adds unnecessary complexity to the process and was eventually abandoned by G-Ray.[11] Instead the medium-term focus was put on using very high resistivity GaAs wafers as an absorber layer.

The use of SAB introduces the added complexity of the bonding interface embedded within the detector structure. The conversion between X-rays and electron-hole pairs occurs within the absorber layer but the readout is implemented in the CMOS chip, and thus the signal created by the moving charges needs to propagate across this interface. As discussed in section 3.1.3, while the interface formed by SAB in general can be conductive, the defects introduced during bonding in many cases hinder the charge transport across the interface. And as shown, the existing electrical characterizations of the bonding interface are usually limited to measuring I/V curves, thus only investigating the stationary charge transport across the interface. Two PhD thesis projects carried out as part of or closely related to the NOVIPIX project investigated the influence of the bonding interface on transient signals in more detail. Both Arik Jung [14] and Jacopo Bronuzzi [52] in their respective thesis came to the conclusion that when bonding wafers of the same type (i.e. N- to N-type or P- to P-type) the defects present in the amorphous layer inhibit proper charge collection. Both note on the possibility of improved charge collection in the case of bonding wafers of opposite type (i.e. P- to N-type). The main argument supporting this claim is that in an ideal reverse biased P/N junction the highest electric field is present at the location of the junction. It is argued that this high electric field enables charges to cross the bonding interface and therefore improves charge collection in bonded sensors. This argumentation is par-

---

[11] The growth of Ge and SiGe pillars on patterned substrates continues to be investigated in the academic context [83–85].

tially based on the assumption that the presence of the interface defects as trap states will lead to the formation of a double Schottky barrier [69, 70, 86] and that a high electric field will aid the transport of charges across this barrier. When placing the P/N junction at the bonding interface it was assumed that the depletion region would grow in a symmetric fashion into the N- and P-side starting from the interface, to eventually deplete the full detector volume. This approach was chosen by G-Ray as a baseline design for building their detectors. Initial detectors were built by bonding a P-type high resistivity silicon absorber layer to N-type CMOS readout wafers.[12] Arik Jung documents initial X-ray illumination measurements with a proof-of-concept sensor built this way [14]. But, as noted by Arik Jung, the measurements do not allow for a quantitative analysis of the sensor efficiency, and thus do not allow to confirm that the chip is indeed depleting symmetrically from the bonding interface towards both sides. The measurements also do not allow to confirm that the interaction of X-ray photons in the absorber layer (P-type) generate a detectable signal in the readout chip (on the other side of the bonding interface). But, based on these results, G-Ray went on to built a full sized X-ray image sensor prototype (named the BNP). This chip, as well as the results from initial measurement carried out with the chip as part of this thesis, are presented in section 3.3.

3.2.1 *Modified bonding process*

In [14] it was shown, that the thickness of the amorphous layer in SAB correlates with the energy used for Ar sputtering. Thus G-Ray employed a modified version of SAB for the production of their samples in order to reduce the thickness of the amorphous layer at the interface as much as possible. The assumption being, that a thinner amorphous layer has fewer overall defects and thus enables improved charge collection. The modified bonding process includes the removal of the native oxide via a dip in diluted HF just before insertion of the wafers into the bonding machine. This leaves behind a hydrophobic hydrogen-terminated surface. Thus, the subsequent activation step inside the ultra high vacuum (10^{-8} mbar) only has to remove the hydrogen passivation on the bonding surfaces which can done at much lower Ar sputtering energies than traditionally employed in SAB [15, 87].

---

[12] Silicon is used as an absorber layer for the first prototypes while the process of bonding high-Z absorber layers (e.g. GaAs) was being optimized.

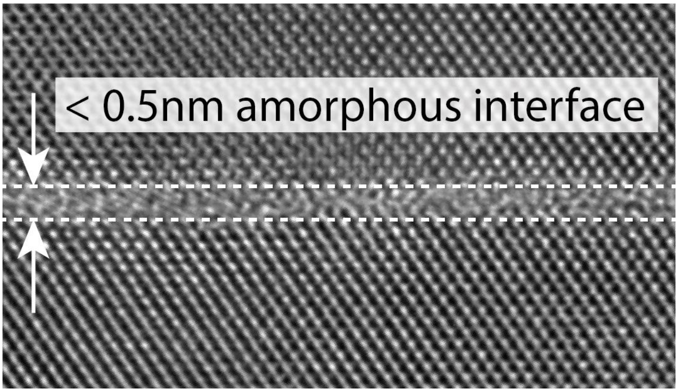

FIGURE 3.3: High resolution transmission electron microscope image of a silicon/silicon bonding interface produced by G-Ray. Between the two crystalline regions an amorphous layer with a thickness $< 0.5\,\text{nm}$ is visible. Reproduced from [88] with permission.

G-Ray heavily modified their existing EV Group (EVG) *ComBond* bonding machine, installing a new Ar ion source which allowed to use an Ar plasma instead of an Ar beam for the cleaning step [14]. They also improved the vacuum system of the machine in order to allow for longer plasma cleaning times without re-oxidation of the wafer surfaces. The trade-off between the Ar energy, cleaning time, vacuum level and bond strength is discussed in more detail in section 5.6 of [14]. Using their modified process, G-Ray was able to demonstrate bonding interfaces with an amorphous layer thickness of less than 0.5 nm, as shown in figure 3.3.

The modified process was employed by G-Ray for fabricating the BNP prototypes (presented in the next section). As part of this thesis a first attempt of bonding simple diode samples was carried out using the modified G-Ray process, but was unsuccessful. The final samples fabricated as part of this thesis were not bonded by G-Ray but by EVG on a non-modified EVG *ComBond* machine using the traditional SAB process [89, 90]. See section 4.1 for a detailed description of the simple diode fabrication.

3.3 THE BIGNOVIPIX PROTOTYPE

The BigNovipix (BNP) was developed by G-Ray as a proof-of-concept of a large area wafer-bonded detector. It was per se not intended as a

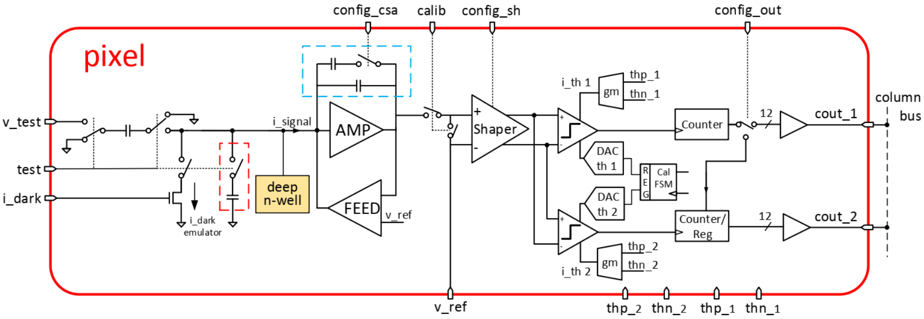

Figure 3.4: High-level circuit diagram of a single pixel of the BNP. The signal is amplified via a CSA, followed by a configurable shaper and two discriminators. The discriminator thresholds are the same for all pixels across the sensor and are set via analog bias voltages. The two discriminators can either be used concurrently or in a double buffer configuration for concurrent data acquisition and readout. Figure reproduced from [88] with permission.

commercial product, but G-Ray intended to sell the BNP as part of their *latenium Evaluation kit* [88].

READOUT CHIP The readout chip was designed by CSEM and fabricated by LFoundry in a 150 nm CMOS process. It was designed for N-type wafers with a resistivity of 1 kΩ cm and to be bonded to a P-type absorber layer. Thus the active P/N junction is formed at the bonding interface. The pixels pitch is 100 µm with a total of 240 × 300 pixels [88]. Each pixel contains a charge sensitive amplifier (CSA), followed by a shaper stage and by two separate discriminators, each applying a globally set threshold. Together with two dedicated 12-bit counters per pixel the discriminators allow for basic multispectral imaging [88]. The high-level schematic of a single pixel is shown in figure 3.4, and figure 3.5b shows a high-level block diagram of the readout chip.

DETECTOR INTEGRATION Prior to the bonding of the readout wafers to the absorber layers, the processed CMOS wafers were temporarily bonded to a carrier wafer. The backside of the readout wafer (CMOS bulk) was then thinned to the desired thickness via grinding and CMP. The CMP step also ensures the necessary surface roughness for bonding. The bonding via SAB was carried out by G-Ray in a dedicated cleanroom using the

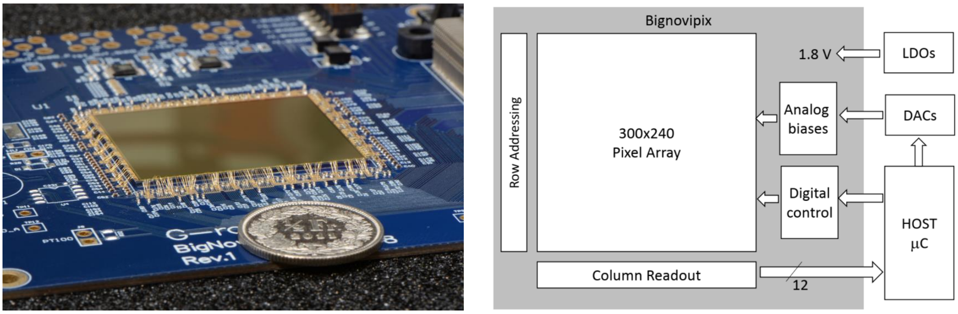

(a) Close up image of a BNP sensor wire-bonded to a carrier PCB. The size of the die is ca. 26 mm × 31 mm.

(b) High level block diagram, documenting the operation and image readout of the BNP.

FIGURE 3.5: Overview of the BNP sensor fabricated by G-Ray. Both figures reproduced from [88] with permission.

modified EVG *ComBond* bonding machine (see section 3.2.1). Some bonded sensor wafers were annealed at very low temperatures (ca. 200-300 °C). After releasing the CMOS carrier wafer the backside of the bonded stack (the exposed surface of the absorber layer) was metallized with a central bias pad and guard rings. Finally, the sensors were diced and wire-bonded to a data acquisition board developed by CSEM [88].[13] Figure 3.5a shows an image of a fully processed and wire-bonded BNP sensor on the custom printed circuit board (PCB).

3.3.1 *Initial characterization*

Several samples of the first BNP production run were received at ETHZ for characterization. Their P-type silicon absorber layer have a thickness of ca. 400 µm and a resistivity of $> 5\,\mathrm{k\Omega\,cm}$, and the BNP readout chip a N-type substrate with a resistivity of ca. $1\,\mathrm{k\Omega\,cm}$ and a thickness of ca. 10-20 µm. These samples proved to be sensitive to X-rays. Some example X-ray images are shown in figure 3.6. But initial measurements showed a very high leakage current in the order of tens of mA at low reverse bias voltages. In addition the reverse bias current was not stable and generally increased over time. In certain cases, after operating the chip in a steady state for tens of minutes, an exponential runaway of the current occurred. These initial

---

[13] Later prototypes were assembled on a new (FPGA-based) data acquisition system, but no tests with this new system were carried out as part of this thesis.

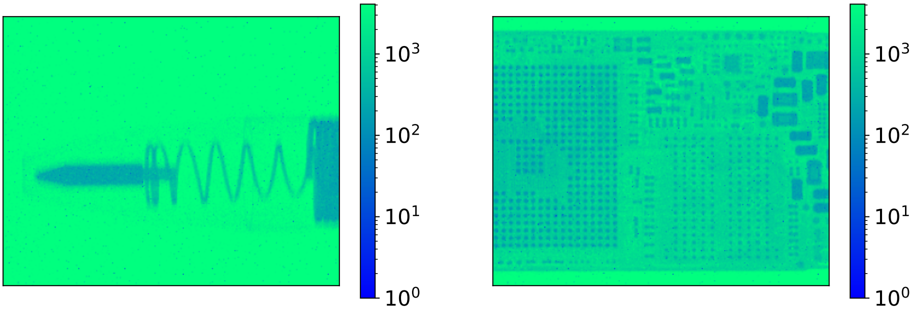

(a) Showing a ballpoint pen.

(b) Showing a solid state drive.

FIGURE 3.6: Example X-ray images acquired with the BNP samples as part of the characterization at ETHZ. The color scale shows the number of counts for each pixel.

samples could not reliably be temperature stabilized and it is thus possible that the observed behaviour is linked to thermal effects. But the leakage current also exhibited a hysteresis, with the initial current after applying a bias voltage being dependent on how long the chip had been turned off beforehand. The long time scale (minutes to hours) which was necessary to recover the initial leakage current state indicates that this hysteresis is not purely due to thermal effects. A possible explanation for the observed high leakage currents is the occurrence of a punch-through effect between the P-type absorber layer and the deep P-wells which encapsulate the pixel electronics in the readout chip. Assuming that the thin N-type CMOS substrate is fully depleted when applying very moderate bias voltages, a substantial hole-current can flow between the two P-type regions [91].

In general, the very high leakage currents did not allow to reverse bias the samples above 50 V for measurements with X-rays and other radiation sources. Under the assumption of a symmetric depletion of the P-type absorber and the N-type CMOS substrate reverse bias voltages in excess of 300 V would have been necessary for fully depleting the entire chip. Various measurements with a 60 keV X-ray cabinet were carried out. Exposing the absorber side of the samples to low energy X-rays gave qualitative indications that a particle interaction happening in the absorber can lead to a detectable signal in the readout chip, and thus, that the bonding interface can be *transparent* to signals. But it was not possible to quantify this observation. Using the measurement of the X-ray source spectrum with an Amptek *X123* X-ray spectrometer[14] as a reference, an estimation of the detector efficiency could be obtained. The reference spectrum was extrapolated to the location of the BNP sample and the number of X-ray photons absorbed by the BNP substrate and absorber was estimated. Comparing this number to the maximum count rate observed with the BNP indicated a detection efficiency in the order of 10 %. To what extent this low efficiency is due to the only partial depletion of the detector or due to additional effects linked to the bonding interface could not be quantified. But these measurements again gave qualitative indications that signals could indeed cross the bonding interface [92]. Long duration measurements with the X-ray source further showed that the detected X-ray rate decreases over time. This issue might be linked to the time-dependent increase in leakage current, as both effects occur with similar characteristic times. But while the leakage current tended to increase with time, the detected X-ray rate decreased during the same time frame. As observed with the leakage current, the X-ray count rate also showed a clear hysteresis: two subsequent long duration measurements did not detect the same rate of X-ray photons. Re-running the same acquisition after a longer break (the next day) led to a recovery of the originally observed count rate.

Overall, the characterization of the initial BNP samples raised more questions than answers. Most importantly, the measurements with these samples did not allow to conclude if the bonded absorber layer substantially contributed to the signal detected by the BNP, or if only the substrate of the BNP CMOS readout chip was sensitive to X-rays. The observed effects could not conclusively be attributed to either problems with the BNP chip itself or the presence of the bonding interface. Overall the BNP detector is a too complex system for probing the fundamental questions about the behaviour of the bonding interface and its influence on the formation of signals within the detector. This led to the decision to pursue the fabrication and investigation of simple bonded pad diodes, as presented in the remaining chapters of this thesis.

---

[14] Manufacturer website: `https://www.amptek.com/`

4

FABRICATION OF WAFER-WAFER BONDED DIODE SAMPLES

> *A door shall always be open - under any circumstances - if not, it will be opened!*
>
> — Hilbert

As discussed in the previous chapter, the bonded BigNovipix (BNP) sensor prototypes fabricated by G-Ray Medical Sàrl (G-Ray) show various non-idealities and do not allow to conclusively investigate the behaviour and influence of the bonding interface on the signal collection. Therefore it was decided to fabricate simple bonded pad diodes with no integrated electronics. These samples allow to directly investigate the effects of the bonding interface based on measurements of analog signals. One of the major fabrication challenges for these samples (apart from the bonding itself) is creating good ohmic metal-semiconductor contacts, in order to not have any additional parasitic effects. In this work this is solved via high dose ion beam implantation. A cross section of such a bonded pad diode is shown in figure 4.1. The P/N-junction is formed by bonding a P-type to an N-type wafer, thus, in the ideal case, forming an abrupt junction diode. The general structure, with the P/N junction placed at the bonding interface, is equivalent to the approach used by G-Ray. The two contacts are formed on the front and back side of the bonded wafer stack. The samples are fabricated by bonding silicon (Si) to Si wafers, similar to the BNP prototypes received from G-Ray.[1] High resistivity float-zone wafers are used, as commonly employed for fabricating particle pixel sensors [13, 41].

The first section of this chapter discusses the design of the fabrication process in details. This is followed by the documentation of the actual fabrication run, which was mainly carried out at the Binning and Rohrer Nanotechnology Center (BRNC) cleanroom facility. An overview of the

---

[1] Fabricating and testing samples with high-Z (e.g. GaAs) wafers bonded to Si are foreseen for a future run, pending the results acquired with the Si-Si samples.

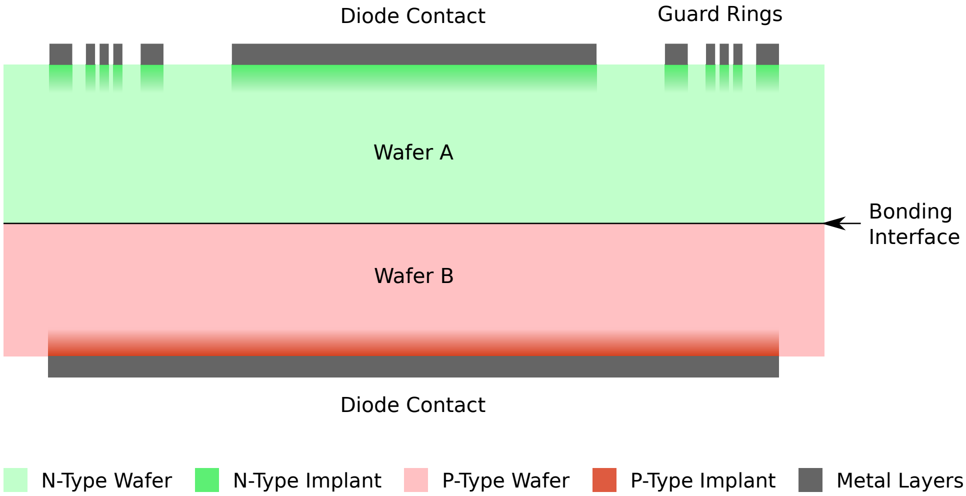

FIGURE 4.1: Schematic cross section view of a bonded diode sample as fabricated for this thesis. The P/N junction is formed by bonding two wafers of opposite types. The N-side contact is surrounded by guard rings while the P-side contact is a simple metal pad. Both P- and N-side contacts have a high dose implantation to improve the contact resistivity. The drawing is not to scale.

fabricated samples is given, and the results of quality control measurements carried out during the fabrication are documented.

FAILED FIRST PRODUCTION RUN The fabrication process presented in this chapter is the second attempt at fabricating these samples (internally labelled *Run 2*). The first attempt (internally labelled *Run 1*) failed during the bonding of the samples. The two runs have a very similar process, with the following differences: *Run 1* used 150 mm wafers instead of the 100 mm wafers of *Run 2*,[2] and in *Run 1* the contact metallization was carried out before the bonding. This imposed the deposition of a 1 µm thick SiO_2 layer via plasma-enhanced chemical vapor deposition (PECVD) in order to protect the metal during the bonding process. Further, in *Run 1* the chemical mechanical polishing (CMP) step was carried out by the author at the Center of MicroNanoTechnology (CMi) at EPFL, and the bonding was attempted by G-Ray using their modified bonding process

---

[2] 150 mm wafers were initially chosen due to the (wrong) assumption that bonding 100 mm wafers would pose problems. For the second attempt 100 mm wafers were chosen as the equipment at BRNC is better adapted for this wafer size.

(see section 3.2.1). The bonding of *Run 1* failed as this protective oxide layer was not compatible with the hydrofluoric acid (HF) dip of the modified bonding process, damaging the contact metallization. In addition, it is quite likely that the polishing via CMP, attempted by the author, was not of sufficient quality to yield good bonds. This chapter presents the fabrication process for *Run 2*, wich improved on these weak points of *Run 1* and which led to successful bonding.

CONTRIBUTION The fabrication process was designed by the author, with inputs from the BRNC operations team and from contacts at G-Ray. The author himself carried out all fabrication steps, except for the ion beam implantation, the implant annealing, the CMP and the bonding, which were carried out by external partners. The quality control measurements were executed by the author, excluding the scanning acoustic microscopy (SAM) measurements which were provided by the bonding partner.

4.1 PROCESS DEVELOPMENT

The overall process design is driven by the two key steps: the bonding via surface activated bonding (SAB) and the creation of ohmic contacts via ion beam implantation. The ion beam implantation is followed by a doping activation step via high-temperature annealing. This imposes that the ion beam implantation needs to be carried out before bonding, as the subsequent high-temperature step otherwise would lead to an annealing of the bonding interface. This is not desired given that the goal is to study the influence and behaviour of the non-annealed bonding interface, as it would be the case when bonding fully processed CMOS wafers. As observed in the first failed production run, bonding wafers with existing metal layers adds additional complexity and therefore the contact metallizations are created after successful bonding. Thus the overall process can be summarized by the following major steps:

1. etching of alignment marks (section 4.1.1),
2. contact doping via ion beam implantation (section 4.1.2),
3. bonding via SAB (section 4.1.3),
4. creation of metal contacts via lift-off (section 4.1.4),

5. and laser dicing of the bonded wafers (section 4.1.5).

The individual process steps are presented in detail in the following sections.

4.1.1 *Alignment marks*

The contact doping and the metallization of each sample is using structured patterns. Therefore both of these steps involve photolithography with dedicated masks. The first step, the ion beam implantation, generally does not leave behind any visible structures on the wafer surface which could be used for alignment during the later metallization photolithography step. Thus, it is necessary to create dedicated alignment marks on the wafer surface, which can be used for the alignment of all subsequent photolithography steps.

IMPLEMENTATION The alignment marks are formed using reactive-ion etching (RIE) to create patterned trenches in the silicon surface with a nominal depth of 100 µm.[3] The etching is carried out with an Oxford *PlasmaPro NPG 80* machine using a standard Si etching recipe. A *AZ1505* positive photoresist is used for the mask. The detailed process steps are listed in the appendix A.2. An example mask set of the implement alignment marks is shown in figure 4.2a. Coarse alignment is done via the central cross structure. The horizontal and vertical lines surrounding the cross implement vernier scales with an offset of 2 µm. The critical dimension of the diode structures is in the order of 20 µm, and thus an alignment to a precision of 2 µm is sufficient. The alignment marks themselves are aligned relative to the wafer flat.

4.1.2 *Contact doping*

Depositing a metal layer on a semiconductor substrate does not automatically lead to a good electrically conductive (ohmic) contact between the two. Under idealistic considerations, the behaviour of a metal-semiconductor interface is governed by the difference in the work function of the metal and

---

[3] The actual depth of the marks is not important, as long as a sufficiently large contrast is created between etched and non-etched areas. Due to process variations the actually etched trenches tended to be deeper than 100 µm.

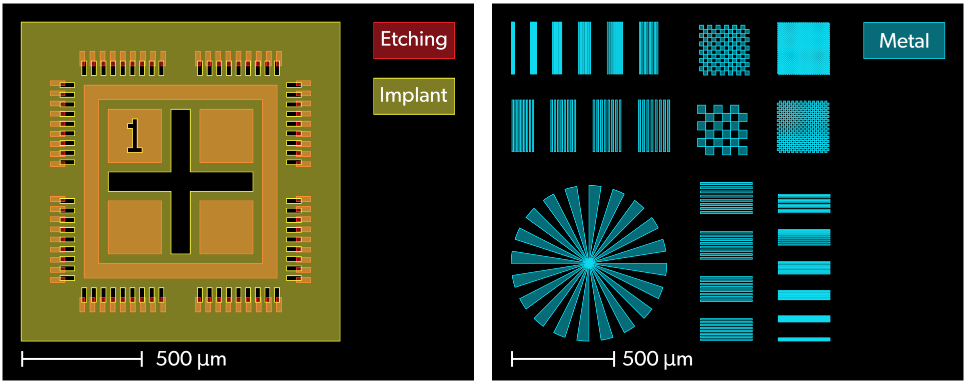

(a) Illustration of the alignment mark structure used for this fabrication process. The cross in the middle is used for coarse alignment and fine alignment is done via the horizontal and vertical vernier scales along the edges.

(b) Resolution test structures

FIGURE 4.2: Different elements of the mask set.

the electron affinity of the semiconductor [17, 93]. When a metal layer is brought into contact with a semiconductor, the Fermi levels in both materials align, which leads to the formation of either a depletion or accumulation zone at the interface. The exact behaviour depends on the type of the semiconductor and the metal work function. This behaviour is illustrated in figure 4.3a for the case of an N-type semiconductor in contact with a high-work-function metal. In this simple model, the height of the resulting barrier is given by

$$\phi_B = \phi_m - \chi \tag{4.1}$$

with ϕ_m the metal work function and χ the semiconductor electron affinity. Such a barrier inhibits the passage of charges between the semiconductor and the metal, leading to a non-linear (non-ohmic) relationship between the potential across the contact and the current flowing through it. In reality, secondary effects play a major role in the behaviour of a metal-semiconductor contact. Experimentally it has been shown that the contact barrier often does not follow the simple relationship shown in (4.1) [93]. The precise behaviour of the contact is very complex, depending on many different factors, including the crystal orientation, the surface preparation

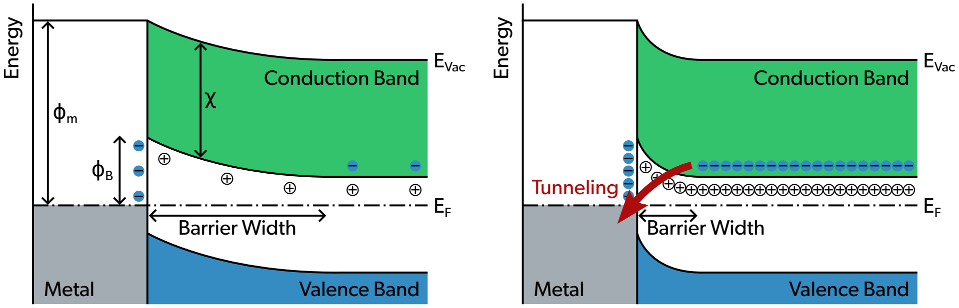

(a) With low N-doping.

(b) With high N-doping.

FIGURE 4.3: Behaviour of an ideal metal-semiconductor contact in the case of an N-type semiconductor in contact with a high-work-function metal. E_F is the Fermi energy level and E_{Vac} the vacuum energy level.

before metal deposition and the exact chemical composition of the metal-semiconductor interface [93]. The contact behaviour can be dominated by the presence of interface defects, leading to the pinning of the Fermi level and making the contact barrier nearly independent of the metal work function [93]. But, while in general the simplistic idea of a barrier being created solely due to the difference in work function and electron affinity is not correct, the interface between a metal and a semiconductor usually leads to the formation of a potential barrier.

There are various approaches for creating ohmic contacts between metal and silicon layers, and to reduce the contact resistance between the two. These include

- the selection of metals with appropriate work functions,
- alloying the contact metal with the silicon to form so called silicides,
- or creating a region of high doping concentration at the contact interface.

In modern semiconductor processes a combination of these approaches is usually employed. For the fabrication of the samples in this thesis the third option is chosen. The width of the barrier shown in figure 4.3a is dependent on the silicon doping concentration N at the metal-silicon interface. Increasing the doping concentration $N^{++} \gg N$ has the effect of reducing the width of the barrier. Below a certain width the conduction between metal and silicon is dominated by tunnelling of charges through the barrier, thus creating an ohmic contact. This is illustrated in figure 4.3b. Further increasing the contact doping concentration in general leads to a lower contact resistance. Thus, for the fabrication of the wafer-wafer bonded diode samples a contact doping of $N_C \approx 1 \times 10^{20}\,\mathrm{cm}^{-3}$ is targeted, both for the N and the P side [46].

IMPLEMENTATION The contact doping is created via ion beam implantation of boron (B) into the P wafers and phosphorus (P) into the N wafers respectively, and is carried out by Ion Beam Services S.A. as a service.[4] A SiO_2 layer (cap oxide) with a thickness of a few tens of nano meters protects the wafer surface during the implantation [46]. The cap oxide, together with an industry standard 7° off-axis implantation, also reduces the channelling of implanted ions in the semiconductor crystal [46]. For simplicity reasons, standard photoresist (PR) is chosen as the mask material for the implantation step. A 3 µm thick layer of positive photoresist is deposited on top of the cap oxide and structured via standard photolithography. The stopping range of the implanted ions is well below 1 µm and thus the chosen photoresist thickness ensures more than adequate protection of areas not to be doped [94]. In the designed process, the use of such a thick mask layer is possible as the minimal feature size is of the order of 20 µm.[5] The ion beam implantation leads to highly cross-linked photoresist which needs to be removed using plasma ashing [46]. The implantation leads to a narrow doping distribution with a maximum doping at a distance d_{max} below the wafer surface, which is dependent on the implantation energy. The ion beam implantation step is therefore followed by a thermal diffusion step which broadens the doping distribution and ensure a maximum doping concentration at the wafer surface. This steps also ensures proper activation of the doping by reconstructing the silicon crystal damaged during implantation and by embedding the dopant atoms into the crystal lattice [46].

The Synopsys Sentaurus TCAD (Sentaurus) Process simulation program is used to optimize the doping process parameters, such as the implantation energy, and temperature and duration of the thermal activation. The simu-

---

[4] Company website: `https://www.ion-beam-services.com/`

[5] The thickness of the mask layer directly influences the minimum feature size achievable in a given process. More advanced processes might use SiO_2 or poly-Si as mask layers [46]. These materials have a much higher stopping power for ions and thus thinner mask layers can be used during implantation.

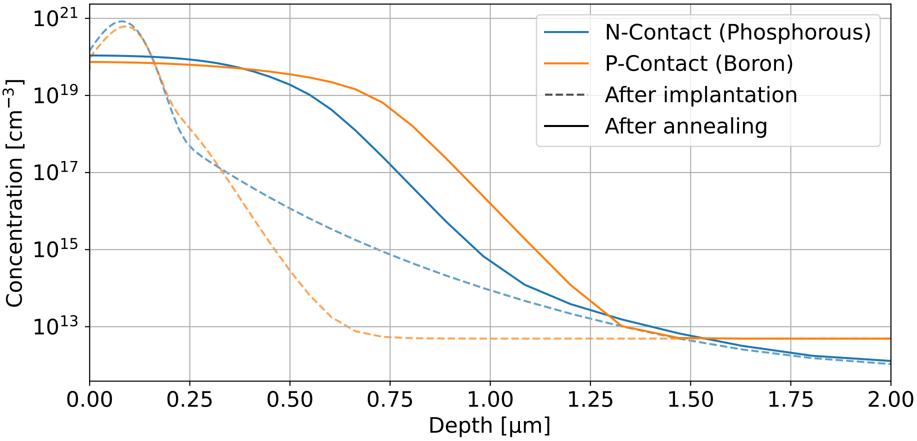

FIGURE 4.4: Contact doping profiles as simulated with Sentaurus using the parameters presented in table 4.1. For these simulations bulk doping concentrations of $N_A = 4.9 \times 10^{12}\,\mathrm{cm}^{-3}$ and $N_D = 7.3 \times 10^{11}\,\mathrm{cm}^{-3}$ are assumed.

lation includes the cap oxide deposition, the ion beam implantation and the diffusion / activation step. The resulting contact doping distributions for both N- and P-wafers is shown in figure 4.4. Table 4.1 summarizes the properties of the contact doping step as designed for this process. The detailed process steps are listed in the appendix A.3.

DISCUSSION OF THE CONTACT DEPTH The contact doping depth is to some extent chosen arbitrarily. But the finally chosen depth of $\approx 1\,\mu\mathrm{m}$,

Parameter		**N-Type Contact**	**P-Type Contact**
Dopant element		Phosphorous	Boron
Implantation energy	keV	80	30
Implantation dose	cm^{-2}	8×10^{15}	6×10^{15}
Activation temperature	°C	1000	1000
Activation time	min	50	70

TABLE 4.1: Ion beam implantation and doping activation parameters of the developed process. The values have been optimized via TCAD simulations.

with a doping concentration higher than $1 \times 10^{19}\,\mathrm{cm}^{-3}$ at a depth of $0.5\,\mu\mathrm{m}$, enables the contact to still function even in the case of minor surface damage.[6] When operating the samples as sensors, this highly doped layer can not fully be depleted and thus leads to a thin region at the sample surface without an electric drift field. This does not pose any problems for the investigation at hand, but needs to be considered in certain highly specialized applications, such as the detection of very low energy X-rays which interact very close to the sensor surface [95].

4.1.3 *Surface activated wafer bonding*

The bonding is carried out using SAB according to the principle explained in section 3.1.3. As previously noted, one of the main requirements for successful bonding with SAB is that the surfaces to be bonded have a roughness of less than 0.5 nm [54]. The wafers used for fabricating the bonded samples are double sided polished prime wafers [96]. But the backsides of the wafers (i.e. the surfaces to be bonded) come into contact with various cleanroom surfaces (such as hotplates, vacuum carriers etc.) during the different photolithography, etching and ion beam implantation steps. Thus, the roughness of the surfaces to be bonded can not be guaranteed any more after all these steps. Therefore the wafer backsides are polished again right before bonding using CMP. Any contact of the wafer backsides with cleanroom surfaces might also lead to the introduction of contamination. To remove these potential contaminants, a few tens of µm of Si is removed from the wafer backsides via a grinding process.

IMPLEMENTATION The grinding and polishing is carried out by Optim Wafer Services as a service.[7] Approximately 25 µm of Si is removed via grinding before the polishing. The polishing via CMP is carried out with the requirement of achieving a surface roughness compatible with SAB. G-Ray previously has made use of the polishing service of Optim and thus it is known that their CMP process is compatible with wafer bonding. The bonding is carried out by EV Group (EVG)[8] as a service, using an EVG *ComBond* machine. As the *ComBond* machine nominally handles 200 mm wafers,

---

[6] For example, any oxidation of the surface and subsequent removal of that oxide via HF would remove a certain amount of the highly doped silicon at the wafer surface.

[7] Company website: `https://www.optimwaferservices.com/`

[8] Company website: `https://www.evgroup.com/services`

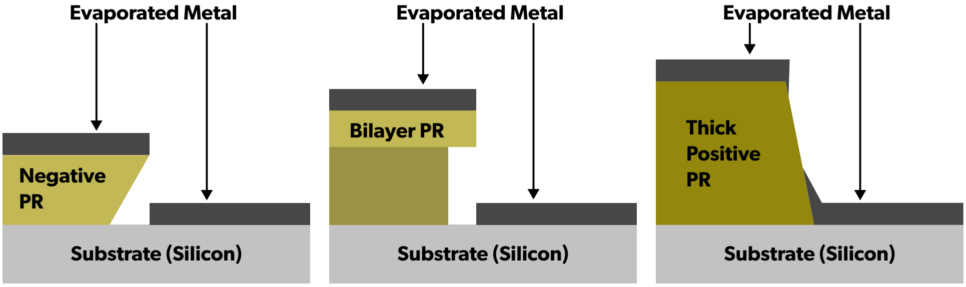

(a) Negative PR (b) Bilayer PR (c) Thick positive PR

FIGURE 4.5: Simplified illustration of the different approaches for metal patterning via lift-off, making use of different types of photoresist (PR).

the 100 mm wafers were mounted to carrier wafers using small patches of vacuum-suitable carbon tape. The detailed process steps are listed in the appendix A.4.

4.1.4 *Contact metallization*

Two commonly used processes for creating patterned metal layers on wafers are etching and lift-off. In the first case a uniform metal layer is deposited on the wafer, followed by a photolithography step. Using the patterned photoresist as a mask layer the metal is selectively (wet) etched, leaving behind the metal regions which are protected by the photoresist. The etchant solution is usually adapted to one specific type of metal, and thus etching multi metal layer stacks in a single process step is generally not feasible. For this reason lift-off is used for creating the metal contacts on the bonded diode samples. In a lift-off process a photolithography step first creates a patterned photoresist layer. This is followed by the deposition of metal across the wafer. The desired contacts are formed by the metal which is deposited in regions with no photoresist present. The metal deposited on top of the photoresist is subsequently removed by dissolving the photoresist and thus lifting the excess metal off. The photoresist underneath the metal can only be dissolved starting from the side walls and thus certain precautions need to be taken for a successful lift-off. First, the thickness of the photoresist layer needs to be larger than the thickness of the final metal layer [46]. Second, the side walls of the photoresist can not be covered by metal. To fulfil the second requirement metal is preferably deposited using evaporation which has a better directionality compared to deposition by sputtering. To further prevent metal from coating the photoresist side walls, a negative photoresist, leading to side walls with negative slopes (figure 4.5a), or a bilayer photoresist process, leading to an undercut (figure 4.5b), can be used [46]. As an alternative the use of a very thick layer of positive photoresist is also possible, but generally leads to less optimal results as partial deposition of metal on the sloped side walls occurs (figure 4.5c).

IMPLEMENTATION The metal contacts of the two bonded wafers are created sequentially, starting with the N-side contacts. A bilayer lift-off process is used for the N-Side, using positive *AZ1505* photoresist for patterning and *Lor5b* resist for creating an undercut. Metal is then deposited using evaporation, creating a stack of 5 nm chromium (Cr), 100 nm aluminium (Al) and 20 nm gold (Au). The chromium is used for better adhesion of the metal to the silicon substrate and the gold layer provides protection from surface oxidation. Immediately prior to metal evaporation, the native oxide on the silicon wafer is removed by in-situ sputter etching in the evaporation machine. The lift-off is carried out in dimethyl sulfoxide (DMSO).

During the fabrication of the P-side contacts, the finished N-side metal contacts are protected using a layer of standard positive photoresist. This protective layer is not compatible with a baking step at 180 °C necessary for the bilayer lift-off process with *Lor5b*. Therefore, the P-contact lift-off is carried out using a thick 3 µm layer of standard positive photoresist.[9] This is acceptable, as the P-side metal contacts do not have small structures given that no guard rings are present on this side. Metal deposition via evaporation is the same as for the N-side contacts and lift-off is again carried out in DMSO. The lift-off step also directly removes the protective layer covering the existing N-side contacts. The detailed processing steps are listed in appendix A.5 and A.6.

---

[9] Lift-off using a negative *AZ 2020nLof* photoresist was attempted with very unreliable results. Large metal regions often failed to be lifted-off completely. The exact cause for this is unknown and was not further investigated.

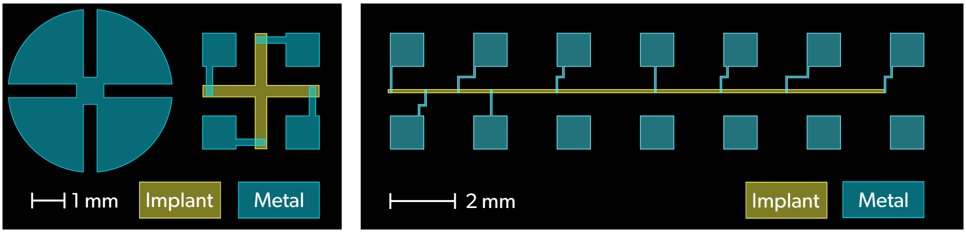

(a) Van der Pauw structures (b) Transmission line model (TLM) structure

Figure 4.6: Different electrical test structures implemented on the wafers and used for process control. Description in the text.

4.1.5 *Dicing*

Dicing of wafers is most commonly carried out via blade dicing, using a dicing saw equipped with a thin diamond blade. Blade dicing is limited to making straight cuts across the wafer, and thus regular rectangular dicing grids are best adapted for blade dicing. As pad diodes with different sizes are fabricated on the same wafer, separating the individual diodes by blade dicing would be very laborious. Therefore it was decided to dice the bonded wafers using laser dicing. In laser dicing either the laser head or the wafer to be cut is mounted to an X-Y stage, and thus the wafer can be cut into arbitrary shapes.

IMPLEMENTATION The laser dicing is carried out by Synova S.A. as a service using their *Laser MicroJet* system.[10] The wafers are cut in multiple passes and with a dicing width of ca. 60 µm.[11] To protect the bonded wafers during dicing, a protective photoresist layer is applied to both sides, and subsequently removed after dicing. The detailed processing steps are liste in appendix A.7.

4.1.6 *Process test structures*

Different types of test structures are implemented on the wafers, allowing to monitor various quantities during the fabrication process.

---

[10] Company website: `https://www.synova.ch/`

[11] The multiple laser passes leave behind characteristic parallel lines which are visible in figure 6.13a.

RESOLUTION TEST STRUCTURES Resolution test structures are used to visually asses the quality of the different photolithography steps. To do so, each mask has multiple of the following structures implemented: horizontal and vertical line patterns, checkerboard patterns, and radial line patterns, as illustrated in figure 4.2b. After exposure and development of a given photolithography step, the minimum achievable feature size can be assessed by inspecting these patterns under a microscope.

VAN DER PAUW TEST STRUCTURES Van der Pauw test structures are implemented for measuring both the metal and contact implant sheet resistance. The test structures are shown in figure 4.6a. By forcing a current I between two adjacent contacts and measuring the voltage V between the two other contacts the sheet resistivity can be calculated as $\rho_S = \frac{\pi}{\ln 2}\frac{V}{I}$ [97].

TRANSMISSION LINE MODEL TEST STRUCTURES The metal-silicon contact resistivity is measured using a linear TLM test structure. The resistance between contacts spaced at various distances is measured. Assuming that the current between two contacts flows in a channel of width W, the measured resistances can be modelled as

$$R(d) = \rho_S \frac{d}{W} + 2R_C \tag{4.2}$$

with ρ_S the sheet resistivity, d the distance between contacts and R_C the contact resistance. Thus, from a linear fit of the measured data $R(d)$, ρ_S as well as R_C can be extracted. The contact resistivity can then be estimated by $\rho_C = \frac{R_C^2 W^2}{\rho_S}$ [97, 98]. Figure 4.6b shows the implemented TLM test structure. The conductive channel is defined via the high dose contact implantation.[12]

4.1.7 *Photolithography Masks*

The developed process involves three different photolithography steps: the alignment mark etching, the contact implantation and the lift-off of the metal contacts. The same alignment marks are etched into N-type and P-type wafers, allowing for the use of a single mask for this photolithography step. The shape of the contact implant and the contact metallization is

---

[12] The conductive channel is not further separated from the silicon substrate. But given the high resistivity of the underlying bulk, the current can be assumed to primarily flow inside the implanted channel.

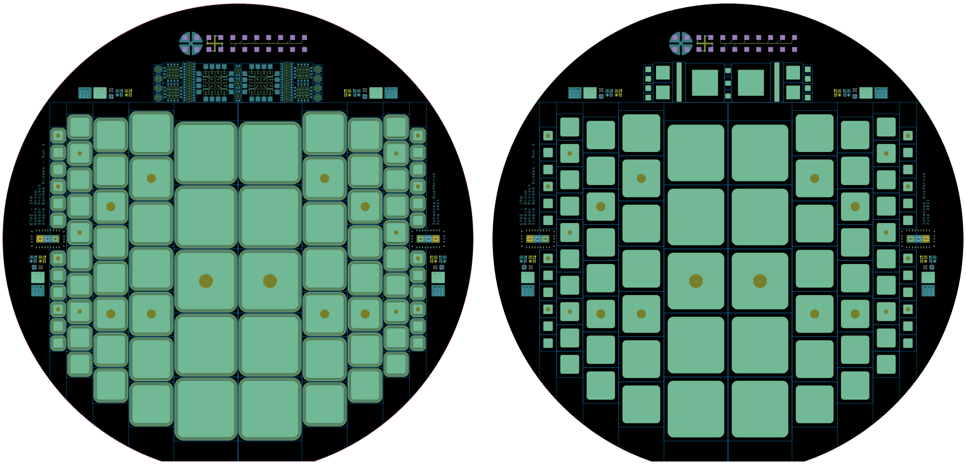

(a) N-type wafers

(b) P-type wafers

Figure 4.7: Full mask set used in the fabrication of the bonded diode samples.

	B	**C**	**D**	**E**	**F**
Contact Size [mm^2]	12 × 12	8 × 8	6 × 6	4 × 4	2 × 2
Total Size [mm^2]	13.6 × 13.6	9.6 × 9.6	7.6 × 7.6	5.6 × 5.6	3.6 × 3.6
Count	10	14	16	20	24

Table 4.2: Overview of the different diode sizes implemented on a single wafer. The total size is larger than the contact size due to the presence of the guard rings on the N-side.

different for the N- and P-type wafers, which allows to form guard rings on the N-type wafers. Therefore distinct N- and P-type wafer masks are created for the two remaining photolithography steps. Accordingly a total of five different masks are necessary. Figure 4.7 shows the mask set for both the N- and P-type wafers. The bulk of the implemented structures are pad diodes of different sizes. A subset of these diodes have a circular opening in the N- and P-side metallization, allowing for top and bottom transient current technique (TCT) measurements. Diodes with different contact sizes are implemented on a single bonded wafer pair, as summarized in table 4.2. A detailed view of an **E** diode (with a circular TCT opening) is shown in figures 4.8a and 4.8b.

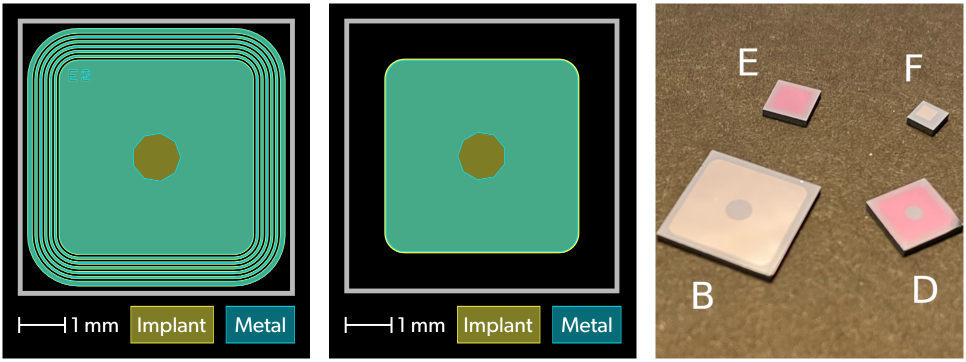

(a) N-side mask (b) P-side mask (c) Fabricated diodes

FIGURE 4.8: Detail view of the bonded diode structures. On the N-side each diode is marked with a (per wafer) unique identifier integrated into the metal layer. The masks shown in 4.8a and 4.8b are for a diode of type **E**.

MASK DESIGN The masks are designed in a parametric fashion using the Python programming language and making use of the Gdspy library.[13] Individual objects on the mask (e.g. a pad diode or a test structure) are implemented as individual classes, allowing for easy reuse and adaption of these objects without the need to manually recreate them. This was highly beneficial when switching from the initial 200 mm wafer design for the failed *Run 1* to a design using 100 mm wafers in the successful *Run 2*.[14] The masks are fabricated by the author in the BRNC cleanroom, using a Heidelberg Technology *DWL 2000* laser writer. The mask fabrication process steps are listed in the appendix A.1.

4.2 PRODUCTION RUN

The results presented in this thesis are based on three bonded wafer pairs. All three bonded pairs have gone through the same processing steps and are structurally equivalent. Table 4.3 lists the specifications of the wafers used. To accurately recreate the behaviour of bonded P/N diodes as used in particle pixel detectors, high resistivity float zone wafers are used as substrates.

---

[13] Online available at: `https://github.com/heitzmann/gdspy`

[14] The source code used for generating these mask sets is available online on Github at `https://github.com/deragent/ETHZ-BondedDiodes-Masks`.

Label	Type	Size	Thickness	Resistivity	Doping
W300 - 309	P (Boron) ⟨1 0 0⟩	100 mm	$500 \pm 7\,\mu m$	$> 10\,k\Omega\,cm$	$< 2 \times 10^{12}\,cm^{-3}$
W400 - 409	N (Phosphorous) ⟨1 0 0⟩	100 mm	$490 \pm 8\,\mu m$	7-10 kΩ cm	$(4\text{-}6) \times 10^{11}\,cm^{-3}$

TABLE 4.3: Specifications of the wafers used for this production run. All values are as specified by the wafers supplier, except for the thickness which represents the values measured after polishing via CMP, and the doping concentrations which are calculated based on the specified resistivities.[15]

SAMPLE LABELLING The three bonded wafer pairs are named **P301401**, **P302402** and **P303403**,[16] and are all fabricated by bonding a P-type to an N-type wafer. Each individual pad diode is given a unique label based on the name of the wafer pair, the label of the diode size and an index number (starting from 0). As an example, the diode labelled **P301401-E2** is the diode of size **E** with index 2 from the bonded wafer pair **P301401**. For the different diode sizes see table 4.2. Figure 4.8c shows an image of various diced diodes.

4.2.1 *Quality control*

SCANNING ACOUSTIC MICROSCOPY SAM measurements were carried out by EVG following the bonding of each wafer pair. The SAM scans were carried out using a *SAM 450* from PVA Tepla with a 110 MHz transducer and a step size of ca. 200 µm. SAM scans of two bonded wafer pairs are shown in figure 4.9. The scan of **P310401** shows an overall good bond quality, with one major particle-induced void and a few smaller unbonded regions towards the edge of the wafer. The SAM results from the other bonded wafer pairs show similar or better results, with a maximum of two major particle-induced voids per bonding.

BONDING MISALIGNMENT During the bonding the wafers were manually aligned based on the locations of the wafer flats, and thus a certain misalignment between the P- and N-side is expected. The misalignment

---

[15] Resistivity calculations are facilitated by `https://www.pvlighthouse.com.au/resistivity`.

[16] The number is a combination of label of the two bonded wafers. For example P301401 is created by bonding wafer W301 (P-type) to wafer W401 (N-type).

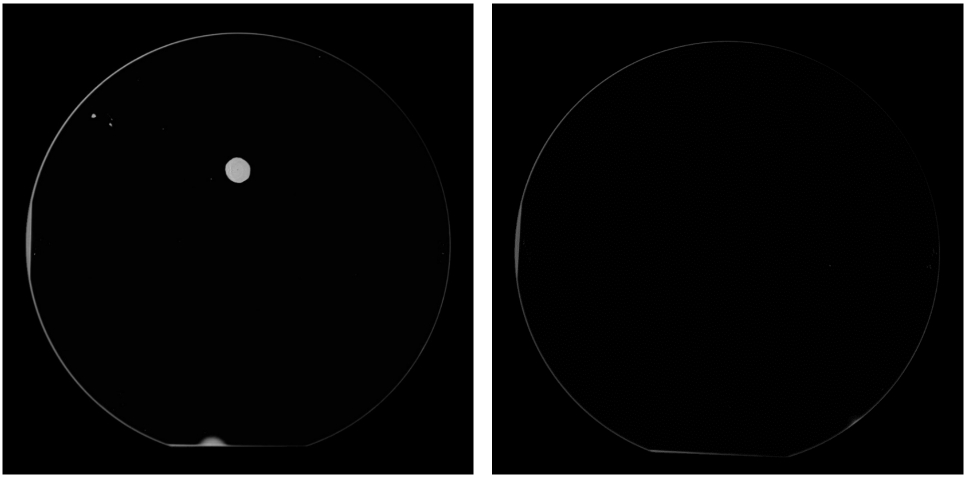

(a) P301401 (b) P303403

FIGURE 4.9: Example results from the SAM measurements carried out by EVG right after bonding. On the sample **P301401** voids due to the inclusion of particles are visible. Overall the scans show a very good bonding quality.

of pair **P301401** was measured after dicing, based on an image of the P-side.[17] As the laser dicing is aligned with the N-side metallization, the misalignment between N- and P-side can be estimated from the misalignment between the dicing lines and the P-side metallization. Figure 4.10a shows an extract from the recorded image with the dicing lines marked in green and the P-side metallization orientation shown in red. The misalignment between the green and red lines is clearly visible. In the centre of this sample a shift in $\Delta x = 0.73\,\text{mm}$ and $\Delta y = 0.30\,\text{mm}$ is measured as well as an angular misalignment of $\Delta\theta \approx 1.4°$. Given the angular misalignment, towards the edges of the 100 mm wafer the maximum shift in x and y is expected to be $\Delta y_{max} \approx \Delta x_{max} \approx 2\,\text{mm}$. Diode samples located towards the edges of the wafers thus have a noticeable shift of the P-side metallization, as shown in figure 4.10b. But due to the size of the fabricated diode samples, as well as their uniform structure, this shift should not have any major effects, especially not with respect to the behaviour of the bonding interface.

---

[17] The image was acquired using an office image scanner. The bonded pair was placed on the flat scanner surface (in a protective enclosure) which allowed to take a completely flat and uniform image.

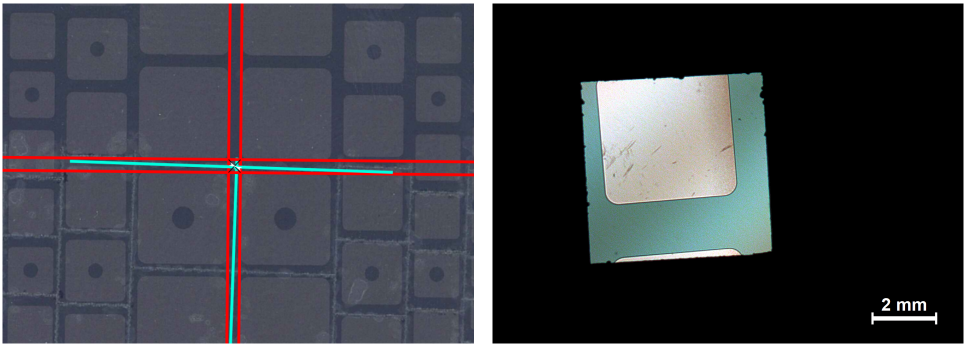

(a) Estimation of the bonding misalignment based on a image scan of the P-side of pair **P301401** after dicing.

(b) Image of a diced diode, showing the effect of the bonding misalignment which leads to a shift of the P-side metal contact.

FIGURE 4.10: Analysis of the misalignment of the P- and N-wafer after bonding.

The misalignment of the other samples was not precisely evaluated, but visually all samples show a similar misalignment.

OHMIC CONTACT RESISTANCE The contact resistivity of multiple samples was measured using the fabricated TLM test structures. For P-type wafers the measured contact resistivities are in the range $(0.05 - 0.44)\,\Omega\,\mathrm{cm}^2$ and for N-type wafers in the range $(3.1 - 4.2) \times 10^{-3}\,\Omega\,\mathrm{cm}^2$.[18] Accordingly the smallest fabricated diodes, with a contact size of $2\,\mathrm{mm} \times 2\,\mathrm{mm}$ have a contact resistance below $R_C^{(P)} = 11\,\Omega$ and $R_C^{(N)} = 0.11\,\Omega$ for P- and N-type contacts respectively. Compared to the high resistivity of the wafer substrates these resistances are negligible.

I/V CURVES Measured I/V curves confirm a rectifying diode like behaviour of the fabricated samples. Components from the TCT setup (see section 6.2) were reused for measuring the I/V curves, including the source measure unit (SMU) for biasing as well as the sample stage for temperature control at 24 °C.[19] The I/V curves were measured for six samples of each

---

[18] The P-type contacts show a much higher average resistivity and a much larger spread. This is most likely due to the accidental removal of the cap-oxide before the doping activation by thermal annealing, leading to surface damage on the P-wafers. See also appendix A.3.

[19] The samples were directly connected to the SMU without passing via the bias tee, to not limit the measurements via the internal $100\,\mathrm{k}\Omega$ resistor of the bias tee.

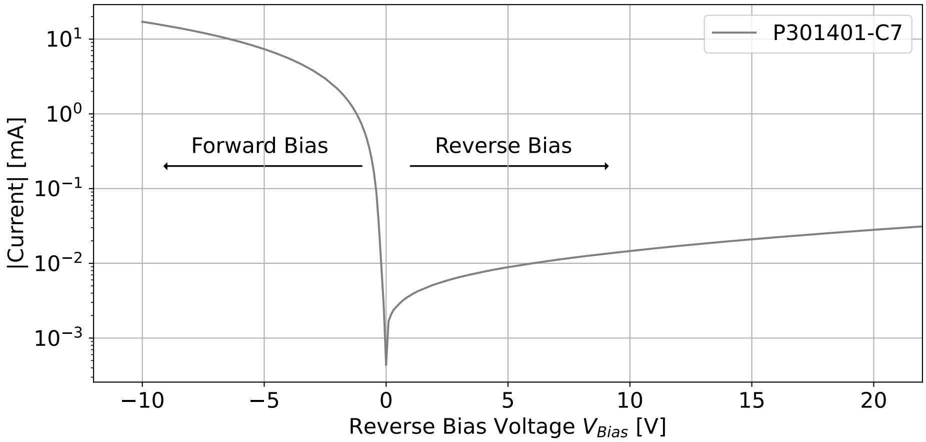

FIGURE 4.11: Example I/V curve of the sample **P301401-C7** showing a clear rectifying diode-like behaviour.

diode type of **P301401**.[20] Figure 4.11 shows an example I/V curve of a type **C** diode of **P301401** around $V_{Bias} = 0\,\text{V}$. A three order magnitude difference between the forward and reverse bias current can be seen. Figure 4.12 shows the averaged I/V behaviour of each diode type across a wider range of reverse bias voltages. In reverse bias, a strong dependency of the bias current on the applied reverse bias voltage can be observed, leading to substantial leakage currents at higher bias voltages. This has also been observed in existing literature [57, 71]. The main reason for fabricating diodes of different sizes is to investigate the source of the observed high reverse bias current. The current could be caused by effects related to the defects in the amorphous bonding layer, in which case it is expected to scale with the area of the diode $I \propto A$. An alternative source for high reverse bias currents is conduction via the edges of the diodes. Given that the P/N junction is formed by bonding, the high electric field which is present in the depletion region will also extend to the edges of the diode. In combination with the rough dicing edges which potentially present a high defect density, this could lead to high edge leakage currents. If the edge leakage current is dominant, the overall reverse bias current should scale with $I \propto \sqrt{A}$.

---

[20] The measurement of one type E sample is excluded from the analysis presented here, as it shows an excessively high bias current compared to all other samples.

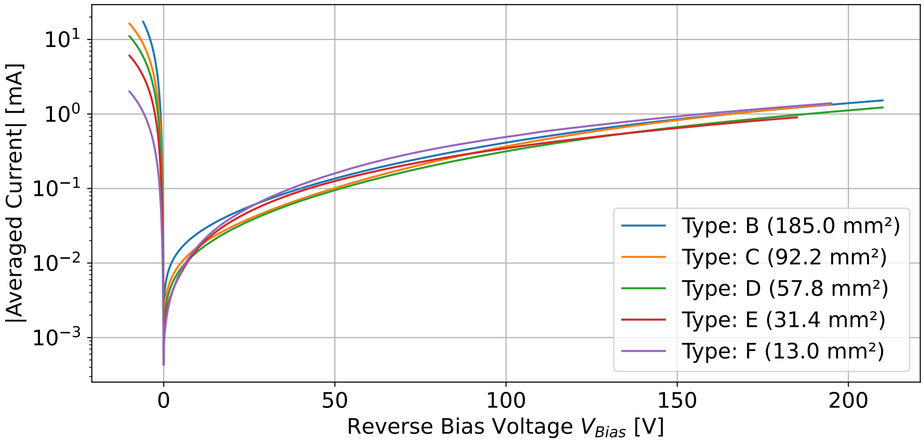

FIGURE 4.12: Average I/V curve for each diode type as measured with samples from **P301401**. In forward bias ($V_{Bias} < 0$) a clear dependency between the bias voltage and the diode size is visible. In reverse bias all diode types appear to have similar leakage currents independent of their size.

Figure 4.13 shows the diode current as a function of the diode area for various values of V_{Bias}. The data clearly indicates that the conduction in forward bias is proportional to A and thus forward conduction is happening via the bulk. On the other hand, in the presented reverse bias cases there is no clear relationship between the diode area and the current. Independent of the diode size, the observed reverse currents show a large spread and are of similar absolute value for all measured diodes. This is also visible in figure 4.12. Observing the reverse bias current in a log-log plot, as shown in figure 4.14a, gives a more differentiated view. The data shows two distinct regimes, one at very low reverse bias voltages ($V_{Bias} \ll 10\,\mathrm{V}$) and a second one with $V_{Bias} > 10\,\mathrm{V}$. At very low voltages there is a clear relationship between the diode area and the reverse bias current. This is highlighted in figure 4.14b, which shows that in this case the current is again proportional to the diode area $I \propto A$ indicating conduction via the bulk. At higher bias voltages this relationship disappears. The main cause for this seems to be that the point of transition between the two regimes is different for each measured sample.

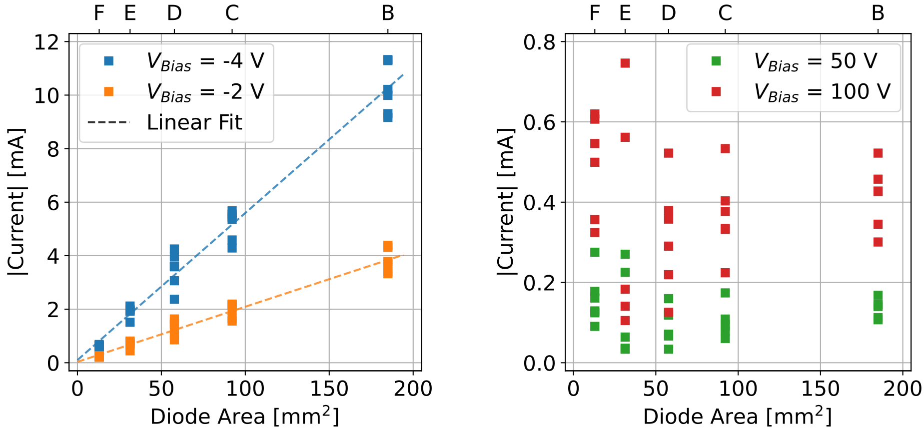

(a) Forward bias

(b) Reverse bias

FIGURE 4.13: Current as a function of the diode surface are at various bias voltages for all measured samples of **P301401**. Note the different y-scales of the two plots.

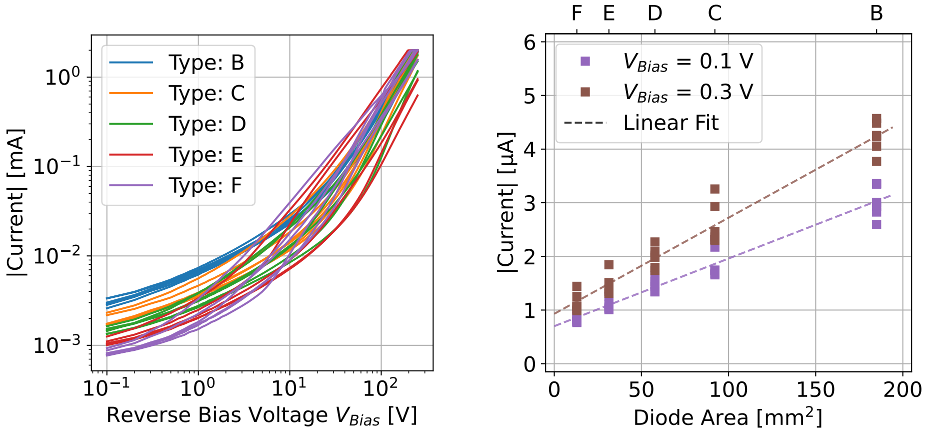

(a) Log-log plot of the reverse current of all samples.

(b) Current vs. diode area for very low reverse bias voltages.

FIGURE 4.14: Detailed view of the reverse bias current behaviour of all measured samples of **P301401**.

In the ideal Shockley diode model the reverse saturation current (below breakdown) is due to the diffusion of minority carriers into the depletion region, and it is not dependent on the applied bias voltage [17]. In silicon the contribution to the reverse bias current by generation can not be ignored. The generation current is proportional to the size of the depletion region and thus shows a dependency on the reverse bias voltage in the form of

$$I_{Gen} \propto \sqrt{V_{Bias}} \text{ for } V_{Bias} \gg V_{Bi} \tag{4.3}$$

with V_{Bi} the built-in potential of the P/N junction [17]. But the slopes of the curves above $V_{Bias} > 10\,\mathrm{V}$ shown in the log-log plot in figure 4.14a indicate a relationship in the form of

$$I \propto V_{Bias}^2. \tag{4.4}$$

This indicates that the observed bias current is not due to generation in the depletion region. The precise source of the current is not known and is not further investigated in this work. Accordingly, this work can also not explain why and at what reverse bias voltage the transition between the two regimes happens, which are visible in figure 4.14a. With the available data it is not possible to conclude if the reverse bias current at $V_{Bias} > 10\,\mathrm{V}$ is via the bulk, via the edges of the fabricated diodes or via a mixture of both.

5

METAL CONTAMINATION OF THE BONDING INTERFACE

> *The basic function of a tree is to provide an opportunity for climbing.*
>
> — Hilbert

This chapter documents the structural and chemical analysis of the bonding interface. In order to evaluate the quality of the bonding interface of the fabricated samples, scanning transmission electron microscope (STEM) measurements were carried out, with the main goal of estimating the thickness of the amorphous layer at the interface. At the same time energy-dispersive X-ray spectroscopy (EDXS) measurements were carried out to assess the chemical composition of the interface layer. These measurements show a significant presence of iron and other metals at the bonding interface. Such a contamination is unexpected, as surface activated bonding (SAB) should lead to a pure silicon to silicon bond. To investigate the presence of contaminants before the bonding, total reflection X-ray fluorescence spectroscopy (TXRF) measurements were carried out on unbonded wafers. No significant presence of metals is observed on the unbonded wafer surfaces. Separate investigations by the bonding provider (EVG) finally revealed that the metal contamination is due to the specific bonding machine used for the sample fabrication.

CONTRIBUTION The STEM and EDXS measurements and the corresponding sample preparation were carried out by members of the Scientific Center for Optical and Electron Microscopy (ScopeM) at ETHZ, mainly by Dr. Eszter Barthazy Meier, Dr. Peng Zeng and Dr. Fabian Gramm. The TXRF measurements were carried out at the Physikalisch-Technische Bundesanstalt (PTB) in Berlin, with help of the X-ray Spectrometry group headed by Dr. Burkhard Beckhoff and with Dr. Philipp Hönicke responsible for the data acquisition and initial analysis. The author was responsible for the design and coordination of the measurement campaigns, as well as the subsequent data analysis.

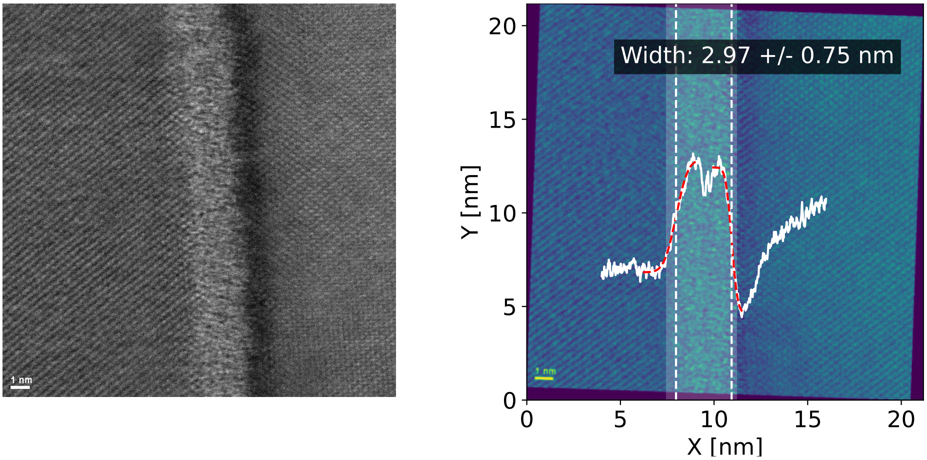

(a) STEM image of the bonding interface acquired at 5000 k magnification.

(b) Estimation of the amorphous layer thickness. Description of the process in the text.

FIGURE 5.1: STEM-based interface characterization of a sample from **P301401**. Images previously published in [99].

5.1 STEM AND EDXS MEASUREMENTS

High definition STEM measurements were carried out with a Hitachi *HD 2700* STEM on a sample taken from the bonded pair *P301401*. The lamella preparation was carried out by focused ion beam (FIB) milling using gallium ions. Figure 5.1a shows the bonding interface observed on this sample at a magnification of ×5000 k. The amorphous bonding interface is clearly visible in between the two crystalline regions of the wafer bulks. To estimate the thickness of the amorphous bonding interface the image was rotated to have the interface in a vertical orientation, followed by a projection onto the x-axis of the average image intensity. The white inset curve in figure 5.1b shows this average image intensity and the interface is visible as a region with higher average intensity. The two flanks of the intensity curve are fitted with a modified error function (ERF)

$$I_{L,R}(x) = A \cdot \mathrm{erf}\left(\frac{x - \mu_{L,R}}{\sqrt{2}\sigma_{L,R}}\right) + I_{\mathrm{offset}} \tag{5.1}$$

to extract the width of the amorphous interface as

$$d_{\mathrm{if}} = (\mu_R - \mu_L) \pm (\sigma_R + \sigma_L) = 2.97 \pm 0.75\,\mathrm{nm} \tag{5.2}$$

The interface width of ca. 3 nm is of similar magnitude as in existing publications [58, 68, 89].

During the same measurement campaign EDXS measurements were carried out on the same sample. These measurements highlight the presence of metal contaminants, namely iron (Fe), chromium (Cr), nickel (Ni) and titanium (Ti).[1] The localized quantifications of these elements (as shown in figure 5.2) show that the contamination is limited to the bonding interface. The contaminating signals can therefore not come from the EDXS machine but are a part of the measured sample. Two additional samples were evaluated (from wafer pairs *P302402* and *P306307*), which showed an equivalent metal signal. For all three samples the atomic concentrations of the observed elements were quantified in three different regions: left and right of the interface, and directly on the bonding interface. Figure 5.3a shows the relative concentration of the elements within the three regions for each of the samples. All samples exhibit an iron contamination of ca. 2 - 5 % at the interface, as well as smaller traces of the other metal elements.[2] Under the assumption that a relative concentration of 100 % corresponds to the atomic density of silicon of $4.96 \times 10^{22}\,\mathrm{cm}^{-3}$ [10], the absolute density of the metal contamination is calculated across the interface. The resulting distribution for the sample **P301401** is shown in figure 5.3b. Integrating this distribution in the range -5 - 5 nm allows to calculate an approximation of the interface surface density of the contaminating elements at the interface, shown in table 5.1.[3] The order of magnitude of the metal contamination surface density becomes important when comparing to the results obtained from TXRF measurements presented in the next section.

---

[1] The presence of these specific metals indicates that the original source of contamination is likely from stainless steel, which usually contains Fe, Cr and Ni, and sometimes also Ti.

[2] In addition to the metal elements there is also argon (Ar) present at the interface. This is not unexpected, as Ar ions are used for the sputter cleaning of the wafer surface during the surface activated wafer bonding [58].

[3] In [100] it was observed that the STEM sample preparation via FIB milling can widen the distribution of contaminating atoms. This is due to diffusion of the contaminating atoms when the sample heats up during the processing. In [101] a similar behaviour is observed due to annealing. Thus, the integration range was chosen larger than the width of the amorphous layer as estimated from the STEM measurement.

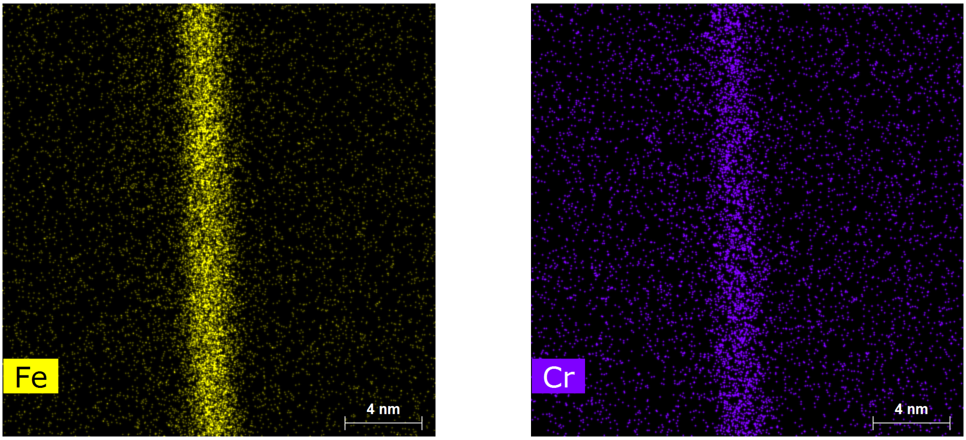

(a) Iron (Fe)

(b) Chromium (Cr)

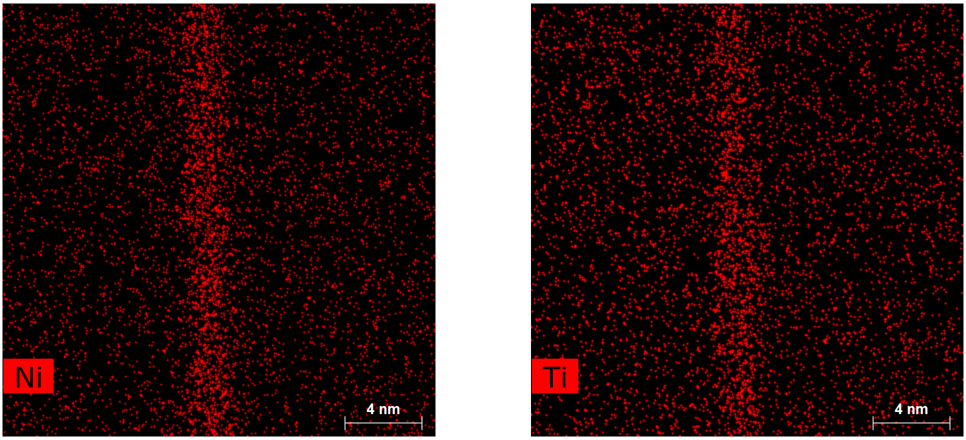

(c) Nickel (Ni)

(d) Titanium (Ti)

FIGURE 5.2: 2D map of the contaminating metal elements observed via EDXS on a sample of **P301401**. The contaminating elements are highly localized at the bonding interface. This strongly suggests that these elements are present in the sample and must have been introduced before or during bonding.

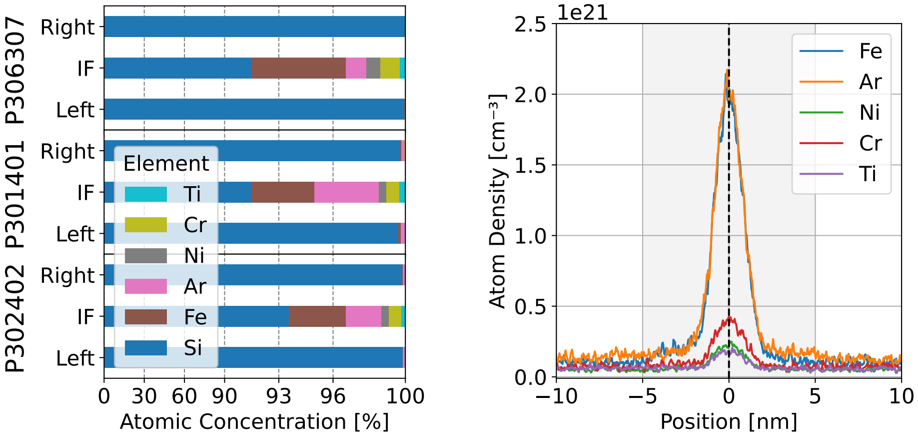

(a) Quantification of the elements left of, right of and directly on the bonding interface. *Note*: The x-axis has a non-linear scale.

(b) Cross section of the contaminating elements across the bonding interface. The interface is at $x = 0\,\mathrm{nm}$.

FIGURE 5.3: Quantification of the metal contamination observed at the interface via EDXS measurements.

Sample	**Ar [cm^{-2}]**	**Fe [cm^{-2}]**	**Ni [cm^{-2}]**	**Cr [cm^{-2}]**	**Ti [cm^{-2}]**
P306307	$4.3 \cdot 10^{14}$	$1.9 \cdot 10^{15}$	$3.0 \cdot 10^{14}$	$4.0 \cdot 10^{14}$	$1.3 \cdot 10^{14}$
P301401	$5.5 \cdot 10^{14}$	$5.2 \cdot 10^{14}$	$9.1 \cdot 10^{13}$	$1.5 \cdot 10^{14}$	$8.5 \cdot 10^{13}$
P302402	$5.1 \cdot 10^{14}$	$8.4 \cdot 10^{14}$	$2.0 \cdot 10^{14}$	$2.0 \cdot 10^{14}$	$7.6 \cdot 10^{13}$

TABLE 5.1: Surface density of the interface contamination observed on multiple samples.

5.2 TXRF MEASUREMENTS OF UNBONDED WAFERS

The results from the EDXS measurements presented in the previous section raise the question about the source of this metal contamination. There are three possible contamination sources: the initial wafer processing (alignment marks and contact doping related), the chemical mechanical polishing (CMP) before the bonding, or the wafer-wafer bonding itself. A contamination stemming from the initial wafer processing can not directly be excluded, but seems unlikely as 20 µm of silicon is removed from the bonding surface as part of the CMP step (see section 4.1.3).[4] In order to investigate whether the contamination is introduced before or during the wafer-wafer bonding, the surface contamination of unbonded wafers is measured. These wafers have gone through the same processing steps as the bonded wafers, up to and including the CMP. Accordingly, if the metal is introduced before or during the polishing, these wafers should also show the contamination. The detection of iron, showing the highest contamination level, is used as a sign for a metal contamination in general. To measure the chemical composition of the unbonded wafer surfaces, TXRF is employed. TXRF is similar to EDXS in the sense that the chemical composition of a material is investigated by measuring and characterizing the spectrum of X-rays emitted from the sample under investigation. The difference lies in how the atoms of the sample are being excited to emit characteristic X-ray lines. In the case of EDXS this is achieved by a beam of focused electrons, for example directly in a scanning electron microscope (SEM) or transmission electron microscope (TEM). Depending on the acceleration voltage used, these electrons penetrate into the sample up to a depth of multiple µm [102]. Accordingly, X-ray fluorescence occurs from any material up to this depth. Thus, EDXS is not adapted for measuring the chemical composition of a thin ($\approx$ nm) layer of atoms on top of a bulk material, as the recorded spectrum would be dominated by the signal from the bulk material. On the other hand, TXRF uses an X-ray beam which undergoes total reflection on the surface of the sample to excite the atoms. To have total reflection, the X-ray beam hits the sample at a very shallow angle and the sample needs to have a polished surface. The advantage is that the totally reflected X-ray beam only interacts with approximately the top 3 nm of the sample,

---

[4] It is precisely for this reason that the CMP step is designed to remove a large amount of material, to also remove any surface contamination due to preceding processing steps.

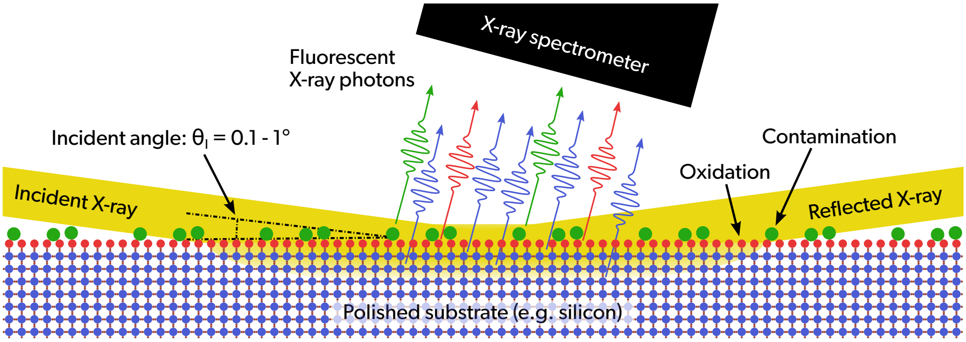

FIGURE 5.4: Schematic view of the principle behind TXRF measurements. A very shallow collimated X-ray beam undergoes total reflection on the sample surface. The interaction of the X-ray beam with the sample leads to the emission of fluorescent X-ray photons from the top few nm of the sample material. This makes TXRF very sensitive to trace surface contaminations. Figure not to scale.

which makes the method sensitive to surface layer contaminations [103]. Figure 5.4 illustrates the principle of TXRF.

The TXRF measurements were carried out at the Bessy II light source of the Helmholtz-Zentrum Berlin on a setup built and operated by the X-ray Spectrometry group of the PTB [103, 104]. The reference-free measurements with an excitation photon energy of 850 eV do not show any signs of iron contamination on the unbonded wafers. A total of four wafers were measured: **W308**, **W309**, **W408** and **W409**. An example TXRF spectrum is shown in figure 5.5a. The iron detection threshold for these measurements is $1 \times 10^{12}\,\text{cm}^{-2}$, which is worse (higher) than the theoretically achievable threshold. This is due to a fluorine (F) contamination overlapping with the Fe-L fluorescence lines. A possible source of the F contamination is Teflon (PTFE) coatings within the TXRF vacuum chamber, used for reducing friction in moving parts. The location of the fluorine K_{α_1} line and the (undetected) iron L lines are indicated in the mentioned figure. As the iron contamination observed via EDXS has a surface density two orders of magnitude higher ($\approx 1 \times 10^{14}\,\text{cm}^{-2}$) than the detection threshold of the TXRF measurements it can be concluded that the observed metal contamination is not present on the wafers prior to the bonding step.

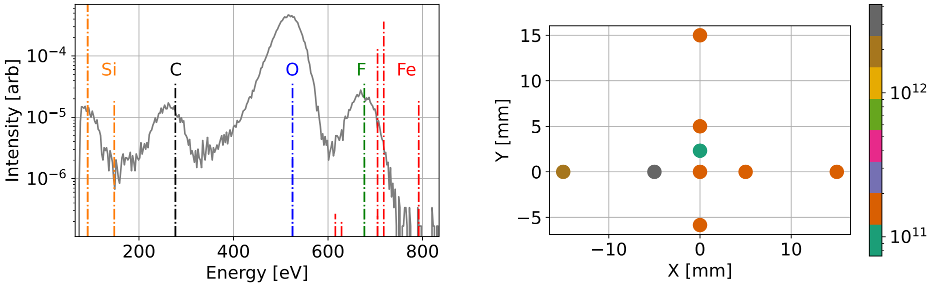

(a) Example TXRF spectrum. The only visible elements are Si, C, O and F. The F peak overlaps with potential Fe peaks, leading to an increase of the detection threshold of Fe. No Fe above a concentration of $1 \times 10^{12}\,\mathrm{cm}^{-2}$ is observed.

(b) Result from the TXRF measurement of **W309** on the *KMC* X-ray beam line. The colour scale gives the measured Fe concentration in cm^{-2} at different locations on the wafer. Location $(0, 0)$ corresponds to the centre of the wafer.

FIGURE 5.5: Results from the TXRF measurements of unbonded wafers.

TXRF measurements of one wafer (**W309**) was carried out on a second X-ray beam line (labelled *KMC*), allowing for excitation photon energies up to 10 keV [105]. The measurement was carried out with a photon energy of 7 keV which allows to excite and observe the K_α and K_β lines of iron. These lines are not sensitive to the fluorine contamination and thus allow for a more sensitive (lower) iron detection threshold. A metal surface contamination in the order of $(0.1 - 1) \times 10^{12}\,\mathrm{cm}^{-2}$ is detected. Figure 5.5b shows the measured spatial distribution of this contamination. The observation of iron on the surface does not invalidate the previous conclusion, as the measured contamination level is again much lower than the values observed in the EDXS measurements. The source of the low iron contamination observed with TXRF is not known and has not been further investigated.

5.3 DISCUSSION

Following these investigations, EVG confirmed that the observed contamination was introduced during the wafer-wafer bonding. The introduction of metal at the bonding interface during the low-temperature wafer bonding is not uncommon, as reported in [14, 57, 100, 101]. The metal contamination stems from the parasitic Ar sputtering of the vacuum vessel of the bonding machine. As these vessels are commonly made from stainless steel, contamination with metal elements as observed can occur. To prevent this kind of contamination certain bonding machines are equipped with silicon coated panels inside the Ar sputtering module [14]. This was also the case for the machine used by G-Ray, leading to contamination-free bonds in their prototypes [15]. The use of a bonding machine without such panels for the samples presented here is due to the oversight by the author and the (wrong) assumption that all modern bonding machines are equipped with such panels.

The consequence of this contamination is that the results and observations presented in this thesis have to be analysed taking into account the presence of these metal elements at the bonding interface. As will be shown in chapter 7, the fabricated samples show an asymmetric depletion behaviour where only the P-side of the structures can be depleted. This behaviour is likely influenced by the presence of the contaminating metal elements at the bonding interface. Section 7.3.1 will discuss how different levels of contamination might influence the behaviour of bonded sensor diodes.

6

TRANSIENT CURRENT TECHNIQUE (TCT)

> *Cars are interesting machines, but only when looked at from a distance.*
>
> — Emmy

This chapter introduces the operational principle of transient current technique (TCT). Different approaches for charge injection are presented and the prompt current analysis method is discussed. TCT is the main measurement technique used to analyse the behaviour of the fabricated bonded diode samples. To carry out these measurements, a TCT system was set up at ETHZ. An overview of the different components, as well as the structure of the implemented software, is given. The characterization of the electrical front-end, including the signal amplification system, is documented. To simplify the handling of samples, a special sandwich-type sample holder was designed, which is also documented here. This holder allows to instal samples in the TCT setup without the need for wire-bonding. Finally, the edge polishing of samples employed for edge TCT measurements is documented.

CONTRIBUTION The first section of this chapter gives an overview of the principles of TCT based on existing literature. The TCT setup at ETHZ, described in the second section, was assembled and commissioned by the author, including the complete implementation of the control and data handling system using Python. The sandwich-type sample holder, presented in the third section, was designed, tested and optimized by the author. The last section describes the edge polishing procedure used by the author for sample preparation.

6.1 PRINCIPLE OF TCT

The fundamental idea of transient current technique, as indicated by its name, is to record the transient current signals induced in a sensor, originating from the injection and subsequent propagation of charges (see section 2.3). Analysing the recorded signal curves allows to extract various

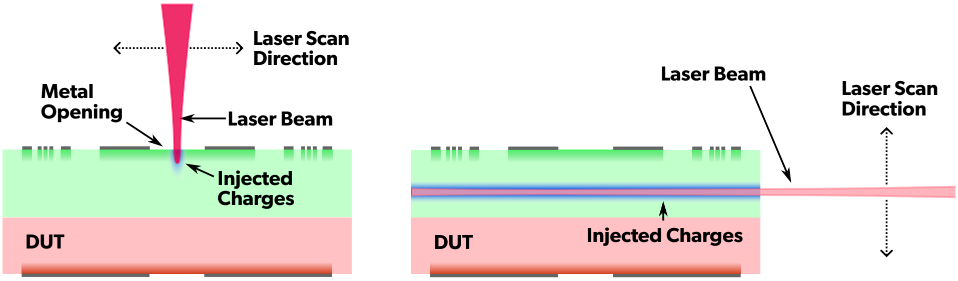

(a) Surface TCT using a red laser.

(b) Edge TCT using a IR laser.

FIGURE 6.1: Schematic view of surface and edge TCT charge injection via laser. The DUT is illustrated by a bonded pad diode. Image is not to scale.

types of inherent parameters of the device under test (DUT), such as the shape of the electric field inside the sensor, charge collection efficiency maps or even the behaviour of trap states [106–108]. Most TCT systems used for sensor characterization inject charges into the DUT via pulsed lasers. Laser injection, as well as alternative charge injection methods, is described in the following section 6.1.1. Modern systems often have the ability to move the DUT using motorized translation stages and are thus labelled as scanning TCT systems. Laser based TCT measurements are classified as either surface TCT (top / bottom) or edge TCT, depending from which side the sample is illuminated with laser light. In surface TCT, the sample is illuminated from either the top or bottom side contact. This allows for 2D scanning of samples, especially important in the case of strip or pixel sensors. In edge TCT the sample is illuminated through the side-walls exposed by the dicing of the DUT. This allows for scanning along the transverse axis of a sensor, for example to investigate the electric field in function of the depth. Both concepts are illustrated in figures 6.1a and 6.1b. For surface TCT, openings in the contact metallizations need to be foreseen to enable TCT measurements (see also section 4.1.7). In the case of edge TCT, the edge of the DUT needs to be prepared via polishing for best results (see section 6.4).

A TCT system usually consists of the following main components:

- charge injection (e.g. via lasers),
- electrical frontend (e.g. bias-tee and amplifier),

- data acquisition (e.g. oscilloscope and control computer),
- mechanical system (e.g. motorized translation stages),
- and thermal control (e.g. via Peltier elements).

The various components are further described in more detail in the context of the TCT system commissioned at ETHZ, presented in section 6.2.

6.1.1 *TCT charge injection*

LASER BASED TCT The most commonly used method for charge injection in modern TCT systems is via pulsed lasers. The wavelength of the laser is chosen to emulate the interaction behaviour of certain particles, or to study certain specific aspects of a sensor. For silicon (Si) based sensors, red lasers (for example $\lambda_{Red} = 660\,\mathrm{nm}$), emulating α like interactions, and near infrared (IR) lasers (for example $\lambda_{IR} = 1064\,\mathrm{nm}$), emulating MIP-like interactions, are two of the most commonly used laser wavelengths. For edge TCT measurements, IR lasers are generally employed as they allow to generate charges across the entire sensor at the given depth. Using a red laser in surface TCT mode allows to record drift signals dominated by either electrons or holes, depending on which side of the sensor the charges are injected [109]. The laser pulse should be as short as possible. A too long laser pulse can lead to a distortion of the rising edge of the TCT signal. Optimal performance in spatial resolution is achieved by finding the focus of the laser via knife edge scans [110]. One of the major advantages of laser based TCT is the ability to suppress noise by averaging multiple recorded waveforms, enabled by a stable trigger signal delivered by the laser driver. This allows to investigate signals which are hidden by the noise floor of the acquisition system. In addition, the location of the laser charge injection is clearly defined in space and can be known with a high accuracy. Laser based TCT measurements are used for the results presented in chapter 7 and for some measurements in chapter 9.

TWO PHOTON ABSORPTION TCT Two photon absorption (TPA) TCT is a special case of laser based TCT. It uses a laser wavelength at which the material of the DUT has a negligible single photon absorption. Using a highly focused laser with a short pulse width, it is possible for electron-hole pairs to be created inside the material via two photon absorption [111]. As

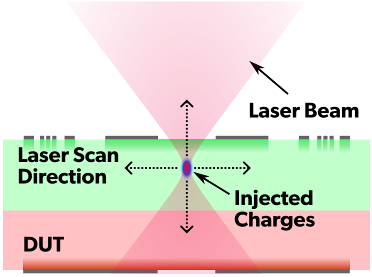

FIGURE 6.2: Illustration of the principle of TPA TCT. Electron-hole pairs are only created at the focus point via two photon absorption, allowing to fully 3D scan a detector.

the probability of photon absorption is proportional to the square of the laser intensity $P(\mathrm{TPA}) \propto I^2_{Laser}$, the creation of charges via TPA is limited to a small area around the point of focus [112]. Thus, TPA TCT creates charges within a small and clearly defined volume inside the DUT, and therefore, by moving the point of focus, TPA TCT allows to scan the entire 3D volume of a sensor. This principle is illustrated in figure 6.2. TPA TCT is a very novel technique, enabled in part by the continuing improvement of high power ultra short pulsed laser [113]. The use of TPA for sensor characterization via TCT was developed in the context of the CERN RD50 collaboration and first presented by I. Vila et al. in 2014 [114]. A TPA TCT system built and commissioned by the Solid State Detectors group at CERN [115] was used as part of this thesis, as presented in section 7.2.1.

RADIATION SOURCE BASED TCT The interaction of particles from a radiation source or particle beam can also be used for charge injection in a DUT. Using a radioactive source, a separate trigger is not always available (such as with α or γ particles) and thus the waveform acquisition needs to be triggered on the TCT signal itself. Therefore sufficiently low noise levels are required and no trivial waveform averaging is possible. Radiation sources further present the trade-off between high rate (without using any collimation) and a well known interaction location (with a very strict collimation). Using a particle beam for TCT measurements can allow for the use of an external trigger while also giving precise information about the location of the interaction. But beam tests are in general very time and labour intensive and thus not practical for day-to-day TCT measurements. The advantage of using radiation sources or particle beams for TCT is that the energy deposit of a single event can be very well estimated. Laser based TCT measurements rely on a separate calibration in order to reconstruct the equivalent energy deposit for a given laser energy. Such a calibration is commonly carried out using an α source or MIP-like interacting particles. An α source is used for most of the measurements presented in chapter 9.

ELECTRICAL INJECTION J. Bronuzzi presented a novel approach of injecting charges via electrical pulses in his PhD Thesis [52]. In this approach, special electrodes used for charge injection are integrated into a device during fabrication. The motivation behind this approach is that it would allow to generate TCT pulses even during normal operation of a device, for example once a pixel sensor is fully integrated into a larger detector structure. This approach is not used in this thesis and not further discussed here.

6.1.2 *Prompt current method*

According to the Shockley-Ramo theorem, the induced current from a moving charge is given by (2.9)

$$I_R(t) = q\vec{v}(\vec{x}(t)) \cdot \vec{W}_F(\vec{x}(t)).$$

with $\vec{v}$ the velocity of the charge and $\vec{W}_F$ the weighting field of the sensor. In an edge TCT measurement $N_{e,h}$ electrons-hole pairs are generated by the laser injection at $t = 0\,\mathrm{s}$ at a position $\vec{x}_0$. According to the Shockley-Ramo theorem and given the mobility of electrons and holes in the sensor material, the induced current instantaneously after the charges are created is given by

$$\begin{aligned} I_R(t=0,\vec{x}_0) &= eN_{e,h}\vec{W}_F(x_0)\left[\vec{v}_e(\vec{x}_0)+\vec{v}_h(\vec{x}_0)\right] \\ &= eN_{e,h}\vec{W}_F(\vec{x}_0)\left[\mu_e(\vec{E}(\vec{x}_0))+\mu_h(\vec{E}(\vec{x}_0))\right]\vec{E}(\vec{x}_0) \end{aligned} \tag{6.1}$$

This quantity is called the prompt current. In the case of a pad diode, treated as a 1D problem, this simplifies to

$$\begin{aligned} I_R(t=0,x_0) &= eN_{e,h}\frac{1}{d}\left[v_e(x_0)+v_h(x_0)\right] \\ &= eN_{e,h}\frac{1}{d}\left[\mu_e(E(x_0))+\mu_h(E(x_0))\right]E(x_0) \end{aligned} \tag{6.2}$$

with $W_F = \frac{1}{d}$ and d the thickness of the pad diode [35]. Thus, by recording the prompt current in function of the position using an edge-TCT scan, one can recreate the velocity profile across the pad diode. In the general case, the mobility values are not constant due to velocity saturation. Accordingly, the recovered velocity profile is not a proportional representation of the electric field, but the profile can still give a general idea of the overall field shape. Adding the constraint that the bias voltage is determined via the electric field as

$$V_{Bias} = \int_0^d E(x)dx \tag{6.3}$$

the precise electric field can be recovered by solving the resulting differential equation. This is the prompt current method as proposed in [106].

In reality, sampling the recorded TCT current exactly at $t = 0$ is not viable, as the inherent low pass filtering nature of the electronics front-end leads to a non-zero rise time of the recorded current. Under the assumption that the drift velocity of the charges does not substantially change during the front-end limited rise time of the TCT pulse, and given that the electronics response is linear, the recorded signal I_{TCT} at t_{pc} close to 0 is proportional to the induced signal I_R at $t = 0$

$$I_P(x_0) = I_{TCT}(t_{pc}, x_0) = A_{t_{pc}} I_R(0, x_0). \tag{6.4}$$

$A_{t_{pc}}$ is a constant factor which represents the electronics front-end response for a given t_{pc}.[1] The exact value to chose for t_{pc} is a trade-off between accuracy and signal to noise ratio. If t_{pc} is chosen too small, the recorded TCT signal is still very small and thus the influence of the system noise becomes dominant. If t_{pc} is chosen too large, the signal is already influenced by the drift of the charges and therefore does not any more represent the initial prompt current. These cases are illustrated in figure 6.3. Previous research has used $t_{pc} = 300 - 600\,\text{ps}$ [106, 116]. The precise zero time $t = 0$ is usually not known and needs to be extracted from the data. One approach is to linearly fit the rising edge of the TCT pulse and to define the zero intercept of this fit as $t = 0$, as illustrated in 6.3.

---

[1] The recorded TCT signal is usually amplified and the factor $A_{t_{pc}}$ also encapsulates the corresponding gain G.

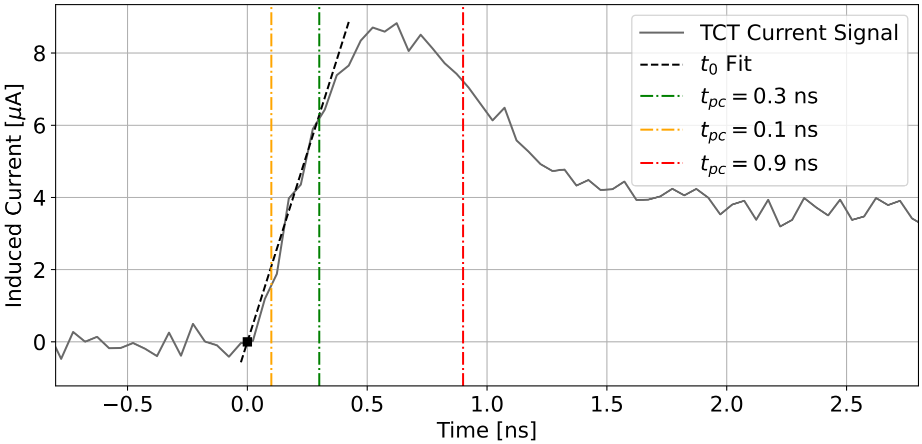

FIGURE 6.3: Simulated TCT signal illustrating the timing for a prompt current analysis. The t_0 time is given by a linear fit of the rising edge intercepting the x-axis. Different t_{pc} are highlighted, with $t_{pc} = 0.1\,\text{ns}$ leading to bad signal-to-noise ratio and $t_{pc} = 0.9\,\text{ns}$ leading to distortion due to changes in the drift velocity.

Based on the Shockley-Ramo theorem, and under the assumption that no charges are lost due to recombination or trapping, one can show that

$$Q(x_0) = \int_0^\infty I_R(t, x_0)dt = eN_{e,h}(x_0) \tag{6.5}$$

$$GQ(x_0) = \int_0^\infty I_{TCT}(t, x_0)dt = GeN_{e,h}(x_0) \tag{6.6}$$

with G the front-end gain of the signal acquisition chain. This allows to define the weighted prompt current as presented in [116]

$$\begin{aligned} I_W(x_0) &= \frac{I_P(x_0)}{\int_0^\infty I_{TCT}(t, x_0)dt} = \frac{A_{t_{pc}} I_R(0, x_0)}{GeN_{e,h}(x_0)} \\ &= \frac{A_{t_{pc}}}{Gd} \left[\mu_e(E(x_0)) + \mu_h(E(x_0))\right] E(x_0) \end{aligned} \tag{6.7}$$

The weighted prompt current does not depend on the deposited charge, which is of interest in situations where the number of electron-hole pairs $N_{e,h}$ is not constant across all measurements. This is for example the case towards the edges of a device when a part of the laser beam is no longer illuminating the sample.

EXTENDED SHOCKLEY-RAMO THEOREM As presented, the derivation of the prompt current method is based on the principle of current induction via the Shockley-Ramo theorem. In sections 2.3.1 and 2.4 the limitations of the Shockley-Ramo theorem are discussed in more detail and an extended Shockley-Ramo theorem is presented for the case of partially depleted detectors. As shown in (8.38), in the case of a 1D detector (pad diode) with conductive (non-depleted) layers the current induced according to the extended Shockley-Ramo theorem is given by

$$I_E(t) = -\int_{-\infty}^{\infty} \hat{W}_V(t-t') \left(\frac{eN_{e,h}}{d} \left(v_e(x(t')) + v_h(x(t')) \right) \right) dt' \tag{6.8}$$

with $\hat{W}_V(t)$ a time-dependent reduced weighting vector and $\hat{W}_V(t<0) = 0$. Assuming that t_{pc} is chosen in such a way that the velocity of the charges does not substantially change for $t \in [0, t_{pc}]$, (6.8) can be approximated as

$$\begin{aligned} I_E(t_{pc}, x_0) &= -\int_{-\infty}^{\infty} \hat{W}_V(t_{pc}-t') \left(\frac{eN_{e,h}}{d} \left(v_e(x_0) + v_h(x_0) \right) \right) dt' \\ &= -\int_{-\infty}^{\infty} \hat{W}_V(t_{pc}-t') dt' \left(\frac{eN_{e,h}}{d} \left(v_e(x_0) + v_h(x_0) \right) \right) \\ &= A^E_{t_{pc}} I_R(0, x_0) \end{aligned} \tag{6.9}$$

This shows that the prompt current method can still be applied in the case of pad diodes with non-depleted layers.[2] It needs to be noted that the new proportionality factor $A^E_{t_{pc}}$ is now in general dependent on the bias voltage, as the reduced weighting vector $\hat{W}_V(t)$ is dependent on V_{Bias}.[3] This is not the case for the original prompt current method, where $A_{t_{pc}}$ only depends on properties of the front-end electronics. Therefore, in the case of partially depleted detectors, one needs to be careful when comparing prompt current curves recorded at different bias voltages! Finally, the principle of the weighted prompt current is also still valid, as under the extended Shockley-Ramo theorem (6.5) still holds as

$$Q(x_0) = \int_0^{\infty} I_E(t, x_0) dt = eN_{e,h}(x_0) \ \ [18]. \tag{6.10}$$

---

[2] The argument presented here is equivalent to the reasoning when choosing t_{pc} to account for the rise time of the electronics front-end. In both cases, the electronics response and the extended Shockley-Ramo theorem, the effect can be applied via a convolution with the corresponding system response.

[3] Changing the bias voltage can lead to a change in the thickness of the undepleted layers, thus modifying $\hat{W}_V(t)$ as shown section 8.3.2.

6.2 ETHZ TCT MEASUREMENT SETUP

6.2.1 *Hardware Setup*

As part of this thesis a new TCT setup was commissioned at ETHZ, based on the *Large Scanning TCT* system acquired from Particulars d.o.o.[4] The main components delivered by Particulars are

- the laser system, including a red (660 nm) and IR (1064 nm) laser, and the lens system,
- the electrical front-end, including a bias-tee, a 53 dB amplifier and a high voltage supply filter,
- the mechanical system, including an X-Y sample stage with integrated Peltier elements, and Z focusing stage,
- and an aluminium enclosure.

The following additional components, not supplied by Particulars, are necessary to operate the system

- various power supplies, including for the amplifier and the Peltier elements,
- a high voltage bias supply for biasing the DUT,
- an oscilloscope for acquiring the waveforms,
- and a computer for controlling the system.

An image of the final setup can be seen in figure 6.4. All configurable components, such as the various power supplies, the laser driver, the oscilloscope and the X-Y-Z stage controllers are connected to the control computer via either Ethernet or USB. The entire setup can be controlled from the Debian based computer. Section 6.2.2 describes the custom control and acquisition software in more detail.

---

[4] Product webpage: `http://www.particulars.si/products.php?prod=LargeScanTCT.html`

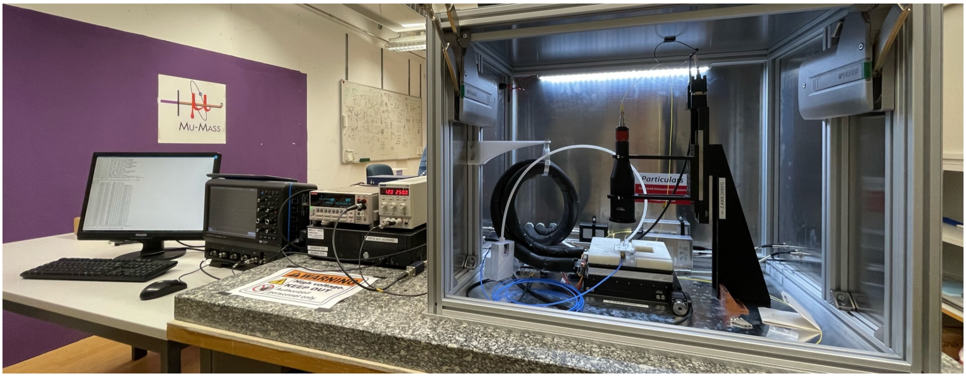

FIGURE 6.4: View of the TCT system commissioned at ETHZ.

6.2.1.1 *Laser system*

The red and IR lasers are fibre coupled lasers based on Thorlabs laser diodes. Particulars supplies the lasers with an integrated driver which is able to generate pulses widths down to ca. 350 ps and repetition rates of up to 1 MHz. The driver generates a trigger signal, synchronized with each laser pulse, which is used for triggering the data acquisition on the oscilloscope. The optical system includes a beam expander and a focusing lens, built with components from Thorlabs. The red laser beam spot can be focused down to a full width at half maximum (FWHM) of $< 8\,\mu m$ and the IR laser to a FWHM of $< 11\,\mu m$.

6.2.1.2 *Mechanical system*

The X-Y sample stage allows to automatically position the DUT with a precision of ca. $1\,\mu m$. The laser is focused via the Z stage having the same precision. Both X-Y and Z movements are implemented using motorized translation stages from Standa Ltd. The X-Y sample stage integrates a set of Peltier elements which are coupled to a heat remover plate with ports for an external water cooling system. The aluminium enclosure protects the system from dust and accidental manipulation. It is not fully light-tight and does not provide sufficient electromagnetic shielding. For the measurements presented in this thesis, additional electromagnetic shielding is provided by the custom sandwich-type sample holder (see section 6.3 for details).

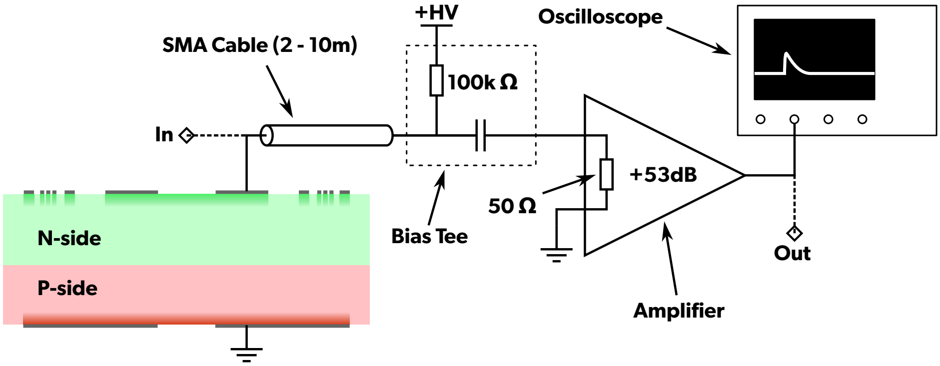

FIGURE 6.5: Schematic view of the biasing and signal path used in the ETHZ TCT system. Detailed description in the text.

6.2.1.3 *Biasing and signal acquisition*

The biasing and signal acquisition scheme is shown in figure 6.5. Biasing and signal acquisition is carried out from the N-side of the diode samples, making use of a bias-tee for biasing. Biasing via the P-side of the diode samples without using a bias-tee while collecting signals on the N-side is also possible, but was not employed for this work. The bias voltage is provided by a Keithley 2410 source measure unit (SMU) which can source a maximum of $I_{Bias,max} = \pm 20\,\mathrm{mA}$ at up to $V_{Bias,max} = \pm 1000\,\mathrm{V}$. The bias voltage is filtered via the *F-01 A* high voltage filter provided by Particulars. The *AM-02A* amplifier provided by Particulars has a nominal gain of 53 dB.[5] All components in the signal path have a nominal matched impedance of 50 Ω, except the bonded sample itself. Due to the capacitive nature of the (reverse biased) diode sample, its apparent impedance is highly frequency dependent. Thus any signal reflected at the bias tee input or the amplifier input is re-reflected at the diode sample. In order to separate these reflections from the primary pulse in the time domain signal, a long coaxial cable is inserted between the DUT and the bias tee.

The overall electronics front-end gain was characterized by injecting TCT-like pulses with a signal generator at the point marked *In* in figure 6.5. The amplified test pulses were recorded with the oscilloscope at the point marked *Out*. This gain measurement includes the attenuation of the signal

---

[5] See section 6.2.4 for a discussion of operating the amplifier at below nominal gain.

Cable Length	**Cable Type**	**Delay**	**Overall Gain**
3.05 m	Thorlabs *SMM120*	15 ns	51.52 dB
10 m	H&S *ENVIROFLEX 142*	47 ns	51.16 dB

TABLE 6.1: Measured overall electronics front-end gain with different SMA cables. The gain values include the contribution from the SMA cable, the bias tee and the amplifier.

in the long coaxial cable, the effect of the bias tee, the amplifier gain, and the attenuation in the coaxial cable leading to the oscilloscope. The measurements were carried out while operating the amplifier at full nominal gain and without any bias voltage applied to the bias tee. Table 6.1 shows the resulting overall gain for two different coaxial cables. It can be observed that the overall gain is lower than the nominal amplifier gain, mainly due to the attenuation in the coaxial cable. These gain values are used for comparative simulations (see section 8.3.4).

6.2.1.4 *Temperature Control*

Temperature control is achieved via the Peltier elements integrated into the sample stage. They have a total power of 200 W and theoretically allow for a maximum $\Delta T \approx 40\,°\mathrm{C}$. A foam-filled 3D printed cover has been added to limit the heat loss via the ca. 20 cm × 20 cm large sample stage (the cover is visible in figure 6.4). The Peltier elements are powered by a lab power supply and regulation of the sample temperature is assured by a simple PID controller implemented on a Raspberry Pi. As a regulation input either the temperature of the sample stage or the temperature measured directly on the sample holder (see section 6.3) is used. The excess heat from the Peltier elements is extracted via water cooling to the outside of the enclosure by a Lauda *Loop L100* chiller.

6.2.2 *Control and acquisition software*

Particulars provides a LabVIEW based closed source application for controlling the TCT setup and for executing automatic scans. This software package was considered to be used in the TCT setup, but was ultimately rejected for multiple reasons:

- The software is closed source and therefore any adaption needs to be carried out by Particulars. Such adaptions are necessary to include the readout of the Waverunner oscilloscope used in the setup.
- To fully control all devices of the system multiple programs are necessary. This includes individual programs for general control, laser control and temperature control.
- The control is only possible via the LabVIEW user interface. Each scan therefore needs to be set up and configured manually and automation is not trivially possible.
- The software only runs on Microsoft Windows. This complicates integration into the existing lab environment running primarily under Linux.
- The software has no integrated analysis capability. It is therefore necessary to invoke additional software packages in order to look at the recorded data. These additional steps are especially tedious when doing trial and error investigations of new samples.

Under consideration of these points the decision was taken to implement a new control framework from ground up. The following are the main design requirements for this control framework:

- Shall be running under Linux.
- Shall control the entire setup from one single framework.
- Shall allow to execute scans based on text configuration files.
- Shall store the data in an open and accessible file structure.
- Shall allow for automatic *online* analysis of the recorded data.

The new control framework is implemented using the Python programming language.[6] Figure 6.6 shows a diagram documenting the software architecture of the framework. The lowest level of the software stack implements communication interfaces via Ethernet (VXI11 or IP), USB and serial ports for communicating with the various components of the setup.

---

[6] The source code of the TCT control framework is published online on Github at `https://github.com/deragent/ETHZ-TCT-Control`.

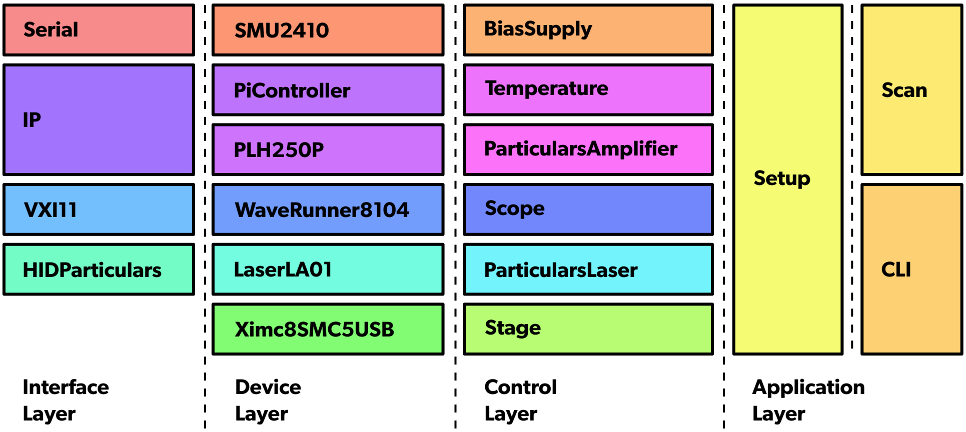

FIGURE 6.6: Software stack of the ETHZ TCT setup control framework. The lowest level is on the left and the highest level on the right.

These interface classes are used by the device classes on the next level above, which abstract individual commands to be sent to the devices. The control classes one level above implement more complex routines, making use of the lower level device classes for executing individual actions. The two main application programs, the automatic scan control and the manual command line interface (CLI), are built on top of the control layer.

6.2.2.1 *Automatic TCT scan control*

The scan control utility is a command line application which allows to run automatic scans of system parameters. For example, a diode sample can be scanned in the X-Y plane, acquiring one or multiple waveforms at each X-Y position. YAML based configuration files are used to specify the scan to be executed. The advantage of such a configuration file, compared to a graphical user interface (GUI), is the possibility of creating complex scan patterns and the ability to easily save and reuse existing scan configurations. A simplified example configuration file is shown in listing 6.1. The *meta* section defines metadata about the setup, DUT and the scan to be executed. This information is stored together with the acquired data. The *limits* section defines the absolute maximum voltage and current of the SMU, and the *scope* section defines the number of triggers used for averaging by the oscilloscope. In the *setup* section the initial parameters for various components of the setup are given. Parameters which are not specified (such

Listing 6.1: Example YAML based TCT scan config for the ETHZ TCT setup. The config implements a X-Y scan at one specific bias voltage. Detailed description in the text.

```yaml
meta:
  name: ’X-Y Scan’
  description: ’2D Scan of a sample in X and Y’
  operator: ’Johannes Wuethrich’
  laser: ’Particulars 660nm’
  aperture: ’Medium’
  sample: ’E2’
  wafer: ’P301401’
  side: ’P-Side’

limits:
  voltage: 1000              # HV bias voltage limit [V]
  current: 0.002             # HV bias current limit [A]

scope:
  average: 100               # Oscilloscope averaging [-]

setup:
  gain: 100                  # Relative amplifier gain [%]
  hv: 120                    # HV bias voltage [V]
  focus: 73                  # Focus (Z) distance [mm]
  frequency: 50e3            # Laser repetition rate [Hz]
  dac: 290                   # Laser pulse configuration [-]

end: off

scan:
  - x: lin(-3, 3, 7)         # Sample X positions [mm]
  - y: lin(-3, 3, 7)         # Sample Y positions [mm]

analysis:
  title: ’Integrated Signals vs. X-Y Position’
  x: x
  y: y
  plot: integral()           # Integral of the TCT pulse
```

Listing 6.2: Folder and file structure of the data generated and saved by a single TCT scan. Detailed description in the text.

```
[YYYYMMDD]-[HHMMSS]_x-y-scan /
    log.log
    meta /
        info.yaml
        config.yaml
        list.csv
    plot /
        Plot3D_stage.x-stage.yVSintegral().pdf
    data /
        A0.hdf5
        A1.hdf5
        ...
        A48.hdf5
```

as x and y) are not modified. The *end* section defines the state to be set after the end of the scan routine. In the presented case all components are turned off. In the *scan* section each entry specifies one dimension of the parameter space to be scanned. In the given example a 7×7 X-Y scan is carried out by iterating over all 7 y positions at each x position, and acquiring a TCT waveform for each of the combinations of x and y. Finally, the scan routine also allows to automatically create summary plots of the acquired data. In the example case a 2D heat map is plotted with the TCT pulse integral defining the colour (3rd axis) at each x and y position. The direct generation of plots allows for quick iterations, especially when positioning samples and focusing the laser, as no external analysis script needs to be executed.

DATA STORAGE Each scan is stored in a dedicated data directory. The overall structure of a data directory is shown in listing 6.2. The name of the directory is derived from the *name* specified in the config file, prefixed with the date and time of the scan. The *info.yaml* file contains the *meta* section from the config file, and the *config.yaml* contains the full config file used to execute the scan. The *list.csv* file contains a CSV table with one row for each acquired scan point. The data contained in the columns of this file include the current set state of the setup (such as x and y positions and the bias voltage), but also measured quantities (such as temperatures and bias currents) at each data point. The *plot* directory contains PDF versions of the plots generated at the end of the scan, as specified in the *analysis* section of

Listing 6.3: Example commands of the command-line utility used for manually controlling the ETHZ TCT setup.

```
# stage position
    X:    2mm
    Y:    0.15mm
    Z:    76.5mm
# stage goto x 3
# bias voltage 200
# bias current
    = 20.5 uA
# laser on
```

the config file. The acquired time domain TCT curves are stored in the *data* directory, with one HDF5 file per acquired curve. Each curve is sequentially numbered with the number being equal to the corresponding row index in the *list.csv* file.

6.2.2.2 *Manual command-line based control*

For setting up a measurement and manual operation of the setup, a CLI is implemented which allows to control all components of the TCT setup. The CLI utility implements a simple hierarchical command structure. Each component of the setup is attributed a command group with individual subcommands. The utility implements auto completion and a history of previously used commands. Listing 6.3 shows some command examples with the corresponding outputs. In the normal workflow the CLI utility is used to manually set up a sample on the TCT setup, find the point of interest of the sample and verify the correct operation. After this setup, one or multiple scans are run automatically using the SCAN utility. Given that the CLI utility implements a remote view of the oscilloscope screen, all this work can be executed fully remotely, for example by making use of X-forwarding over SSH. Only the installation and exchange of the samples needs to be carried out physically in the lab.

6.2.3 *Online data analysis utility*

In order to have a better overview of all acquired TCT scans, an online data analysis utility was implemented.[7] The utility presents itself as a web page accessible over the internet. The web server is implemented in Python using the open-source Flask framework[8] and is running on the same computer as used for controlling the TCT setup. Three different views are implemented:

DATASET OVERVIEW This view allows to access and review the metadata and config files of all recorded scans. The log file written during the scan execution, as well as the plots generated at the end of a scan, is also accessible. Figure 6.7a shows an example view of the overview page.

WAVEFORM BROWSER This view allows to visualize individual time domain TCT curves. Curves from the same or different scans can be compared directly. Figure 6.7b shows an example view of the waveform browser.

SIMULATION BROWSER This view allows to compare a recorded time domain TCT curve with a simulated curve. The parameters of the simulated curve can be manually set in the online interface. More details about the simulation model are given in section 8.3, where also an example view is shown in figure 8.2.

The data of individual scans is available for download from the *Dataset Overview* page, to be used for more in depth analyses.

6.2.4 *Amplifier operation at partial gain*

As per the documentation of the manufacturer, the amplifier of the TCT system can be operated below the nominal supply voltage in order to reduce the amplification gain. The amplifier has a nominal gain of 53 dB at 12 V which can be reduced down to 39 dB at ca. 6 V supply voltage [117]. During initial measurements with the ETHZ TCT setup, an unexpected secondary pulse was observed in the time domain TCT signal (highlighted in figure 6.8). Investigations revealed that this additional pulse is related to

---

[7] The source code of the online data analysis utility is published online on Github at `https://github.com/deragent/ETHZ-TCT-Online`.

[8] Flask is online available at `https://flask.palletsprojects.com/`.

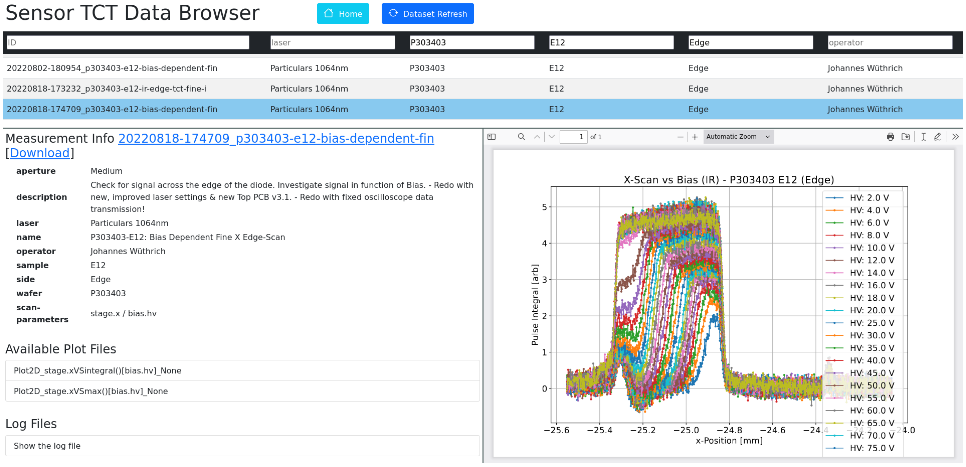

ID	laser	P303403	E12	Edge	operator
20220802-180954_p303403-e12-bias-dependent-fin	Particulars 1064nm	P303403	E12	Edge	Johannes Wüthrich
20220818-173232_p303403-e12-ir-edge-tct-fine-i	Particulars 1064nm	P303403	E12	Edge	Johannes Wüthrich
20220818-174709_p303403-e12-bias-dependent-fin	Particulars 1064nm	P303403	E12	Edge	Johannes Wüthrich

Measurement Info 20220818-174709_p303403-e12-bias-dependent-fin [Download]

aperture	Medium
description	Check for signal across the edge of the diode. Investigate signal in function of Bias. - Redo with new, improved laser settings & new Top PCB v3.1. - Redo with fixed oscilloscope data transmission!
laser	Particulars 1064nm
name	P303403-E12: Bias Dependent Fine X Edge-Scan
operator	Johannes Wüthrich
sample	E12
side	Edge
wafer	P303403
scan-parameters	stage.x / bias.hv

Available Plot Files

Plot2D_stage.xVSintegral()[bias.hv]_None

Plot2D_stage.xVSmax()[bias.hv]_None

Log Files

Show the log file

(a) The *Dataset Overview* page allows to access all the meta-data of the scans acquired with the TCT setup. It also allows to view the summary plots generated as part of the scan procedure (see section 6.2.2.1).

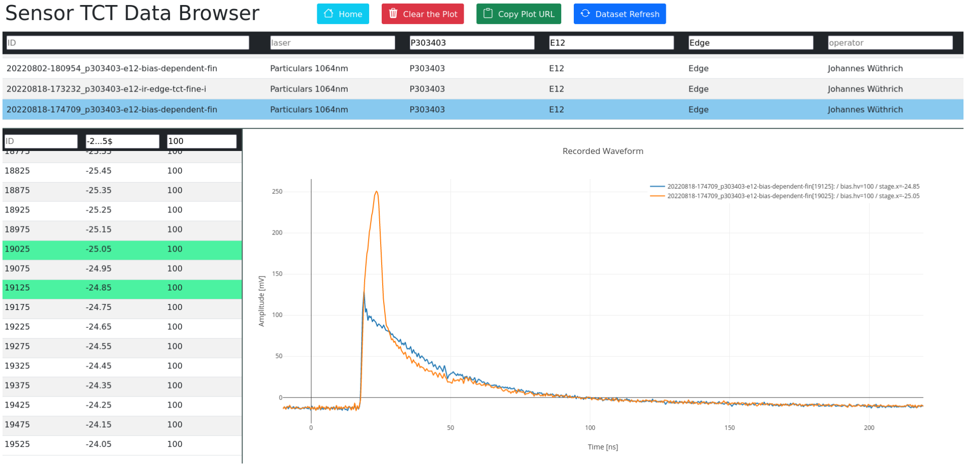

ID	laser	P303403	E12	Edge	operator
20220802-180954_p303403-e12-bias-dependent-fin	Particulars 1064nm	P303403	E12	Edge	Johannes Wüthrich
20220818-173232_p303403-e12-ir-edge-tct-fine-i	Particulars 1064nm	P303403	E12	Edge	Johannes Wüthrich
20220818-174709_p303403-e12-bias-dependent-fin	Particulars 1064nm	P303403	E12	Edge	Johannes Wüthrich

ID	-2...5$	100
18825	-25.45	100
18875	-25.35	100
18925	-25.25	100
18975	-25.15	100
19025	-25.05	100
19075	-24.95	100
19125	-24.85	100
19175	-24.75	100
19225	-24.65	100
19275	-24.55	100
19325	-24.45	100
19375	-24.35	100
19425	-24.25	100
19475	-24.15	100
19525	-24.05	100

(b) The *Waveform Browser* page allows to plot the time-domain TCT curves recorded as part of scans. It allows to plot curves from multiple different scans for quick comparisons.

FIGURE 6.7: Views of the TCT online data interface.

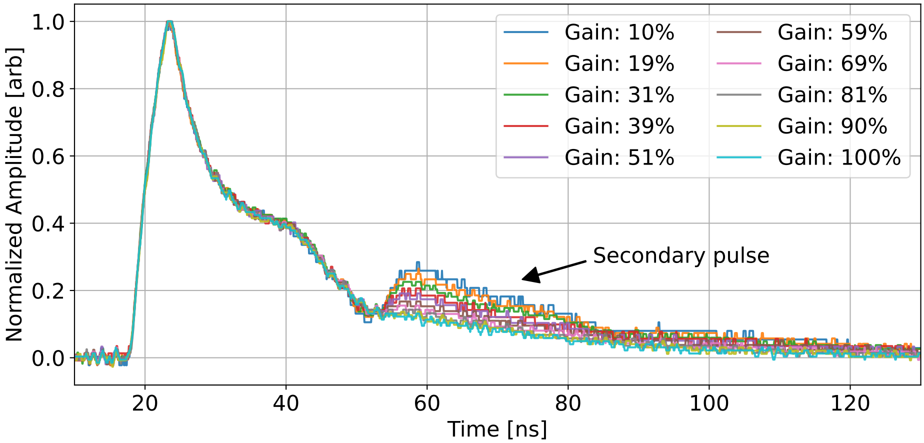

Figure 6.8: TCT pulses recorded with the Particulars *AM-02* amplifier operating at different gain levels. To facilitate the comparison, all pulses are normalized to an amplitude of 1. A secondary pulse becomes prominent when operating the amplifier at lower gain values.

operating the amplifier at partial gains. Figure 6.8 shows that the additional pulse disappears when operating the amplifier at 100 % of its nominal gain, and that the second pulse is more prominent the lower the gain is. Measurements of the scattering parameters (S-parameters)[9] of the amplifier operated at different bias voltages show that the gain of the amplifier indeed changes when reducing the supply voltage (see figure 6.9a).[10] But the measurements also show that the input reflection coefficient of the amplifier increases with reduced supply voltages (see figure 6.9b). A potential explanation is that the (50 Ω) input matching of the amplifier is dependent on the supply voltage and that lower supply voltages lead to an impedance mismatch. This would lead to more reflections at below nominal supply voltages. As the precise design of the amplifier is not known to the author, a final explanation of the observed phenomenon can not be given. For any subsequent measurements the amplifier gain was strictly set to 100 % gain.

---

[9] The S-parameters represent the behaviour of a (linear) electronic circuit at different frequencies under the assumption of matched loads. The parameters are usually given as a square matrix with the number of columns and rows being equal to the number of ports.

[10] The S-parameters were measured with a Keysight *P5004A* vector network analyser (VNA).

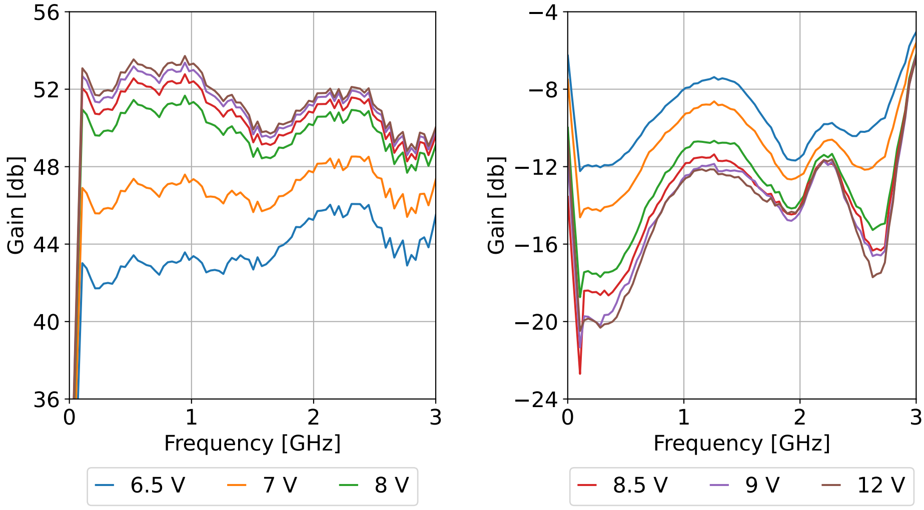

(a) Amplifier gain (S21)

(b) Input reflection (S11)

FIGURE 6.9: Amplifier gain and input reflection of the Particulars *AM-02* amplifier at different supply voltages, measured with a Keysight *P5004A* VNA. Lower supply voltages lead to an increase of the input reflections.

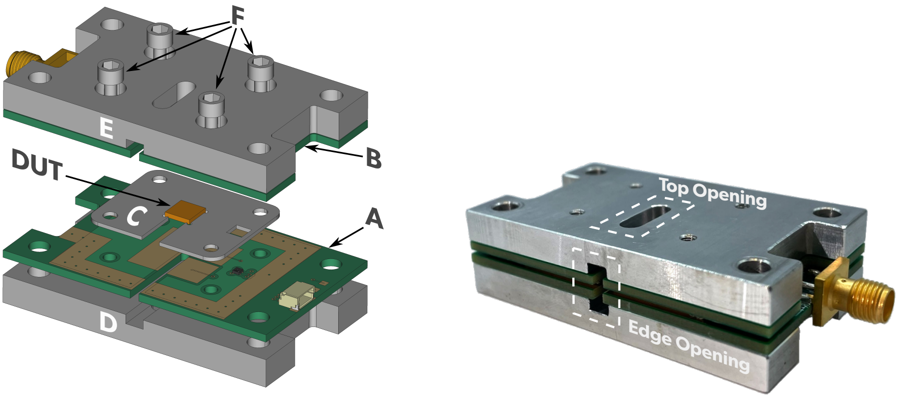

(a) Exploded view of the sandwich-type sample holder.

(b) Image of the assembled sample holder, indicating the openings used for top and edge TCT.

FIGURE 6.10: The sandwich-type sample holder. The exploded view shows the diode sample (DUT), PCBs (A and B), the 3D-printed spacer piece (C), metal support pieces (D and E) and tensioning screws (F). Figures previously published in [99].

6.3 SANDWICH-TYPE SAMPLE HOLDER

This section includes an excerpt of the publication *TCT investigation of the one-sided depletion of low-temperature covalently bonded silicon sensor P-N diodes* by Wüthrich et al. [99].

Various research groups have designed and fabricated special printed circuit boards (PCBs) and sample holders for TCT measurements [109, 118–120]. These holders all have in common that the DUT needs to be connected via wire bonding. To remove the need for a wire bonding machine, a sandwich-type holder which clamps the DUT in between two custom PCBs was designed and optimized. The connection to the DUT is made by bringing into contact the metallization on the surfaces of the DUT with the PCB top metal layer. Figure 6.10a shows an exploded view of the sample holder assembly and figure 6.10b shows a picture of the assembled sample holder. The diode sample (DUT) is laterally held in place by a 3D printed spacer piece marked C in figure 6.10. The spacer piece is slightly thinner than the DUT in order to ensure that the contact pressure is fully applied to

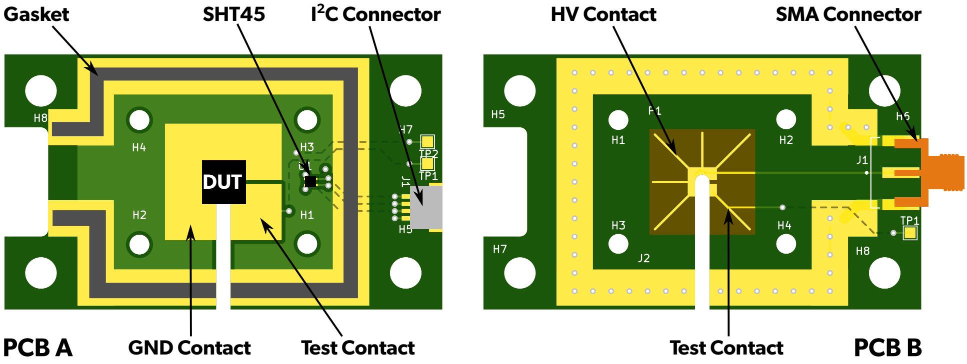

FIGURE 6.11: Annotated top layer view of the two PCBs used in the sandwich-type sample holder. PCB A includes temperature and humidity readout via a Sensirion *SHT45* sensor. PCB B shows the specially designed low capacitance contact and the matched $50\,\Omega$ transmission line up to the SMA connector. Figure previously published in [99].

the DUT. The two PCBs (marked A and B) enclose the DUT from both sides. A metal piece supports each PCB from the back side (marked D and E). The screws (marked F) are used to tighten the sandwich which ensures good electrical contact between the DUT and the PCBs [121]. It is important that the support pieces are made of a stiff material which does not allow for any flex (i.e. aluminium), as any flexing of the PCBs leads to a bad contact.

The PCBs have a special metal patterning allowing to measure the contact resistance between PCB and DUT using a common hand-held multimeter. Figure 6.11 shows the layout of the two PCBs. The metal region which is in contact with the DUT is split into two isolated parts which are individually connected to test points on the PCB. In figure 6.11 these two parts are marked *GND Contact* and *Test Contact* for PCB A, and *HV Contact* and *Test Contact* for PCB B. After installation of a sample diode, these isolated parts are shorted together by the surface metallization of the DUT. By measuring the resistance between the test points, one can probe the contact resistance between the DUT and the PCB and thus verify that a good contact has been established. The PCBs are fabricated with an electroless nickel immersion gold (ENIG) surface plating. The thin gold surface coating does not only resist oxidation but also provides improved surface planarity, especially compared to a hot air solder leveling (HASL) type surface finish [122].

PCB A in figure 6.11 creates the ground (GND) connection with the P-side of the diode samples. A Sensirion *SHT45* sensor, read out via a dedicated I2C connection, is mounted on the PCB, to enable temperature and humidity measurements in close proximity to the DUT. The GND potential is supplied from PCB B to PCB A via compressible and conductive gaskets.[11] These gaskets are mounted on the area marked accordingly on PCB A. Once the sandwich is assembled, the gaskets create a connection with the corresponding area on PCB B. The gaskets together with dedicated GND planes on each PCB form a Faraday cage around the DUT. This greatly reduces the noise pickup and enables better data acquisition within the Particulars TCT setup, which by itself does not provide sufficient shielding.

The PCB B in figure 6.11 creates the high-voltage (HV) connection with the N-side of the DUT. HV and GND are supplied to the PCB B via the edge mounted SMA connector. The signal is collected via the N-side HV contact. One challenge of such a sandwich-based sample holder is the reduction of the parasitic capacitance introduced in parallel with the DUT. The various metal layers of the two PCBs act as parallel plate capacitors. In order to reduce these added parasitic capacitances, one can either reduce the surface area or move the surfaces farther apart.[12] Accordingly, the GND planes which form the Faraday cage have been moved to the outermost layers of the 4-layer PCB stacks. To reduce the parasitic capacitance of the metal layers in contact with the DUT, the area of the metal contact on PCB B was minimized, taking the form of the star-like structure in the centre of the PCB. The parasitic capacitance of a fully assembled sample holder is $C_{para} \approx 8.2\,\mathrm{pF}$ as measured with a Keysight *U1733C* LCR-meter at 100kHz. This value neither includes the capacitance of the DUT nor the capacitance of the electronics front-end. The HV contact traces are designed to have a $50\,\Omega$ impedance matching when fabricating the PCBs using the *JLC04161H-7628* 4-layer impedance control stack-up from JLCPCB.[13]

As marked in figure 6.10b, there are openings in the metal support structures as well as the PCBs which allow for laser illumination via the N- and P-side of the DUT, as well as via the edge of the DUT. This enables the

---

[11] For example the gasket model *3020301* produced by Würth Elektronik.

[12] According to the capacitance calculated via the infinite plane approximation $C = \epsilon \frac{A}{d}$, with A the plate area, d the plate separation and ϵ the permittivity.

[13] See `https://jlcpcb.com/impedance`.

sample holder to be used for both top/bottom and edge TCT measurements without remounting the DUT. Overall the following advantages of this type of sandwich-type holder can be identified:

- No specialized tools (i.e. wire boding) are necessary for mounting a sample.
- Mounting a new sample is very quick and the sample holder can be reused without any issues.
- The sample holder provides shielding to noise pickup.
- It allows for top/bottom and edge TCT measurements.

Compared to traditional sample holders, making use of wire bonding, there are certain disadvantages:

- The sandwich structure leads to a higher parasitic capacitance.
- It can only be used for pad diodes with reasonably large metal contacts.
- It can not be used for samples which are sensitive to pressure.
- There is no trivial way of separately connecting guard rings.

6.4 EDGE POLISHING

Samples to be investigated with edge TCT need to have their sidewalls polished as a preparatory step. Any roughness in the side walls will lead to variations in the amount of laser light absorbed by the sample, giving rise to apparent variations in detection efficiency. Very rough side surfaces can also cause reflection and refraction of the laser light, which can lead to an apparent signal in locations where the device is non-sensitive. These different effects are illustrated in figure 6.12.

For this work, the edge polishing is carried out manually in a multi step process, inspired by [123, 124]. A coarse polishing is first carried out using different grades of lapping paper with grain sizes of 30 µm, 3 µm and 0.02 µm.[14] The fine polishing is carried out using a diamond paste

---

[14] The used lapping sheets are procured from Thorlabs with part numbers *LF30D*, *LF3D* and *LFCF*.

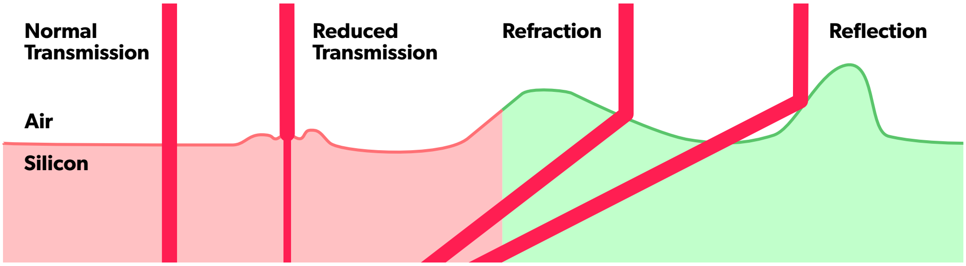

FIGURE 6.12: Different effects leading to bad edge TCT measurement results due to non-polished sample edges.

with a grain size of 0.1 µm applied via cotton swabs.[15, 16] Figure 6.13 shows the progress after each step in the polishing process. Edge polishing is especially important in the case of the bonded diode samples fabricated for this thesis, as the dicing was carried out using laser dicing (see section 4.1.5). The laser dicing is usually carried out in multiple passes, with each pass cutting to a certain depth. This results in characteristic parallel structures on the diode side walls, as can be seen in figure 6.13a. Thus, starting with a very large grain size of 30 µm allows to quickly remove these large surface variations. The importance of edge polishing is highlighted in figure 6.14. It shows the result of an edge TCT measurement carried out before and after polishing. In the pre-polishing curve the repetitive structures from the laser dicing are clearly visible as peaks and valleys. Laser light reflected and refracted at these irregularities also gives the appearance that the N-side of the sample produces signals. As will be discussed in chapter 7, this is not the case and the curve recorded after polishing indeed shows no signal in the N-side.

---

[15] The diamond paste is procured from RS Pro with part number *315-5125*.

[16] Classic, over the counter, cotton swabs showed the best results. It was also attempted to apply the diamond paste with cleanroom type swabs (RS PRO *177-1331*) with non satisfying results, as not enough pressure could be applied for good polishing.

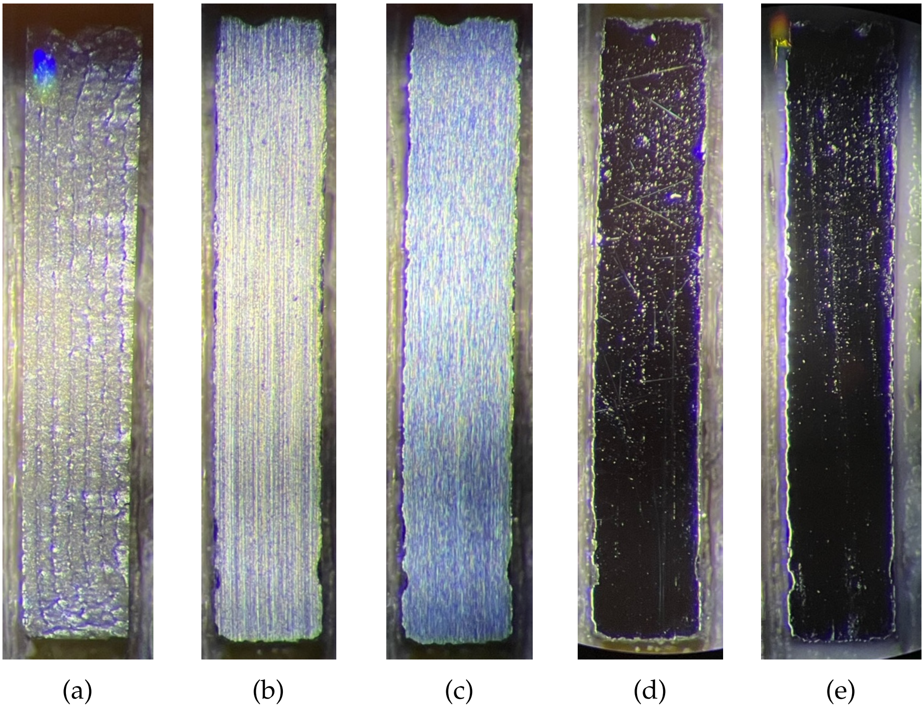
(a) (b) (c) (d) (e)

FIGURE 6.13: Microscopic view of a sample edge at various stages of polishing. From left to right: unpolished edge after laser dicing; after polishing with 30 µm grain lapping paper; after polishing with 3 µm grain lapping paper; after polishing with 0.02 µm grain lapping paper; and after polishing with the diamond paste using a cotton swab. The samples were illuminated with a ring light. Thus, the more polished the surface is, the less light is diffusively reflected into the objective of the microscope and the darker the edge appears in the image. Figure previously published in [99].

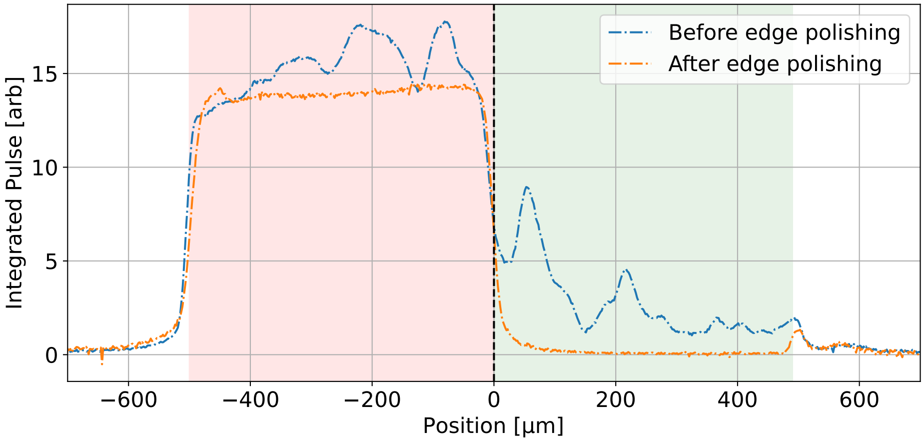

FIGURE 6.14: Comparison of the edge TCT curves recorded before and after polishing of the sample edge. Before polishing the sample shows a high spatial variation in the collected signal. The unpolished edge also leads to an apparent collection of signal in the undepleted N-side (also see chapter 7). The x-axis is the position across a diode, with $x = 0\,\mu\text{m}$ the location of the bonding interface. The curves have been manually normalized for better comparison. Data was taken with a bias of 80 V and using sample *P301401-E2*.

7

DEPLETION BEHAVIOUR OF BONDED P/N JUNCTIONS

Every day is a good day to go outside!
— Emmy

The main question investigated in this thesis is how signals are created and collected in wafer-wafer bonded structures. As seen in section 2.3, electrons and holes moving within a semiconductor induce a current on the readout electrodes which represents the detected signal. This movement is dominated by the drift of charges within an electric field. As elaborated, in semiconductor detectors this electric field is created by applying a reverse bias across a P/N junction, thus creating an electric field within the depleted region. Therefore, it is clear that having a precise understanding of the depletion behaviour of the bonded samples will lead to a better understanding of the signals collected from such structures.

The principle method used for investigating the depletion behaviour of the bonded samples is transient current technique (TCT) measurements. Initial measurements with red and infrared (IR) laser illumination via the top and bottom TCT openings of the samples indicated a highly asymmetric depletion behaviour. More detailed analyses strongly implied that only the P-side of the bonded samples can be depleted, whereas the N-side is not depleted at all. Edge TCT measurements directly confirm this hypothesis, and the finding is also confirmed by independent measurements using a two photon absorption (TPA) TCT setup at CERN [115]. Based on this observation, an empirical P/N++/N model is proposed, which allows to correctly represent the observed depletion behaviour in simulations. Theoretical considerations show that already a small concentration of interface defects, acting as donors or acceptors, might influence the depletion behaviour of P/N junctions fabricated via surface activated bonding (SAB).

CONTRIBUTION All TCT measurements presented in this chapter, with the exception of the TPA TCT measurements, were carried out by the author, including the sample preparation. The TPA TCT measurements were carried out by Sebastian Pape of the Solid State Detectors group at

CERN, in the presence of the author. The analysis of all measurements was carried out by the author.

7.1 TOP / BOTTOM TCT MEASUREMENTS

Top and bottom TCT measurements, using the red laser (660 nm), are carried out on a total of 6 samples taken from 3 different bonded wafer pairs. The following six samples are used: **P301401-E2**, **P301401-E12**, **P302402-E2**, **P302402-E12**, **P303403-E2** and **P303403-E12**.[1] These samples are equal, apart from variations in the resistivities of the substrates. Samples of size **E** were selected, based on a trade-off between ease of handling and having a low overall bias current. The red laser light is absorbed within ca. 20 µm of silicon and thus mimics the signal observed from an α-particle. Before each measurement, the laser beam is focused on the sample surface using the knife-edge technique employing the edge of the metallization opening. TCT curves are acquired at reverse bias voltages generated by the source measure unit (SMU) in the range $V_{SMU} = 0 - 650\,\text{V}$. The effective bias voltage on the sample is lower due to the voltage drop across the resistance in the bias-tee

$$V_{Bias} = V_{SMU} - R_{Tee} I_{Bias}. \tag{7.1}$$

The acquired (averaged) TCT waveforms are baseline corrected. Figure 7.1 shows the resulting pulse integrals in function of the applied bias voltage for all measured samples

$$S(V_{Bias}) = \int_{t_{start}}^{t_{end}} I_{V_{Bias}}(t)dt \tag{7.2}$$

with $I_{V_{Bias}}(t)$ the recorded time domain TCT pulse at a given V_{Bias}. It is immediately obvious that the depletion behaviour of the samples is highly asymmetric. In the case of illumination from the P-side, the samples first do not record any significant signal, followed by a strong increase and finally a plateau of collected signal at a bias voltage of $V > V_{Red}$. This behaviour agrees with a depletion region starting from the bonding interface, growing into the P-side of the bonded structures until finally reaching the surface of the P-side. At this point all charges generated by the red laser are collected via drift and the measured signal reaches a plateau. The voltage V_{Red} thus represents the bias voltage at which the entire P-side is depleted.

---

[1] See section 4.2 for details on the sample labelling.

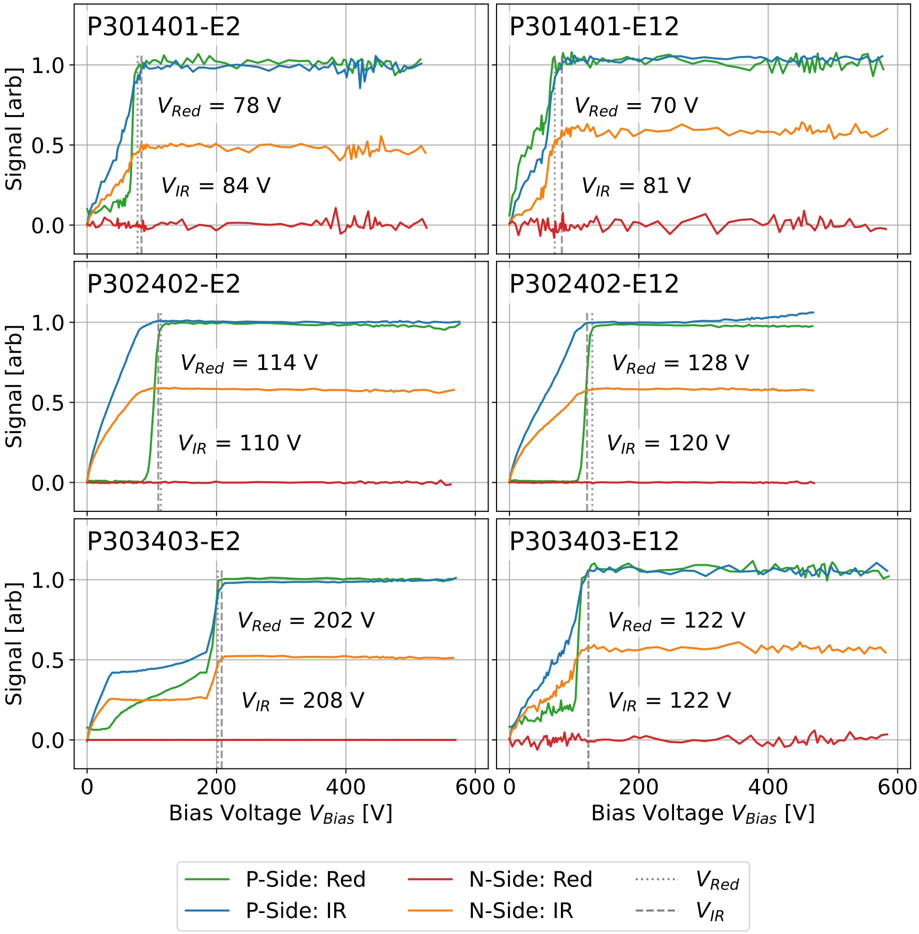

FIGURE 7.1: Integrated signal vs. bias voltage for the six samples in the case of top and bottom TCT using the red and IR lasers. To enable better comparison, two normalization factors have been applied to the curves of each sample: one for the red laser measurements and one for the IR laser measurements.

For the measured samples, the observed values for V_{Red} are in the range of 70-210 V. The spread of observed values is indicative of bulk doping concentration variations of the P-wafers. The different behaviours of the curves at voltages below V_{Red} are discussed in section 7.3. Conversely, in the case of illumination via the N-side the behaviour is very different. No signal is being observed up to a bias voltage of 450 V for all measured samples, a value which is much higher than any of the observed V_{Red}. This is surprising, as one would naively expect a somehow symmetric depletion behaviour of the P- and N-side. The boron doped P-wafers used for the sample fabrication have a resistivity of $\rho_P \geq 10\,\mathrm{k\Omega\,cm}$, and the phosphor doped N-wafers a resistivity of 8 - $10\,\mathrm{k\Omega\,cm}$, as per the manufacturer specifications (see table 4.3). This is equivalent to a doping concentration of $N_A \leq 1.32 \times 10^{12}\,\mathrm{cm}^{-3}$ and $N_D = (4.40 - 5.52) \times 10^{11}\,\mathrm{cm}^{-3}$ for the P- and N-wafers respectively. Thus, under the assumption that the bonded P/N junction shows a normal depletion behaviour, if the P-side is fully depleted at a bias of V_{Red}, a significant part of the N-side should also be depleted at the same bias. The full depletion of the N-side should be observable at reasonable bias voltages.[2]

Equivalent measurements are also carried out using the IR laser (1064 nm) of the TCT setup. The IR laser is not fully absorbed within the bonded structures but can rather penetrate the entire sample. The resulting curves of the integrated TCT pulses as a function of the bias voltage is also shown in figure 7.1. In this case already very low bias voltages lead to a signal being recorded. Due to the penetrating nature of the IR laser, there are always a certain number of free charges being created within even partial depletion volumes. The recorded signal thus gradually increases from $V_{Bias} = 0\,\mathrm{V}$ up to $V_{Bias} = V_{IR}$, after which it stays constant. The curves in figure 7.1 show that $V_{IR} \approx V_{Red}$ for all samples. Under IR laser irradiation, a wider depletion region should lead to a higher overall collected signal, as the wider depletion region collects more of the created e/h pairs. Thus, the observed plateau of signal collected for $V_{Bias} > V_{IR}$ indicates that the depletion region does not grow any further beyond this point. Given that $V_{IR} \approx V_{Red}$ one can therefore conclude that the depletion of the bonded

---

[2] In this context, full depletion of the P-side only refers to depletion of the bulk. In reality, there is always a thin non-depleted layer at the surface of the P-side due to the high doping concentration of the ohmic contacts. It is precisely this layer which would provide the additional charges necessary for further depleting the N-side once the bulk of the P-side has been fully depleted.

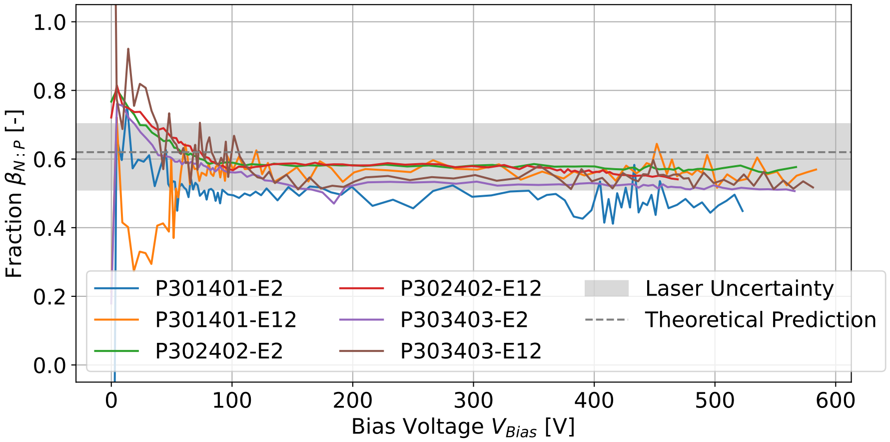

FIGURE 7.2: Fraction of the integrated TCT signal under IR laser illumination of P-side vs. N-Side. At low bias voltages the values are not stable due to only partial depletion of the P-side. For the theoretical prediction see the text.[3]

structure progresses until the full depletion of the P-side bulk, and then stops. As the N-wafers have a uniform bulk, there is no reason for the depletion of the N-side to suddenly stop after only partial depletion. The red laser measurements have shown that a full depletion of the N-side is not possible and thus the only logical hypothesis is that the N-side is not depleting at all.

Under this hypothesis the signal observed with the IR laser from the N- and P-side is compared. For each sample these two measurements were carried out back to back, and thus the laser intensity can be considered approximately equal for both measurements. Given the hypothesis that only the P-side is being depleted, one expects a higher collected signal when exposing the P-side to the IR laser. This is due to the exponential decay of the laser intensity within the silicon, which leads to more electron-hole pairs being created towards the exposed surface than deeper within the

---

[3] The data for the sample P301401-E2 stems from one of the very first measurements acquired. These initial measurements had worse noise behaviour and less stringent environmental controls than later measurements, which is visible in the presented data. For technical reasons the sample could not be remeasured later on. It is included here for completeness.

structure. Based on the recorded data, the fraction of signal collected in N-side illumination vs. P-side illumination is calculated as

$$\beta_{N:P} = \frac{S_N\left(V_{Bias}\right)}{S_P\left(V_{Bias}\right)} \tag{7.3}$$

Figure 7.2 shows this fraction for all measured samples. As expected, the signal collected in P-side exposure is larger than in N-side exposure ($\beta_{N:P} < 1$). Based on the hypothesis that only the P-side is depleting, the fraction $\beta_{N:P}$ can be predicted theoretically based on the known absorption of IR laser light in silicon as

$$\beta_{N:P} = \frac{B \cdot A_{Si}(t_P) \cdot T_{Si}(t_N) \cdot I_{IR}}{B \cdot A_{Si}(t_P) \cdot I_{IR}} = T_{Si}(t_N) = e^{-\alpha_{Si} t_N} \tag{7.4}$$

with I_{IR} the IR laser intensity arriving at the sample surface, $T_{Si}(d)$ the relative transmission of IR light through a silicon layer of thickness d, $A_{Si}(d)$ the relative absorption of IR light in a silicon layer of thickness d, B a constant representing the TCT pulse acquisition, and t_P and t_N the thickness of the P- and N-side respectively.[4] The fraction is simply given by fraction of light transmitted through the (assumed non-depleted) N-side. With $\alpha_{Si} = 9.76^{+3.98}_{-2.56}\,\mathrm{cm}^{-1}$ for the IR laser ($\lambda_{IR} = 1064 \pm 10\,\mathrm{nm}$)[5] and a nominal N-side thickness of $t_N = 490\,\mu\mathrm{m}$, the theoretically predicted fraction is

$$\beta_{N:P} \approx 0.62^{+0.08}_{-0.09}, \tag{7.5}$$

with the uncertainty stemming from the laser wavelength variations [126]. The observed values of $\beta_{N:P}$ (as presented in figure 7.2) are compatible with the theoretical prediction. This presents a strong argument that indeed no depletion is occurring in the N-side of the fabricated samples.

7.2 EDGE TCT MEASUREMENTS

All previously presented arguments supporting P-side-only depletion are based on indirect observations. To conclusively confirm the hypothesis, edge TCT measurements are carried out on the same samples as investigated

---

[4] The interaction of the laser light with silicon follows the Beer-Lambert law and thus $A_{Si}(d) = 1 - e^{-\alpha_{Si} d}$ and $T_{Si}(d) = e^{-\alpha_{Si} d}$, with α_{Si} the wavelength dependent linear absorption coefficient of silicon [10].

[5] The value for α_{Si} is calculated via `https://refractiveindex.info/`, based on data from [125].

in the last section. For these measurements the IR laser is used. The edge TCT curves are acquired by scanning along the axis perpendicular to the bonding interface in steps of $\Delta z = 2\,\mu\text{m}$ and by scanning the reverse bias voltage between $2 - 600\,\text{V}$ in variable steps. The recorded TCT pulses are again baseline corrected and the pulse integral is calculated as a measure of the collected signal at each measurement point. Figure 7.3 presents the resulting integrated signals for a few selected bias voltages. This data shows that no signal is collected when injecting charges in the N-side at any of the measured bias voltages. Therefore, no electric field is present in the N-side, which confirms the hypothesis that the N-sides of the bonded samples do not deplete. The curves also show that the P-side indeed depletes towards the P-side contact with increasing reverse bias voltages, starting from the bonding interface.

7.2.1 *TPA TCT reference measurement*

In order to independently validate these results, equivalent measurements are carried out using a two photon absorptions TCT measurement setup located at CERN. This TPA TCT setup is extensively used in the context of the RD-50 collaboration, for the characterization of new pixel detectors to be used in future upgrades of the Large Hadron Collider (LHC) experiments [115]. The TPA TCT setup belongs to the Solid State Detectors group, led by Michael Moll, and the measurements were prepared and carried out by Sebastian Pape. A $\lambda_{TPA} = 1550\,\text{nm}$ laser with a pulse width of approx. 400 fs creates a focused beam spot with a volume of ca. $1\,\mu\text{m} \times 1\,\mu\text{m} \times 20\,\mu\text{m}$ [115, 127]. The **P301401-E2** sample is scanned from the P-side surface using a step size of $\Delta z \approx 3.77\,\mu\text{m}$. Figure 7.4a presents the measured integrated signal in function of the position for selected reverse bias voltages. A direct comparison between the data from the CERN TPA and the ETHZ TCT setup in figure 7.4b shows a good agreement between the two measurements. This independently confirms the previous findings obtained with the ETHZ TCT setup.

7.3 EMPIRICAL P/N++/N MODEL

When depleting a normal P/N-junction, the holes of the P-type region are filled with electrons originating from the N-type region. In the fabricated samples the N-side does not deplete, and therefore can not provide the

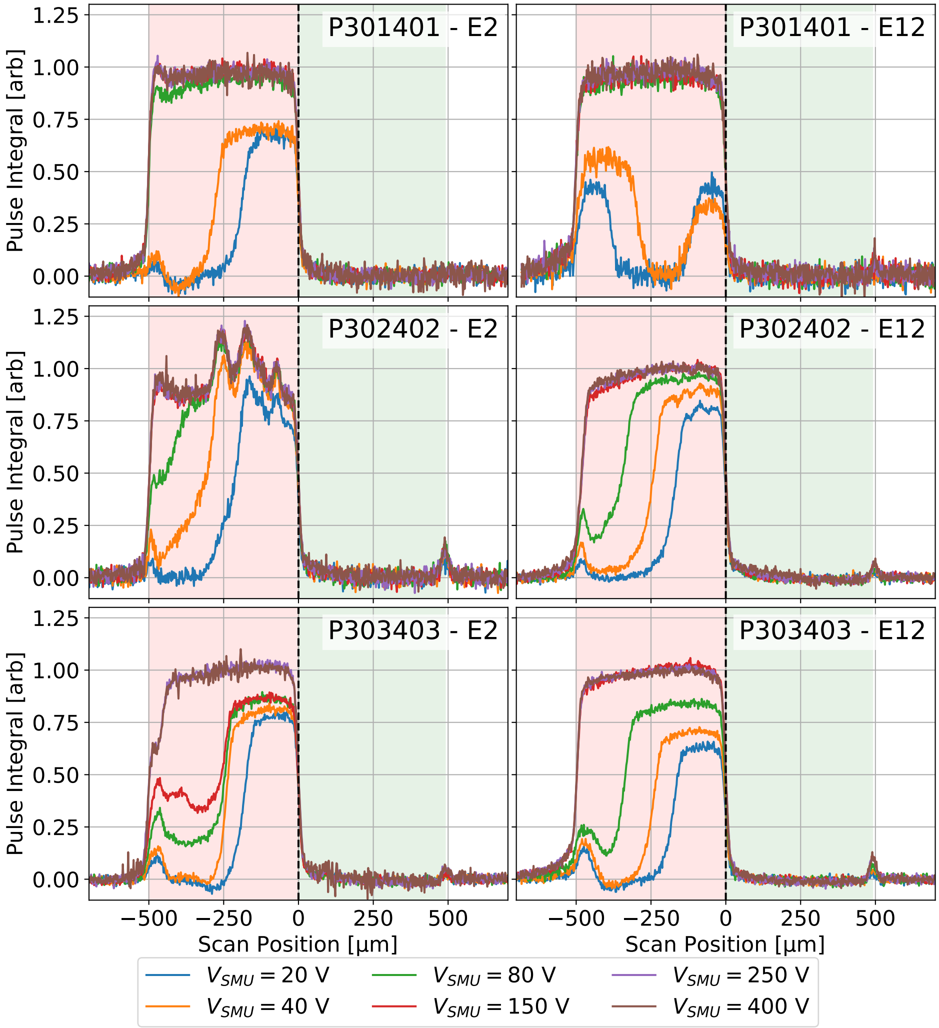

FIGURE 7.3: Integrated signal measured via edge TCT as a function of the position across the diode. The bonding interface is located at $x = 0\,\mu\text{m}$, and the P- and N-sides are shown with a red and green background respectively. It is clearly visible that no depletion occurs in the N-side of the bonded structures. An arbitrary scaling factor is applied for each sample, to allow for better visual comparison between the different samples. V_{SMU} represents the bias voltage applied by the SMU and not the effective bias voltage across the sample.

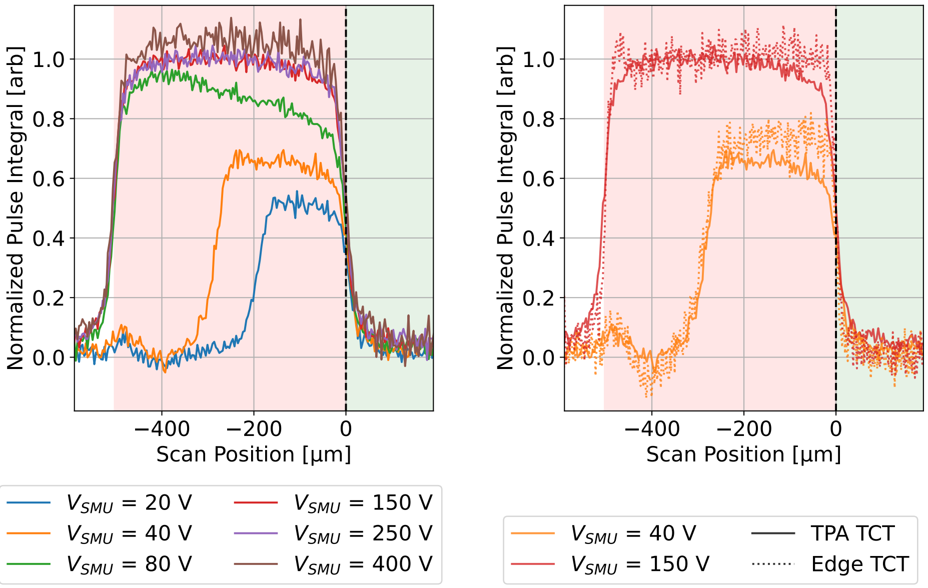

(a) TPA TCT data

(b) Comparison between edge TCT (at ETHZ) and TPA TCT (at CERN).

FIGURE 7.4: Integrated signal measured via TPA TCT for the sample **P301401-E2**. The location of the bonding interface is at $x = 0\,\mu\text{m}$. P-side and N-side are shown with a red and green background respectively.

electrons necessary for depleting the P-side. Given the high defect density and, in the case of the fabricated samples, metal contamination of the bonding interface separating the P- from the N-side, it seems clear that the free electrons are entirely provided by this interface. The bonding interface of the bonded samples thus acts like a highly doped N++ region. For the purpose of analysing the depletion behaviour, as well as the signal generation in the samples, the bonded samples can therefore be empirically modelled as a P/N++/N-structure. To investigate the depletion behaviour, the exact value of the (assumed) N++ doping concentration is not important, as long as $N_{N++} \gg N_A$ in order to guarantee that no depletion of the actual N-side is occuring. Thus, from a depletion point of view, the N-side can be ignored and the observed behaviour is the same as an abrupt one-sided P/N++-junction. It has to be noted that this simple empirical model is only set up to correctly represent the macroscopic depletion behaviour. It does not represent the microscopic behaviour of the bonding interface and therefore does not allow to model other parameters, as for example the reverse bias leakage current.

Consequently, the electric field under reverse bias is expected to be maximal on the P-side of the bonding interface and to drop off linearly towards the P-side contact. A similar profile is expected for the velocity of the charges drifting within the depletion region given that $v_{e/h}(x) = \mu_{e/h}(E(x))E(x)$. But the velocity drop towards the P-side contact will not be linear due to the occurrence of velocity saturation (see also section 8.3.1.4).[6] As discussed in section 6.1.2, the weighted prompt current method allows to extract cross-sectional profiles which are related to the carrier velocity and by extension to the electric field strength. The extracted profiles of the six measured samples are shown in figure 7.5. Four of the six samples behave as expected under the empirical P/N++/N model: **P301401-E2**, **P302402-E2**, **P302402-E12** and **P303403-E12** all show a maximum drift velocity at the bonding interface, and a close to linear drop off towards the P-side contact.[7]

Two samples show an irregular behaviour which can not be explained by the P/N++/N model. **P301401-E12** shows an inverted drift velocity profile

---

[6] Velocity saturation becomes important for electric fields above $1 \times 10^3\,\mathrm{V\,cm^{-1}}$, which corresponds to reverse bias voltages in the order of 100 V and above for the geometry of the bonded samples [10].

[7] The increase in drift velocity at the P-side contact (at ca. $-500\,\mu\mathrm{m}$) is due to the distortion of the electric field by the contact implant.

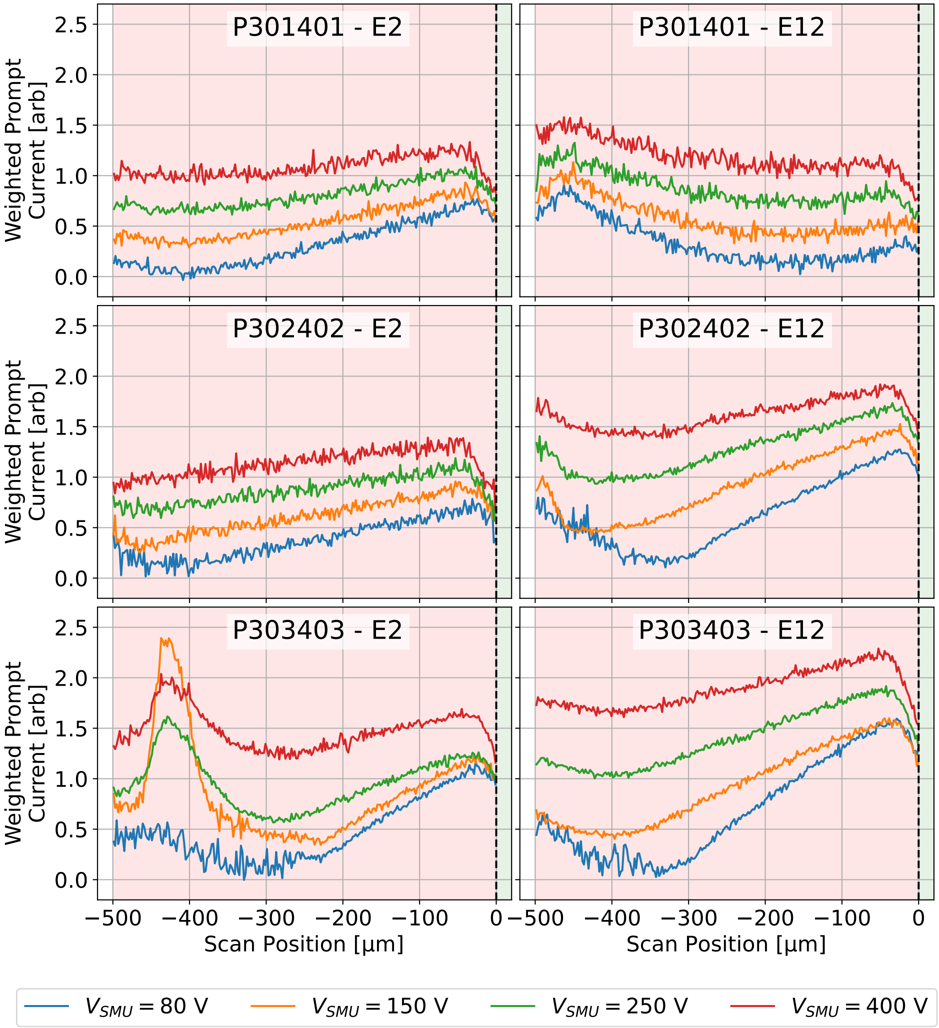

FIGURE 7.5: Weighted prompt current curves extracted from the edge TCT measurements of all six samples. The interface is located at $x = 0\,\mu m$. The curves are only calculated for the P-side as no signal is observed in the N-side. The curves of the different samples are normalized for better comparison.

with a decrease towards the bonding interface. **P303403-E3** shows a very strong peak in drift velocity in the bulk of the P-side. This behaviour is potentially attributed to accidental / parasitic doping of these samples during the processing of the wafers, linked to limited cleanliness control in the user cleanroom. The observed behaviour of these two samples strongly resembles the behaviour of irradiated sensors, exhibiting a double peak electric field due to doping inversion [128]. The exact source of the observed behaviour has not been investigated further and the two irregular samples are excluded from further analysis.[8] The irregular behaviour of these two samples can also be observed in the curves presented in figure 7.1. For both samples the curves recorded with the red laser illuminating the P-side show signal being recorded below the full P-side depletion voltage V_{Red}. All other sample show very little to no signal being collected at low bias voltages and a near vertical increase in collected signal at around V_{Red}.

7.3.1 *Critical interface defect density*

Investigating the precise microscopic behaviour of the amorphous layer at the bonding interface, including the present metal contamination, is beyond the scope of this thesis. But, as previously stated, based on the macroscopic observation of the one-sided depletion behaviour of the fabricated samples, one can conclude that the interface, overall, behaves like a layer with a high density of donor-like impurities. From the available data it is not possible to attribute this behaviour to either the amorphous silicon layer or to the contaminating metal elements. Therefore it is also not possible to draw any conclusions about the depletion behaviour of a P/N junction fabricated by bonding high resistivity wafers under ideal conditions, meaning without metal contamination. On the other hand, it is rather trivial to estimate the critical interface defect density which would lead to such a one-sided depletion of a bonded P/N junction. Assuming a P-side doping concentration of $N_A = 5 \times 10^{11}\,\mathrm{cm}^{-3}$ and a nominal P-side thickness of $d_P = 500\,\mu\mathrm{m}$ this critical interface defect density is

$$N_{I,crit} = d_P N_A = 2.5 \times 10^{10}\,\mathrm{cm}^{-2}. \tag{7.6}$$

---

[8] The curves of P302402-E2 presented in figure 7.3 show peculiar peaks and troughs, giving the impression that this sample also behaves irregularly. But these variations in signal stem from an imperfect polishing of the edge, leading to more or less laser light being absorbed by the sample. The sample shows a nominal depletion behaviour, as confirmed by the corresponding weighted prompt current analysis in figure 7.5.

This estimation assumes that all of these defects are active and of donor type. In section 5.1 the density of the metal contamination introduced at the interface due to the bonding process was measured to be in the order of $N_{Metal} > 1 \times 10^{14}\,\mathrm{cm}^{-2}$ and thus about four orders of magnitude higher than the estimated critical density. Therefore, even if only a fraction of the metal contaminants act as donor type defects, it is very plausible to attribute the observed one-sided depletion to the presence of this contamination. An equivalent estimation can of course also be made under the assumption that the interface is dominated by acceptor type defects, which could lead to a one-sided depletion of the N-side only.

These considerations show that, in the case of using high resistivity wafers, the depletion behaviour of a bonded P/N structure is very sensitive to low densities of interface defects acting as donors or acceptors. And it is possible that very low concentrations of metal or other contaminants are sufficient to provoke a modified depletion behaviour as observed here. As shown in section 5.2, total reflection X-ray fluorescence spectroscopy (TXRF) measurements revealed a small residual concentration of metal elements already present on the unbonded wafers. Thus, even with a perfect bonding process (using silicon coated panels), this could lead to a contamination of the bonding interface with a defect concentration high enough to influence the depletion behaviour. Such low contamination densities are usually also not detectable by energy-dispersive X-ray spectroscopy (EDXS) measurements, which are the standard process used to assess the chemical composition of the bonding interface.[9] On the other hand, the non-terminated silicon (Si) bonds of the amorphous layer might by themselves (in parts) act as donors or acceptor type defects and thus influence the depletion behaviour of high resistivity wafers without the need for any additional contamination. Overall, the assumption that a P/N junction fabricated via SAB will show the depletion behaviour predicted by the abrupt junction model is fallacious, especially in the case of using high resistivity wafers. Rather, the depletion behaviour of such structures needs to be investigated on a case by case basis.

---

[9] Very high count EDXS measurements can be sensitive to a mass fraction of ca. 0.01 % [102]. For a 3 nm thick bonding interface this would correspond to an iron contamination with a surface density of $\approx 1 \times 10^{12}\,\mathrm{cm}^{-2}$ at the interface.

8

SIMULATION OF TIME-DOMAIN SIGNALS

5 o'clock in the morning is a fine time to miau!
— Hilbert

A short introduction of simulating time-domain (transient) signals in semiconductor sensors using technology computer-aided design (TCAD) is given in the first section of this chapter. One major downside of simulating transient signals with TCAD is the long simulation time. As an alternative, time-domain signal can be simulated by using charge propagation and signal induction based on the Shockley-Ramo theorem. The second part of this chapter presents a simple charge propagation algorithm and gives a short overview of existing software frameworks for executing such simulations. In the third part, a simple simulation model for the fabricated bonded samples is presented, based on the principle of charge propagation. This model makes use of the extended Shockley-Ramo theorem (as presented in section 2.4) to correctly simulate the signals in samples with only partial depletion. The equivalent electrical front-end circuit model is discussed and a small review of the performance of the implemented simulation model is given.

CONTRIBUTION The overview of transient simulations via TCAD, as well as the overview of charge propagation based simulation, was written by the author based on existing literature and on his personal experience. The simple charge propagation based simulation model was written by the author from ground up.

8.1 TCAD BASED SIMULATIONS

This section is written from the perspective of a user of the Synopsys Sentaurus TCAD (Sentaurus) workbench[1] which is widely used in the particle physics community. The other major TCAD software suite is Silvaco TCAD (Silvaco)[2] which has a very similar scope as Sentaurus in the type

---

[1] Product website: `https://www.synopsys.com/silicon/tcad.html`.

[2] Product website: `https://silvaco.com/tcad/`.

of supported simulations and models. There exist various open-source TCAD software packages, such as DEVSIM[3], Archimedes[4] or NanoTCAD ViDES[5] to name a few.[6] But none of the open-source software packages offers the same wide application range as the commercial tools. Sentaurus and Silvaco are also heavily used in the semiconductor processing industry. The concepts described below apply to both of these software packages.

TCAD simulations are based on solving the differential equations which govern the electrical behaviour of semiconductors.[7] For transient signal simulations, one of the fundamental differential equations to be solved is the movement of charges inside the device, constrained by the continuity equations

$$\nabla \cdot \vec{J}_n = e(R_n - G_n) + e\frac{\partial n}{\partial t} \tag{8.1}$$

$$\nabla \cdot \vec{J}_p = e(R_p - G_p) + e\frac{\partial p}{\partial t} \tag{8.2}$$

for electrons ($\Box_n$) and holes ($\Box_p$). J_n and J_p denote the current densities, n and p the charge carrier densities, R_n and R_p the recombination rates and G_n and G_p the generation rates. The default transport model used in Sentaurus is the drift-diffusion model, which relates the current densities to the movement of charges via drift in an electric field and via diffusion. The drift-diffusion equations take the form[8]

$$\vec{J}_n = -e\mu_n n \nabla \Phi + eD_n \nabla n \tag{8.3}$$

$$\vec{J}_p = +e\mu_p p \nabla \Phi - eD_p \nabla p \tag{8.4}$$

with μ_n and μ_p the mobility of the charge carriers, Φ the electrostatic potential, and D_n and D_p the diffusion coefficients [130]. The set of fundamental

---

[3] Available at `https://devsim.org/`.

[4] Available at `https://www.gnu.org/software/archimedes/`.

[5] Available at `http://vides.nanotcad.com/vides/utilities/vides`.

[6] An extensive list of different (open-source) TCAD software packages is available at `https://tcadcentral.com`.

[7] In this context only the simulation of semiconductor devices with TCAD is discussed. Other types of TCAD simulations, such as fabrication process simulations, are not further discussed here.

[8] The equations presented here use a general formulation. The precise equations used by Sentaurus TCAD are available in the Sentaurus manual [129].

equations is completed by the Poisson's equation, relating the electrostatic potential to the excess charge density

$$\nabla \cdot (\epsilon \nabla \Phi) = e(n - p - N_D + N_A) \tag{8.5}$$

with ϵ the permittivity, and N_D and N_A the doping concentrations of the semiconductor [130]. Sentaurus also implements alternative charge transport models, such as the thermodynamic model, the hydrodynamic model and the Monte Carlo model, which can be activated depending on the device under investigation [129, 130]. It is exactly the large set of available models which makes TCAD software packages so powerful. This does not only include models for charge transport, but also models for various generation and recombination processes, mobility models, models for trapping of charges, models for tunnelling effects and many more. These models can be available for different types of semiconductor materials. Nevertheless, the largest and most complete set of models and default parameters exists for silicon (Si), it being the default material used for most modern semiconductor processes.

The set of differential equations, making up a model to be simulated, is solved using finite element analysis (FEA) and numerical integration in time. To apply FEA to the problem, the simulated device needs to be represented by a mesh. An example (2D) mesh of a device is shown in figure 8.1. The mesh is the result of the first step in a typical TCAD simulation chain. Using a CAD like program or a dedicated scripting language a geometrical 2D or 3D model of the device to be simulated is created. This step also involves assigning properties, such as the material type, and the doping type and concentration, to each region of the device. Further, the locations of the electrical contacts are defined. Based on this model, the TCAD software creates the desired mesh. The second step in the chain is the actual simulation based on the principle of FEA. To simulate time domain signals a transient simulation is carried out. But TCAD also offers the possibility of other types of simulations, such as stationary (DC), AC or noise simulations.

The main disadvantage of simulating transient current technique (TCT) time domain signals (and any transient signals) using TCAD is the high simulation time. The time necessary for solving the differential system using FEA for a single point in time is dependent on the number of nodes

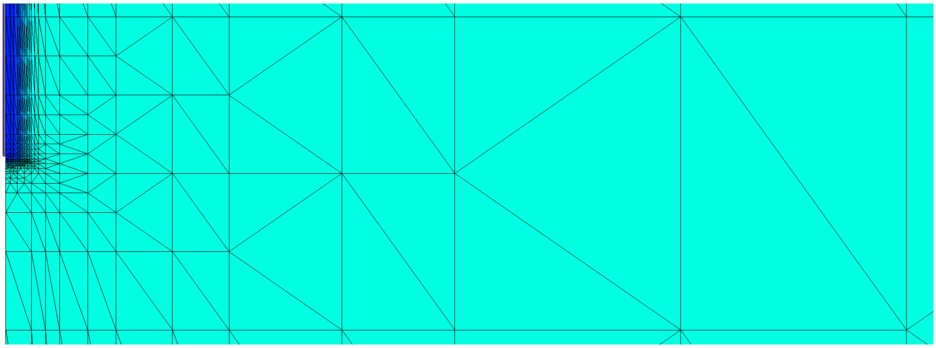

Figure 8.1: Example of the mesh created in Sentaurus TCAD at a corner of the P-side contact of a bonded diode. As there is a rapid change in doping concentration due to the contact doping, the mesh has been refined close to the contact. Within the bulk there is no change in doping and thus a coarser mesh can be used.

in the mesh. Thus, the more detailed a given structure is (leading to more mesh points) and the faster changes occur in time (leading more time steps necessary), the longer a transient TCAD simulation will take. It is not unheard of for individual transient TCAD simulations to take multiple minutes to days, especially when simulating transient signal using full 3D models [131]. This generally makes TCAD unsuitable for time domain TCT simulations with a large set of different simulation parameters, for example when trying to extract physical parameters from TCT measurements via fitting of template functions. Therefore, often the alternative approach of simulating time domain signals via propagation of charges is employed, which will be presented in the next section.

8.2 SIMULATION VIA CHARGE PROPAGATION

The simulation of time domain TCT signals via charge propagation is based on two underlying principles.[9] First, the electric field is assumed to be static within the the detector. This implies that the electric field does not change due to the presence and movement of the injected charges and that the electric field configuration is solely given by the (constant) detector bias.

---

[9] The exact same principles are of course also valid for real signal generated in sensors. The difference between real signals and TCT signals only lies in the way the free electron-hole pairs are created inside the detector.

And second, that the signal collected on the readout electrodes is given by the Shockley-Ramo theorem. The Shockley-Ramo theorem is discussed in detail in section 2.3.1.

8.2.1 *Simulation algorithm*

A simulation of time domain signals via charge propagation generally includes the following steps:

1. Calculation of the weighting field for the given detector geometry.
2. Calculation of the static electric field within the biased detector.
3. Definition of the number and initial position of the injected charges.
4. Propagation of the charges across the detector and calculation of the induced current via the Shockley-Ramo theorem.
5. Application of the electronics front-end response to the current signal.

In trivial cases it is possible to calculate the weighting field analytically, for example for highly symmetric or simple infinite plane geometries. Alternatively, TCAD or other FEA solvers are used to calculate the weighting field numerically. The same applies to the electric field within the detector. The distribution of charges created by the particle interaction can either be approximated analytically (for example a simple exponentially decaying distribution from a laser interaction) or simulation software such as Geant4[10] can be used to obtain more realistic charge creation profiles. The application of the electronics front-end response can be done via an additional electronics circuit simulation or, in simple cases, by convolution of the induced current signal with the step response of the electronics front-end.

The core of the simulation is the charge propagation, which essentially solves the following differential equation

$$\vec{x}_i(t) = \vec{x}_{s,i} + \int_0^t \vec{v}(\vec{x}_i(t'), q_i)dt' \tag{8.6}$$

---

[10] Geant4 is online available at `https://geant4.web.cern.ch/`.

where $\vec{x}_i(t)$ and q_i are the position and charge of an electron or hole i, and $\vec{x}_{s,i}$ is its starting location. The instantaneous velocity in the case of simulating drift only is given by

$$\vec{v}(\vec{x}, q) = \vec{E}(\vec{x})\, \mu(T, \vec{E}(\vec{x}))\, \mathrm{sgn}(q), \tag{8.7}$$

based on the local electric field $\vec{E}$ and the mobility $\mu(T, \vec{E})$ of the given charge type. In this example the mobility is dependent on the (constant) temperature T as well as the local electric field in order to account for velocity saturation occurring at high electric fields [17]. Models where the mobility depends on the doping concentration are also possible [129], as well as assuming a constant mobility for simple cases. More elaborate simulation models modify the velocity term by adding a random component to model the effect of the diffusion of charges. The end time of a simulation is usually determined dynamically by taking into account various factors, such as a set maximum integration time, the charge reaching a boundary, or potentially recombination or trapping of charges. Based on $\vec{x}_i(t)$, the current induced on a given readout electrode can then be calculated using the Shockley-Ramo theorem as

$$I_{ind}(t) = \sum q_i\, \vec{v}(\vec{x}_i(t), q_i) \cdot \vec{W}_F(\vec{x}_i(t)) \tag{8.8}$$

by summing over all free charges, and with $\vec{W}_F$ the weighting field corresponding to the readout electrode of interest.

The numerical calculation of the integral shown in (8.6) is usually carried out in an iterative way using discrete time steps. In addition, charges are usually not propagated individually but as charge packets, where the charges in each packet have the same starting position and charge type. The choice of how many charges to group into a packet is a trade off between the accuracy and the speed of the simulation (see also section 8.3.5.1). Especially when including diffusion in the simulation, having too few charge packets can lead to erroneous results, as all charges in a packet would undergo the same diffusion. The pseudo-code version of a charge propagation algorithm is shown in listing 8.1. The example algorithm propagates all charge packets in parallel and directly calculates the induced current within the iterative loop. It does not use a fixed time step but rather a fixed maximum propagation distance Δx for improved accuracy. Therefore the applied time step is calculated based on the maximum charge velocity and the set propagation distance.

Listing 8.1: Pseudo code version of a simple charge propagation algorithm for time domain signal simulations.

```
$\vec{x}_i$ := Starting position of charge packet $i$
$q_i$ := Total charge of packet $i$
$\Delta x$ := Fixed maximum propagation distance
$j$ := 0
$t_curr$ := 0

while $t_{curr}$ < $t_{max}$ do
  $\vec{v}_i$ := v($\vec{x}_i$, $q_i$)

  $I_{ind}$ := $\sum q_i \vec{v}_i \cdot \vec{W}_F(\vec{x}_i)$

  $v_{max}$ := max($|\vec{v}_i|$)
  $\Delta t$ := $\Delta x / v_{max}$
  $\vec{x}_i$ := $\vec{x}_i + \vec{v}_i \Delta t$
  Remove charges outside of boundaries

  $t_{curr}$ := $t_{curr} + \Delta t$
  $t_j$ := $t_{curr}$
  $signal_j$ := $I_{ind}$
  $j$ := $j + 1$
end while
```

As stated, the main advantage of simulating time domain signals via charge propagation over a simulation using TCAD is the time necessary for running the simulation. This is illustrated by some performance tests that had been carried out in the context of the TIMESPOT project simulating 3D silicon sensors using TCAD and a dedicated charge propagation simulation software (see also section 8.2.2). A single charge propagation simulation took less than 1 s, whereas an equivalent transient TCAD simulation took over 30 h [131]. On the other hand, the main limitations of the charge propagation simulation come from the simplicity of this approach. Any effect going beyond the simple drift of charges in an electric field needs to be implemented as a special addition to the simulation model. This includes concepts such as diffusion of charges, generation and recombination of charges, and trapping and de-trapping of charges. In contrast, the established TCAD software tools include models for these effects out of the box. Some of the existing charge propagation frameworks, presented in section 8.2.2, also implement certain or all of these concepts as an extension to the simple algorithm presented here. Another effect which is not trivial to implement in charge propagation is the plasma effect. When a high density of charges is created locally inside a sensor, the presence of these free charges modifies the local electric field, leading to a shielding of the imposed drift field. For example the interaction of α particles can lead to such clouds with very high charge densities. The resulting signal has a slower rise time and a wider pulse width, because the core of the deposited charge cloud initially does not drift due to being shielded from the drift field. Only the edges of the charge cloud are removed by the drift field, which gradually reduces the size of the initial charge cloud. The delay is often characterized by a plasma time t_P [10, 132]. Charge propagation simulations do not trivially model this effect, as, per construction, the electric field in the simulation is assumed to not be affected by the presence of the injected charges.

It should be noted that the principle of simulating time domain signals via charge propagation does not only apply to semiconductor detectors, but more generally to any type of sensor where signal is induced from the drift of charges. Especially gaseous detectors, such as micromesh gaseous detectors (MICROMEGAS) or resistive plate chambers (RPC) detectors are commonly simulated using the same principle. The next section will briefly present some existing charge propagation software packages, some of which were explicitly developed for simulating gaseous detectors.

8.2.2 *Existing simulation frameworks*

Time domain signal simulation via charge propagation is implemented in various existing simulation frameworks and software packages:

AP2 Allpix Squared (AP2)[11] is a modular framework for the end-to-end simulation of radiation detectors [133]. The particle interaction is simulated via Geant4. Modules of varying complexity are available for the propagation and collection of charges within the detector. The *TransientPropagation* module implements signal induction via the Shockley-Ramo theorem as described in this section. It makes use of a fourth-order Runga-Kutta-Fehlberg method for solving the integral in (8.6) [134]. Electric field maps and weighting fields generated with external tools (such as TCAD) can be imported. It further allows to simulate various electronics frontends and digitization methods.

GARFIELD++ Garfield++[12] is a C++ port of the original Garfield FORTRAN toolkit for the simulation of gaseous detectors [135]. Garfield++ added the possibility of simulating semiconductor detectors, but the main area of application currently is micropattern gaseous detectors. The *AvalancheMV* and *Sensor* classes implement charge propagation and signal induction as previously described. Electric field maps and weighting fields generated with various external tools can be imported.

WEIGHTFIELD2 Weightfield2[13] is a 2D simulator for silicon and diamond detectors [136]. Its main use case is to simulate the signal within strip detectors and the program does not have any flexibility to simulate other types of detector geometries. The electric field and the weighting field are calculated on a fixed grid within the software package. It solves the charge propagation integral via simple integration as discussed before.

---

[11] AP2 is available at `https://allpix-squared.docs.cern.ch/`.

[12] Garfield++ is available at `https://garfieldpp.web.cern.ch/garfieldpp/`.

[13] Weightfield2 is available at `http://personalpages.to.infn.it/~cartigli/Weightfield2/`.

KDETSIM KDetSim[14] was specifically created to make reference simulations for TCT measurements [137]. It can simulate detector geometries in 1D, 2D and 3D space, for certain predefined detector structures (including pad, strip, pixel and 3D detectors). The electric field and the weighting field are calculated on an orthogonal mesh within the software framework. The charge propagation integral is solved using a fixed step size in space.

TRACS TRACS[15] is very similar in scope to Weightfield2, its main purpose being the 2D simulation of strip and pad detectors [138]. The electric field and weighting fields are calculated as part of the software package. Its main distinction compared to other simulation packages is the inherent multi-threading, which allows to use TRACS to fit measured curves via repetitive simulation. The charge propagation is implemented using a fourth-order Runga-Kutta integration method.

TCODE TimeSPOT Code for Detector simulation (TCode)[16] is a program developed for the simulation of 3D sensors in the context of the TIMESPOT collaboration [139]. The program works with simple configuration files and the electric field and the weighting field need to be provided from external tools. The charge propagation integral is solved via a fourth-order Runga-Kutta method.

A full and detailed comparison between all these software packages is beyond the scope of this work. A comparison between KDetSim, TRACS and Weightfield2 can be found in [140].

8.3 SIMULATION MODEL FOR BONDED DIODES

Based on the principle of charge propagation as presented in this chapter, a Python based simulation model is implemented for the bonded P/N samples fabricated as part of this thesis. The main goal of this model is to enable very fast and fully parametrized simulations of time-domain TCT signals, and thus to allow for fitting of curves via manual adjustments of parameters. Simulating a TCT curve takes approximately 0.5 - 1 s with the implemented model. The Python implementation combined with the

---

[14] KDetSim is available at `https://www-f9.ijs.si/~gregor/KDetSim/`.

[15] TRACS is available at `https://github.com/IFCA-HEP/TRACS`.

[16] TCode is available at `https://github.com/MultithreadCorner/TCode`.

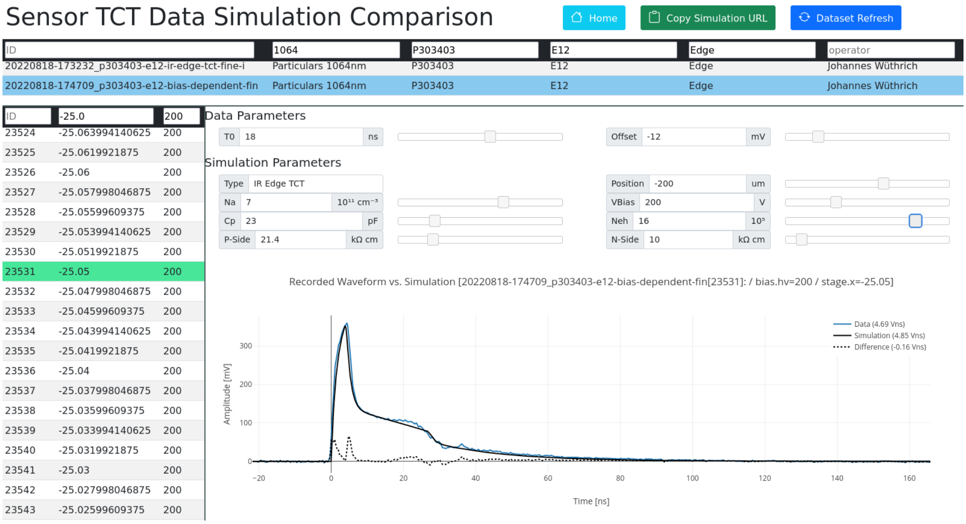

Sensor TCT Data Simulation Comparison

ID	1064	P303403	E12	Edge	operator
20220818-173232_p303403-e12-ir-edge-tct-fine-i	Particulars 1064nm	P303403	E12	Edge	Johannes Wüthrich
20220818-174709_p303403-e12-bias-dependent-fin	Particulars 1064nm	P303403	E12	Edge	Johannes Wüthrich

ID	-25.0	200
23524	-25.063994140625	200
23525	-25.0619921875	200
23526	-25.06	200
23527	-25.057998046875	200
23528	-25.05599609375	200
23529	-25.053994140625	200
23530	-25.0519921875	200
23531	-25.05	200
23532	-25.047998046875	200
23533	-25.04599609375	200
23534	-25.043994140625	200
23535	-25.0419921875	200
23536	-25.04	200
23537	-25.037998046875	200
23538	-25.03599609375	200
23539	-25.033994140625	200
23540	-25.0319921875	200
23541	-25.03	200
23542	-25.027998046875	200
23543	-25.02599609375	200

Data Parameters

T0 18 ns
Offset -12 mV

Simulation Parameters

Type IR Edge TCT
Na 7 10^{11} cm⁻³
Cp 23 pF
P-Side 21.4 kΩ cm
Position -200 um
VBias 200 V
Neh 16 10^5
N-Side 10 kΩ cm

Recorded Waveform vs. Simulation [20220818-174709_p303403-e12-bias-dependent-fin[23531]: / bias.hv=200 / stage.x=-25.05]

FIGURE 8.2: View of the online simulation interface, allowing to directly compare individual measured TCT curves with results from the charge propagation simulation model presented in this chapter. The fast (< 1 s) simulation time allows for direct user interaction and the fitting of curves by manually adjusting the model parameters.

short simulation time allow to integrate the simulation into the online data analysis utility (see section 6.2.3). This allows to directly compare measured TCT curves with simulated curves, while having freely adjustable model parameters. A view of the online simulation interface is shown in figure 8.2. This simulation model is not based on an existing simulation framework, but implemented using the Python programming language making use of the NumPy [141] and SciPy [142] libraries.[17]

The simulation model is specifically implemented for the bonded diodes fabricated as part of this thesis. Thus, it takes the observed asymmetric depletion behaviour into account by using the empirical P/N++/N model where only the P-side of the fabricated structures is being depleted (see

---

[17] An initial version was created using the Pandas library [143, 144]. Pandas offers a lot of very convenient functionality, but this convenience comes at a large processing overhead. This leads to Pandas DataFrame operations being ten times or more slower than equivalent operations using pure NumPy [145]. Therefore the final implementation uses only NumPy data structures.

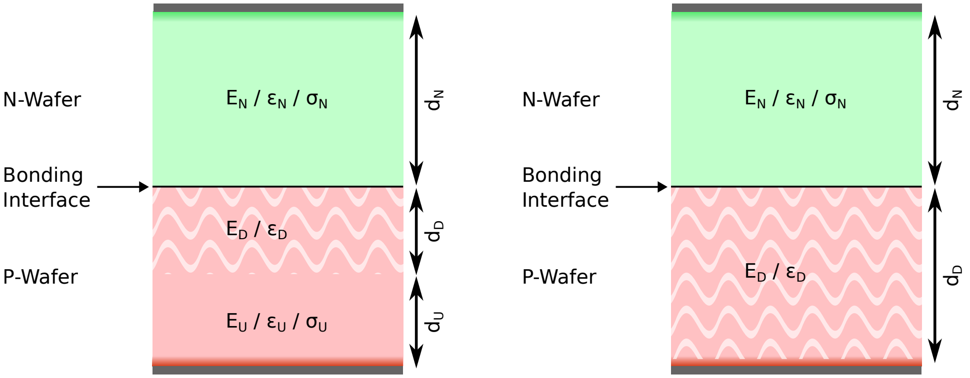

(a) Case A: Partially depleted P-side (b) Case B: Fully depleted P-side

FIGURE 8.3: Schematic view of the two cases taken into account for the charge propagation simulation model of the fabricated bonded diodes. The depleted (non-conductive) layer is indicated by the white wave pattern. The remaining layers are non-depleted (conductive).

chapter 7). The N-side is always considered non-depleted and no drift occurs within this side of the structure. Two cases need to be distinguished:

CASE A The P-side is not fully depleted. This leads to one non-conductive layer, the depleted region of the P-side, being sandwiched between two conductive layers, the N-side and the non-depleted part of the P-side.

CASE B The P-side is fully depleted. In this case there are only two layers, the conductive N-side and the non-conductive P-side.

Both cases are schematically shown in figure 8.3. Given that the contacts of the fabricated pad diodes are much larger than the total thickness of the structure ($L_C \gg d$), the contacts are approximated as infinite planes and the problem is considered to be one-dimensional.

The simulation is implemented by the following high-level calculation steps:

1. Generation of a distribution of injected charges, according to the type of interaction to be simulated.
   The distribution is calculated in N discrete bins (charge packets), and results in two lists x_i and q_i representing the position and total charge of each packet.

2. Propagation of the charge packets and calculation of the induced current according to the traditional Shockley-Ramo theorem.
   The algorithm shown in listing 8.1 is used. The result of this step is the series $(t_j^{'}, i_j^{'})$ representing the time and induced current of each simulation step.

3. Resampling of the uneven time sequence $(t_j^{'}, i_j^{'})$ into evenly space samples separated by $\Delta t = 50\,\mathrm{ps}$.
   The Δt was chosen to be equal with the TCT oscilloscope sampling time. The result is the evenly spaced sequence (t_j, i_j)

4. Application of the delayed response due to the conductive medium (extended Shockley-Ramo theorem) via convolution with the reduced weighting vector.
   See section 8.3.3 for details. The result is the series (t_j, I_j).

5. Application of the equivalent electronics circuit response via a convolution of its impulse response.
   The result is the series (t_j, V_j), where V_j is the simulated voltage signal recorded by the TCT oscilloscope.

The electric field, the mobility model, the extended Shockley-Ramo weighting vector and the equivalent electronics response are all calculated analytically and are documented in the following sections.

8.3.1 *Physical models*

8.3.1.1 *Geometry*

As stated, the simulation is carried out in 1D. The bonding interface is set to be at position $x_I = 0\,\mu\mathrm{m}$. The average thickness of the P-type wafers (after CMP) is $d_P \approx 503\,\mu\mathrm{m}$ and the P-side contact is thus placed at $x_P = -503\,\mu\mathrm{m}$. Given the average thickness of the N-type wafers (after CMP) of $d_N \approx 490\,\mu\mathrm{m}$ the N-side contact is placed at $x_N = 490\,\mu\mathrm{m}$. The P-side contact is assumed to be grounded $V(x_P) = 0\,\mathrm{V}$ and for reverse biasing the P/N junction a positive bias voltage is applied to the N-side contact $V(x_N) = V_{Bias}$. Both the P- and N-side are assumed to have uniform properties, with a constant permittivity $\epsilon_P = \epsilon_N = \epsilon_{Si}\epsilon_0$, constant conductivities σ_N and σ_P, and constant doping levels N_A and N_D for the P- and N-Side respectively.

8.3.1.2 *Injected charge distribution*

The following charge distributions are implemented, representing different types of charge injection modes.

RED LASER (TOP) Charge injection via the red laser ($\lambda_{Red} = 660\,\mathrm{nm}$) from the top or bottom surface. The resulting distribution takes the form of an exponential decay with an attenuation length $\mu_{Red} \approx 3.42\,\mu\mathrm{m}$.[18]

IR LASER (TOP) Charge injection via the IR laser ($\lambda_{IR} = 1064\,\mathrm{nm}$) from the top or bottom surface. The resulting distribution takes the form of an exponential decay with an attenuation length $\mu_{IR} \approx 1.03\,\mathrm{mm}$.[19]

IR LASER (EDGE) Charge injection via the IR laser in edge TCT mode. The resulting distribution is Gaussian shaped due to the Gaussian beam shape with $\sigma_{IR} \approx 10\,\mu\mathrm{m}$. [20]

α INTERACTION Charge injection via α particles (from an Am-241 source). The resulting distribution takes the shape of a Bortfeld distribution [148]. Its integral and the location of the peak are dependent on the α energy and are determined via SRIM simulations (see section 9.1.1).[21]

The different distribution shapes are illustrated in figure 8.4.

8.3.1.3 *Electric field*

Given the empirical P/N++/N model the electrical field within the N-side is assumed to be zero by construction, and thus

$$E(x) = 0\,\mathrm{V\,m^{-1}} \text{ for } x > x_I. \tag{8.9}$$

For the electric field within the P-side the two cases (A and B shown in figure 8.3) have to be considered separately. The depletion width in function of reverse bias for an abrupt P/N++ junction is given by

$$W_{dep} = \sqrt{\frac{2\epsilon_{Si}\epsilon_0}{eN_A} V_{Bias}} \ \text{[10]}, \tag{8.10}$$

---

[18] Calculated for silicon via `https://refractiveindex.info/` based on [146].

[19] Calculated for silicon via `https://refractiveindex.info/` based on [147].

[20] As determined by the laser focusing procedure via a knife edge scan.

[21] Using the *pybragg* Python package, available at `https://github.com/flome/pybragg`.

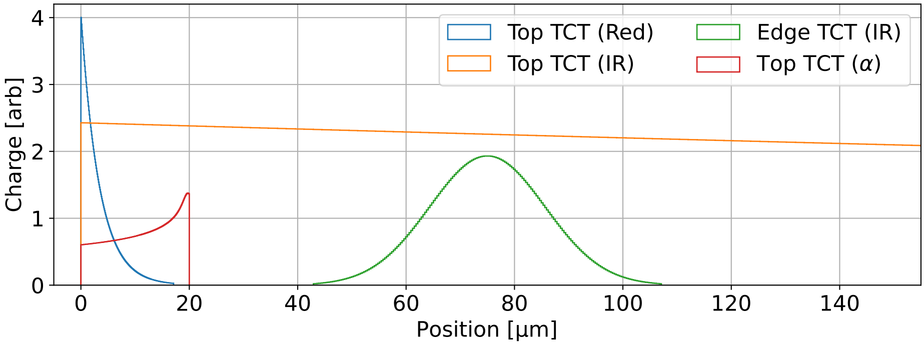

FIGURE 8.4: Shapes of the different deposited charge distributions, implemented as described in the text. In this plot the top surface is at 0 µm. All curves have an arbitrary scaling factor for better visual comparison.

as the N++ region is assumed to be infinitesimally small and thus no voltage drop occurs across this region. The voltage necessary for fully depleting[22] the P-side is given by

$$V_{dep} = \frac{eN_A}{2\epsilon_{Si}\epsilon_0} d_P^2. \tag{8.11}$$

Accordingly, for reverse bias voltages $V_{Bias} < V_{dep}$ case A (partially depleted P-side) and for $V_{bias} \geq V_{dep}$ case B (fully depleted P-side) applies.

Within the depleted region a constant fixed charge density of $\rho_D = -eN_A$ is present. The electric field is calculated by solving the one dimensional Poisson's equations

$$\frac{d^2V}{dx^2} = -\frac{\rho(x)}{\epsilon_{Si}\epsilon_0} \tag{8.12}$$

with $V(x_P) = 0\,\mathrm{V}$ and $V(x_I) = V_{Bias}$.

---

[22] This model ignores the presence of the contact doping, which leads to a thin undepleted layer just below the contact metallization.

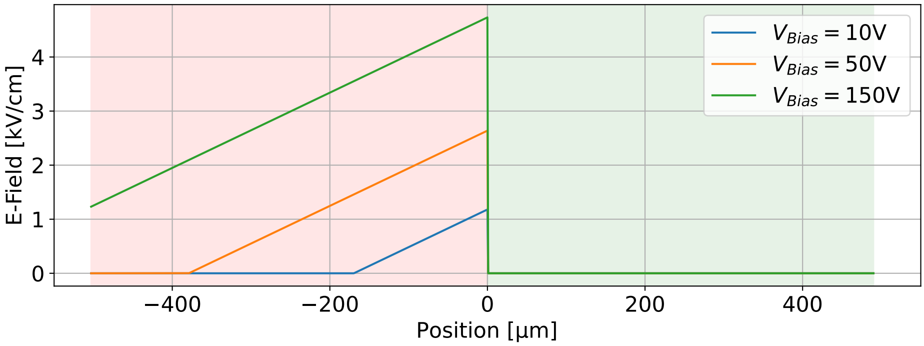

FIGURE 8.5: Example electric field configurations at various bias voltages. To generate the example curves the P-side full depletion voltage is assumed to be 88 V, which correspond to a P-side doping of $N_A \approx 4.5 \times 10^{11}\,\mathrm{cm}^{-2}$. The bonding interface is located at $x = 0\,\mu$m.

CASE A In case A the depletion region extends from $x_D = -W_{dep}$ to x_I. Thus $\rho(x)$ and $E(x)$ are given by

$$\rho(x) = \begin{cases} 0, & \text{for } x_P \leq x \leq x_D \\ -eN_A, & \text{for } x_D < x \leq x_I \end{cases} \tag{8.13}$$

$$E(x) = \begin{cases} 0, & \text{for } x_P \leq x \leq x_D \\ -\frac{eN_A}{\epsilon_{Si}\epsilon}(x - x_D), & \text{for } x_D < x \leq x_I \end{cases} \tag{8.14}$$

CASE B In case B the depletion region extends across the entire P-side from x_P to x_I. Thus $\rho(x)$ and $E(x)$ are given by

$$\rho(x) = -eN_A, \text{ for } x_P < x \leq x_I \tag{8.15}$$

$$E(x) = -\frac{V_{Bias} - V_{dep}}{d_P} - \frac{eN_A}{\epsilon_{Si}\epsilon}(x - x_D), \text{ for } x_P < x \leq x_I \tag{8.16}$$

Some example E-field configurations are shown in figure 8.5 for both cases A and B.

8.3.1.4 *Mobility model*

The simulation implements a temperature and E-field dependent mobility model. Given the high bias voltages necessary for fully depleting the P-side,

	Electrons	**Holes**	**Unit**
μ_L	1417	470.5	$\mathrm{cm^2\,V^{-1}\,s^{-1}}$
ζ	2.5	2.2	1
$v_{sat,0}$	$1.07 \cdot 10^7$	$8.37 \cdot 10^6$	$\mathrm{cm\,s^{-1}}$
$v_{sat,exp}$	0.87	0.52	1
β_0	1.109	1.213	1
β_{exp}	0.66	0.17	1
T_{ref}	300	300	K

TABLE 8.1: Parameters of the implemented field dependent mobility model. Based on [129, 134].

an E-field dependent mobility model is necessary to account for velocity saturation. Due to the low bulk doping concentration of the fabricated samples, doping dependency of the mobility is not considered.[23] The temperature dependent constant mobility is given by a phonon-scattering model [150] as

$$\mu_{const}(T) = \mu_L \left(\frac{T}{T_{ref}}\right)^{-\zeta}. \tag{8.17}$$

The saturation velocity of charge carriers is given by the Canali velocity saturation model

$$v_{sat}(T) = v_{sat,0} \left(\frac{T}{T_{ref}}\right)^{-v_{sat,exp}}. \tag{8.18}$$

Finally, the temperature and E-field dependent mobility is given by the extended Canali high-field saturation model [151]

$$\beta = \beta_0 \left(\frac{T}{T_{ref}}\right)^{\beta_{exp}} \tag{8.19}$$

$$\mu(T, E) = \frac{\mu_{const}(T)}{\left[1 + \left(\frac{\mu_{const}(T)\cdot E}{v_{sat}(T)}\right)^{\beta}\right]^{\frac{1}{\beta}}} \tag{8.20}$$

The parameters for both electrons and holes are listed in table 8.1. The implemented model represents the default mobility model for silicon employed in

---

[23] The dependence of the mobility on the doping only becomes relevant for doping concentrations of ca. $1 \times 10^{15}\,\mathrm{cm^{-3}}$ and above [149].

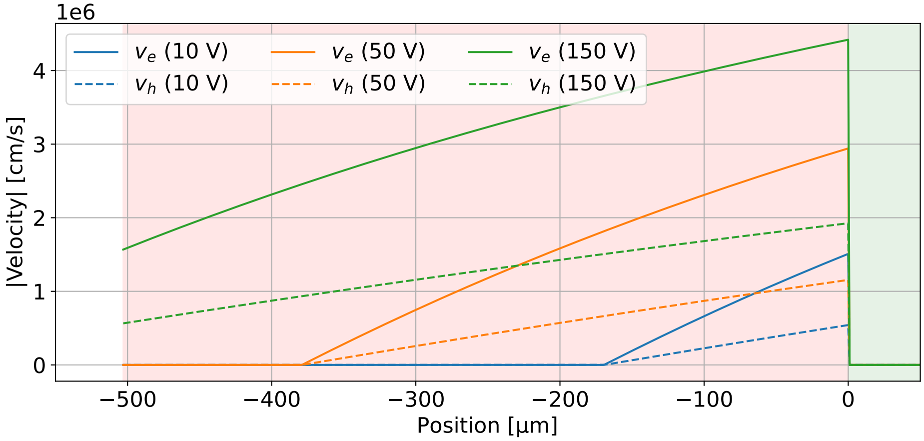

FIGURE 8.6: Electron (v_e) and hole (v_h) drift velocities in the case of the E-field configurations shown in figure 8.5. At low bias voltages the velocities increase linearly towards the interface indicating that no velocity saturation is occurring. At high bias voltages the velocity curves exhibit a pronounced curvature indicating a dependency of the mobility on the electric field.

Sentaurus [129]. It is equivalent to the default mobility model implemented in AP2 [134]. The effect of the velocity saturation is highlighted in figure 8.6.

8.3.2 *Weighting vectors*

To calculate the weighting vectors the P-side contact is assumed to be at ground and the signal is collected on the N-side contact.[24] The case B is more trivial and is thus presented first. The derivation for both cases is summarized here and the full mathematical derivation is given in the appendix B. In the following derivation $\epsilon = \epsilon_{Si}\epsilon_0$, with $\epsilon_{Si} = 11.68$ the relative permittivity of silicon.

---

[24] In the case of a trivial 1D structure with two opposite contacts, the form of the weighting vector is the same for both contacts, one having the opposite sign of the other.

CASE B: FULLY DEPLETED P-SIDE The schematic representation is shown in figure 8.3b. In the electrostatic case, the voltage across the device can directly be expressed in function of the electric fields as

$$V = d_N E_N + d_D E_D \tag{8.21}$$

given that ϵ_N and ϵ_D are constant within their respective regions. The continuity of the displacement field at the interface between the two regions leads to

$$D_N = D_D \quad \Rightarrow \quad \epsilon_N E_N = \epsilon_D E_D. \tag{8.22}$$

Inserting this into (8.21) leads to

$$E_D = \frac{V}{d_D + d_N \frac{\epsilon_D}{\epsilon_N}} = \frac{\epsilon_N V}{d_D \epsilon_N + d_N \epsilon_D}. \tag{8.23}$$

To find the time-dependent weighting vector, the concept presented in section 2.4 is used, applying a voltage pulse $\mathcal{L}\{V_0 \delta(t)\} = V_0$ and replacing $\epsilon_N = \epsilon + \frac{\sigma_N}{s}$ and $\epsilon_D = \epsilon$ in the Laplace domain. The weighting vector within the active (depleted) region is thus given by

$$\begin{aligned} W_V(s) = E_D(s)|_{V:=V_0} &= V_0 \frac{\epsilon + \frac{\sigma_N}{s}}{d_D \epsilon + d_D \frac{\sigma_N}{s} + d_N \epsilon} \\ &= \frac{V_0}{d}\left(1 + \frac{d_N}{d_D}\frac{1}{\tau}\frac{1}{s + \frac{1}{\tau}}\right) \end{aligned} \tag{8.24}$$

with $d := d_N + d_D$ and $\tau = \frac{d\epsilon}{d_D \sigma_N}$. Applying the inverse Laplace transform leads to the desired time domain weighting vector

$$W_V(t) = \mathcal{L}^{-1}[W_V(s)] = \frac{V_0}{d}\left(\delta(t) + \frac{d_N}{d_D}\frac{1}{\tau} e^{-\frac{t}{\tau}} \Theta(t)\right) \tag{8.25}$$

with $\Theta(t)$ the Heaviside step function.

CASE A: PARTIALLY DEPLETED P-SIDE The schematic representation is shown in figure 8.3a. The derivation of case A is similar to case B, but with an additional layer, the non depleted part of the P-side. Thus the voltage across the device is given by

$$V = E_U d_U + E_D d_D + E_N d_N, \tag{8.26}$$

and the continuity of the displacement field between the three regions gives

$$D_D = D_N \quad \Rightarrow \quad \epsilon_D E_D = \epsilon_N E_N \ \text{ and} \tag{8.27}$$

$$D_D = D_U \quad \Rightarrow \quad \epsilon_D E_D = \epsilon_U E_U. \tag{8.28}$$

This leads to an electric field within the active region of

$$E_D = \frac{V}{d_D + d_U \frac{\epsilon_D}{\epsilon_U} + d_N \frac{\epsilon_D}{\epsilon_N}} = \frac{\epsilon_U \epsilon_N V}{d_D \epsilon_U \epsilon_N + d_U \epsilon_N \epsilon_D + d_N \epsilon_U \epsilon_D}. \tag{8.29}$$

Again, applying a voltage pulse $\mathcal{L}[V_0 \delta(t)] = V_0$ and replacing $\epsilon_N = \epsilon + \frac{\sigma_N}{s}$, $\epsilon_U = \epsilon + \frac{\sigma_P}{s}$ and $\epsilon_D = \epsilon$ leads to

$$\begin{aligned} W_V(s) &= E_D(s)|_{V:=V_0} \\ &= V_0 \frac{(\epsilon s + \sigma_P)(\epsilon s + \sigma_N)}{(\epsilon s + \sigma_P)(\epsilon s + \sigma_N) d_D + \epsilon s d_U (\epsilon s + \sigma_N) + \epsilon s d_N (\epsilon + \sigma_P)}. \end{aligned} \tag{8.30}$$

It can be shown that this is equivalent to

$$W_V(s) = \frac{V_0}{d} \left(1 + \frac{b}{\tau_1} \frac{1}{s + \frac{1}{\tau_1}} + \frac{c}{\tau_2} \frac{1}{s + \frac{1}{\tau_2}} \right) \tag{8.31}$$

with $d := d_D + d_U + d_N$ and

$$\begin{aligned} \lambda_{1,2} &= \frac{(d - d_N)\sigma_N + (d - d_U)\sigma_P}{2d} \\ &\mp \frac{\sqrt{((d - d_N)\sigma_N + (d - d_U)\sigma_P)^2 - 4 d_D d \sigma_P \sigma_N}}{2d}, \end{aligned} \tag{8.32}$$

$$\tau_1 = \frac{\epsilon}{\lambda_1}, \tag{8.33}$$

$$\tau_2 = \frac{\epsilon}{\lambda_2}, \tag{8.34}$$

and b and c the solution of the following linear system

$$\begin{pmatrix} \lambda_1 & \lambda_2 \\ 1 & 1 \end{pmatrix} \begin{pmatrix} b \\ c \end{pmatrix} = \begin{pmatrix} \frac{d_N}{d}\sigma_N + \frac{d_U}{d}\sigma_P \\ \frac{d_U}{d_D} + \frac{d_P}{d_D} \end{pmatrix}. \tag{8.35}$$

Applying the inverse Laplace transform to (8.31) is trivial and leads to

$$W_V(t) = \mathcal{L}^{-1}[W_V(s)] = \frac{V_0}{d} \left(\delta(t) + b \frac{1}{\tau_1} e^{-\frac{t}{\tau_1}} \Theta(t) + c \frac{1}{\tau_2} e^{-\frac{t}{\tau_2}} \Theta(t) \right) \tag{8.36}$$

It should be noted, that the expression for $W_V(t)$ for both cases contains a Dirac $\delta(t)$ term corresponding to the current induced directly by the drifting charges, as well as one exponential term per conductive layer.

8.3.3 *Application of the extended Shockley-Ramo theorem via convolution*

According to (2.18), in the case of the extended Shockley-Ramo theorem the current induced by moving electrons and holes is given by

$$I^{ind}_{e,h}(t) = -\frac{q_{e,h}}{V_0}\int_0^t \vec{W}_V[\vec{x}_{e,h}(t'), t-t']\vec{v}_{e,h}(t')dt'. \tag{8.37}$$

In the specific case of the bonded pad diodes the following observations hold:

- the problem is purely one-dimensional,
- the weighting vector W_V only depends on t and is constant in x,
- it can be expressed as $W_V(t) = \frac{V_0}{d}\hat{W}_V(t)$ with $\hat{W}_V(t<0) = 0$,
- and no drift happens before $t = 0$ and thus $v_{e,h}(t<0) = 0$.

Thus

$$\begin{aligned} I^{ind}_{e,h}(t) &= -\frac{q_{e,h}}{V_0}\int_0^t W_V(t-t')v_{e,h}(t')dt' \\ &= -\frac{q_{e,h}}{V_0}\int_{-\infty}^{\infty} \frac{V_0}{d}\hat{W}_V(t-t')v_{e,h}(t')dt' \\ &= -\int_{-\infty}^{\infty} \hat{W}_V(t-t')\left(\frac{q_{e,h}}{d}v_{e,h}(t')\right)dt' \end{aligned} \tag{8.38}$$

The second term inside the integral is equal to the current induced in a pad diode according to the classic Shockley-Ramo theorem.[25] Thus, one can first calculate the current induced according to the traditional Shockley-Ramo theorem $i'_{e,h}(t)$. In the case of the bonded diodes the current induced by the extended Shockley-Ramo theorem can then be calculated by a convolution of $i'_{e,h}(t)$ with the reduced weighting vector, defined as

$$\hat{W}_V(t) = \frac{d}{V_0}W_V(t). \tag{8.39}$$

The reduced weighting vector encapsulates the response of the conductive layers to the drifting charges. Figure 8.7 shows the form of the reduced weighting vector $\hat{W}_V$ for case B and for multiple depletion widths in case A, for the geometry described before and using reasonable substrate conductivity values. It is clearly visible that the case B is the limit of case A when the P-side fully depletes ($d_D \rightarrow d_P$) as one would expect.

---

[25] The negative sign is present or not, according to if the current flowing into or out of the electrode is calculated.

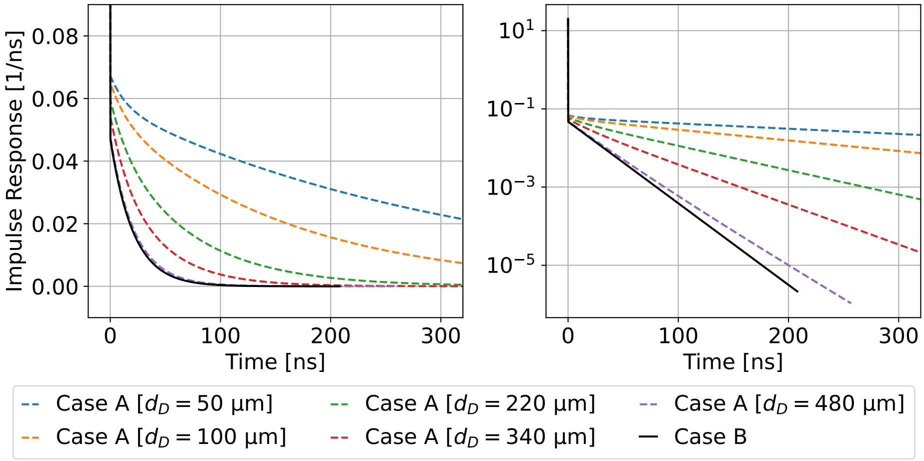

FIGURE 8.7: Shape of the reduced weighting vector $\hat{W}_V(t)$ for various cases of partial depletions of the P-side (case A) and for the full depletion of the P-side (case B). The curves are calculate with $\rho_P \approx 20\,\mathrm{k\Omega\,cm}$ and $\rho_N \approx 10\,\mathrm{k\Omega\,cm}$, which are reasonable values representing the fabricated samples (see table 4.3).

8.3.4 *Electronics equivalent circuit*

The equivalent electrical circuit describing the detector and the front-end electronics is made up of three components: the equivalent impedance Z_S of the sample, the parasitic capacitance C_H of the sample holder,[26] and the input impedance $R_L = 50\,\Omega$ of the amplifier.[27] The simple 1D structure of the diode sample can be represented by discrete resistances and capacitances: a depleted layer is represented by a single capacitance and a conductive layer is represented by a capacitance in parallel with a resistance [19]. Figure 8.8 shows the equivalent circuits for both cases A and B. The capacitance and resistance values of the equivalent sensor circuits are given by

$$C_\square = \epsilon_{Si}\epsilon_0 \frac{A}{d_\square} \quad \text{and} \quad R_\square = \rho_\square \frac{d_\square}{A} \tag{8.40}$$

---

[26] For a discussion of the sample holder capacitance see section 6.3.

[27] The effect of the coaxial cable between the sample and the amplifier, acting as a $50\,\Omega$ transmission line with attenuation, is accounted for by a modified gain value of the amplifier (see section 6.2.1.3).

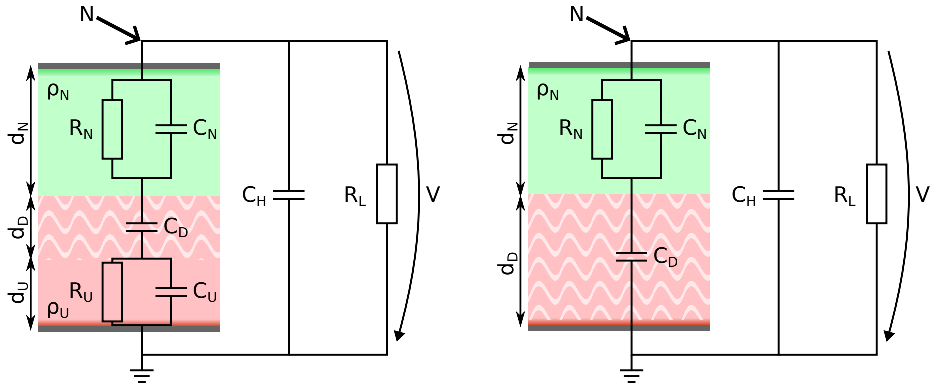

(a) Case A: Partially depleted P-side (b) Case B: Fully depleted P-side

FIGURE 8.8: Equivalent circuit model of the sensor and the front-end electronics of the TCT system. C_H is the parasitic capacitance of the holder and R_L the input impedance of the front-end amplifier. To calculate the voltage V, the simulated current is imposed onto the node marked N. The attenuation of the long coaxial cable is accounted for in the measured overall front-end gain (see table 6.1).

with A the total area of the diode sample and the $\square$-symbol a placeholder for the possible subscripts (U, D and N). The signal recorded by the oscilloscope (excluding amplification) is the voltage V over the resistance R_L. Using the extended Shockley-Ramo theorem the current I induced onto the grounded N-side electrode is calculated. This current is then imposed onto the node marked N in figure 8.8 as an ideal current source. It follows for the voltage

$$V(s) = Z_{tot}(s) I(s), \quad \text{with} \quad Z_{tot}(s) = Z_S(s) \parallel \frac{1}{sC_H} \parallel R_L \tag{8.41}$$

in the Laplace domain.[28] As the sensor impedance $Z_S(s)$ itself is a combination of capacitors and resistances in series and parallel, the full analytical expression of $Z_{tot}(s)$ is very convoluted. But it can easily be evaluated using any library for symbolic computations, such as SymPy [152].[29] The bode plot of the transfer function $Z_{tot}(i\omega)$ is shown in figure 8.9 (assuming a set of reasonable values for ρ_N and ρ_P) for case A, with various depletion widths d_D, and for case B. It is obvious that the transfer function shows

---

[28] As the P-side contact is grounded, the current induced onto the P-contact does not contribute to the signal voltage V.

[29] SymPy is online available at `https://www.sympy.org/`.

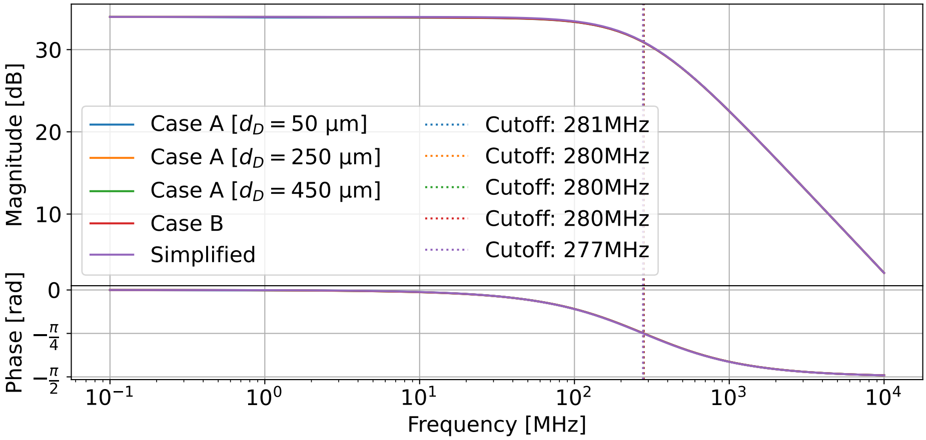

FIGURE 8.9: Bode plot of the $Z_{tot}(i\omega)$ transfer function for different cases. It can be seen that there is virtually no difference between the different cases and that the simplified transfer function shows an equivalent behaviour. These curves are calculated with $\rho_N = 10\,\mathrm{k\Omega\,cm}$ and $\rho_P = 20\,\mathrm{k\Omega\,cm}$ which are reasonable values representing the fabricated samples (see table 4.3).

negligible differences between the different cases, which is due to the large resistivity of the P- and N-substrates. Thus, the electronics response can be approximated by ignoring the substrate resistances and Z_{tot} becomes

$$Z_{tot}(s) = \frac{1}{s(C_S + C_H)} \parallel R_L \quad \text{with} \quad C_S = \epsilon_{Si}\epsilon_0 \frac{A}{d_N + d_P}. \tag{8.42}$$

Applying the inverse Laplace transform to the simplified transfer function leads to the impulse response of the equivalent electronics circuit

$$z_{tot}(t) = \frac{1}{C_S + C_H} \exp\left(-\frac{t}{(C_S + C_H)R_L}\right) \Theta(t) \tag{8.43}$$

which is used for the simulations in this thesis.

8.3.5 *Simulation performance*

Figure 8.10 shows the simulated time domain curve for an example simulation configuration. The different curves represent the signal obtained at different steps in the simulation chain:

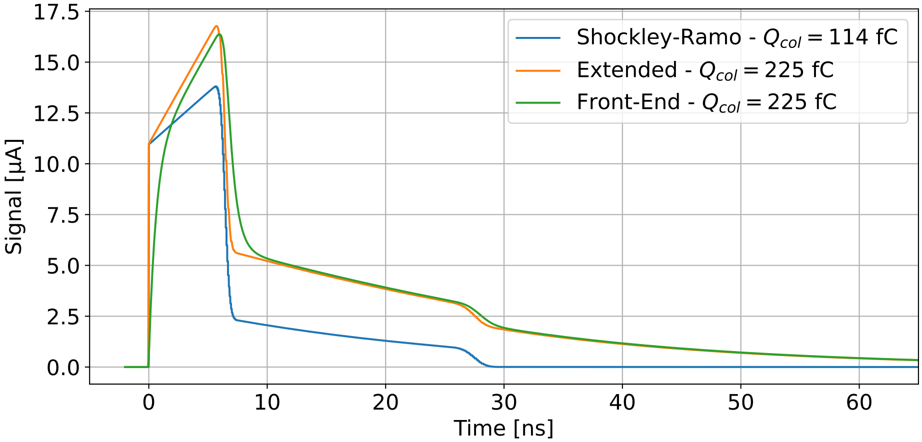

FIGURE 8.10: Example curves simulated with the presented simulation model. The signals at various steps in the simulation process are shown, see text for details. In the shown configuration the P-side is fully depleted, the charge deposit is as for an infrared (IR) laser exposure in edge TCT mode and the front-end gain has been set to 1. The separate drift of electrons and holes can clearly be seen.

SHOCKLEY-RAMO Induced current signal based on the traditional Shockley-Ramo theorem.

EXTENDED Induced current signal after applying the effect of the extended Shockley-Ramo theorem.

FRONT-END Signal including the low-pass filtering effect of the front-end electronics.

Compared to the traditional Shockley-Ramo theorem, the extended theorem leads to an additional long exponential tail due to the non-depleted N-side. Overall the signal has a higher amplitude and a higher overall pulse integral. The increase in collected signal can be observed from the integrated collected charge Q_{col} indicated in the legend of the mentioned figure. The inclusion of the front-end response leads to slower rise and fall times but does not change the overall pulse integral.

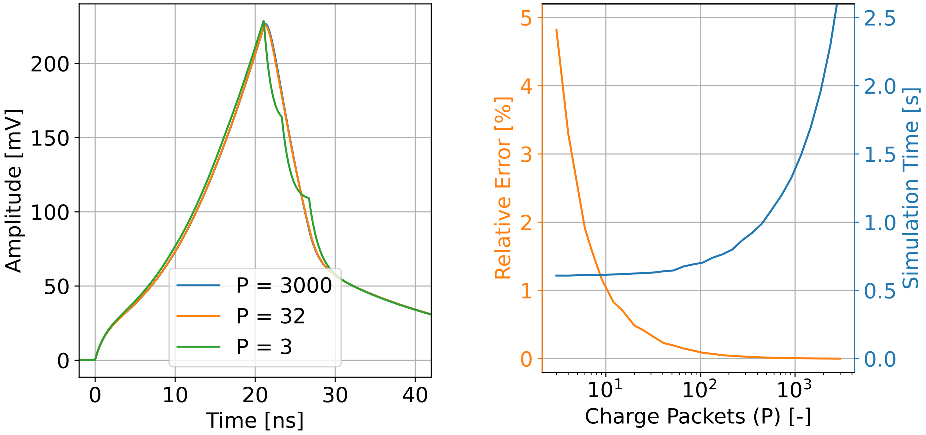

(a) Example signal simulated with different number of charge packets P.

(b) Simulation time and relative error in function of the number of charge packets P.

FIGURE 8.11: Evaluation of the performance and accuracy of the simulation model, based on an example simulation. The example simulates injection of charges via an α particle into a sensor with a P-side full depletion voltage of ca. 135 V and a bias voltage of 145 V.

8.3.5.1 *Run time*

The runtime complexity of the simulation algorithm presented here is $\mathcal{O}(N\,P)$, with N the number of points simulated in time, and P the number of distinct charge packets being simulated. The goal of the presented model is to generate time domain curves to be compared with the data acquired by the TCT setup. Accordingly, the simulated signals should be compatible with the $f_s = 20\,\mathrm{GS\,s^{-1}}$ sampling rate of the oscilloscope, which allows for little flexibility on the number of points in time to be simulated. On the other hand, the number of charge packets to be simulated can be chosen in a trade-off between simulation time and accuracy of the simulation. Figure 8.11a illustrates the effect of having different numbers of charge packets for an example simulation with α particle based charge injection. Having a very small number of charge packets leads to non-physical steps in the signal, as the individual charge packets arrive at the boundaries of the sensor and are subsequently removed from the drift.[30] The blue line in figure 8.11b shows the simulation time in function of the number of charges packets for the same example simulation. The orange line in the same figure shows the relative error

$$\mathrm{Err}_{rel} = \frac{\int |V_P(t) - V_{3000}(t)|dt}{\int |V_{3000}(t)|dt} \tag{8.44}$$

with $V_P(t)$ the signal simulated with P charge packets and $V_{3000}(t)$ the signal simulated with 3000 charge packets, which is taken as the golden standard. From this plot is clear that using reasonably low numbers of charge packets ($P \approx 50$) leads to a small relative error while exhibiting a simulation execution time of less than $T_{Sim} < 0.7\,\mathrm{s}$.[31]

8.3.5.2 *Limitations*

There are two main limitations of the simulation model presented in this section. The first one concerns the treatment of the problem as purely 1-dimensional. A 1D approximation is most valid right in the centre of the fabricated bonded samples, where, due to the large size of the pad diodes, the electric field indeed should only exhibit a vertical component across the sample. In the case of signals acquired with the americium-241 (Am-241) source, as presented in chapter 9, this approximation should be valid as the signals are mainly created in the centre of the samples. On the other hand, for edge TCT measurements carried out close to the P- and N-side contact a non-negligible lateral component of the electric field is most likely present. Comparing such measurements with results from the presented simulation model thus need to be done with care. The second limitation concerns the general limitations of charge propagation simulations. Effects such as generation and recombination as well as trapping and de-trapping of charges within the P-side bulk are not implemented. Given that the samples have a very low doping density and have not been irradiated it is not expected for these effects to play a major role. Finally, any local modification of the electric field due to the presence of the injected charges is not considered. This explicitly includes the self-shielding of high charge

---

[30] These steps would be even more pronounced without the low-pass filtering effect of the electronics front-end.

[31] The absolute execution time was measured on a machine with a first generation Intel-i5 CPU (launched in 2009), running at a nominal frequency of 2.66 GHz. Performance would be substantially better on a more modern computer.

densities (plasma effect). This effect is certainly present in the measurements using the Am-241 source, as the interaction of α particles produces up to 1.3×10^6 electron-hole pairs within a volume of $\approx 1 \times 10^4\ \mu\mathrm{m}^3$ (see also section 9.2.1). Finally, implementing a simulation model in Python leads to some inherent limitations on the execution time. Both the accuracy (by simulating more charge packets) and the execution time could most likely be improved by implementing the core simulation routine in C or C++.

9

TIME-DOMAIN SIGNALS OF BONDED SENSORS

> *Laptops are the perfect heated beds!*
>
> — Emmy

During the investigation of the depletion behaviour of the bonded samples a long exponential tail is observed on the recorded time-domain signals. Figure 9.1 shows some example transient current technique (TCT) curves to highlight this exponential tail. The exponential tail has a characteristic time in the order of tens of ns. Measurements at different temperatures showed a small inverse correlation between the temperature and the characteristic time of the exponential tail. Measurements with a reference diode provided by Particulars [108] do not show this exponential tail. The exponential tail is also present in the measurements carried out at CERN using the two photon absorption (TPA) TCT setup built with completely different components. These observations exclude the possibility that the exponential tail is due to the TCT measurements setup but indicate that the observed tail has a physical origin in the bonded samples.

The long tail can not reasonably be explained based on a simulation model employing the classic Shockley-Ramo theorem with the following parameters: the P-side doping N_a, the bias voltage V_{Bias}, the combined sensor and parasitic capacitance C and the number of electron-hole pairs created by the laser N_{eh}. The bias voltage is given by the measurement setup and the P-side doping can be estimated from the P-side full depletion voltage (see figure 7.1). Using reasonable values for the total capacitance C, the exponential tail can not be reproduced. Employing very high values of C and a high number of created charges N_{eh}, the tail can be approximated, but this leads to a bad representation of the main TCT pulse. In order to reduce the number of undetermined parameters in the simulation model, TCT measurements employing an americium-241 (Am-241) α source were carried out. The known energy distribution of the emitted α particles allows to predict the energy deposited in the bonded sample and thus the number

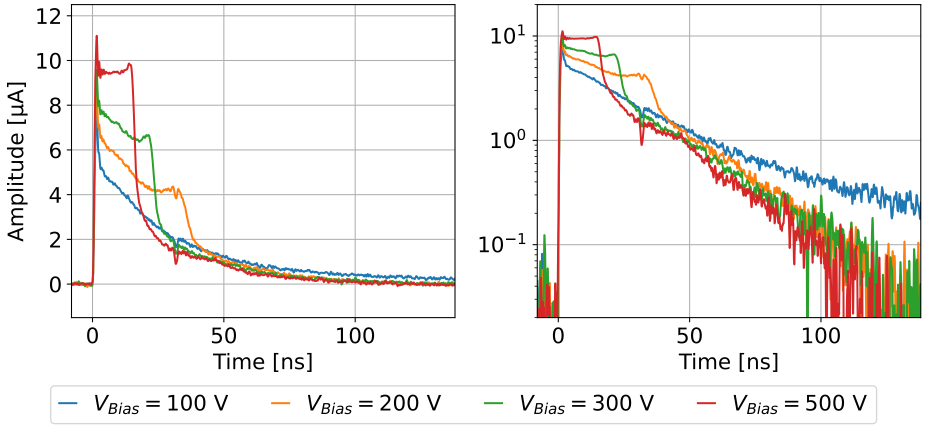

FIGURE 9.1: Example TCT time domain curves highlighting the presence of a long exponential tail with a characteristic time in the order of tens of ns. This data has been acquired with **P303403-E12** in IR edge TCT mode. The notch at $\approx 30\,\text{ns}$ is due to signal reflections at the front-end electronics. The same curves are shown with a linear and logarithmic y-scale.

N_{eh} of electron-hole pairs created.[1] These measurements therefore fix the last free parameter of the simulation model. This investigation eventually led to the discovery of the importance of the extended Shockley-Ramo theorem when simulating the bonded diode samples (presented in section 2.4).

CONTRIBUTION All work in this chapter, including the α source measurements, the simulation of the α energy deposit, and the data vs. simulation comparison based on the simulation model presented in section 8.3, was carried out by the author.

9.1 TCT MEASUREMENTS WITH AN AM-241 α SOURCE

The Am-241 α source has an activity of $A_{2023} = 53\,\text{kBq}$.[2] The emission probability of the three main α energies of Am-241 are given in table 9.1.

---

[1] The TCT setup does not allow to quantitatively predict the laser intensity and thus the number of laser injected electron-hole pairs.

[2] The activity of the source was last measured in the year 2000 to be $A_{2000} = 55\,\text{kBq}$ and was extrapolated to 2023 based on its half-life time of $T_{1/2} = 432.6\,\text{yr}$ [153].

	$\alpha_{0,2}$	$\alpha_{0,4}$	$\alpha_{0,6}$
Energy [keV]	5485.56 ± 0.12	5442.86 ± 0.12	5388.25 ± 0.13
Probability [%]	84.45 ± 0.10	13.23 ± 0.10	1.66 ± 0.03

TABLE 9.1: Most probable α energies emitted by the decay of Am-241. All other energies have a probability of less than 1 %. Data from [153].

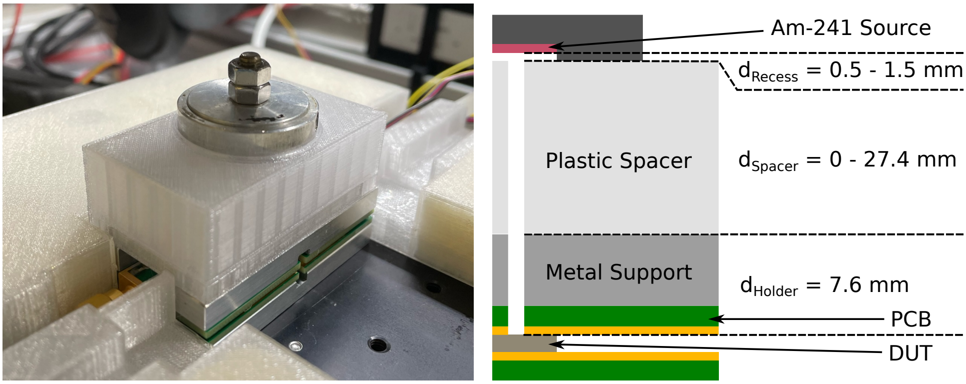

(a) Image of the source placed on top of the spacer and sample holder inside the TCT setup.

(b) Cross section view of the source placed on top of the spacer pieces and the sample holder.

FIGURE 9.2: Illustrations of the source placement for the α measurements.

The source is open, i.e. the radioactive material is directly exposed to air, and thus no α energy is lost in any window material. To not have potential radioactive contamination of the measured samples, the source can not be brought in direct contact with the bonded diode samples. Accordingly, the α particles lose a fraction of their energy in the air gap between the source and the sample. This effect is exploited to carry out measurements with α particles of different energies interacting with the samples, by varying the air gap distance. To do so, spacer pieces were 3D printed to separate the source and sample by a known and consistent distance. The spacers have a rim which firmly holds the source in place. Figure 9.2a shows the source placed on top of the plastic spacer pieces, which in turn are placed on the sandwich-type sample holder and figure 9.2b shows a cross section view of the entire stack. The recession distance $d_{Recess} = 0.5 - 1.5\,\mathrm{mm}$ of the source is unknown and can not mechanically be measured for contamination pro-

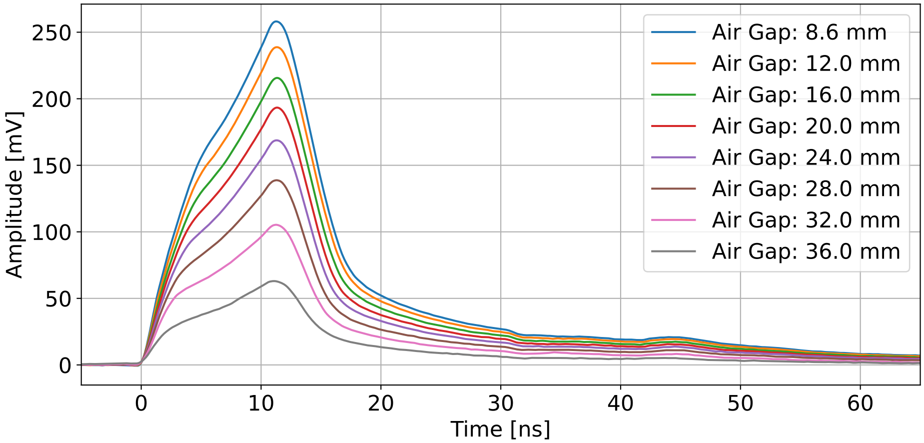

FIGURE 9.3: Averaged time domain TCT signals measured with the Am-241 α source with different air gap distances. The artefact between 30-45 ns is due to signal reflections at the electronics front-end.

tection reasons. It is visually estimated which explains the large uncertainty. The total nominal air gap distance used for the measurements is given by

$$d_{Gap} = d_{Holder} + d_{Spacer} + d_{Recess} = [8.6, 12, 16, 20, \ldots, 36] \text{ mm}$$

The next section discusses the simulation of the energy deposited by the α particles in more detail. Exposure of the bonded diode sample to the α particles is via the P-side as the range of the particles is not large enough to penetrate through the undepleted N-side.

The measurements are carried out inside the TCT setup (as presented in section 6.2) but without using the pulsed laser. The samples are temperature stabilized to $T_S \approx 10\,°\text{C}$ and exposed to atmospheric lab air, no N_2 flushing is employed. Sample **P303403-E12** with a P-side depletion voltage of ca. 120 V is used for the measurements. As full depletion of the P-side is necessary to detect the α signals, the measurements is taken with a bias voltage of $V_{Bias} = 250\,\text{V}$. The electronic signal chain is the same as for laser based TCT measurements, with the exception that no dedicated trigger signal is available. Instead, the oscilloscope directly triggers on the TCT pulses coming from the α particles. The noise present on the recorded signals leads to a shift in time between subsequent triggers, which does not allow to directly average the signals on the oscilloscope. But averaging is necessary in order to reduce the system noise. To allow for proper averaging, a T_0 time is calculated individually for each recorded signal. The initial rising flank of the signal is detected via a constant fraction discrimination and the precise T_0 is given by the x-axis intercept of a linear fit of the initial raising flank. This is equivalent to the method used in the context of the prompt current analysis as shown in figure 6.3. The curves shifted in time to their respective T_0 are then averaged for each air gap distance value. The resulting averaged curves are shown in figure 9.3.

9.1.1 *Simulation of the deposited E_α energy using SRIM*

To estimate the energy deposited by the α particles in the bonded samples in function of the air gap, the *The Stopping and Range of Ions in Matter* (SRIM-2013) program is used [154]. The α particles from the Am-241 source are emulated by *He*-ions with an energy of $E_{Ion} = 5485\,\mathrm{keV}$.[3] First, the absorption of α energy in the air gap is simulated by propagating these ions across a layer of air. The result of the simulation is the function $\hat{E}_{ionized}(x)$ representing the distribution of energy absorbed by the air via ionization at a distance x from the source. Based on this data the α energy deposited in a bonded diode sample $E_{sample}(d_{Gap})$ placed at a distanced d_{Gap} from the source can be calculated via

$$E_{sample}(d_{Gap}) = E_{ion} - \int_0^{d_{Gap}} \hat{E}_{ionized}(x)dx \tag{9.1}$$

The energy lost via ionization in air directly depends on two parameters: the density (ρ_{Air}) and the composition of the air. The density is dependent on the temperature (T_{Air}) and the pressure (p_{Air}).[4] Both, the density as well as the composition, are dependent on the relative humidity of the air RH_{Air}.

---

[3] A single α energy is chosen for simplicity. The average α energy as per the data in table 9.1 is ca. 1 % lower than the mode of the α distribution.

[4] Ignoring influences from relative humidity (i.e. assuming $RH_{Air} = 0\%$) the density of the air based on the ideal gas law is given by $\rho_{Air} = \frac{p_{Air} \cdot m_{Air}}{k_B \cdot T_{Air}}$ with m_{Air} the molar mass of air and k_B the Boltzmann constant.

For the measurements presented in the previous section 9.1 the following parameter ranges are considered:[5]

TEMPERATURE $T = 10 - 12\,°\mathrm{C}$

AIR PRESSURE $p = 94 - 97\,\mathrm{kPa}$

RELATIVE HUMIDITY $RH = 40 - 70\,\%$

SRIM simulations are carried out for all 8 possible combinations of the extreme values of the given ranges. The two combinations leading to the smallest and largest amount of energy deposited in the sample are given in table 9.2 together with the corresponding energy deposit for each air gap. In the comparison of simulation and data presented in the next section, these energy ranges are used as an uncertainty range. Another source of uncertainty in the measured signal arises from the presence of a thin undepleted layer at the sample surface, due to the high dose contact implant, which affects the accurate determination of the number of electron-hole pairs contributing to the signal. This undepleted layer has an approximate thickness of 1 µm, based on the designed contact implant distribution (see figure 4.4). To account for this possible reduction in signal, the distribution of the deposited energy in silicon for each case in table 9.2 is simulated with SRIM. In each case the integral of the energy deposited in the 1 µm layer directly below the metal contact is used as an additional uncertainty.[6] The simulated energy deposits in silicon are shown in figure 9.4 These simulations are further used to estimate the locations of the resulting Bragg peaks. This information is used to properly configure the charge deposit distribution in the simulation model (see section 8.3.1).

---

[5] The temperature and relative humidity are directly measured on the sample holder. The pressure is taken from a local weather station on the ETHZ campus.

[6] Not all the charges created in this 1 µm layer are lost, as some of them will be collected via drift.

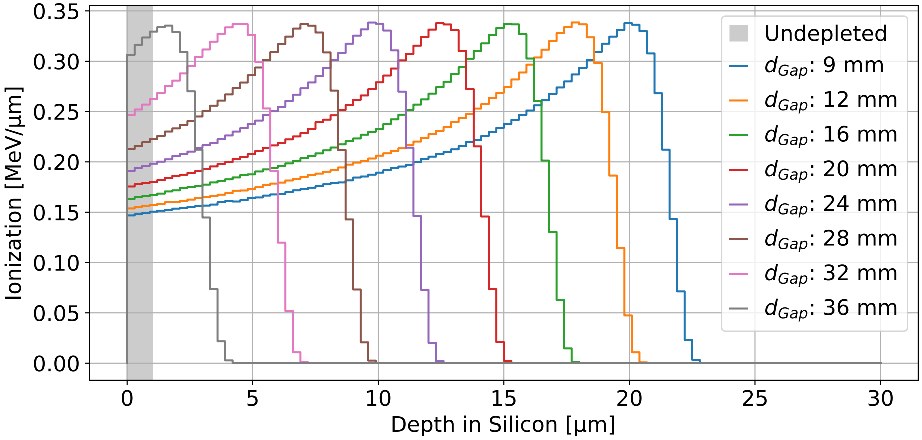

FIGURE 9.4: Distribution of the energy deposited by the α particles for the different air gap distances. The curves are simulated for the configuration leading to the largest amount of energy lost in air: $T = 10\,°C$, $p = 97\,kPa$ and $RH = 40\,\%$.

Air Gap	**Smallest Deposited Energy**	**Largest Deposited Energy**
	$T = 10\,°C$	$T = 12\,°C$
	$p = 97\,kPa$	$p = 94\,kPa$
	$RH = 40\,\%$	$RH = 70\,\%$
8.6-9.1 mm	4.70 MeV	4.79 MeV
12-12.5 mm	4.38 MeV	4.47 MeV
16-16.5 mm	3.98 MeV	4.09 MeV
20-20.5 mm	3.56 MeV	3.67 MeV
24-24.5 mm	3.10 MeV	3.22 MeV
28-28.5 mm	2.60 MeV	2.73 MeV
32-32.5 mm	2.02 MeV	2.17 MeV
36-36.5 mm	1.33 MeV	1.52 MeV

TABLE 9.2: Energy deposited in the P-side of the bonded samples by an α particle emitted from an Am-241 source. The values are based on simulations with SRIM. The smallest and largest amount of energy deposited in the bonded samples are shown, based on different environmental conditions.

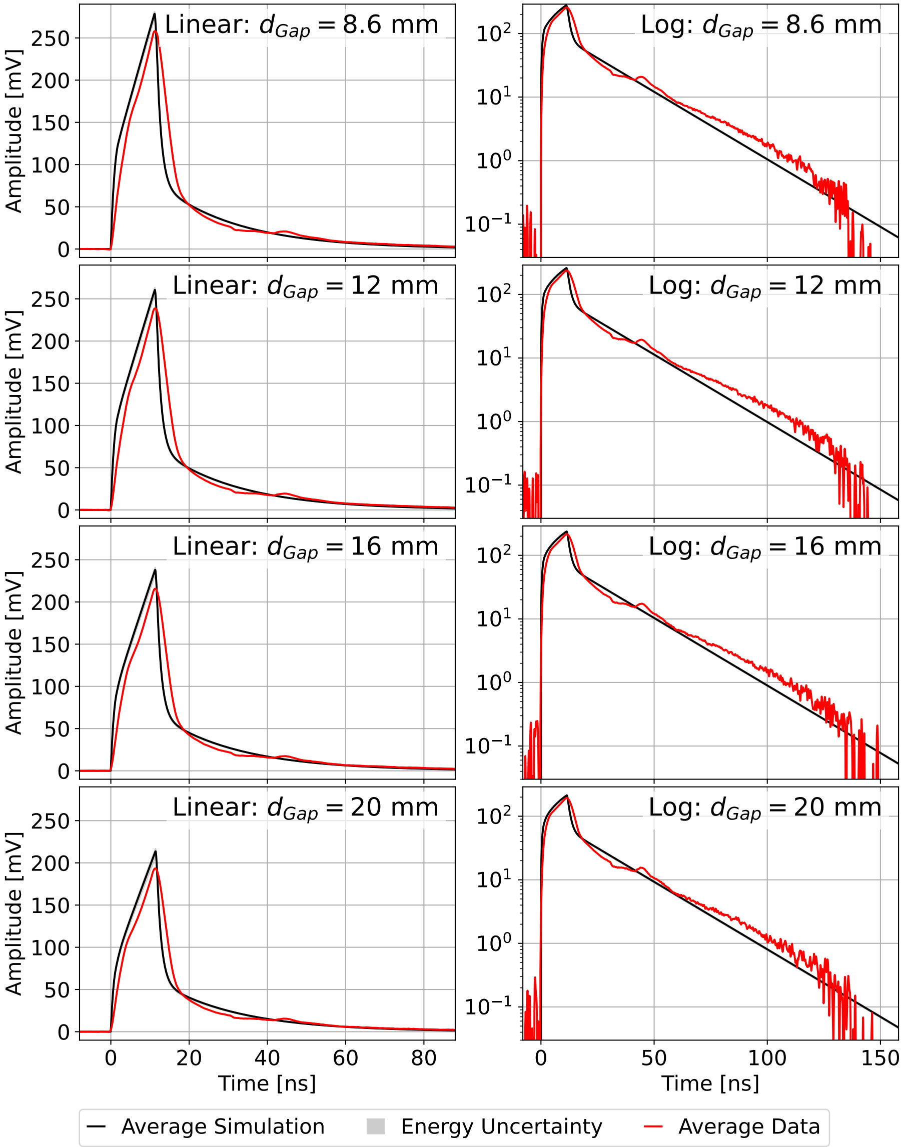

(a) $d_{Gap} \in (8.6, 12, 16, 20)$ mm

FIGURE 9.5: Comparison between simulated and measured α TCT curves. The simulations are based on the simple simulation model including the extended Shockley-Ramo theorem (presented in section 8.3) and simulations of the α energy deposit carried out with SRIM. A very good overall agreement between simulation and measurement is observed.

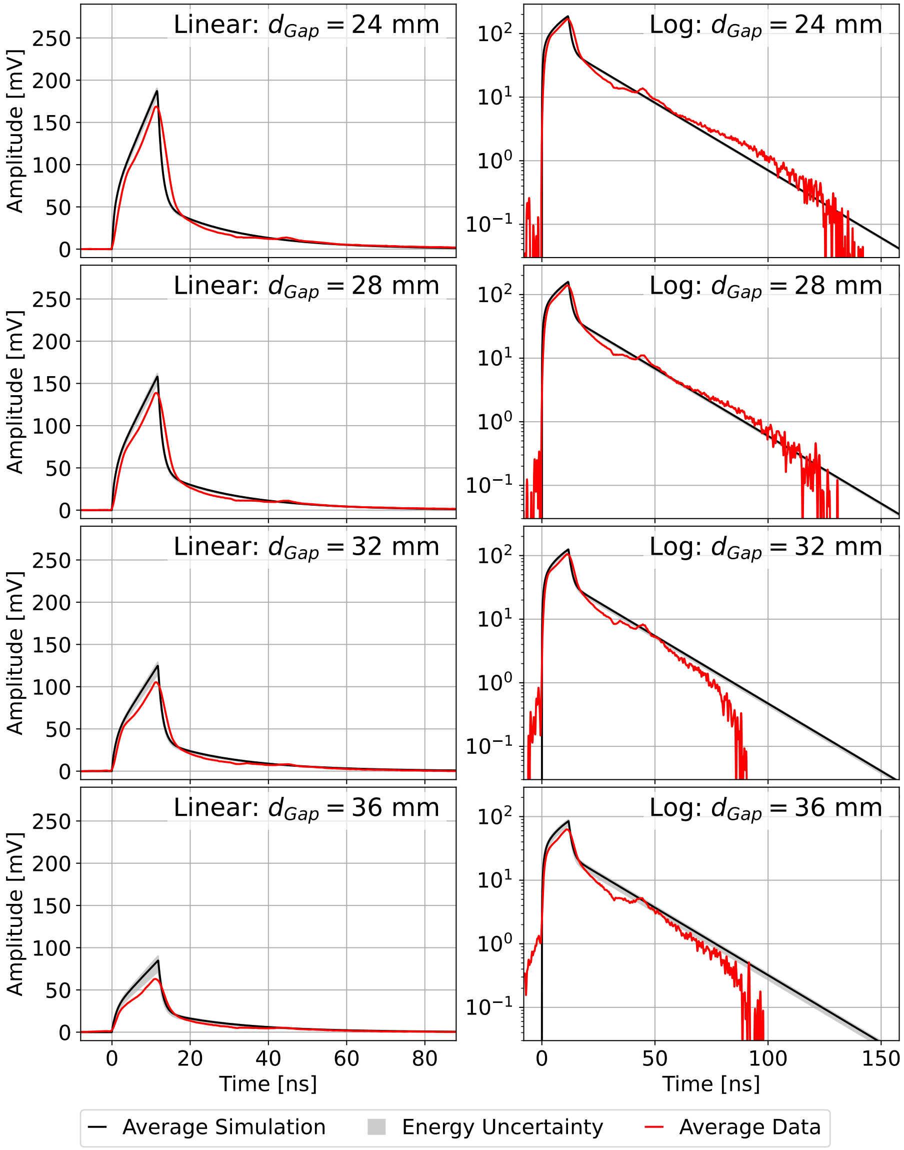

(b) $d_{Gap} \in (24, 28, 32, 36)$ mm

FIGURE 9.5: (continued) The simulation in particular allows for a good reproduction of the long exponential tail. The pedestal-like artefact visible for $t < 0$ ns on the curves with $d_{Gap} = 32$ mm and 36 mm is due to an imprecise fitting of T_0 because of the low signal-to-noise ratio in these cases.

9.2 COMPARISON WITH SIMULATION

The comparison of the averaged measured TCT signals and the simulated predicted curves is shown in figures 9.5a and 9.5b. The simulated curves are based on the simple simulation model and the SRIM simulations. The overall agreement between simulation and measurement is very good. Both the signal amplitude and the overall signal shape are correctly predicted by the simulation model. The plots with a logarithmic y-scale show that the long exponential tails are also well reproduced by the simulation model based on the extended Shockley-Ramo theorem.

The simulation model also accurately predicts the amount of integrated signal, which is proportional to the collected charge, for the given measurements. The comparison of measured and simulated integrated signal is shown in figure 9.6. The biggest discrepancy occurs for the measurements with the largest air gaps. This is not surprising, as for these measurements most of the α energy is lost in the air and the Bragg peak inside the silicon occurs close to the sample surface (see figure 9.4). Thus, the corresponding simulations are very sensitive to any effects which have not been taken into account and which lead to additional energy loss of the α particles. Such effects include the, on average, lower emitted α energy due to the α spectrum of Am-241 (see table 9.1), a small loss of energy when an α particle exits the source material, and the possibility of detecting signals from α particles which have crossed the ca. 100 nm thick contact metallization. All of these effects would lead to an on average lower deposited α energy.

9.2.1 *Observation of the plasma effect*

The main differences between the measured and simulated α time domain signals shown in figure 9.5 are the shapes of the raising and falling edges of the main TCT pulses. The measured curves show a slower rise and fall time compared to the simulated signals. As discussed in section 8.3.5, one major effect which is not implemented in the simple simulation model is the so called plasma effect. When a particle interacts with a semiconductor detector such that it deposits most of its energy in a very small volume, the resulting charge cloud can lead to a local shielding of the drift field. Accordingly the signal exhibits a slower rise time and a partially delayed drift [10]. Figure 9.7a shows the initial raising edge of the measured α

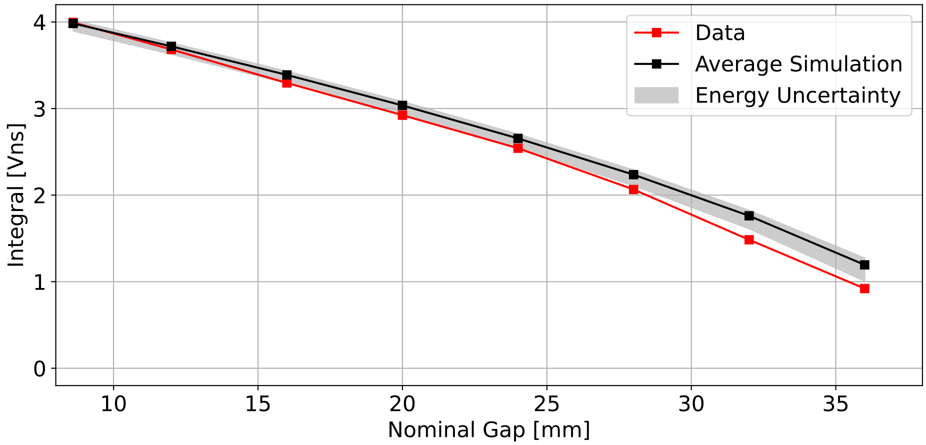

FIGURE 9.6: Comparison of the measured and simulated integrated signal. The simulation predicts the integrated signal well, except for measurements with a large air gap distance. See text for discussion.

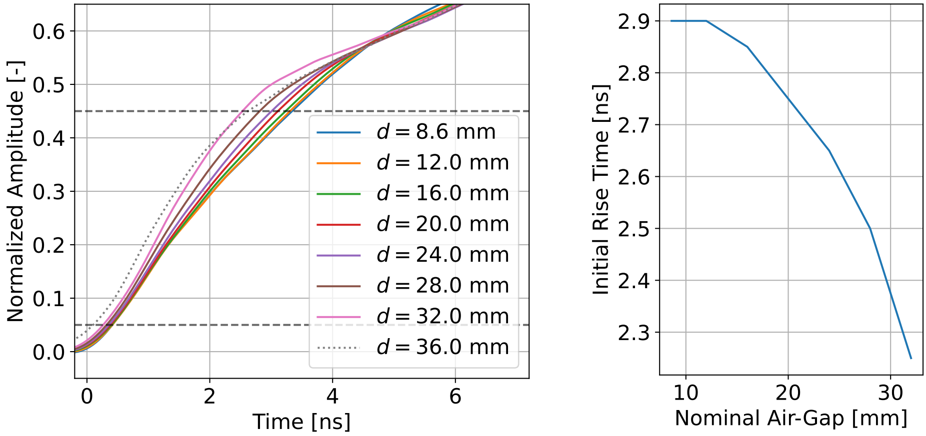

(a) Initial raising edge of all averaged α curves normalized to an amplitude of 1.

(b) Calculated between the two horizontal lines in figure (a)

FIGURE 9.7: Signals from Am-241 interactions with a lower number of injected electron-hole pairs (a larger gap) show a faster rise time. This indicates the presence of plasma effects due to the high local density of charges. The measurement with $d_{Gap} = 36\,\text{mm}$ is excluded from this analysis, due to the inaccurate fitting of T_0 in the case of a low signal-to-noise ratio.

time domain curves normalized to a maximum amplitude of 1. It is clearly visible that the cases with the largest air gaps, and thus the lowest number of created electron-hole pairs, show the fastest rise times, as plotted in figure 9.7b. This qualitatively agrees well with the expected behaviour due to the plasma effect. The difference in the shapes of the falling edges can also partially be attributed to the plasma effect, as it leads to a lengthening of the observed pulses compared to the simulated ones. In addition, some of the charges created in the undepleted contact layer will be collected via drift, which also leads to a stretching of the pulses.

These results show that the empirical P/N++/N model, combined with the extended Shockley-Ramo theorem, is able to correctly predict the time domain pulse behaviour of the bonded samples. This excludes second order effects which have not been included in the presented simulation model, such as the plasma effect or charges deposited in the undepleted region being collected via drift. The results also indicate that the bonding interface, apart from modifying the depletion behaviour of the samples, does not fundamentally alter the formation of the transient signal in the case of the presented bonded diode samples.

9.3 INFLUENCE OF THE BIAS VOLTAGE ON THE EXPONENTIAL TAIL

The application of the extended Shockley-Ramo theorem to the fabricated diode samples predicts a long exponential tail on the TCT time domain signals (see section 8.3.3). This exponential tail is caused by the response of the undepleted (conductive) layers of the samples, and its characteristic time constant depends on the size of the undepleted regions, as shown in figure 8.7. Thus, at V_{Bias} below the P-side full depletion voltage, the exponential tail is dependent on the applied bias voltage. This behaviour can be illustrated based on the edge TCT measurements presented in section 7.2. The movement of holes in an electric field which linearly decreases towards $E = 0\,\mathrm{V\,m^{-1}}$ also leads to an exponentially decaying component of the induced signal. But the characteristic time of that exponential decay is fixed as $\tau_h = \frac{\epsilon_0 \epsilon_{Si}}{e \mu N_a}$ and does not depend on the bias voltage or the depletion width.[7] To reduce the influence of this additional exponential decay, time domain signals are selected where the movement of electrons dominates.

---

[7] This follows from the definition of the carrier mobility as $v(t) = \dot{x}(t) = \mu\, E(x(t))$ with the electric field in the form of $E(x) = -\frac{e N_a}{\epsilon_0 \epsilon_{Si}} x$.

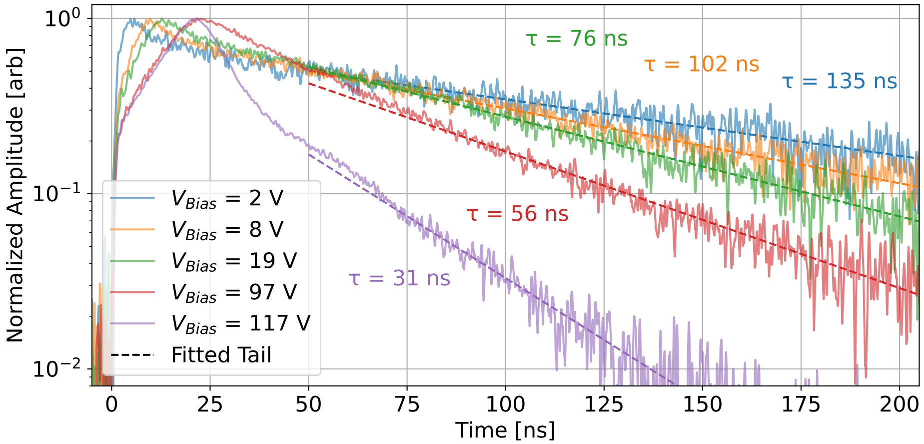

FIGURE 9.8: A selection of time domain TCT curves from edge TCT measurements of **P301401-E12**. The curves are chosen so that the main contribution of the signal is from electrons drifting towards the bonding interface. The curves show a dependency of the long exponential tail on the applied bias voltage, which is caused by the dependency of the depletion width on the bias voltage.

For multiple bias voltages the P-side depletion width $W_{Dep}(V_{Bias})$ is estimated based on the data of the edge scan profiles, as shown in figure 7.3. Following this, time domain TCT curves are selected where the charge injection happens close to $x \approx -W_{Dep}(V_{Bias})$. In these cases the holes stop drifting nearly immediately and the major part of the signal is from drifting electrons. A selection of such curves is shown in figure 9.8 for the sample **P303403-E12**. The presented curves clearly show the behaviour as predicted by the extended Shockley-Ramo theorem. Increasing the bias voltage reduces the width of the undepleted part of the P-side of the fabricated samples, and thus reduces the characteristic time of the exponential tail. At $V_{Bias} = 117\,\mathrm{V}$ the P-side is nearly fully depleted and the characteristic time of the decaying tail is being dominated by the presence of the undepleted N-side.

10

CONCLUSION AND OUTLOOK

> *The leg of my favourite human is a very fine place to rub my head against.*
>
> — Hilbert

CONCLUSION This thesis investigated the use of surface activated bonding (SAB), also called low-temperature covalent wafer bonding, for the fabrication of particle pixel detectors. Fabricating detectors via SAB allows to integrate multiple types of semiconductor materials in a monolithic like structure without the need for bump bonding. Building such heterostructure detectors is especially interesting in the context of X-ray image detectors, where the use of high-Z absorber layers is beneficial for improved detector efficiency. But SAB introduces as thin amorphous layer at the bonding interface, which has a high density of defects and which is sensitive to trace impurities that can drastically affect its electrical properties. In order to make use of SAB for detector fabrication, the influence of this interface layer on the generation and collection of signal needs to be well understood and investigated in detail.

To do so, simple bonded pad diodes were fabricated using SAB, with the goal of investigating the signal formation via transient current technique (TCT) measurements. These diodes were implemented by bonding high resistivity N- and P-type silicon (Si) wafers, thus placing the sensor P/N junction at the bonding interface. A dedicated fabrication process was developed to ensure high quality ohmic contacts for both the N- and P-side metal contacts. Scanning acoustic microscopy (SAM) measurements showed an overall good mechanical bonding quality of the fabricated samples and I/V measurements confirmed a rectifying diode behaviour. Scanning transmission electron microscope (STEM) measurements showed a ca. 3 nm wide amorphous layer at the interface. But energy-dispersive X-ray spectroscopy (EDXS) measurements, carried out in tandem with the STEM measurements, revealed the presence of unexpected contaminating metal elements at the interface, namely iron, nickel, chromium and titanium. The source of this contamination was investigated with total reflection X-ray fluorescence spectroscopy (TXRF) measurements of unbonded wafer, revealing no contamination on the wafers pre bonding. Separate investigations by the bonding supplier confirmed that the metal contamination was introduced during the bonding process, due to the use of a bonding machine without silicon coated side panels.

To investigate the signal generation in the fabricated samples, a TCT system was commissioned at ETHZ based on components acquired from Particulars d.o.o. A custom Python based control framework was implemented, together with a web based data analysis utility. Further, a simulation model using the principle of charge propagation and signal induction via the Shockley-Ramo theorem was implemented. The simulation model is fully parametric and specifically designed for the simulation of time domain TCT signals and for comparing them with the data acquired using the TCT setup. The model includes an extension of the Shockley-Ramo theorem for simulating structures with conductive layers.

Top/bottom and edge TCT measurements of the fabricated samples show an asymmetric depletion behaviour. Only the P-side of the samples can be depleted and thus only this side exhibits an electric field. This finding is independently confirmed by comparative measurements on a two photon absorption (TPA) TCT system. This one-sided depletion behaviour is attributed to the presence of the contaminated bonding interface and allows for the definition of an empirical P/N++/N model, where the interface acts as a strongly doped N-type region. It can not be excluded that this observed one-sided depletion is an artefact of the confirmed presence of metal contaminants at the bonding interface. This limits the general validity of the observed behaviour and does not allow to make any conclusion about the depletion behaviour of equivalent structures with a non-contaminated bonding interface. But theoretical considerations indicate that even very low densities of active donor- or acceptor-like defects at the bonding interface can drastically alter the depletion behaviour, especially when using high resistivity and thus very low doped substrates. It can not be excluded that the intrinsic defects of the amorphous bonding layer have a similar effect. Edge TCT measurements present a very powerful technique for investigating the depletion behaviour in specific bonding configurations.

Time domain TCT curves with an Am-241 α source were recorded. These measurements were carried out with different air gap distances between the source and the sample, thus modulating the α-energy deposited within the sample. The deposited energy, and by extension the number of electron-hole pairs created by the α radiation, was predicted using SRIM simulations, taking into account environmental parameters such as air temperature, pressure and humidity. The developed simulation model shows a very good absolute agreement between the measured α signals and the simulated time domain signals for the different amounts of energy deposited. The inclusion of the extended Shockley-Ramo theorem in the simulation model is crucial for this good agreement. The presented results show that the presence of the bonding interface, apart from modifying the depletion behaviour, does not have any detrimental impact on the formation of signals. Overall, the simulation model is able to correctly predict the time domain signals from first principles.

FUTURE WORK Due to the (unwanted) contamination of the bonding interface with metal elements, the results presented in this thesis do not allow to make a general conclusion with respect to using SAB for fabricating particle detectors. But this also presents a clear path forward for a new production run of bonded diode samples, making use of a bonding machine with silicon-coated panels which inhibit this type of metal contamination. The framework presented in this thesis allows for the efficient fabrication and analysis of such new samples. This would allow to answer the question if a one-sided depletion behaviour is also present under ideal bonding conditions.

Another avenue of exploration is to investigate to what extend a sensor structure exhibiting a one-sided depletion behaviour can be used for pixel detectors. The results of this thesis have shown that under certain conditions bonded P/N junction show a consistent one-sided depletion behaviour. If this is due to the metal contamination or inherent to the amorphous bonding interface is up to investigations. But it indicates that such a behaviour can most likely be forced by selectively engineering the bonding interface via dedicated doping pre bonding. The possibility of forcing a one-sided depletion behaviour of the P- or N-side, by doping the interface N- or P-type respectively, needs to be investigated. This would allow for the possibility of fabricating bonded detectors where, by design, the absorber layer is depleting but not the CMOS readout substrate. As shown in this thesis, the behaviour of such structures can be simulated via charge propagation, by taking into account the extended Shockley-Ramo theorem. Pixelated detectors exhibit a much more complex weighting field and weighting vector compared to the pad detectors presented in this thesis. In pixel detectors the major part of the signal induction occurs from the charge movement close to the pixel. And thus, having a (thin) non-depleted layer close to the pixel contact might have a noticeable impact on properties such a charge sharing, collection time and signal efficiency. Based on the principles presented in this thesis it is possible to in detail study the effects of a (thin) non-depleted CMOS substrate.

The analysis of the behaviour of bonded P/N junctions made up of two different materials (for example Si and GaAs) presents another very important step forward. The main challenge for such an investigation comes from the limitation that many clean-rooms only allow to either process Si based structures or III/V-type materials. Thus, for the fabrication of bonded hetero-structures a suitable cleanroom would need to be found. Alternatively, a modification of the fabrication process is necessary to ensure that the bonding itself is the last step of the process. Creation of hetero-junctions also brings the added complexity of the mismatch in band gap and electron affinity of the two materials. This adds additional effects on top of the presence of the interface defects, which are also present when bonding Si to Si.

A

DETAILED FABRICATION PROCESS

See chapter 4 for the discussion of the various fabrication process steps.

A.1 MASK FABRICATION

(1) MASK WRITING
(1.1) **Laser writing** (Heidelberg Technology DWL 2000)

(2) MASK DEVELOPMENT
(2.1) **Resist development** (In a beaker) – AZ440K 1:4 for ca. 30-50 s
(2.2) **Rinsing** (In a beaker) – DI water
(2.3) **Mask drying** (N_2 gun)

(3) MASK ETCHING
(3.1) **Chromium etching** (TechniEtch Cr01) – For ca. 50 s
(3.2) **Rinsing** (In a beaker) – DI water
(3.3) **Mask drying** (N_2 gun)

(4) RESIST REMOVAL
(4.1) **Resist strip** (In beakers) – Acetone and IPA followed by DI water
(4.2) **Mask drying** (N_2 gun)
(4.3) **Mask cleaning** (ATMsse OptiWet ST30)
Mask clean recipe using two piranha etching steps

A.2 ALIGNMENT MARK ETCHING

(5) WAFER MARKING
(5.1) **Wafer number** (Diamond-tip scribe)
Mark each wafer with its number

(6) PHOTOLITHOGRAPHY
(6.1) **Dehydration bake** (ATMsse OPTIhot HB20) – 2 min @ 180 °C
(6.2) **Particle removal** (N_2 gun)

(6.3) **HDMS coating** (ATMsse OPTIhot VB20)
(6.4) **Resist spinning** (ATMsse OPTIcoat SB20)
AZ1505 @ 4000 min^{-1} for 40 s
(6.5) **Resist baking** (ATMsse OPTIhot HB20) – 60 s at 110 °C
(6.6) **Resist exposure** (Süss MA6) – For 1.8 s (hard contact)
(6.7) **Resist development** (In a beaker) – AZ440K 1:4 for ca. 25 s
(6.8) **Rinsing** (In a beaker) – DI water
(6.9) **Wafer drying** (ATMsse OPTIspin SB20)

(7) DRY ETCHING

(7.1) **Particle removal** (N_2 gun)
(7.2) **Reactive ion etching** (Oxford PlasmaPro NPG 80)
Si etch (ca. 73 nm min^{-1}) for 85 s

(8) RESIST REMOVAL

(8.1) **Resist strip** (In beakers) – Acetone and IPA followed by DI water
(8.2) **Plasma ashing** (PVA Tepla GIGAbatch 310M) – At 600 W for 10 min

A.3 CONTACT DOPING

(9) CAP OXIDE DEPOSITION

(9.1) **Particle removal** (N_2 gun)
(9.2) **PECVD SiO_2 deposition** (STS MESC Multiplex CVD)
Ca. 20 nm SiO_2 deposition

(10) PHOTOLITHOGRAPHY

(10.1) **Dehydration bake** (ATMsse OPTIhot HB20) – 2 min @ 180 °C
(10.2) **Particle removal** (N_2 gun)
(10.3) **HDMS coating** (ATMsse OPTIhot VB20)
(10.4) **Resist spinning** (ATMsse OPTIcoat SB20)
AZ4533 @ 4000 min^{-1} for 40 s
(10.5) **Resist baking** (ATMsse OPTIhot HB20) – 60 s at 110 °C
(10.6) **Resist exposure** (Süss MA6) – For 8.2 s (hard contact)
(10.7) **Resist development** (In a beaker) – AZ440K 1:3 for ca. 60 s
(10.8) **Rinsing** (In a beaker) – DI water
(10.9) **Wafer drying** (ATMsse OPTIspin SB20)

(11) RESIST HARD BAKE

(11.1) **Bake on hotplate** (ATMsse OPTIhot HB20) – 1 min @ 120 °C

(11.2) **Bake in oven** (Heraeus UT 6060) – 25 min @ 140 °C

(12) ION IMPLANTATION

(12.1) *Service* **Ion beam implantation** (Ion Beam Services S.A.)
P (Boron) implant: $6 \times 10^{15}\,\mathrm{cm}^{-2}$ @ 30 keV - Tilt: 7°
N (Phosphorus) implant: $8 \times 10^{15}\,\mathrm{cm}^{-2}$ @ 80 keV - Tilt: 7°

(13) RESIST REMOVAL

(13.1) **Plasma ashing** (PVA Tepla GIGAbatch 310M) – At 600 W for 20 min

(14) DOPING ACTIVATION

(14.1) *Service* **RCA cleaning** (CMi EPFL)
Including HF dip[1]

(14.2) *Service* **Activation and drive-in (Furnace)** (CMi EPFL)
P (Boron) implant: 70 min @ 1000 °C
N (Phosphorus) implant: 50 min @ 1000 °C

A.4 WAFER BONDING

(15) BACKSIDE POLISHING

(15.1) *Service* **Grinding** (Optim Wafer Services)
Removal of 20 µm silicon

(15.2) *Service* **Chemical-mechanical polishing** (Optim Wafer Services)
To achieve the required surface roughness (see section 4.1.3)

(16) BONDING

(16.1) *Service* **Surface activated bonding** (EV Group)

---

[1] The RCA cleaning also included an HF-dip which removed the cap oxide before the thermal diffusion. This led to some surface damage during the diffusion step, mainly occurring on the P-type wafers. Transmission line model (TLM) measurements showed that the contact resistivity is still acceptable, despite the presence of these surface damages (see section 4.2.1). Any future process should have a protective oxide layer during doping annealing.

A.5 CONTACT METALLIZATION: N-SIDE

Note: These steps are carried out on the N-side of the bonded wafer pairs.

(17) PHOTOLITHOGRAPHY

(17.1) **Dehydration bake** (ATMsse OPTIhot HB20) – 3 min @ 180 °C
(17.2) **Particle removal** (N_2 gun)
(17.3) **Resist spinning** (ATMsse OPTIcoat SB20)
Lor5b @ 6000 min^{-1} for 60 s
(17.4) **Resist baking** (ATMsse OPTIhot HB20) – 5 min at 180 °C
(17.5) **Resist spinning** (ATMsse OPTIcoat SB20)
AZ1505 @ 4000 min^{-1} for 60 s
(17.6) **Resist baking** (ATMsse OPTIhot HB20) – 60 s at 110 °C
(17.7) **Resist exposure** (Süss MA6) – For 1.2 s (hard contact)
(17.8) **Resist development** (In a beaker) – AZ440K 1:4 for ca. 45 s
(17.9) **Rinsing** (In a beaker) – DI water
(17.10) **Wafer drying** (ATMsse OPTIspin SB20)
(17.11) **Plasma descum** (PVA Tepla GIGAbatch 310M)
At 200 W for 30 s (on Al plate)

(18) METAL DEPOSITION

(18.1) **Evaporation** (Evatec BAK501 LL)
2 min high etch
5 nm chromium
100 nm aluminium
20 nm gold

(19) LIFT OFF

(19.1) **Lift off** (DMSO in a beaker) – On a hotplate (140 °C) for ca. 1.5 h
(19.2) **Rinsing** (In a beaker) – DI water for at least 3 min
(19.3) **Wafer drying** (N_2 gun)
(19.4) **Cleaning** (In beakers)
Acetone followed by IPA in an ultrasonic bath
(19.5) **Wafer drying** (N_2 gun)

(20) PROTECTIVE COATING

(20.1) **Dehydration bake** (ATMsse OPTIhot HB20) – 3 min @ 180 °C

(20.2) **Resist spinning** (ATMsse OPTIcoat SB20)
AZ4533 @ 6000 min^{-1} for 40 s
(20.3) **Resist baking** (ATMsse OPTIhot HB20) – 60 s at 110 °C

A.6 CONTACT METALLIZATION: P-SIDE

Note: These steps are carried out on the P-side of the bonded wafer pairs.

(21) PHOTOLITHOGRAPHY

(21.1) **Particle removal** (N_2 gun)
(21.2) **HDMS coating** (ATMsse OPTIhot VB20)
(21.3) **Resist spinning** (ATMsse OPTIcoat SB20)
AZ4533 @ 6000 min^{-1} for 60 s
(21.4) **Resist baking** (ATMsse OPTIhot HB20) – 60 s at 110 °C
(21.5) **Resist exposure** (Süss MA6) – For 8.2 s (hard contact)
(21.6) **Resist development** (In a beaker) – AZ440K 1:3 for ca. 50 s
(21.7) **Rinsing** (In a beaker) – DI water
(21.8) **Wafer drying** (ATMsse OPTIspin SB20)
(21.9) **Plasma descum** (PVA Tepla GIGAbatch 310M)
At 200 W for 30 s

(22) METAL DEPOSITION

(22.1) **Evaporation** (Evatec BAK501 LL)
2 min high etch
5 nm chromium
100 nm aluminium
20 nm gold

(23) LIFT OFF

(23.1) **Lift off** (DMSO in a beaker) – On a hotplate (140 °C) for ca. 1.5 h
(23.2) **Rinsing** (In a beaker) – DI water for at least 3 min
(23.3) **Wafer drying** (N_2 gun)
(23.4) **Cleaning** (In beakers)
Acetone followed by IPA in an ultrasonic bath
(23.5) **Wafer drying** (N_2 gun)

A.7 DICING

(24) PROTECTIVE COATING

(24.1) **Cleaning** (In beakers)
Acetone followed by IPA in an ultrasonic bath
(24.2) **Wafer drying** (N_2 gun)
(24.3) **N-side coating** (ATMsse OPTIcoat SB20)
AZ4533 @ 6000 min^{-1} for 40 s
(24.4) **Resist baking** (ATMsse OPTIhot HB20) – 60 s at 110 °C
(24.5) **P-side coating** (ATMsse OPTIcoat SB20)
AZ4533 @ 6000 min^{-1} for 40 s
(24.6) **Resist baking** (ATMsse OPTIhot HB20) – 60 s at 110 °C

(25) DICING

(25.1) *Service* **Laser MicroJet® dicing** (Synova S.A.)
Followed by UV curing of the dicing tape

(26) DE-TAPING

(26.1) **Protective resist removal** (In beakers)
Acetone followed by IPA
(26.2) **Diode drying** (N_2 gun)

B

DERIVATION OF THE WEIGHTING VECTORS FOR THE BONDED SAMPLES

The derivations shown here follow the principle outlined in [4]. Figures B.1a and B.1b show the configurations under consideration in the case of a partially depleted P-side (case A) and a fully depleted P-side (case B) respectively. See section 2.4 for a discussion of the physical implications of the formulas derived here.

$D_\square$, $E_\square$ and $\epsilon_\square$ represent the displacement field, the electric field and the permittivity in a given region $\square$ respectively. $\epsilon = \epsilon_{Si}\epsilon_0$ represents the permittivity of silicon with $\epsilon_{Si} = 11.68$. $\sigma_\square$ and $d_\square$ represent the conductivity and the thickness of a given layer $\square$ respectively.

B.1 CASE A: PARTIALLY DEPLETED P-SIDE

In this case, the device is made up of three homogeneous regions (see figure B.1a): the undepleted and thus conductive N-side (subscript $\square_N$), the depleted and non-conductive part of the P-side (subscript $\square_D$), and the undepleted and conductive part of the P-side (subscript $\square_U$).

The continuity of the D field at the bonding interface gives

$$D_D = D_N \text{ and } \epsilon_D E_D = \epsilon_N E_N, \tag{B.1}$$

and the continuity of the D field within the P-side gives

$$D_D = D_U \text{ and } \epsilon_D E_D = \epsilon_U E_U. \tag{B.2}$$

The voltage across the device is given by

$$V = E_U d_U + E_D d_D + E_N d_N,^1 \tag{B.3}$$

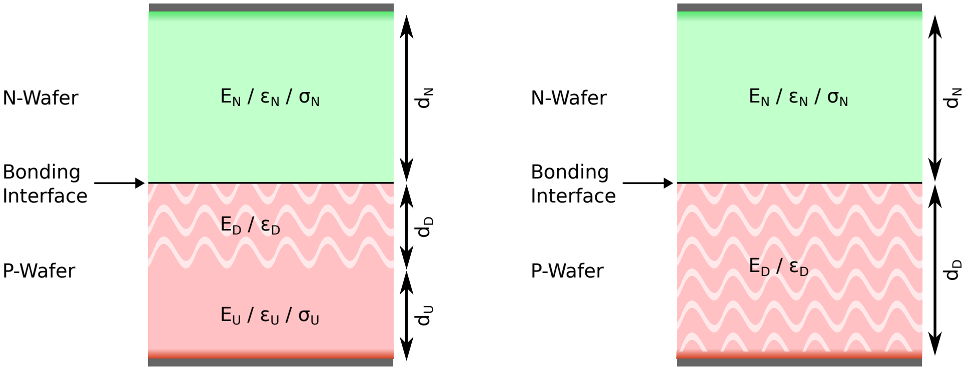

(a) Case A: Partially depleted P-side

(b) Case B: Fully depleted P-side

FIGURE B.1: Schematic view of the two cases taken into account for applying the extended Shockley-Ramo theorem to the fabricated bonded diodes. The depleted (non-conductive) layers are indicated by the white wave pattern. The remaining layers are non-depleted (conductive). Reprint of figure 8.3.

which, by using (B.1) and (B.2), can be rearranged to

$$V = E_D \frac{\epsilon_D}{\epsilon_U} d_U + E_D d_D + E_D \frac{\epsilon_D}{\epsilon_N} d_N$$

$$E_D = \frac{V}{d_D + d_U \frac{\epsilon_D}{\epsilon_U} + d_N \frac{\epsilon_D}{\epsilon_N}} = \frac{\epsilon_U \epsilon_N V}{d_D \epsilon_U \epsilon_N + d_U \epsilon_N \epsilon_D + d_N \epsilon_U \epsilon_D}. \tag{B.4}$$

Applying a Dirac voltage pulse $\mathcal{L}[V_0 \delta(t)] = V_0$ and replacing $\epsilon_N = \epsilon + \frac{\sigma_N}{s}$, $\epsilon_U = \epsilon + \frac{\sigma_P}{s}$ and $\epsilon_D = \epsilon$ (according to [4, 18]) leads to

$$W_V(s) = E_D(s)|_{V:=V_0} \tag{B.5}$$

$$= V_0 \frac{1}{d_D + \epsilon \left(\frac{d_U}{\epsilon + \frac{\sigma_P}{s}} + \frac{d_N}{\epsilon + \frac{\sigma_N}{s}} \right)}$$

$$= V_0 \frac{\left(\epsilon + \frac{\sigma_P}{s}\right) \left(\epsilon + \frac{\sigma_N}{s}\right)}{\left(\epsilon + \frac{\sigma_P}{s}\right) \left(\epsilon + \frac{\sigma_N}{s}\right) d_D + \epsilon d_U \left(\epsilon + \frac{\sigma_N}{s}\right) + \epsilon d_N \left(\epsilon + \frac{\sigma_P}{s}\right)}$$

$$= V_0 \frac{(\epsilon s + \sigma_P)(\epsilon s + \sigma_N)}{(\epsilon s + \sigma_P)(\epsilon s + \sigma_N) d_D + \epsilon s d_U (\epsilon s + \sigma_N) + \epsilon s d_N (\epsilon + \sigma_P)}. \tag{B.6}$$

---

1 The electric field within a given region is constant, as no charges are present (in the static case). As elaborated in section 2.3.1, the space charge created by reverse biasing the detector can be ignored for the application of the Shockley-Ramo theorem.

for the weighting vector in the active region (the depleted part of the P-side). Defining $d := d_U + d_D + d_N$, the denominator of (B.6) can be written as

$$\begin{aligned}
&(\epsilon s + \sigma_P)(\epsilon s + \sigma_N)d_D + \epsilon s d_U(\epsilon s + \sigma_N) + \epsilon s d_N(\epsilon + \sigma_P) \\
&\quad = d_D\epsilon^2 s^2 + d_U\epsilon^2 s^2 + d_N\epsilon^2 s^2 \\
&\qquad + d_D\epsilon s\sigma_N + d_D\epsilon s\sigma_P + d_U\epsilon s\sigma_N + d_N\epsilon s\sigma_P \\
&\qquad + d_D\sigma_P\sigma_N \\
&\quad = \epsilon^2 s^2(d_D + d_U + d_N) \\
&\qquad + \epsilon s(d_D\sigma_N + d_D\sigma_P + d_U\sigma_N + d_N\sigma_P) + d_D\sigma_P\sigma_N \\
&\quad = d\left(\epsilon^2 s^2 + \epsilon s\frac{d_D\sigma_N + d_D\sigma_P + d_U\sigma_N + d_N\sigma_P}{d} + \frac{d_D}{d}\sigma_P\sigma_N\right) \\
&\quad = d\left(\epsilon^2 s^2 + \epsilon s\frac{(d - d_N)\sigma_N + (d - d_U)\sigma_P}{d} + \frac{d_D}{d}\sigma_P\sigma_N\right).
\end{aligned} \tag{B.7}$$

This polynomial can be factorized as $d(\epsilon s + \lambda_1)(\epsilon s + \lambda_2)$ with

$$\begin{aligned}
\lambda_{1,2} = {} & \frac{(d - d_N)\sigma_N + (d - d_U)\sigma_P}{2d} \\
& \mp \frac{\sqrt{((d - d_N)\sigma_N + (d - d_U)\sigma_P)^2 - 4d_D d\sigma_P\sigma_N}}{2d}.
\end{aligned} \tag{B.8}$$

Using this factorization the original fraction (B.6) can be reformulated using partial fraction expansion

$$\begin{aligned}
W_V(s) &= \frac{V_0}{d}\frac{(\epsilon s + \sigma_P)(\epsilon s + \sigma_N)}{(\epsilon s + \lambda_1)(\epsilon s + \lambda_2)} = \frac{V_0}{d}\frac{\epsilon^2 s^2 + \epsilon s(\sigma_P + \sigma_N) + \sigma_P\sigma_N}{(\epsilon s + \lambda_1)(\epsilon s + \lambda_2)} \\
&= \frac{V_0}{d}\left(A + \frac{B}{\epsilon s + \lambda_1} + \frac{C}{\epsilon s + \lambda_2}\right) \\
&= \frac{V_0}{d}\left(\frac{A(\epsilon s + \lambda_1)(\epsilon s + \lambda_2) + B(\epsilon s + \lambda_2) + C(\epsilon s + \lambda_1)}{(\epsilon s + \lambda_1)(\epsilon s + \lambda_2)}\right) \\
&= \frac{V_0}{d}\left(\frac{\epsilon^2 s^2 A + \epsilon s(A(\lambda_1 + \lambda_2) + B + C) + (A\lambda_1\lambda_2 + B\lambda_2 + C\lambda_1)}{(\epsilon s + \lambda_1)(\epsilon s + \lambda_2)}\right),
\end{aligned} \tag{B.9}$$

leading to the following set of equations

$$1 = A \tag{B.10}$$

$$\sigma_P + \sigma_N = A(\lambda_1 + \lambda_2) + B + C \tag{B.11}$$

$$\sigma_P\sigma_N = A\lambda_1\lambda_2 + B\lambda_2 + C\lambda_1. \tag{B.12}$$

From the factorization of the denominator polynomial one obtains

$$\lambda_1 + \lambda_2 = \frac{(d-d_N)\sigma_N + (d-d_U)\sigma_P}{d} \tag{B.13}$$

$$\lambda_1\lambda_2 = \frac{d_D}{d}\sigma_P\sigma_N, \tag{B.14}$$

and using the ansatz $B = b\lambda_1$ and $C = c\lambda_2$ leads to

$$\sigma_P + \sigma_N = (1+b)\lambda_1 + (1+c)\lambda_2 \tag{B.15}$$

$$\sigma_P\sigma_N = (1+b+c)\lambda_1\lambda_2 = (1+b+c)\frac{d_D}{d}\sigma_P\sigma_N, \tag{B.16}$$

which can be simplified

$$b\lambda_1 + c\lambda_2 = \frac{d_N}{d}\sigma_N + \frac{d_U}{d}\sigma_P \tag{B.17}$$

$$1+b+c = \frac{d}{d_D} = \frac{d_D + d_U + d_P}{d_D}. \tag{B.18}$$

Thus, b and c are the solutions of the following linear system

$$\begin{pmatrix} \lambda_1 & \lambda_2 \\ 1 & 1 \end{pmatrix} \begin{pmatrix} b \\ c \end{pmatrix} = \begin{pmatrix} \frac{d_N}{d}\sigma_N + \frac{d_U}{d}\sigma_P \\ \frac{d_U}{d_D} + \frac{d_P}{d_D} \end{pmatrix} \tag{B.19}$$

$W_V(s)$ thus takes the form

$$\begin{aligned} W_V(s) &= \frac{V_0}{d}\left(1 + \frac{b\lambda_1}{\epsilon s + \lambda_1} + \frac{c\lambda_2}{\epsilon s + \lambda_2}\right) \\ &= \frac{V_0}{d}\left(1 + \frac{b}{\tau_1}\frac{1}{s+\frac{1}{\tau_1}} + \frac{c}{\tau_2}\frac{1}{s+\frac{1}{\tau_2}}\right) \end{aligned} \tag{B.20}$$

with $\tau_1 = \frac{\epsilon}{\lambda_1}$ and $\tau_2 = \frac{\epsilon}{\lambda_2}$. Applying the inverse Laplace transform, one obtains

$$W_V(t) = \mathcal{L}^{-1}[W_V(s)] = \frac{V_0}{d}\left(\delta(t) + b\frac{1}{\tau_1}e^{-\frac{t}{\tau_1}}\Theta(t) + c\frac{1}{\tau_2}e^{-\frac{t}{\tau_2}}\Theta(t)\right) \tag{B.21}$$

with $\Theta(t)$ the Heaviside step function.

The Dirac $\delta(t)$ term corresponds to the prompt response to the drifting charges, which is equivalent to the traditional Shockley-Ramo theorem. The two exponential terms represent the response from the two non-depleted and thus conductive layers.

B.2 CASE B: FULLY DEPLETED P-SIDE

In this case, the device is made up of two homogenous regions (see figure B.1b): the undepleted and thus conductive N-side (subscript $\square_N$), and the depleted and non-conductive P-side (subscript $\square_D$). The mathematical derivation is analogous to the case A.

The continuity of the D field at the bonding interface gives

$$\epsilon_D E_D = \epsilon_N E_N. \tag{B.22}$$

Thus, the voltage across the device

$$V = E_D d_D + E_N d_N \tag{B.23}$$

can be rearranged as

$$\begin{aligned} V &= E_D d_D + E_D \frac{\epsilon_D}{\epsilon_N} d_N \\ E_D &= \frac{V}{d_D + d_N \frac{\epsilon_D}{\epsilon_N}} = \frac{\epsilon_N V}{d_D \epsilon_N + d_N \epsilon_D}. \end{aligned} \tag{B.24}$$

Applying a Dirac voltage pulse $\mathcal{L}[V_0 \delta(t)] = V_0$ and replacing $\epsilon_N = \epsilon + \frac{\sigma_N}{s}$ and $\epsilon_D = \epsilon$ (according to [4, 18]) leads to

$$\begin{aligned} W_V(s) = E_D(s)|_{V:=V_0} &= V_0 \frac{\epsilon + \frac{\sigma_N}{s}}{d_D \epsilon + d_D \frac{\sigma_N}{s} + d_N \epsilon} \\ &= V_0 \frac{\epsilon s + \sigma_N}{\epsilon s d_D + d_D \sigma_N + d_N \epsilon s} \\ &= \frac{V_0}{d_D + d_N} \frac{(d_D + d_N)\epsilon s + \sigma_N d_D + \sigma_N d_N}{(d_D + d_N)\epsilon s + \sigma_N d_D} \\ &= \frac{V_0}{d_D + d_N} \left(1 + \frac{\sigma_N d_N}{(d_D + d_N)\epsilon s + \sigma_N d_D} \right) \\ &= \frac{V_0}{d_D + d_N} \left(1 + \frac{\sigma_N d_N}{(d_D + d_N)\epsilon} \frac{1}{s + \frac{d_D \sigma_N}{(d_D + d_N)\epsilon}} \right) \end{aligned} \tag{B.25}$$

for the weighting vector in the active region (the fully depleted P-side). With $d := d_N + d_D$ and $\tau = \frac{(d_N + d_D)\epsilon}{d_D \sigma_N} = \frac{d\epsilon}{d_D \sigma_N}$ this can be written as

$$W_V(s) = \frac{V_0}{d} \left(1 + \frac{d_N}{d_D} \frac{1}{\tau} \frac{1}{s + \frac{1}{\tau}} \right) \tag{B.26}$$

Finally, applying the inverse Laplace transform gives

$$W_V(t) = \mathcal{L}^{-1}[W_V(s)] = \frac{V_0}{d}\left(\delta(t) + \frac{d_N}{d_D}\frac{1}{\tau}e^{-\frac{t}{\tau}}\Theta(t)\right) \tag{B.27}$$

with $\Theta(t)$ the Heaviside step function.

The Dirac $\delta(t)$ term again represents the prompt response to the drifting charges, equivalent to the traditional Shockley-Ramo theorem. The exponential term represents the response due to the conductive N layer.

LIST OF ACRONYMS

AC	Alternating current
Al	Aluminium
Am-241	Americium-241
AP2	Allpix Squared
APD	Avalanche photodiode
Ar	Argon
Au	Gold
B	Boron
BNP	BigNovipix
BRNC	Binning and Rohrer Nanotechnology Center
CAD	Computer-aided design
C	Carbon
CdTe	Cadmium telluride
CdZTe	Cadmium zinc telluride
CERN	European Organization for Nuclear Research
CLI	Command line interface
CMi	Center of MicroNanoTechnology at EPFL
CMOS	Complementary metal-oxide-semiconductor
CMP	Chemical mechanical polishing
Cr	Chromium
Cr	Chromium
CSA	Charge sensitive amplifier
CSEM	Swiss Center for Electronics and Microtechnology
CSV	Comma-separated values
DC	Direct current
DMAPS	Depleted monolithic active pixel sensors

DMSO	Dimethyl sulfoxide
DUT	Device under test
EDXS	Energy-dispersive X-ray spectroscopy
ENIG	Electroless nickel immersion gold
EPFL	École polytechnique fédérale de Lausanne
ERF	Error function
ETHZ	Eidgenössische Technische Hochschule Zürich
EVG	EV Group
FEA	Finite element analysis
Fe	Iron
F	Fluorine
FIB	Focused ion beam
FPGA	Field-programmable gate array
FWHM	Full width at half maximum
GaAs	Gallium arsenide
Ge	Germanium
GND	Ground (electrical)
G-Ray	G-Ray Medical Sàrl
GUI	Graphical user interface
HASL	Hot air solder leveling
HDF5	Hierarchical Data Format 5
HF	Hydrofluoric acid
HV	High-voltage
IP	Internet Protocol
IR	Infrared
LGAD	Low gain avalanche detector
LHC	Large Hadron Collider
LIDAR	Light detection and ranging
MAPS	Monolithic active pixel sensors
MEMS	Microelectromechanical systems

MICROMEGAS	Micromesh gaseous detectors
MIP	Minimum ionizing particle
Ne	Neon
Ni	Nickel
NOVIPIX	Novel Integrated Pixel X-ray Detectors
O	Oxygen
PCB	Printed circuit board
PDF	Portable Document Format
PECVD	Plasma-enhanced chemical vapor deposition
PID	Proportional-integral-derivative controller
PMT	Photomultiplier tube
P	Phosphorus
PR	Photoresist
PSL	Photostimulated luminescence
PTB	Physikalisch-Technische Bundesanstalt
PTFE	Teflon
RIE	Reactive-ion etching
RMS	Root mean square
RPC	Resistive plate chambers
SAB	Surface activated bonding
SAM	Scanning acoustic microscopy
ScopeM	The Scientific Center for Optical and Electron Microscopy
SEM	Scanning electron microscope
Sentaurus	Synopsys Sentaurus TCAD
SiGe	Silicon-germanium
Silvaco	Silvaco TCAD
Si	Silicon
SMU	Source measure unit
SNF	Swiss National Science Foundation

SOI	Silicon on insulator
SPAD	Single-photon avalanche diode
S-parameters	Scattering parameters
SPICE	Simulation Program with Integrated Circuit Emphasis
SRIM	Stopping and Range of Ions in Matter
SSH	Secure Shell Protocol
STEM	Scanning transmission electron microscope
TCAD	Technology computer-aided design
TCode	TimeSPOT Code for Detector simulation
TCT	Transient current technique
TEM	Transmission electron microscope
Ti	Titanium
TLM	Transmission line model
TPA	Two photon absorption
TXRF	Total reflection X-ray fluorescence spectroscopy
USB	Universal Serial Bus
VNA	Vector network analyser
W	Tungsten
XRII	X-ray image intensifier

BIBLIOGRAPHY

1. Noether, E. Invariante Variationsprobleme. deu. *Nachrichten von der Gesellschaft der Wissenschaften zu Göttingen, Mathematisch-Physikalische Klasse* **1918**, 235. `https://eudml.org/doc/59024` (2023) (1918).
2. Lederman, L. M. & Hill, C. T. *Symmetry and the beautiful universe* ISBN: 978-1-59102-242-8 (Prometheus Books, Amherst, N.Y, 2004).
3. Kimberling, C. Emmy Noether, Greatest Woman Mathematician. *The Mathematics Teacher* **75**, 246. doi:`10.5951/MT.75.3.0246` (1982).
4. Riegler, W. An application of extensions of the Ramo–Shockley theorem to signals in silicon sensors. *Nuclear Instruments and Methods in Physics Research Section A: Accelerators, Spectrometers, Detectors and Associated Equipment* **940**, 453. doi:`10.1016/j.nima.2019.06.056` (2019).
5. Glasser, O. *Wilhelm Conrad Röntgen und die Geschichte der Röntgenstrahlen* de. doi:`10.1007/978-3-642-79312-7` (Springer, Berlin, Heidelberg, 1995).
6. Seibert, J. A. Flat-panel detectors: how much better are they? *Pediatric Radiology* **36**, 173. doi:`10.1007/s00247-006-0208-0` (2006).
7. Parks, E. T. & Williamson, G. F. Digital Radiography: An Overview. *The Journal of Contemporary Dental Practice* **3**, 23. doi:`10.5005/jcdp-3-4-23` (2005).
8. Hoheisel, M. Review of medical imaging with emphasis on X-ray detectors. *Nuclear Instruments and Methods in Physics Research Section A: Accelerators, Spectrometers, Detectors and Associated Equipment*. *Proceedings of the 7th International Workshop on Radiation Imaging Detectors* **563**, 215. doi:`10.1016/j.nima.2006.01.123` (2006).
9. Panta, R. K. *et al. First human imaging with MARS photon-counting CT* in *2018 IEEE Nuclear Science Symposium and Medical Imaging Conference Proceedings (NSS/MIC)* (2018), 1. doi:`10.1109/NSSMIC.2018.8824513`.
10. Knoll, G. F. *Radiation detection and measurement* ISBN: 978-0-470-13148-0 (John Wiley & Sons, 2010).

11. *Technical Design Report for the ATLAS Inner Tracker Pixel Detector* eng. Tech. rep. ATL-TDR-030 (CERN, Geneva, 2017). `https://cds.cern.ch/record/2285585/`.
12. Yarema, R. *Advances in Bonding Technologies* University of Bonn, 2014. `https://indico.cern.ch/event/309449/contributions/1679992/`.
13. Kolanoski, H. & Wermes, N. *Particle detectors: fundamentals and applications* First edition. ISBN: 978-0-19-885836-2 (Oxford University Press, Oxford ; New York, NY, 2020).
14. Jung, A. S. *SiGe/Si Epitaxy and Wafer Bonding Applied to X-ray Detectors* PhD thesis (ETH Zurich, 2018). doi:`10.3929/ethz-b-000275347`.
15. Razek, N. *et al.* Low temperature covalent wafer bonding for X-ray imaging detectors. *Japanese Journal of Applied Physics*. doi:`10.7567/1347-4065/ab4970` (2019).
16. Gröning, P., Despont, M. & von Känel, H. *Novel Integrated Pixel X-ray Detectors 'NOVIPIX' - SNF Grant 147639* 2013. `https://data.snf.ch/grants/grant/147639` (2023).
17. Sze, S. M. & Ng, K. K. *Physics of semiconductor devices* 3rd ed. ISBN: 978-0-471-14323-9 (Wiley-Interscience, Hoboken, N.J, 2007).
18. Riegler, W. Induced signals in resistive plate chambers. *Nuclear Instruments and Methods in Physics Research Section A: Accelerators, Spectrometers, Detectors and Associated Equipment* **491**, 258. doi:`10.1016/S0168-9002(02)01169-5` (2002).
19. Riegler, W. Extended theorems for signal induction in particle detectors VCI 2004. *Nuclear Instruments and Methods in Physics Research Section A: Accelerators, Spectrometers, Detectors and Associated Equipment. Proceedings of the 10th International Vienna Conference on Instrumentation* **535**, 287. doi:`10.1016/j.nima.2004.07.129` (2004).
20. Delpierre, P. A history of hybrid pixel detectors, from high energy physics to medical imaging. *Journal of Instrumentation* **9**, C05059. doi:`10.1088/1748-0221/9/05/C05059` (2014).
21. Groom, D. E., Mokhov, N. V. & Striganov, S. I. MUON STOPPING POWER AND RANGE TABLES 10 MeV–100 TeV. *Atomic Data and Nuclear Data Tables* **78**, 183. doi:`10.1006/adnd.2001.0861` (2001).
22. Lechner, A. Particle Interactions with Matter. *CERN Yellow Reports: School Proceedings* **5**, 47. doi:`10.1201/9780429488887-7` (2018).

23. Seltzer, S. *XCOM-Photon Cross Sections Database, NIST Standard Reference Database 8* 1987. doi:`10.18434/T48G6X`.

24. Jochelson, M. S. & Lobbes, M. B. I. Contrast-enhanced Mammography: State of the Art. *Radiology* **299**, 36. doi:`10.1148/radiol.2021201948` (2021).

25. Fang, J. *et al.* Understanding the Average Electron–Hole Pair-Creation Energy in Silicon and Germanium Based on Full-Band Monte Carlo Simulations. *IEEE Transactions on Nuclear Science* **66**, 444. doi:`10.1109/TNS.2018.2879593` (2019).

26. Bussolati, C., Fiorentini, A. & Fabri, G. Energy for Electron-Hole Pair Generation in Silicon by Electrons and α Particles. *Physical Review* **136**, A1756. doi:`10.1103/PhysRev.136.A1756` (1964).

27. Bertuccio, G. & Maiocchi, D. Electron-hole pair generation energy in gallium arsenide by x and γ photons. *Journal of Applied Physics* **92**, 1248. doi:`10.1063/1.1490158` (2002).

28. Chiodini, G. *Diamond particle detectors for high energy physics* in *2011 4th IEEE International Workshop on Advances in Sensors and Interfaces (IWASI)* (2011), 37. doi:`10.1109/IWASI.2011.6004682`.

29. Moffat, N. *et al.* Low Gain Avalanche Detectors (LGAD) for particle physics and synchrotron applications. *Journal of Instrumentation* **13**, C03014. doi:`10.1088/1748-0221/13/03/C03014` (2018).

30. Zhao, Y. *et al.* A new approach to achieving high granularity for silicon diode detectors with impact ionization gain. *Journal of Physics: Conference Series* **2374**, 012171. doi:`10.1088/1742-6596/2374/1/012171` (2022).

31. Riegler, W. & Windischhofer, P. Time resolution and efficiency of SPADs and SiPMs for photons and charged particles. *Nuclear Instruments and Methods in Physics Research Section A: Accelerators, Spectrometers, Detectors and Associated Equipment* **1003**, 165265. doi:`10.1016/j.nima.2021.165265` (2021).

32. Shockley, W. Currents to Conductors Induced by a Moving Point Charge. *Journal of Applied Physics* **9**, 635. doi:`10.1063/1.1710367` (1938).

33. Ramo, S. Currents Induced by Electron Motion. *Proceedings of the IRE* **27**, 584. doi:`10.1109/JRPROC.1939.228757` (1939).

34. Cavalleri, G., Gatti, E., Fabri, G. & Svelto, V. Extension of Ramo's theorem as applied to induced charge in semiconductor detectors. *Nuclear Instruments and Methods* **92**, 137. doi:`10.1016/0029-554X(71)90235-7` (1971).
35. He, Z. Review of the Shockley–Ramo theorem and its application in semiconductor gamma-ray detectors. *Nuclear Instruments and Methods in Physics Research Section A: Accelerators, Spectrometers, Detectors and Associated Equipment* **463**, 250. doi:`10.1016/S0168-9002(01)00223-6` (2001).
36. Rolandi, L., Riegler, W. & Blum, W. *Particle Detection with Drift Chambers* doi:`10.1007/978-3-540-76684-1` (Springer, Berlin, Heidelberg, 2008).
37. Gatti, E., Padovini, G. & Radeka, V. Signal evaluation in multielectrode radiation detectors by means of a time dependent weighting vector. *Nuclear Instruments and Methods in Physics Research* **193**, 651. doi:`10.1016/0029-554X(82)90265-8` (1982).
38. Janssens, D. *et al.* Induced signals in particle detectors with resistive elements: Numerically modeling novel structures (VCI 2022). *Nuclear Instruments and Methods in Physics Research Section A: Accelerators, Spectrometers, Detectors and Associated Equipment* **1040**, 167227. doi:`10.1016/j.nima.2022.167227` (2022).
39. Janssens, D. *et al. Studying signals in particle detectors with resistive elements such as the 2D resistive strip bulk MicroMegas* 2023. `http://arxiv.org/abs/2304.01883` (2023).
40. Garcia-Sciveres, M. & Wermes, N. A review of advances in pixel detectors for experiments with high rate and radiation. *Reports on Progress in Physics* **81**, 066101. doi:`10.1088/1361-6633/aab064` (2018).
41. Abbott, B. *et al.* Production and integration of the ATLAS Insertable B-Layer. *Journal of Instrumentation* **13**, T05008. doi:`10.1088/1748-0221/13/05/T05008` (2018).
42. Dominguez, A. & et al. *CMS Technical Design Report for the Pixel Detector Upgrade* tech. rep. FERMILAB-DESIGN-2012-02, 1151650 (2012). doi:`10.2172/1151650`.
43. DECTRIS AG. *DIRECT Detection - Dectris* 2023. `https://www.dectris.com/technology/hybrid-photon-counting/direct-detection/` (2023).

44. ALICE ITS project. First demonstration of in-beam performance of bent Monolithic Active Pixel Sensors. *Nuclear Instruments and Methods in Physics Research Section A: Accelerators, Spectrometers, Detectors and Associated Equipment* **1028**, 166280. doi:`10.1016/j.nima.2021.166280` (2022).

45. Zhang, C. *et al.* A 30-frames/s, 252x144 SPAD Flash LiDAR With 1728 Dual-Clock 48.8-ps TDCs, and Pixel-Wise Integrated Histogramming. *IEEE Journal of Solid-State Circuits* **54**, 1137. doi:`10.1109/JSSC.2018.2883720` (2019).

46. Franssila, S. *Introduction to microfabrication* 2nd ed. ISBN: 978-0-470-74983-8 (John Wiley & Sons, Chichester, West Sussex [England], 2010).

47. Prince, J., Draper, B., Rapp, E., Kronberg, J. & Fitch, L. Performance of Digital Integrated Circuit Technologies at Very High Temperatures. *IEEE Transactions on Components, Hybrids, and Manufacturing Technology* **3**, 571. doi:`10.1109/TCHMT.1980.1135643` (1980).

48. Geis, M. W. *et al.* CMOS-Compatible All-Si High-Speed Waveguide Photodiodes With High Responsivity in Near-Infrared Communication Band. *IEEE Photonics Technology Letters* **19**, 152. doi:`10.1109/LPT.2006.890109` (2007).

49. Takagi, H. in *3D and Circuit Integration of MEMS* (ed Esashi, M.) 279 (Wiley-VCH, 2021). ISBN: 978-3-527-34647-9. `https://onlinelibrary.wiley.com/doi/10.1002/9783527823239.ch12`.

50. Plößl, A. & Kräuter, G. Wafer direct bonding: tailoring adhesion between brittle materials. *Materials Science and Engineering: R: Reports* **25**, 1. doi:`10.1016/S0927-796X(98)00017-5` (1999).

51. Wang, Y. *et al.* A review of silicon-based wafer bonding processes, an approach to realize the monolithic integration of Si-CMOS and III–V-on-Si wafers, 20 (2020).

52. Bronuzzi, J. *Transient Current Technique Characterization of Bonded Interfaces for Monolithic Silicon Detectors* PhD thesis (EPFL, CERN, 2018).

53. Puers, R. & Cozma, A. Bonding wafers with sodium silicate solution. *Journal of Micromechanics and Microengineering* **7**, 114. doi:`10.1088/0960-1317/7/3/008` (1997).

54. Dragoi, V., Rebhan, B. & Pabo, E. Direct Wafer Bonding Methods: A Practical Process Selection Guide. *ECS Transactions* **98**, 33. doi:`10.1149/09804.0033ecst` (2020).

55. Takagi, H., Kikuchi, K., Maeda, R., Chung, T. R. & Suga, T. Surface activated bonding of silicon wafers at room temperature. *Applied Physics Letters* **68**, 2222. doi:`10.1063/1.115865` (1996).
56. Takagi, H., Maeda, R. & Suga, T. Wafer-scale spontaneous bonding of silicon wafers by argon-beam surface activation at room temperature. *Sensors and Actuators A: Physical* **105**, 98. doi:`10.1016/S0924-4247(03)00087-6` (2003).
57. Liang, J., Miyazaki, T., Morimoto, M., Nishida, S. & Shigekawa, N. Electrical properties of Si/Si interfaces by using surface-activated bonding. *Journal of Applied Physics* **114**, 183703. doi:`10.1063/1.4829676` (2013).
58. Rebhan, B., Vanpaemel, J. & Dragoi, V. 200 mm Ge Wafer Production for Oxide-Free Si-Ge Direct Wafer Bonding. *ECS Transactions* **98**, 87. doi:`10.1149/09804.0087ecst` (2020).
59. Higurashi, E. *et al.* Room-temperature direct bonding of germanium wafers by surface-activated bonding method. *Japanese Journal of Applied Physics* **54**, 030213. doi:`10.7567/JJAP.54.030213` (2015).
60. Uehigashi, Y. *et al.* Electrical properties of Si/diamond heterojunction diodes fabricated by using surface activated bonding. *Diamond and Related Materials* **130**, 109425. doi:`10.1016/j.diamond.2022.109425` (2022).
61. Liang, J. *et al.* Annealing effect of surface-activated bonded diamond/Si interface. *Diamond and Related Materials* **93**, 187. doi:`10.1016/j.diamond.2019.02.015` (2019).
62. Wüthrich, J. & Rubbia, A. On the depletion behaviour of low-temperature covalently bonded silicon sensor diodes. *Journal of Instrumentation* **17**, C10015. doi:`10.1088/1748-0221/17/10/C10015` (2022).
63. Ohno, Y. *et al.* Chemical bonding at room temperature via surface activation to fabricate low-resistance GaAs/Si heterointerfaces. *Applied Surface Science* **525**, 146610. doi:`10.1016/j.apsusc.2020.146610` (2020).
64. Pönninger, A. *Oxide Free Direct Wafer Bonding* Chemnitz, 2015. `https://www.enas.fraunhofer.de/content/dam/enas/Dokumente/Deutsch/News_Events/ChemnitzerSeminare/Seminar_22_SP_2015/Oxide%20Free%20Direct%20Wafer%20Bonding.pdf` (2023).

65. Essig, S. *et al.* Fast atom beam-activated n-Si/n-GaAs wafer bonding with high interfacial transparency and electrical conductivity. *Journal of Applied Physics* **113,** 203512. doi:`10.1063/1.4807905` (2013).

66. Vallin, Ö., Jonsson, K. & Lindberg, U. Adhesion quantification methods for wafer bonding. *Materials Science and Engineering: R: Reports* **50,** 109. doi:`10.1016/j.mser.2005.07.002` (2005).

67. Maszara, W. P., Goetz, G., Caviglia, A. & McKitterick, J. B. Bonding of silicon wafers for silicon-on-insulator. *Journal of Applied Physics* **64,** 4943. doi:`10.1063/1.342443` (1988).

68. Takagi, H., Maeda, R., hosoda, N. & Suga, T. Transmission Electron Microscope Observations of Si/Si Interface Bonded at Room Temperature by Ar Beam Surface Activation. *Japanese Journal of Applied Physics* **38,** 1589. doi:`10.1143/JJAP.38.1589` (1999).

69. Morimoto, M., Liang, J., Nishida, S. & Shigekawa, N. Effects of annealing on electrical properties of Si/Si junctions by surface-activated bonding. *Japanese Journal of Applied Physics* **54,** 030212. doi:`10.7567/JJAP.54.030212` (2015).

70. Reznicek, A., Senz, S., Breitenstein, O., Scholz, R. & Gösele, U. Electrical characterisation of UHV-bonded silicon interfaces. *MRS Proceedings* **681.** doi:`10.1557/proc-681-i4.4` (2001).

71. Shigekawa, N., Watanabe, N. & Higurashi, E. *Electrical properties of Si-based junctions by SAB* in *2012 3rd IEEE International Workshop on Low Temperature Bonding for 3D Integration* (2012), 109. doi:`10.1109/LTB-3D.2012.6238065`.

72. Frenkel, J. On Pre-Breakdown Phenomena in Insulators and Electronic Semi-Conductors. *Physical Review* **54,** 647. doi:`10.1103/PhysRev.54.647` (1938).

73. Predan, F., Reinwand, D., Cariou, R., Niemeyer, M. & Dimroth, F. Direct wafer bonding of highly conductive GaSb/GaInAs and GaSb/GaInP heterojunctions prepared by argon-beam surface activation. *Journal of Vacuum Science & Technology A* **34,** 031103. doi:`10.1116/1.4947118` (2016).

74. Predan, F. *et al.* Effects of thermal annealing on structural and electrical properties of surface-activated n-GaSb/n-GaInP direct wafer bonds. *Journal of Applied Physics* **122,** 135307. doi:`10.1063/1.5002080` (2017).

75. Predan, F., Mueller, R., Hoehn, O., Lackner, D. & Dimroth, F. *Direct wafer bonding for the realization of transparent and electrically conductive heterojunctions in III-V solar cells with highest efficiencies (Conference Presentation)* in *Photonics for Solar Energy Systems VIII* **11366** (International Society for Optics and Photonics, 2020), 1136608. doi:`10.1117/12.2557979`.
76. Takagi, H., Kurashima, Y. & Suga, T. (Invited) Surface Activated Wafer Bonding; Principle and Current Status. *ECS Transactions* **75**, 3. doi:`10.1149/07509.0003ecst` (2016).
77. Han, S. *et al.* Integration of Subcells in III-V//Si Tandem Solar Cells. *Transactions on Electrical and Electronic Materials* **24**, 132. doi:`10.1007/s42341-023-00430-2` (2023).
78. Cariou, R. *et al.* III–V-on-silicon solar cells reaching 33% photoconversion efficiency in two-terminal configuration. *Nature Energy* **3**, 326. doi:`10.1038/s41560-018-0125-0` (2018).
79. Lackner, D. *et al.* Two-Terminal Direct Wafer-Bonded GaInP/AlGaAs//Si Triple-Junction Solar Cell with AM1.5g Efficiency of 34.1%. *Solar RRL* **4**, 2000210. doi:`10.1002/solr.202000210` (2020).
80. Zhang, P., Li, C., He, M., Liu, Z. & Hao, X. The Intermediate Connection of Subcells in Si-based Tandem Solar Cells. *Small Methods*, 2300432. doi:`10.1002/smtd.202300432` (2023).
81. Känel, H. V. Merging incompatible materials. *Europhysics News* **43**, 18. doi:`10.1051/epn/2012402` (2012).
82. Falub, C. V. *et al.* Scaling Hetero-Epitaxy from Layers to Three-Dimensional Crystals. *Science* **335**, 1330. doi:`10.1126/science.1217666` (2012).
83. Arroyo Rojas Dasilva, Y. *et al.* Strain relaxation in epitaxial Ge crystals grown on patterned Si(001) substrates. *Scripta Materialia* **127**, 169. doi:`10.1016/j.scriptamat.2016.09.003` (2017).
84. Arroyo, R. D. *et al.* Effect of thermal annealing on the interface quality of Ge/Si heterostructures. *Scripta Materialia* **170**, 52. doi:`10.1016/j.scriptamat.2019.05.025` (2019).
85. Meduňa, M., Caha, O., Choumas, E., Bressan, F. & von Känel, H. X-ray rocking curve imaging on large arrays of extremely tall SiGe microcrystals epitaxial on Si. *Journal of Applied Crystallography* **54**, 1071. doi:`10.1107/S1600576721004969` (2021).

86. Pike, G. & Seager, C. Dc voltage dependence of semiconductor grain-boundary resistance. *Journal of Applied Physics* **50**, 3414. ISSN: 0021-8979 (1979).

87. Razek, N. *et al. Low temperature covalent wafer bonding for X-ray imaging detectors* in *2019 6th International Workshop on Low Temperature Bonding for 3D Integration (LTB-3D)* (2019), 30. doi:`10.23919/LTB-3D.2019.8735288`.

88. Neves, J. *Towards wafer-scale monolithic CMOS integrated pixel detectors for X-ray photon counting* Vienna, 2019. `https://indico.cern.ch/event/716539/contributions/3246033/` (2019).

89. Flotgen, C., Razek, N., Dragoi, V. & Wimplinger, M. Novel Surface Preparation Methods for Covalent and Conductive Bonded Interfaces Fabrication. *ECS Transactions* **64**, 103. doi:`10.1149/06405.0103ecst` (2014).

90. EV Group (EVG). *EVG ComBond Brochure* 2020. `https://www.evgroup.com/fileadmin/media/products/bonding/Permanent_Bonding/combond/EVG_ComBond_Brochure.pdf` (2023).

91. De Cilladi, L., Corradino, T., Dalla Betta, G.-F., Neubüser, C. & Pancheri, L. Fully Depleted Monolithic Active Microstrip Sensors: TCAD Simulation Study of an Innovative Design Concept. *Sensors* **21**, 1990. doi:`10.3390/s21061990` (2021).

92. Wüthrich, J. *First results with novel pixel detectors based on wafer-wafer bonding* Vienna, 2020. `https://indico.cern.ch/event/813597/contributions/3727951/` (2023).

93. Lüth, H. *Solid Surfaces, Interfaces and Thin Films* doi:`10.1007/978-3-319-10756-1` (Springer International Publishing, Cham, 2015).

94. Glawischnig, H. & Parks, C. *SIMS and modeling of ion implants into photoresist* in *Proceedings of 11th International Conference on Ion Implantation Technology* (1996), 579. doi:`10.1109/IIT.1996.586457`.

95. Zhang, J. *et al.* Development of LGAD sensors with a thin entrance window for soft X-ray detection. *Journal of Instrumentation* **17**, C11011. doi:`10.1088/1748-0221/17/11/C11011` (2022).

96. *SEMI M1-0918: Specification for Polished Single Crystal Silicon Wafers* 2018. `https://store-us.semi.org/products/m00100-semi-m1-specification-for-polished-single-crystal-silicon-wafers`.

97. Deen, M. J. & Pascal, F. in *Springer Handbook of Electronic and Photonic Materials* (eds Kasap, S. & Capper, P.) 1 (Springer International Publishing, Cham, 2017). doi:`10.1007/978-3-319-48933-9_20`.

98. Goetzberger, A. *et al. Research and investigation of inverse epitaxial UHF power transistors* Technical Documentary Report AL TDR 64-207 (AF Avionics Laboratory, Research and Technology Division, Air Force Systems Command, Wright-Patterson Air Force Base, Ohio, 1964), 152. `https://apps.dtic.mil/docs/citations/AD0605376` (2020).

99. Wüthrich, J., Alt, C. & Rubbia, A. TCT investigation of the one-sided depletion of low-temperature covalently bonded silicon sensor P-N diodes. *Journal of Instrumentation* **18**, P05004. doi:`10.1088/1748-0221/18/05/P05004` (2023).

100. Ohno, Y. *et al.* Impact of focused ion beam on structural and compositional analysis of interfaces fabricated by surface activated bonding. *Japanese Journal of Applied Physics*. doi:`10.7567/1347-4065/ab4b15` (2019).

101. Liang, J. *et al.* Characterization of Nanoscopic Cu/Diamond Interfaces Prepared by Surface-Activated Bonding: Implications for Thermal Management. *ACS Applied Nano Materials*. doi:`10.1021/acsanm.9b02558` (2020).

102. Goldstein, J. I. *et al. Scanning Electron Microscopy and X-Ray Microanalysis* doi:`10.1007/978-1-4939-6676-9` (Springer, New York, NY, 2018).

103. Beckhoff, B. *et al.* Reference-Free Total Reflection X-ray Fluorescence Analysis of Semiconductor Surfaces with Synchrotron Radiation. *Analytical Chemistry* **79**, 7873. doi:`10.1021/ac071236p` (2007).

104. Hönicke, P. *et al.* Development and characterization of sub-monolayer coatings as novel calibration samples for X-ray spectroscopy. *Spectrochimica Acta Part B: Atomic Spectroscopy* **145**, 36. doi:`10.1016/j.sab.2018.04.001` (2018).

105. Krumrey, M. & Ulm, G. High-accuracy detector calibration at the PTB four-crystal monochromator beamline. *Nuclear Instruments and Methods in Physics Research Section A: Accelerators, Spectrometers, Detectors and Associated Equipment. Proceedings of the 7th Int. Conf. on Synchrotron Radiation Instru mentation* **467-468**, 1175. doi:`10.1016/S0168-9002(01)00598-8` (2001).

106. Kramberger, G. *et al.* Investigation of Irradiated Silicon Detectors by Edge-TCT. *IEEE Transactions on Nuclear Science* **57**, 2294. doi:`10.1109/TNS.2010.2051957` (2010).

107. Kramberger, G., Cindro, V., Mandić, I., Mikuž, M. & Zavrtanik, M. Determination of detrapping times in semiconductor detectors. *Journal of Instrumentation* **7**, P04006. doi:`10.1088/1748-0221/7/04/P04006` (2012).

108. Kramberger, G., Cindro, V., Mandić, I., Mikuž, M. & Zavrtanik, M. Charge collection studies on custom silicon detectors irradiated up to 1.6·10 ^{17} n $_{eq}$ /cm $^{-2}$. *Journal of Instrumentation* **8**, P08004. doi:`10.1088/1748-0221/8/08/P08004` (2013).

109. Kramberger, G. *Signal development in irradiated silicon detectors* eng. PhD thesis (Stefan Inst., Ljubljana, Ljubljana, 2001).

110. Suzaki, Y. & Tachibana, A. Measurement of the um sized radius of Gaussian laser beam using the scanning knife-edge. *Applied Optics* **14**, 2809. doi:`10.1364/AO.14.002809` (1975).

111. Göppert-Mayer, M. Über Elementarakte mit zwei Quantensprüngen. *Annalen der Physik* **401**, 273. doi:`10.1002/andp.19314010303` (1931).

112. García, M. F. *et al.* High resolution 3D characterization of silicon detectors using a Two Photon Absorption Transient Current Technique. *Nuclear Instruments and Methods in Physics Research Section A: Accelerators, Spectrometers, Detectors and Associated Equipment*. *Proceedings of the Vienna Conference on Instrumentation 2019* **958**, 162865. doi:`10.1016/j.nima.2019.162865` (2020).

113. Strickland, D. *Development of an ultra-bright laser and an application to multi-photon ionization* PhD thesis (1988). `http://hdl.handle.net/1802/32213` (2023).

114. Vila, I. *TPA-TCT: A novel Transient Current Technique based on the Two Photon Absorption (TPA) process* CERN, 2014. `https://indico.cern.ch/event/334251/contributions/780782/attachments/652612/897369/20141118_TPA_TCT_IvanVila.pdf` (2023).

115. Wiehe, M. *Development of a Two-Photon Absorption - TCT system and Study of Radiation Damage in Silicon Detectors* PhD thesis (Albert-Ludwigs-Universität Freiburg im Breisgau, 2021).

116. Pape, S., Currás, E., Fernández García, M. & Moll, M. Techniques for the Investigation of Segmented Sensors Using the Two Photon Absorption-Transient Current Technique. *Sensors* **23**, 962. doi:`10.3390/s23020962` (2023).

117. Particulars. *Particulars Wide Band Current Amplifiers* 2017. `http://www.particulars.si/downloads/ParticularsAmps-Manuals.pdf` (2023).

118. Gallrapp, C. *et al. The TCT+ setup – a system for TCT, eTCT and timing measurements* DESY Hamburg, 2015. `https://indico.desy.de/event/12934/#19-harware-description-cern-sy` (2023).

119. Jansen, H. *PCBs and mounts for TCT* DESY Hamburg, 2015. `https://indico.desy.de/event/12934/contributions/11143/attachments/7546/8888/2015_10_06_TCT-WS_DESY-PCBs.pdf` (2023).

120. Kramberger, G. *Practical advices for using TCT* Jozef Stefan Institute, Ljubljana, 2016. `https://indico.cern.ch/event/572172/contributions/2327549/attachments/1355768/2049134/TipsAndTricks_Particulars.pdf` (2023).

121. Timsit, S. *Electrical contact resistance: properties of stationary interfaces* in *Electrical Contacts - 1998. Proceedings of the Forty-Fourth IEEE Holm Conference on Electrical Contacts (Cat. No.98CB36238)* (1998), 1. doi:`10.1109/HOLM.1998.722422`.

122. Lentz, T. How does Surface Finish affect solder paste performance. *Proceedings of SMTA International* (2018).

123. Wonsak, S. *Sensor Preparation* DESY Hamburg, 2015. `https://indico.desy.de/event/12934/` (2023).

124. Feindt, F. *Edge-TCT for the Investigation of Radiation Damaged Silicon Strip Sensors* 2017. `https://bib-pubdb1.desy.de/record/317731/` (2022).

125. Schinke, C. *et al.* Uncertainty analysis for the coefficient of band-to-band absorption of crystalline silicon. *AIP Advances* **5**, 067168. doi:`10.1063/1.4923379` (2015).

126. Thorlabs. *LPS-1060-FC Spec Sheet* 2015. `https://www.thorlabs.com/drawings/e4cf1452eb12eac4-E03DEDB2-CA9D-3639-0923325C70DD54F5/LPS-1060-FC-SpecSheet.pdf` (2023).

127. Almagro-Ruiz, A. *et al.* Fiber laser system of 1550 nm femtosecond pulses with configurable properties for the two-photon excitation of transient currents in semiconductor detectors. *Applied Optics* **61**, 9386. doi:`10.1364/AO.470780` (2022).

128. Eremin, V., Verbitskaya, E. & Li, Z. The origin of double peak electric field distribution in heavily irradiated silicon detectors. *Nuclear Instruments and Methods in Physics Research Section A: Accelerators, Spectrometers, Detectors and Associated Equipment* **476**, 556. doi:`10.1016/S0168-9002(01)01642-4` (2002).

129. Synopsys, Inc. *Sentaurus™ Device User Guide* tech. rep. Version O-2018.06 (Synopsys, Mountain View, CA, 2018).

130. Schenk, A. *Advanced Physical Models for Silicon Device Simulation* (ed Selberherr, S.) doi:`10.1007/978-3-7091-6494-5` (Springer, Vienna, 1998).

131. Loi, A. & Contu, A. *TCoDe: A new multithread simulator for silicon sensors in HEP applications* in *2019 IEEE Nuclear Science Symposium and Medical Imaging Conference (NSS/MIC)* (2019), 1. doi:`10.1109/NSS/MIC42101.2019.9060015`.

132. Wei, T., Deng, Z., Wang, X. & Li, R. *Transient Signal Simulation in Pixel Semiconductor Detectors under Pulsed High-Flux Radiation* in *2020 IEEE Nuclear Science Symposium and Medical Imaging Conference (NSS/MIC)* (2020), 1. doi:`10.1109/NSS/MIC42677.2020.9507771`.

133. Spannagel, S. *et al.* Allpix2: A modular simulation framework for silicon detectors. *Nuclear Instruments and Methods in Physics Research Section A: Accelerators, Spectrometers, Detectors and Associated Equipment* **901**, 164. doi:`10.1016/j.nima.2018.06.020` (2018).

134. Schütze, P., Spannagel, S., Wolters, K. & Lachnit, S. *Allpix Squared User Manual* Manual Version v3.0.0 (2023).

135. Schindler, H. & Veenhof, R. *Garfield++* 2023. `https://garfieldpp.web.cern.ch/garfieldpp/` (2023).

136. Cenna, F. *et al.* Weightfield2: A fast simulator for silicon and diamond solid state detector. *Nuclear Instruments and Methods in Physics Research Section A: Accelerators, Spectrometers, Detectors and Associated Equipment. Proceedings of the 10th International Conference on Radiation Effects on Semiconductor Materials Detectors and Devices* **796**, 149. doi:`10.1016/j.nima.2015.04.015` (2015).

137. Kramberger, G. *KDetSim - A root based 3D simulation tool for semiconductor detectors* INFN Trieste, 2016. `https://www-f9.ijs.si/~gregor/KDetSim/Presentations/Trst-KDetSim_Talk.pdf`.

138. Calvo, J. *et al.* TRACS: A multi-thread transient current simulator for micro strips and pad detectors. *Nuclear Instruments and Methods in Physics Research Section A: Accelerators, Spectrometers, Detectors and Associated Equipment* **917**, 77. doi:`10.1016/j.nima.2018.11.132` (2019).

139. Loi, A., Contu, A. & Lai, A. Timing optimisation and analysis in the design of 3D silicon sensors: the TCoDe simulator. *Journal of Instrumentation* **16**, P02011. doi:`10.1088/1748-0221/16/02/P02011` (2021).

140. Kramberger, G. *Comparison of non-commercial detector simulation packages* Workshop. Jozef Stefan Institute, Ljubljana, 2016. `https://indico.cern.ch/event/572172/contributions/2334870/attachments/1355712/2048835/ComparissonOfSimulators_2ndTCT.pdf` (2023).

141. Harris, C. R. *et al.* Array programming with NumPy. *Nature* **585**, 357. doi:`10.1038/s41586-020-2649-2` (2020).

142. Virtanen, P. *et al.* SciPy 1.0: fundamental algorithms for scientific computing in Python. *Nature Methods* **17**, 261. doi:`10.1038/s41592-019-0686-2` (2020).

143. McKinney, W. *Data Structures for Statistical Computing in Python* in *Proceedings of the 9th Python in Science Conference* (eds Walt, S. v. d. & Millman, J.) (2010), 56. doi:`10.25080/Majora-92bf1922-00a`.

144. Reback, J. *et al. pandas-dev/pandas: Pandas 1.4.4* 2022. doi:`10.5281/ZENODO.7037953`.

145. Baker, G. *NumPy/Pandas Speed* 2022. `https://ggbaker.ca/732/content/pandas-speed.html` (2023).

146. Aspnes, D. E. & Studna, A. A. Dielectric functions and optical parameters of Si, Ge, GaP, GaAs, GaSb, InP, InAs, and InSb from 1.5 to 6.0 eV. *Physical Review B* **27**, 985. doi:`10.1103/PhysRevB.27.985` (1983).

147. Green, M. A. Self-consistent optical parameters of intrinsic silicon at 300K including temperature coefficients. *Solar Energy Materials and Solar Cells* **92**, 1305. doi:`10.1016/j.solmat.2008.06.009` (2008).

148. Bortfeld, T. & Schlegel, W. An analytical approximation of depth - dose distributions for therapeutic proton beams. *Physics in Medicine & Biology* **41**, 1331. doi:`10.1088/0031-9155/41/8/006` (1996).

149. Masetti, G., Severi, M. & Solmi, S. Modeling of carrier mobility against carrier concentration in arsenic-, phosphorus-, and boron-doped silicon. *IEEE Transactions on Electron Devices* **30**, 764. doi:`10.1109/T-ED.1983.21207` (1983).

150. Jacoboni, C., Canali, C., Ottaviani, G. & Alberigi Quaranta, A. A review of some charge transport properties of silicon. *Solid-State Electronics* **20**, 77. doi:`10.1016/0038-1101(77)90054-5` (1977).

151. Canali, C., Majni, G., Minder, R. & Ottaviani, G. Electron and hole drift velocity measurements in silicon and their empirical relation to electric field and temperature. *IEEE Transactions on Electron Devices* **22**, 1045. doi:`10.1109/T-ED.1975.18267` (1975).

152. Meurer, A. *et al.* SymPy: symbolic computing in Python. *PeerJ Computer Science* **3**, e103. doi:`10.7717/peerj-cs.103` (2017).

153. Chechev, V. P. & Kuzmenko, N. K. *Am-241 Tables* 2010. `http://www.lnhb.fr/nuclides/Am-241_tables.pdf` (2023).

154. Ziegler, J. F., Ziegler, M. D. & Biersack, J. P. SRIM – The stopping and range of ions in matter (2010). *Nuclear Instruments and Methods in Physics Research Section B: Beam Interactions with Materials and Atoms. 19th International Conference on Ion Beam Analysis* **268**, 1818. doi:`10.1016/j.nimb.2010.02.091` (2010).